THÈSE POUR OBTENIR LE GRADE DE DOCTEUR DE L'UNIVERSITE DE MONTPELLIER

En Electronique

École doctorale : Information, Structures, Systèmes (I2S)

Institut d'électronique et des systèmes (IES)

Acoustic characterization of direct bonding energy

Présentée par Amine IKLIL

Le 28 Novembre 2023

Sous la direction de Pr.Emmanuel LE CLEZIO, Pr.Gilles DESPAUX et l'encadrement de Dr.Frank FOURNEL, Dr.Emilie DELOFFRE

Devant le jury composé de

Pr.Rodolphe VAILLON, Professeur des universités, IES, Université de Montpellier	Examinateur
Pr.Jérôme FORTINEAU, Professeur des universités, INSA Centre Val de Loire	Rapporteur
Pr.Mounsif ECH-CHERIF EL-KETTANI, Professeur des universités, Univ Le Havre Normandie	Rapporteur
Pr.Emmanuel LE CLEZIO, Professeur des universités, IES, Université de Montpellier	Directeur de thèse
Pr.Gilles DESPAUX, Professeur des universités, IES, Université de Montpellier	Directeur de thèse
Dr.Franck FOURNEL, Ingénieur-HDR, CEA-LETI, Université de Grenoble	Encadrant de thèse
Dr.Emilie DELOFFRE, Ingénieur, ST-Microelectronics, Crolles	Encadrant de thèse
Dr.Thomas DELAUNAY, Maitre de conférence, IES, Université de Montpellier	Encadrant de thèse

UNIVERSITÉ DE MONTPELLIER

Contents

List of Figures x

List of Tables xii

General introduction 1

Résumé général 7

1 Context of the project 13
- 1.1 Overview on direct bonding . . . 15
  - 1.1.1 3D integration . . . 15
    - 1.1.1.1 Approaches to packaging . . . 15
    - 1.1.1.2 key 3D integration challenges . . . 18
  - 1.1.2 Direct bonding . . . 19
    - 1.1.2.1 Direct bonding application process requirements . . . 20
    - 1.1.2.2 Contact at ambient temperature . . . 22
    - 1.1.2.3 Hydrophilic and Hydrophobic bonding . . . 22
    - 1.1.2.4 Impact of the annealing process . . . 24
- 1.2 Bonding energy characterization techniques . . . 26
  - 1.2.1 DCB test (Double Cantilever Beam) . . . 26
  - 1.2.2 SAM test (Scanning Acoustic Microscopy) . . . 28
    - 1.2.2.1 SAM operating procedure . . . 28
    - 1.2.2.2 Ultrasound and applied characterization techniques . . . 29
    - 1.2.2.3 Type of transducers and acoustic field . . . 31
    - 1.2.2.4 Ultrasonic resolution . . . 33
- 1.3 Acoustic's physics . . . 34
  - 1.3.1 Acoustic impedance . . . 34
  - 1.3.2 Reflection and transmission coefficients . . . 35
  - 1.3.3 From Hooke law to Longitudinal and transverse waves . . . 36
  - 1.3.4 Rayleigh and Lamb waves generalities . . . 39
- 1.4 Acoustic characterization of direct bonding . . . 41
  - 1.4.1 Overview on acoustic characterization of bonding . . . 41
    - 1.4.1.1 Time signal analysis/ Echography . . . 41
    - 1.4.1.2 Resonance approach/ Spectroscopy . . . 41
    - 1.4.1.3 Guided wave approach . . . 42
  - 1.4.2 Bonding energy acoustic characterization . . . 44
  - 1.4.3 Main results and discussion . . . 45
- 1.5 Conclusion . . . 47

2 Feasibility on hydrophilic and hydrophobic samples **49**
2.1 Introduction and hypothesis . . . 50
2.2 Description of the analytical model . . . 50
2.3 Time signal analysis . . . 52
2.3.1 Hydrophobic case . . . 53
2.3.2 Hydrophilic case . . . 56
2.4 Reflection coefficient analysis . . . 60
2.4.1 Hydrophobic case . . . 60
2.4.2 Hydrophilic case . . . 63
2.5 Variation of the bonding interface condition . . . 69
2.5.1 Distance frequency variation based on bandwidth . . . 69
2.5.2 Thickness variation effect on the reflection coefficient . . . 72
2.5.3 Angle variation effect on the reflection coefficient . . . 74
2.5.4 Variation effect based on the acoustic impedance . . . 76
2.6 Sensitivity curves . . . 77
2.7 Conclusion . . . 79

3 Experimental results and measurement constraints **81**
3.1 Introduction and hypothesis . . . 82
3.2 Experimental protocol . . . 82
3.3 Transducer and measurement constraints . . . 88
3.3.1 Transducer characteristics . . . 88
3.3.2 Empty time window position based on the transducer reflection echoes 90
3.4 Reflection coefficient for an bonded and unbonded conditions . . . 92
3.4.1 Experimental results . . . 92
3.4.2 Theoretical and experimental results comparison . . . 93
3.4.3 Noise impact on the cutoff frequency positions . . . 97
3.5 Experimental results . . . 102
3.5.1 A-scan results on hydrophobic samples . . . 102
3.5.2 C-scan results on hydrophobic samples . . . 104
3.5.3 A-scan along the wafer diameter for hydrophobic samples . . . 106
3.6 Conclusion . . . 106

4 Time signal behavior based on the reflection coefficient variation **109**
4.1 Introduction and hypothesis . . . 110
4.2 Infrared and acoustic images of the opposite notch . . . 111
4.3 Δf variation in the opposite notch . . . 112
4.3.1 Opposite notch variation based on the scan position . . . 112
4.3.2 Opposite notch variation for RT - [100°C-400°C] - 500°C samples . . . 113
4.3.3 Zone B study for RT - [100°C-400°C] - 500°C samples . . . 115
4.3.4 Time signal analysis in the opposite notch . . . 116
4.4 Theoretical similarity based on the opposite notch variation . . . 119
4.5 Amplitude variation study based on the acoustic parameters . . . 123
4.6 Conclusion . . . 128

General Conclusion **131**

A Amplitude variation based on the thickness of an semi infinite plate 137
A. Iklil and E. Le Clezio

B Transmission and reflection of ultrasonic waves in layered media 141
D. L. Folds and C. D. Loggin

C Experimental report 147
A. Iklil and G. Despaux

D Noise analysis results 163

E Git repository 167

Bibliography 176

List of Figures

1 Example of an acoustic image representing bonding defects. 3
2 Examples of energy bonding heat map [1] 4

1.1 Exemple of conceptual structure of a 3-D chip [2]. 15
1.2 Schematic Representations of Major 3D Integration Approaches: (a-c) 3D Packaging Technology, (d-f) Wafer-Level transistor Buildup 3D Technology and (g-k) Monolithic 3D ICs [3–5] 16
1.3 Evolution of multi-chip advanced packaging [6] 18
1.4 Through-silicon via providing electrical links with multiple vertically stacked die [7] 19
1.5 Morphological substrate criteria for bonding energy,(1) domed surface,(2) Flatness,(3) microrugosity. 20
1.6 Example of bonding defect caused by particle contamination 21
1.7 Bonding wave observed during the bonding of 200 *mm* silicon wafers by infrared light (IR) [8]. a) After positioning the two substrates on top of each other, contact between the two surfaces is initiated by local pressure, b) Propagation of the bonding wave, c) End of propagation, the wafers are bonded. 22
1.8 Evolution of bond interface sealing according to the annealing temperature for an hydrophilic bond [1, 9]. 24
1.9 Bonding energy for hydrophilic (Blue curve) and hydrophobic (Black curve) samples according to annealing temperature in an anhydrous atmosphere [10]. 25
1.10 Electron density measurements with XRR of the bonding interface for a hydrophobic bond [11]. 25
1.11 principle of the DCB test applied to direct Bonding [1, 12] 26
1.12 infrared visualization of the area stripped by the blade [8] 27
1.13 Operation diagram of the acoustic microscope (a) in reflection, (b) in transmission modes [13]. *A :acoustic beam - B: delay line - C: Samples - D: circulator - E: Input signal - L: Lens - S : Output signal - T : piezoelectric transducer - TG: generating transducer - TD: detecting transducer - In sky blue : coupling liquid.* 28
1.14 Principle of ultrasonic imaging in the case of direct bonding 29
1.15 Example of A-scans showing a perfect bond and a delamination 30
1.16 C-scan and B-scan scanning modes 31
1.17 Example of C-scan applied to direct bonding [14] 31
1.18 Unfocused (a) and focused (b) acoustic beam 32

1.19 Comparison of SAM images obtain by a) 300 MHz transducer with 2.5 mm focal length, b) 200 MHz transducer with 500 μm focal length, b) 400 MHz transducer with 200 μm focal length, b) 1 GHz transducer with 80 μm focal length [15]. 33
1.20 Axial resolution influence on the time signal 33
1.21 Acoustic beams of 200 MHz planar transducer with lateral resolution of 480 μm (a) and 100 MHz focused transducers with lateral resolution of 48.5 μm (b) and their respective transverse sound pressure amplitude profile [1] 34
1.22 Reflection and transmission of a plane wave normally incident between two media A & B. 35
1.23 Schematic of longitudinal (a) and transverse (b) wave propagation 38
1.24 Lamb waves modes. 39
1.25 Evolution of the modulus of the reflection coefficient in the case of a three-layered structure immersed in water [16]. 42
1.26 Spectroscopy measurement method for direct bonding with ΔQ is bonding energy and Δf the frequency distance 44
1.27 Evolution of the reflection coefficient as a function of the interface quality [1]. Young modulus values E = 130, $2.3e^{-3}$, $1e^{-3}$, $0.5e^{-3}$, $0.23e^{-3}$ Gpa. . . 45
1.28 Reflection coefficient for a planar transducer [1] 45
1.29 Reflection coefficient for a focused transducer [1] 46
1.30 Sensitivity of the frequency distance (measured by SAM) according to the bonding energy (measured by DCB test) (1:RT / 2:100°C-400°C / 3:500°C / 4:600°C / 5:1100°C) [1] 46
1.31 Example of a different cartography [1] 47

2.1 geometry of the multi-layer system 51
2.2 Example of time signals produced by the model 52
2.3 Time response of an bonded wafer in the hydrophobic case (SI//SI) 53
2.4 Time response of an unbonded wafer in the hydrophobic case (SI//SI) . . . 54
2.5 Attenuation of the resonating wave in 1.450 mm of silicon (red), 0.725 mm (pink) dip in water 55
2.6 Time response of an bonded wafer in the hydrophilic case (OX//SI) 57
2.7 Time response of an unbonded wafer in the hydrophilic case (OX//SI) . . . 57
2.8 Time response of an unbonded wafer in the second hydrophilic case (OX//OX) 58
2.9 Time response of an bonded wafer in the second hydrophilic case (OX//OX) 59
2.10 Reflection coefficient of hydrophobic extreme cases, in blue SI//SI, in green SI//Air//SI 60
2.11 Reflection coefficient of hydrophilic extreme cases, in blue SI//SI, in green SI//Air//SI associate with symmetrical (Black) and Anti-symmetrical (Red) Lamb modes 62
2.12 Reflection coefficient of an unbonded layer (in green SI//Air//SI) associate with symmetrical (Black) and Anti-symmetrical (Red) Lamb modes corresponding to a half thickness of the full stack 725 μm 62
2.13 Reflection coefficient of hydrophilic extreme cases, in Red OX//OX, in Black OX//water//OX 64

2.14 Reflection coefficient of hydrophilic extreme cases, in Red OX//OX, in Black OX//water//OX between 180 MHz and 190 MHz 65
2.15 Reflection coefficient of hydrophilic extreme cases, in Red OX//OX, in Black OX//water//OX between 182 MHz and 185 MHz (Anti-symmetric) . 65
2.16 Reflection coefficient of hydrophilic extreme cases, in Red OX//OX, in Black OX//water//OX between 185 MHz and 187 MHz (symmetric) . . . 66
2.17 Non-scale diagram showing the anatomy of OX//OX and OX//SI samples 66
2.18 Reflection coefficient of hydrophilic extreme cases, in Red OX//SI, in Black OX//water//SI 67
2.19 Reflection coefficient of hydrophilic extreme cases, in Red OX//SI, in Black OX//water//SI between 180 MHz and 190 MHz 68
2.20 Reflection coefficient based on Table 2.9 parameters along [50 MHz - 200 MHz] bandwidth. 69
2.21 Example of Anti-symmetric peaks position for Table 2.9 configurations . . 70
2.22 Example of symmetric peaks position for Table 2.9 configurations 70
2.23 Variation of the frequency spread along a larger bandwidth for three different configurations 71
2.24 Reflection coefficient of four different bonding layer thickness based on Table 2.10. 72
2.25 Symmetrical peaks of four different bonding layer thickness based on Table 2.10. 73
2.26 Anti-symmetrical peaks of four different bonding layer thickness based on Table 2.10. 73
2.27 Reflection coefficient evolution for an SI//SI bonded (Right) and SI//SI unbonded (Left) case between a range of 0° and 4° 74
2.28 Reflection coefficient evolution for an SI//SI bonded case between a range of 0° and 4° with the projection on 0.3° in blue, 0.6° in orange, 0.9° in green and 1.2° in red 75
2.29 Classical representation of the reflection coefficient for 0.3° in blue, 0.6° in orange, 0.9° in green and 1.2° in red 75
2.30 Reflection coefficient evolution based on the acoustic impedance and the convergence percentage to a perfect bonding 77
2.31 Sensitivity curves according to the sample type. 78
2.32 Sensitivity curves according to the incident wave frequency 78
2.33 Sensitivity curves of Δf variation relative to acoustic impedance of the nanometric bonding layer 80

3.1 Test bench setup with the five goniometers to adjust the transducer angle attack. 83
3.2 Bonding energy value and their respective opposite notch detachment for hydrophobic and hydrophilic samples [CEA] 84
3.3 Phase indicator for a tilted (left) and parallel (right) transducer in regard to the sample. 84
3.4 Example of an experimental time signal promoting the sample surface echo in red and the full background echoes in green. 85

3.5 Example of an experimental spectrum's promoting the sample surface echo FFT in red and the full background echoes FFT in green for 190 MHz ultrasonic transducer. . . . 85
3.6 Example of an experimental normalized reflection coefficient (Blue) and the threshold applied to extract the minima (Red) . . . 86
3.7 Example of an reflection coefficient after a full stretching . . . 87
3.8 Transducer chronograph . . . 88
3.9 Transducer lens echo joined with its frequency spectrum . . . 89
3.10 Transducer chronograph zoomed on the first and the second lens echoes . . 89
3.11 Transducer signalpower chronograph in dB zoomed on the first and the second lens echoes . . . 90
3.12 Time window and its signal power of the first time fragment relative to a distance between the transducer and the sample of 0.825 mm . . . 90
3.13 Time window and its signal power of the second time fragment relative to a distance between the transducer and the sample of 1.58 mm . . . 91
3.14 Figure 3.12 and Figure 3.13 signal power superposition representing a three echoes' time fragments and four echoes' time fragments respectively, using the same color code. . . . 91
3.15 Normalized time signal of an unbonded (green) and an bonded (blue) zone for SI//SI sample in experimental conditions . . . 92
3.16 Normalized FFT spectrum of an unbonded (green) and an bonded (blue) zone for SI//SI sample in experimental conditions . . . 92
3.17 Normalized and corrected reflection coefficient of an unbonded (green) and an bonded (blue) zone for SI//SI sample in experimental conditions . . . 93
3.18 Time signals (a) and their respective reflection coefficients (b) for five different time signal window . . . 96
3.19 Screenshot based on Figure 3.18 emphasizing on the epigraph of the cutoff frequencies for different number of echoes . . . 96
3.20 Theoretical signals of a bonded case noised with white noise for three different SNR ratio levels. . . . 97
3.21 Theoretical signal with a modelized experimental setup noise . . . 99
3.22 Zoom screenshot on the modelized experimental setup noise . . . 99
3.23 Theoretical signal of a bonded case noised with an modelized experimental setup noise for three different SNR ratio levels. . . . 100
3.24 Ten experimental results for the five samples [RT - 100°C-400°C - 500°C - 600°C - 1100°C] represented in stars with previous experimental results displayed in vertical lines [1] using no motorization and no averaging. . . . 102
3.25 Ten experimental results for the five samples [RT - 100°C-400°C - 500°C - 600°C - 1100°C] represented in stars with previous experimental results displayed in vertical lines [1] using no motorization and with averaging [25 sample]. . . . 103
3.26 Ten experimental results for the five samples [RT - 100°C-400°C - 500°C - 600°C - 1100°C] represented in stars with previous experimental results displayed in vertical lines [1] using motorization and no averaging. . . . 104

3.27 Ten experimental results for the five samples [RT - 100°C-400°C - 500°C - 600°C - 1100°C] represented in stars with previous experimental results displayed in vertical lines [1] using motorization and with averaging [25 samples]. . . . 105
3.28 Percentage variation curves of ΔF for RT (blue), [100°C-400°C] (cyan), 500°C (green) and 1100°C (red) over a diameter of 20 cm. [ELC] . . . 106
3.29 Experimental results for the five samples [RT - [100°C-400°C] - 500°C - 600°C - 1100°C] with three background echoes represented in stars and four in circles using 400 averaged samples. . . . 107

4.1 Infrared images on three different hydrophobic samples bonded at various temperature (Left : Room temperature, Center : [100°C-400°C], Right : 1100°C) . . . 111
4.2 25 mm^2 SAM image on the opposite notch emphasizing on the unbonded zone (zone A), the bonded zone (zone C) and the transitory zone (zone B) 111
4.3 Variation of the Δf for three attempt on room temperature [RT] samples . 112
4.4 Variation of the Δf for three samples (RT in blue - [100°C-400°C] in green - 500°C in red) . . . 114
4.5 Zone B variation of the Δf for three samples (RT in blue - [100°C-400°C] in green - 500°C in red) . . . 115
4.6 Δf variation in the opposite notch for [100°C-400°C] sample used in subsection 4.3.4 experiment . . . 116
4.7 Signal behavior on the opposite notch . . . 117
4.8 Signal behavior in zone B on the opposite notch . . . 118
4.9 Reflection coefficient result of the opposite notch area relative to the signals in Figure 4.7 . . . 119
4.10 Time signal of an SI//SI unbonded state with a labeling of the different echoes . . . 120
4.11 Time signal behavior relative to the acoustic impedance variation of the nanometric bonding layer . . . 121
4.12 Magnitude variation in dB for BE 1 . . . 123
4.13 Magnitude variation in dB for BE 2 . . . 124
4.14 Magnitude variation in dB for BE 3 . . . 125
4.15 Magnitude variation in dB for BLE 1 . . . 125
4.16 Magnitude variation in dB for BLE 2 . . . 126
4.17 Magnitude variation in dB for BLE 3 . . . 126
4.18 Magnitude variation of noised BE and BLE (Green : 15 dB SNR - Blue : 25 dB SNR - Red : 40 dB SNR) . . . 128
4.19 Reflection coefficient for three different frequencies . . . 131
4.20 Time signal comparison of two experimental [RT - 1100°C] and a theoretical results emphasizing on the difference between the two extreme samples . . 132
4.21 RT time signal BLE 2 magnitude related to it acoustic impedance . . . 133
4.22 Δf variation at 200 MHz and 70 MHz for the same area . . . 133
4.23 Time signal behavior relative to the acoustic impedance variation of the 10 nm SI//SI bonding layer . . . 134
4.24 Time signal behavior relative to the acoustic impedance variation of the 20 nm SI//SI bonding layer . . . 135

4.25 Time signal behavior relative to the acoustic impedance variation of the 40 nm SI//SI bonding layer . . . 135
4.26 Time signal behavior relative to a simultaneous variation of the acoustic impedance [0 MRay,18 MRay] and the thikness [20 nm, 0 nm] of an SI//SI bonding layer . . . 136

A.1 Schematic diagram of reflection and transmission of the propagation of an ultrasonic wave in a theoretical three-layer made up of a layer of water, silicon and a semi-infinite medium of silicon oxide. . . . 138
A.2 Numerical evolution of the comparison between the surface echo of the silicon layer and the echo reflected by the oxide surface as a function of the thickness wavelength ratio . . . 139

B.1 Reflection and transmission coefficient output based on the analytical model of an bonded SI/SI wafer . . . 146
B.2 Modulation of the reflection and transmission coefficient output based on the analytical model of an bonded SI/SI wafer . . . 146

List of Tables

1.1 3D integration technologies and related applications [5, 17, 18] 17
1.2 Van der Waals energy between two substrates separated with a distance D for Hydrophobic and hydrophilic bonding [11] 23
1.3 Acoustic impedance of different media 35
1.4 Comparison of bonding characterization researches 43

2.1 Unbonded and bonded interface theoretical parameters of the hydrophobic case (SI//SI). 53
2.2 Unbonded and bonded interface theoretical parameters of the hydrophilic case (OX//SI) 56
2.3 Unbonded and bonded interface theoretical parameters of the hydrophilic case (OX//OX) 56
2.4 TOF and amplitude values of the time response of unbonded and bounded hydrophilic layers (OX//SI) 58
2.5 TOF and amplitude values of the time response of unbonded and bounded hydrophilic layer (OX//OX) 59
2.6 Cutoff frequencies of the reflection coefficients based on Figure 2.10 61
2.7 Cutoff frequencies of the reflection coefficients based on Figure 2.13 64
2.8 Cutoff frequencies of the reflection coefficients based on Figure 2.18 67
2.9 Bonding layers intrinsic properties used in subsection 2.5.1 69
2.10 Bonding layers intrinsic properties used in subsection 2.5.2 first part. . . . 72
2.11 Bonding layers intrinsic properties used in subsection 2.5.4 76

3.1 Cutoff frequencies of the reflection coefficients based on Figure 3.17 94
3.2 Cutoff frequencies of an bonded case in theoretical and experimental conditions 94
3.3 Cutoff frequencies of an unbonded case in theoretical and experimental conditions 95
3.4 White noise impact on cutoff frequencies position analysis 98
3.5 Modelized experimental noise impact on cutoff frequencies position analysis 101
3.6 Mean, standard deviation and mean average error for the no motorization and no averaging setup 103
3.7 Mean, standard deviation and mean average error for the no motorization and with averaging setup 104
3.8 Mean, standard deviation and mean average error for the with motorization and no averaging setup 105
3.9 Mean, standard deviation and mean average error for the with motorization and with averaging setup 105

4.1 Opposite notch scan test parameters of the three experiments displayed in Figure 4.4 114

D.1 White noise impact on cutoff frequencies position analysis 164
D.2 Modelized experimental noise impact on cutoff frequencies position analysis 165

General introduction

In the first quarter of the 21st century, microchips are a priceless commodity. From airplanes to smartphones, they're at the center of devices that we use daily. In 2020, more than 932 billion chips were manufactured around the world, feeding a 440 billion euros industry[1]. Those sets of electronic circuits on a small flat piece of silicon deliver better performance, lower cost and new functionalities with each generation. The development of microelectronics started in the early 1960s. The discovery of semiconductor materials and the creation of the transistor made the transition from analog to digital signals possible. This transition facilitated the development of electronic circuits with increasingly powerful functions.

The essential material in the microchip industry is silicon, which is made of sand, one of the most abundant resources in the globe. Silicon wafers are produced using a type of sand called silica sand, which is made of silicon dioxide. Firstly, the silica sand is melted and cast in the shape of cylinder called 'ingot' and, furthermore, sliced into thin wafers. The important characteristic of silicon is its semiconducting property. Unlike other conductive materials, silicon has the ability to modify its conductive properties by mixing it with other materials such as boron or phosphorus, which allows the control of the electrical current flowing into it. These advantages of silicon can provide millions of tiny switches on a wafer by adding and extracting materials to form a multilayered grid of interconnected electronic structures.

For nearly half-century, the semiconductor researchers and manufacturers reduced significantly the size of microchips. The constant progress they have made, combined with the massive production of these components, has allowed them to drastically cut the costs of microelectronic components. Smaller size and lower costs have made it possible for manufacturers to regularly offer new products that are cheaper and more efficient. Today, a microchip the size of a coin contains billions of transistors. These improvements are behind the incredible increase in computing power and memory functions that have brought the technology to its current level. For example, the computer that operated the Apollo missions to the moon was more than twice as powerful as a Nintendo console. A regular domestic computer today has around 100,000 times more processing power, with roughly seven million times more ROM and up to one million times more RAM. This progress on computing power and memory functions opens a new pad to applications such as artificial intelligence, virtual reality and 5G connectivity.

In this race to cost reduction and miniaturization, new methods of microchip manufacturing were developed suchlike 3D integration. This technique aims to assemble

[1]Source : World Semiconductor Trade Statistics

chips one on top of the other in order to reduce mainly the length of connections.Thus, the communication among the inner parts of the chip will be much faster and the power consumption related to the length of paths will be much lower. This new type of configuration provides different technologies in the same element and high performance on the same component.

In order to obtain multi-layer chips, the steps required are bonding, thinning and linking the multiple layers. Firstly, the bonding of silicon wafers is done after their alignment. For this, various bonding techniques can be employed, but in the framework of this research, direct bonding is the one adopted. Thenceforth, thinning and interconnections are made respectively and successively after bonding. Which allows the reduction of thickness and thus facilitates the realization of the interconnections holes also called TSV (Trough Silicon Vias). By repeating this process, a pile of electronic circuits can be made which gives unlimited possibilities.

Evaluation of bonding energy

The core of 3D integration is bonding. In the course of its development, many techniques have been elaborated depending on the nature of surfaces used. Generally, bonding techniques in microelectronics can be classified into three categories. The first dedicated to metal layers such as thermocompression or ultrasonic welding. The second category includes insulating layers, while the last category encompasses techniques such as covalent, anodic and direct bonding [19]. Notably, this last category stands out for its important feature: it achieves a high-quality bonding without the need for any adhesive material.

Direct bonding is one of the solutions that allowed to transform the industry particularly through the development of innovative substrates. It consists of a simple contact, at room temperature and atmospheric pressure, of two sufficiently smooth and clean surfaces in order to create an adhesion. The advantages of direct bonding are high bonding energy, hermeticity and reversibility before annealing. The principle of this technique depends on the formation of low-energy intermolecular bonds such as Van der Waals bonds or hydrogen bonds [20]. To increase the bond strength, a thermal treatment is applied to increase the density of higher energy bonds such as covalent bonds.

Generally, the presence of defects at the bonding interface and bonding energy are the two parameters that determine bonding quality. The bonding energy expressed in J/m^2 and which is relative to the energy necessary to separate two wafers is the main parameter of bond quality. There are several techniques to assess this parameter. Among this technique, the Double Cantilever Beam is the most utilized. Also called DCB, it remains a relatively simple technique to set and easy to interpret. The main idea is to insert a blade in order to detach the two wafers and measure the length of the cleavage. Overall, two major drawbacks of the DCB test are observed. The first is the deterioration of the sample after the test, and the second is the inability to deduce the value of the bonding energy locally on a sample.

Acoustic microscopy as a solution

Acoustic microscopy is a widely used imaging technique in the field of direct bonding. Its main purpose is to detect bonding defects (Figure 1). This *NDT* technique is also involved in the measurement of cleavage distance during the DCB test. It can as well be used to perform topographic analysis of surfaces. In this dynamic, an NDT treatment capable to distinguish between samples based on their bonding energy levels becomes a subject of investigation.

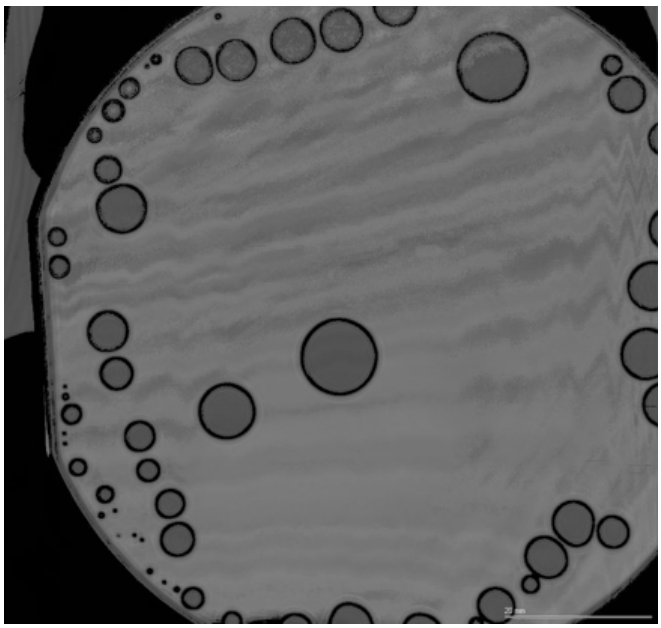

Figure 1: Example of an acoustic image representing bonding defects.

Furthermore, many NDT applications have been developed in order to inspect bonding interfaces. *Benlmostafa and Molinero* presented a numerical modeling of ultrasound propagation in a multi-layer bonded structure [21]. Their study shows the impact of two different bonding conditions on Lamb wave dispersion curves. *Siryabe* proposed an evaluation of the mechanical properties of the interface (modeled by interfacial stiffness) based on Lamb wave transmission coefficient [22]. He found that a poor adhesion is reflected by low values of the interface stiffness, which can be quantified using guided ultrasonic waves. *Lavrentyev and Rokhlin* achieved to determine Lamé parameters and the thickness of an adhesive layer between two substrates. Their measurement is based on the reflection coefficients for two angles of incidence in a frequency range between 3 and 10 MHz [23]. More closely to direct bonding, *Dekious* shows that the difference of bonding quality caused variations in the reflection coefficient at normal incidence [1]. This latest research was the result of a collaboration between CEA LETI, STMicroelectronics and IES to establish a new NDT characterization of bonding energy based on ultrasound microscopy. The major result of this research is the presentation of the first heat maps of bonding energy (Figure 2). This second project summarized by this manuscript is the continuation of the work done in 2016 by *Ali Dekious* Ph.D [1].

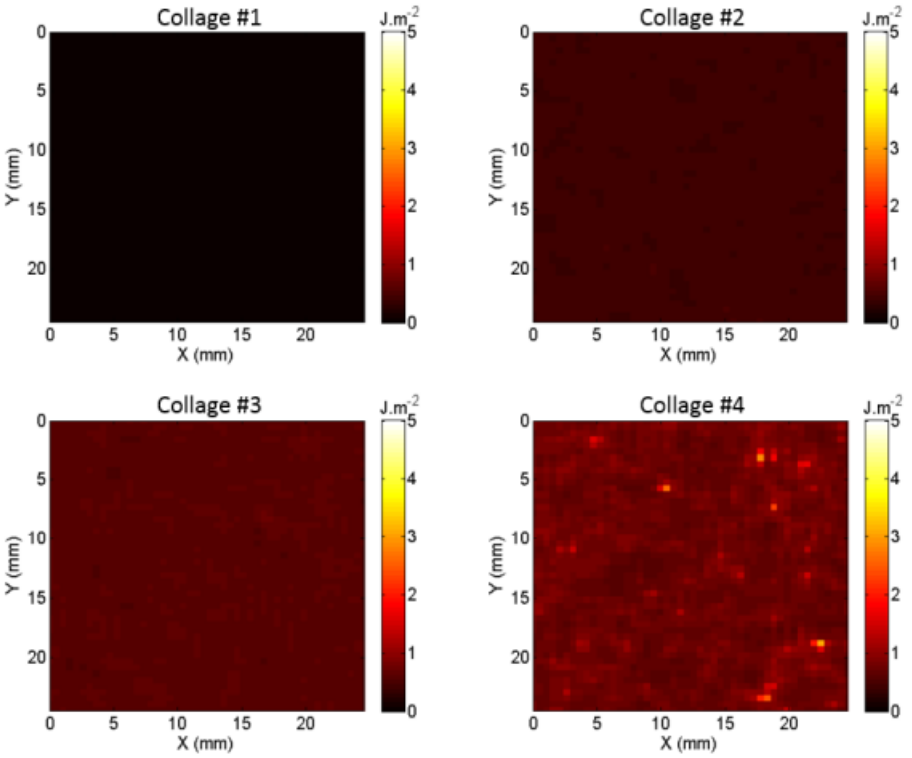

Figure 2: Examples of energy bonding heat map [1]

Presentation of the different chapters

The main objective of this research is to test the feasibility and the repeatability of the developed technique on more complex samples in terms of layering structure. It is thus a question of putting in real conditions the proof of concept established by *Dekious*. To do so, a work of optimization on the test bench was carried after each measurement campaign. This development was also coupled with simulation tools capable of reproducing acoustic signals arising from multi-layer structures similar to the one selected for the experiment. This allows the presentation and analysis of the theoretical and experimental approach of the ultrasonic wave propagation in a multi-layer structure of this type.

In chapter 1, an overview on direct bonding is established to contextualize all the related terminology. This introduction includes definitions and procedures related to both hydrophilic and hydrophobic bonding techniques, as well as the impact of the annealing process on the bonding layer. Additionally, bonding energy characterization techniques such as the Double Cantilever Beam (DCB) and the Scanning Acoustic Microscopy (SAM) are highlighted to define the vocabulary used in the manuscript. Moreover, the chapter discusses general principles of acoustic physics, covering concepts such as acoustic impedance, reflection and transmission coefficients, Hooke law and finally Rayleigh and Lamb waves generalities. The final subsection of chapter 1 presents an overview on acoustic characterization of a bonding layer in general by emphasizing on three main approaches. These are Time Signal Analysis or Echography, Spectroscopy and lastly the Guided Wave approach. All these outlook are deeply analyzed in order to choose the right process in the case of bonding energy acoustic characterization.

In chapter 2, the feasibility on hydrophilic and hydrophobic samples is studied. The analytical model used to simulate the wave propagation in the different anatomies is presented and described. The first subsection provides chronographs for the two extremes which are the bonded and unbonded cases. Time signal analysis provides elements on the wave behavior based on the sample anatomy. This first subsection is complemented by the reflection coefficient analysis which provides a deeper outlook on the anti-symmetrical and symmetrical peaks' behavior on the bonded and unbonded case. Furthermore, complexity is added to the analysis by studying the variation of the bonding interface conditions such as the thickness and intrinsic properties of the bonding layer. The transducer angle and bandwidth impact are also studied to quantify their effect on the reflection coefficient. chapter 2 is summarized with a sensitivity curve that displays several frequencies and emphasis on the first theoretical limitation the bonding energy acoustic characterization encounters.

Next, chapter 3 displays the experimental results and the measurements constraint based on the bench test used in this study. Firstly, the experimental protocol is described based on the improvements established in this study, then the transducer characteristics are discussed to highlight their main features. Secondly, the experimental reflection coefficients for an bonded and unbonded cases are shown to display all the pros and cons observed on the symmetrical and anti-symmetrical peaks. The study of the reflection coefficient under simulated real conditions is also presented, with a focus on the impact of noise on the positions of the cutoff frequencies. This emphasizes the importance of the Signal-to-Noise Ratio (SNR) on the accuracy of the experimental measurements. Lastly, the experimental result on the center of the samples for five annealing temperatures are presented and discussed. finally, chapter 3 concludes with a comparison between the measurements obtained from the old setup and the new setup. Various elements that contribute to the accuracy of the bonding characterization technique are quantified and analyzed. These elements include the Signal-to-Noise Ratio (SNR), the number of used background echoes, the effect of averaging, and the impact of different sample types (hydrophobic and hydrophilic). The comparison allows the understanding of the limitations and improvements achieved with the new setup and the identification of areas for further enhancement.

Finally, chapter 4 goes beyond these limitations and provides answers to all the reflections established in chapter 3. Indeed, chapter 4 presents the spectroscopy technique with a different perspective, offering new and unique insights into the wave propagation in a multi-layer structure. The chapter introduces a novel representation of the acoustic signals, showcasing the behavior of the reflection coefficient and time signals under varying intrinsic properties of the bonding layer. This new outlook provides a deeper understanding of the acoustic responses in different bonding conditions and sheds light on the potential of the spectroscopy technique for characterizing bonding energy. By exploring the patterns of phase cancellation and magnitude variations, the chapter highlights the significance of certain features in the acoustic signals that are crucial for successful bonding characterization.

In general, this thesis provides various insights on the wave propagation in a multi-layer structure. These observations extend beyond the context of bonding

characterization and have potential applications for other structures containing a bonding layer. The results obtained throughout this manuscript are centered around understanding the wave propagation, including both theoretical and experimental findings. The empirical observations derived from the analytical model and experimental attempts make this thesis a comprehensive and valuable resource for applying the spectroscopy technique. The knowledge gained from this research can contribute to the advancement of acoustic characterization techniques and facilitate further investigations in the field of multi-layer structure acoustic characterization.

Résumé général

Le collage direct est une technique d'assemblage qui permet d'obtenir des collages spontanés sans matière adhésive. L'utilisation de cette technique dans le domaine de la microélectronique commence avec la fabrication de structure SOI (Silicon-on-Insulator) [20]. Aujourd'hui, le collage direct est aussi très utilisé au sein des intégrations 3D qui consiste à assembler des puces verticalement afin de réduire la longueur des connexions. Ce qui permet une communication plus rapide entre les différentes puces et une consommation d'énergie réduite. La réalisation d'un collage direct nécessite des conditions morphologiques et chimiques des surfaces des wafers. Ces conditions permettent alors une adhésion spontanée à température ambiante et à pression atmosphérique. Il est important que les surfaces des deux wafers soient parfaitement lisses, propres et planes permettant ainsi la création des liaisons intermoléculaires avec des forces de faible énergie telles que les forces de capillarité et les forces de Van der Waals avec notamment les liaisons hydrogènes. À ce stade, l'énergie de collage exprimée en J/m^2 et qui est relative à l'énergie nécessaire à la séparation des deux surfaces est faible. Pour l'augmenter, un traitement thermique est appliqué afin d'augmenter la densité des liaisons de plus forte énergie de type liaisons covalentes [14].

Dans le cas du collage de silicium et de son oxyde, il existe deux types de collages directs : le collage hydrophobe de Si/Si qui conduit, durant le recuit, à une fermeture de l'interface du collage pour obtenir un seul wafer en silicium, et le collage hydrophile SiO2/SiO2 mettant en œuvre des couches d'oxydes plus ou moins épaisse à la surface du silicium. Selon la nature du collage, des études sur la fermeture de l'interface de collage montrent que l'évolution de la variation de l'énergie de collage en fonction de la température est très différente [10] (Figure 1.9). Cela s'explique par la différence des états de surfaces entre les surfaces hydrophobe et hydrophile. L'énergie de collage est l'un des principaux paramètres d'évaluation des collages directs. Il existe plusieurs techniques pour évaluer cette force. Parmi ces techniques, la technique du double levier à déplacement imposé (Double Cantilever Beam) ou aussi appelé clivage de coin reste la plus utilisée. Le Test DCB reste une technique relativement simple à mettre en place et facile à interpréter. Cette technique consiste à insérer une lame afin de provoquer un décollement des wafers (Figure 1.11). Globalement, deux inconvénients majeurs du test DCB sont observés. Le premier est la détérioration de l'échantillon après le test. Et, le deuxième se résume dans l'incapacité de déduire la valeur de l'énergie de collage localement sur un échantillon. Dans ce manuscrit, l'idée principale est de proposer une alternative au test DCB. Cette technique alternative doit proposer une solution non destructive avec la possibilité de mesurer l'énergie de collage sur l'intégralité de la surface d'un échantillon.

La microscopie acoustique est une solution idéale pour ce type d'application. Grâce à sa résolution latérale et sa rapidité d'exécution, la microscopie acoustique propose des avantages de qualité pour contrôler à la fois la surface et l'interface d'un collage grâce aux ultrasons. La microscopie acoustique est utilisée dans le contexte du collage direct pour des fins d'imagerie pour détecter des défauts de collage (Figure 1). Elle est aussi impliquée dans la mesure de la distance de décollement L pendant le test DCB. Elle peut aussi servir pour effectuer des analyses topographiques des surfaces. Dans cette dynamique, un traitement capable de discriminer des échantillons en se basant sur leurs niveaux d'énergie de collage devient un sujet de questionnement. Dans ce contexte, Dekious [1] montre que la variation de la qualité de collage sur des échantillons hydrophobes provoquait des variations du coefficient de réflexion à incidence normale. Ces variations correspondent à la différence de fréquence entre les pics symétriques et antisymétriques dans le coefficient de réflexion, et elles sont désignées sous le terme de "distance fréquentielle" Δf (Figure 1.28). D'un point de vue expérimental, il présente ces variations sous forme de cartographies d'énergie de collage (Figure 1.31). C'est dans la continuité de ces travaux que le CEA LETI, STMicroelectronics et IES collaborent pour établir une nouvelle technique de caractérisation de l'énergie de collage en utilisant la microscopie acoustique.

L'objectif principal de ce travail est de tester la faisabilité et la répétabilité de la technique développée sur des échantillons plus complexes en termes de structure de stratification. Il s'agit donc de mettre en conditions réelles la preuve de concept établie par *Dekious* [1]. Pour ce faire, un travail d'optimisation sur le banc d'essai a été réalisé après chaque campagne de mesure. Ce développement a également été couplé à des outils de simulation capables de reproduire les signaux acoustiques issus de structures multicouches similaires à celle choisie pour l'expérience. Ceci permet de présenter et d'analyser l'approche théorique et expérimentale de la propagation des ondes ultrasonores dans une structure multicouche de ce type.

Le premier chapitre (chapter 1) est une introduction qui résume la majorité des concepts et terminologies associés à la thématique du collage direct et la microscopie acoustique. Cette partie met en avant les définitions et les procédures relatives aux techniques de collage direct du silicium et son oxyde, ainsi que l'impact du processus de recuit sur la couche du collage. En outre, les techniques de caractérisation de l'énergie de collage telle que la technique du double levier à déplacement imposé ou aussi appelé clivage de coin (DCB) et la microscopie acoustique sont mises en évidence pour mettre en contexte la problématique abordée dans ce travail. Puis, le chapitre aborde les principes généraux de l'acoustique physique, couvrant des concepts tels que l'impédance acoustique, la loi de Hooke et enfin des généralités sur les ondes de Rayleigh et de Lamb. La sous-partie d'après présente une vue d'ensemble de la caractérisation de différent type de collage par microscopie acoustique en mettant l'accent sur trois approches principales. Il s'agit de l'analyse du signal temporel ou échographie, de la spectroscopie et enfin de l'approche par ondes guidées. Finalement, les travaux de recherche issue de la première thèse reliée à ce sujet sont synthétisés et discutés afin de mettre en contexte l'état de l'art de la thématique et mettre en évidence les points les plus essentiels.

Dans le deuxième chapitre (chapter 2), la faisabilité de la technique sur des échantillons hydrophiles et hydrophobes est étudiée. Le modèle analytique utilisé pour simuler la propagation des ondes dans les différentes structures collées est présenté et décrit (Figure 2.1). Ensuite, une analyse approfondie des chronogrammes des signaux acoustiques issue des différentes structures est discutée afin de comprendre le comportement du signal dans les différents cas de figure. Cette partie est complétée par l'analyse des coefficients de réflexion qui fournissent une perspective plus approfondie sur le comportement des pics symétriques et antisymétriques. De plus, l'analyse des variations des conditions de l'interface de collage ajoute un deuxième niveau de complexité, des éléments tels que l'épaisseur et les propriétés intrinsèques de la couche de collage sont prises en considération afin de montrer leurs impacts sur le coefficient de réflexion. L'angle du transducteur et l'impact de la largeur de bande sont également étudiés pour quantifier leurs influences sur le résultat final. Ce chapitre est résumé par une courbe de sensibilité qui affiche l'impact de la fréquence sur le comportement des pics symétrique et antisymétrique, ce qui met l'accent sur la première limitation théorique que rencontre la caractérisation acoustique de l'énergie de collage (Figure 2.33).

Ensuite, le troisième chapitre (chapter 3) présente les résultats expérimentaux ainsi que les contraintes de mesure observées lors de l'utilisation du banc de test développé dans le cadre de cette étude. Dans un premier temps, le protocole expérimental est décrit, en mettant en évidence les améliorations spécifiques apportées dans le cadre de cette recherche. Ensuite, les caractéristiques des transducteurs sont présentées afin de souligner leurs principales spécifications et limitations. Par la suite, les coefficients de réflexion expérimentaux sont présentés et comparés à leurs semblables théoriques pour les deux cas extrêmes : les échantillons collés et les échantillons non collés. Cette comparaison mettra en évidence les avantages et les inconvénients observés sur les pics symétriques et antisymétriques (Table 3.3 - Table 3.2). Nous aborderons également la comparaison entre les coefficients de réflexion observés expérimentalement et ceux prédits théoriquement, en mettant particulièrement l'accent sur l'impact du bruit sur les positions des fréquences de coupure. Cette analyse mettra en lumière l'importance du rapport signal sur bruit (SNR) dans la précision des mesures expérimentales. À cette fin, une étude sur le bruitage des signaux théoriques est effectuée en utilisant du bruit blanc et du bruit simulé, afin de quantifier l'effet du bruit sur la position des pics du coefficient de réflexion (Table 3.4 - Table 3.5). Enfin, le troisième chapitre se conclut par une comparaison entre les mesures obtenues avec le nouveau banc de test. Divers éléments contribuant à la précision de la technique de caractérisation du collage sont quantifiés et analysés. Ces éléments comprennent le rapport signal sur bruit (SNR), le nombre d'échos de fond utilisés, l'effet de la moyenne. La comparaison permet de comprendre les limites et les améliorations obtenues et d'identifier les potentiels points susceptibles d'être améliorés. Finalement, différentes expérimentations sont menées. Les tests réalisés au centre de l'échantillon démontrent la capacité de détecter des échantillons présentant une faible adhérence, tandis que les résultats obtenus avec des échantillons à forte énergie de collage demeurent très compact (Figure 3.29). De plus, des mesures expérimentales révèlent la variation des distances fréquentielles sur un diamètre de 20 cm. Ces résultats démontrent la faisabilité de la caractérisation de l'énergie de collage par microscopie acoustique (Figure 3.28).

Enfin, le quatrième chapitre (chapter 4) va au-delà de ces limitations et fournit des réponses à toutes les réflexions établies dans le troisième chapitre (chapter 3). En effet, cette partie présente la technique de spectroscopie sous un angle différent, offrant des perspectives nouvelles et uniques sur la propagation des ondes dans une structure multicouche. Le chapitre introduit une nouvelle représentation des signaux acoustiques, mettant en évidence le comportement du coefficient de réflexion et des signaux temporels en fonction des propriétés intrinsèques variables de la couche du collage (Figure 4.9 - Figure 4.7). Cette nouvelle perspective permet de mieux comprendre les réponses acoustiques dans différentes conditions de collage et met en lumière le potentiel de la technique de spectroscopie pour caractériser l'énergie de collage.

Tout d'abord, la zone du bord à l'opposée de l'encoche sur les échantillon donne un aperçu du déplacement des pics antisymétrique, qui met en évidence une véritable variation du coefficient de réflexion. Il est observé que cette zone contient trois zones distinctes. La première zone représente un décollement (Zone A). La deuxième zone correspond à une variation brutale du Δf (Zone B). Enfin, une troisième où la variation du Δf reste stable et proportionnelle à une structure entièrement collée (Zone C). Il est conclu que la zone B représente un grand potentiel pour détecter des variations de l'énergie de collage, puisque c'est la seul zone de l'échantillon où on constate un réel déplacement des pics antisymétriques en fonction de l'état du collage (Figure 4.8).

Figure 4.18 montre que le banc de test affiche une limitation liée à l'amplitude des échos issue de l'interaction de l'onde acoustique incidente avec la couche du collage. Cette limitation se traduit par une insuffisance du système d'aquisition à détecter ces signaux car ils sont au-dessus du rapport signal sur bruit. Dans le dispositif expérimental, le rapport signal sur bruit est égal à 25 dB, ce qui limite les échos réfléchie par la couche du collage à -37 dB de magnitude. Le rapport signal sur bruit déforme l'amplitude des échos de font et les écho réfléchi par la couche du collage, ce qui limite le nombre de nuances possibles au niveau du signal temporel. Figure 4.18 montrent qu'un rapport signal sur bruit plus élevé est recommandé pour atteindre des impédances plus élevées, qui sont corrélées avec des valeurs d'amplitude plus faibles. Cette observation peut également être observée en comparant Figure 4.11 et Figure 4.7. Dans les résultats expérimentaux, la valeur de magnitude du bruit ambiant est représentée en bleu ciel, tandis que le bruit ambiant théorique est représenté en vert clair. Cette différence indique que la configuration théorique peut atteindre une magnitude de -80 dB, alors que la configuration expérimentale ne peut atteindre que -40 dB. Dans l'ensemble, l'élément essentiel à prendre en compte afin de réussir ce type de caractérisation est relié à la capacité du système d'acquisition à détecter les minuscules variations d'amplitude issue de l'écho réfléchi par la surface du collage (Figure 4.15). Aujourd'hui, cette limitation ne permet pas de détecter tous les échos susceptibles de représenter l'ensemble des nuances de collage possibles. De plus, il convient de noter que le bruit ambiant peut avoir un impact significatif sur la précision de la localisation des minima locaux au niveau du coefficient de réflexion. Pour améliorer le dispositif, des travaux sur le capteur visant à obtenir plusieurs échos et un système d'acquisition capable de garantir une magnitude atteignant -80 dB sont essentiels pour le succès de cette technique, en se fondant sur les résultats théoriques (Figure 4.18).

Finalement, l'analyse théorique du signal temporel révèle de nouvelles caractéristiques concernant la relation entre l'impédance acoustique de la couche de collage et la résonance du signal temporel. L'observation de ces échos met en évidence leur potentiel, notamment en raison de leur comportement de magnitude décroissante. Cela confirme que cette catégorie d'échos est la plus adaptée à des mesures calibrées et précises. Cette constatation rejoint la remarque précédente concernant l'importance d'avoir un banc de test capable de se libérer des contraintes citées précédemment pour exploiter pleinement ce potentiel (Figure 4.11).

En conclusion, la technique de caractérisation du collage s'est révélée extrêmement prometteuse en tant qu'outil puissant pour l'analyse des matériaux et la caractérisation du collage. Elle peut fournir des informations précieuses sur les propriétés intrinsèques des couches de collage. Toutefois, l'efficacité de la technique dépend fortement de facteurs tels que le rapport signal sur bruit (SNR) et la capacité du capteur à générer un train d'ondes suffisamment long. Des améliorations futures des dispositifs expérimentaux et des techniques de traitement des données pourraient encore étendre les capacités de la technique et élargir son application dans le domaine de la science et de l'ingénierie des matériaux.

Chapter 1

Context of the project

Contents

1.1 Overview on direct bonding 15
1.1.1 3D integration 15
1.1.1.1 Approaches to packaging 15
1.1.1.2 key 3D integration challenges 18
1.1.2 Direct bonding 19
1.1.2.1 Direct bonding application process requirements . . . 20
1.1.2.2 Contact at ambient temperature 22
1.1.2.3 Hydrophilic and Hydrophobic bonding 22
1.1.2.4 Impact of the annealing process 24
1.2 Bonding energy characterization techniques 26
1.2.1 DCB test (Double Cantilever Beam) 26
1.2.2 SAM test (Scanning Acoustic Microscopy) 28
1.2.2.1 SAM operating procedure 28
1.2.2.2 Ultrasound and applied characterization techniques . 29
1.2.2.3 Type of transducers and acoustic field 31
1.2.2.4 Ultrasonic resolution 33
1.3 Acoustic's physics 34
1.3.1 Acoustic impedance 34
1.3.2 Reflection and transmission coefficients 35
1.3.3 From Hooke law to Longitudinal and transverse waves 36
1.3.4 Rayleigh and Lamb waves generalities 39
1.4 Acoustic characterization of direct bonding 41
1.4.1 Overview on acoustic characterization of bonding 41
1.4.1.1 Time signal analysis/ Echography 41
1.4.1.2 Resonance approach/ Spectroscopy 41
1.4.1.3 Guided wave approach 42

1.4.2 Bonding energy acoustic characterization 44
1.4.3 Main results and discussion 45
1.5 Conclusion 47

1.1 Overview on direct bonding

1.1.1 3D integration

3D integration is an essential technique in microelectronics progress. It covers the main approaches and methods to create a vertical electronic circuit. This type of chip contains a large number of technologies in a very compact package (Figure 1.1). One of the first attempt to make this bracket of circuits was carried by Robert W. Haisty, Rowland E. Johnson and Edward W. Mehal in 1964 [24]. Today, we are way ahead by presenting 3D circuits that reduce energy consumption and packaging, increase performances and reliability together with high functionality [25, 26].

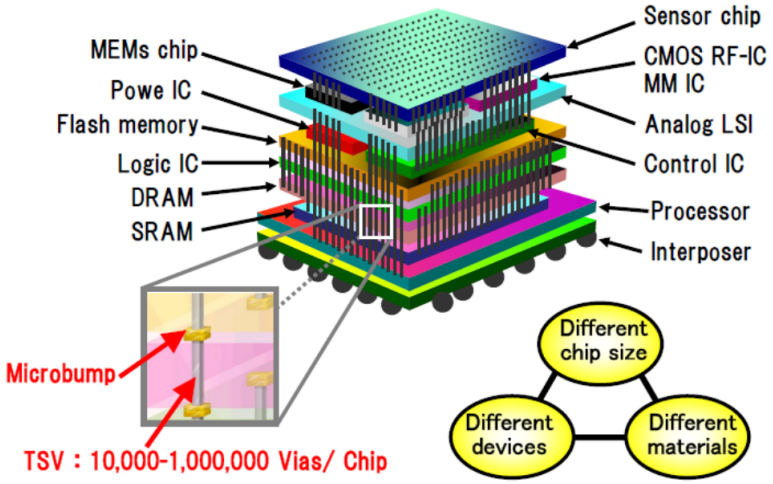

Figure 1.1: Exemple of conceptual structure of a 3-D chip [2].

1.1.1.1 Approaches to packaging

During the progress of this technology, three approaches to manufacture 3D integrated circuits are distinguished [3–5] (Figure 1.2). The first group represented by 3D packaging technologies include techniques such as Multi-chip module (MCM), 3D system in packages (3D SiP) and 3D wafer level package (3D WLP). 3D SiP techniques are based on flip chip technology [27] or package on package (PoP) blocks linked with wire bonds (Figure 1.2 (a)), while 3D WLP use large vias through the silicon substrate to link the dies (Figure 1.2 (b)). The main feature of structures based on 3D WLP is the increase of the integration density and improvement of the design stack. Flip ship technology on the other hand is based on ball grid array to interconnect modules, which allows better power supply to energy-intensive blocks with a lot of supply voltage variations [28]. Moreover, Die-to-Wafer is another approach of 3D integration (Figure 1.2 (c)). It is based on die-to-wafer bonding. This method uses techniques from both wafer fabrication and packaging, such as Through Silicon Vias (TVS) and die pick-and-place, respectively. The main advantage of die-to-wafer is its ability to stack chips with various dimensions and to create more complex chip stacks [5, 28].

The second group is devoted to multi-layer transistors. Figure 1.2(d) present transistors formed inside on-ship interconnection layers on a piece of recrystallized silicon

film [29,30]. Figure 1.2(e) shows transistors on polysilicon films with tungsten inter-layer vias [31]. Figure 1.2(f) illustrate transistors on single-crystal silicon films. Those applications can be implemented in signal amplifiers [5], low-performance memory [31] and very dense circuits [32], respectively.

The last group represented by Figure 1.2 (g-k) are Monolithic 3D integrated circuits. They are manufactured in layers on a single wafer. The 3D ICs are obtained after dicing but before, alignment, thinning, bonding and TVS interconnections are the steps required to realize the stacks. TSV connections can be drilled before/during (via first) or after (via last) bonding. Regarding bonding, four main methods can be highlighted [5] :

- via last, oxide-to-oxide bonding Figure 1.2 (h).
- via last, adhesive bonding Figure 1.2 (i).
- via first, copper-to-copper bonding Figure 1.2 (j).
- via first, bonding metal/adhesive inlaid Figure 1.2 (k).

Monolithic 3D ICs is the most promising method by its ability to process layers separately and using conventional manufacturing techniques. Whether it is *wafer-to-wafer* *die-to-wafer* or *die-to-die* stacking, this approach is more practical compared to the rest and especially when combined with TSV-vertical interconnections.

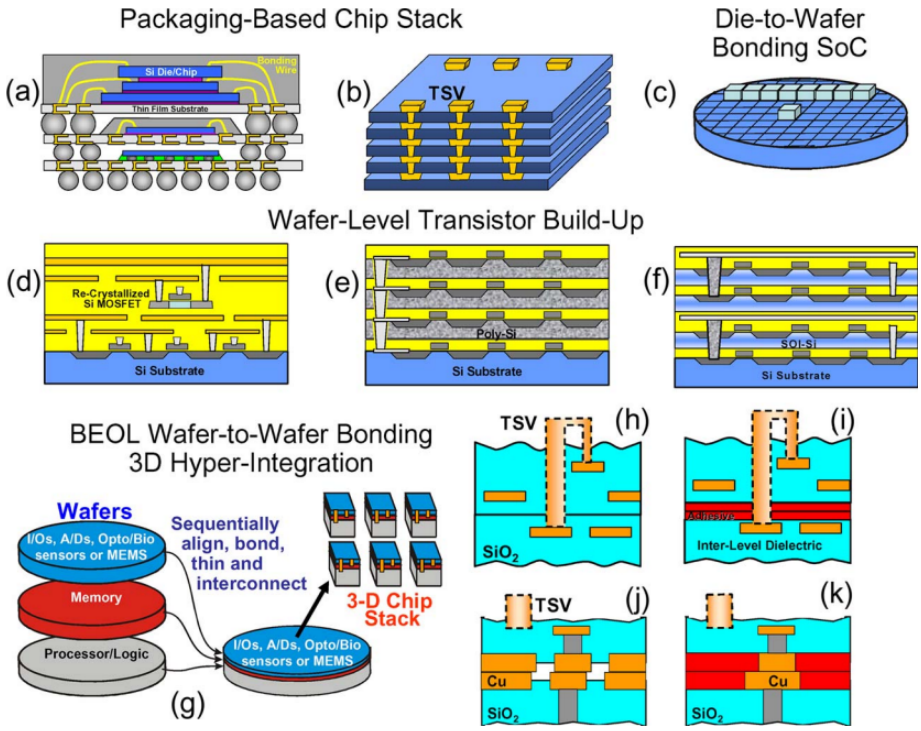

Figure 1.2: Schematic Representations of Major 3D Integration Approaches: (a-c) 3D Packaging Technology, (d-f) Wafer-Level transistor Buildup 3D Technology and (g-k) Monolithic 3D ICs [3–5]

.

All 3D integration techniques offer important key features such as small size, light weight, compact packaging and power reduction. However, each technique is distinguished by its advantages and limitations. 3D packaging technologies (Figure 1.2(a-c)) offers flexibility in terms of design nevertheless cost for large-scale production can be very high. Yet, known good die (KGD) for 3D packaging can provide manufacturability advantages by standardized packaging and reducing cost and complexity. [17]. On another level, 3D transistor buildup technologies (Figure 1.2(d-f)) delivers high-density stacks using photolithography and high volume production can be achievable by Wafer-level process. The main disadvantage of this technology is the limited range of utilized materials due to the thermal effects. For Monolithic 3D ICs (Figure 1.2(g-k)), the important characteristic lies in the ability to design the layers separately. This critical feature enables the design of electrical, RF, thermal and mechanical properties of each layer individually [5]. This flexibility allows the use of different materials with better performance and lower cost. Table 1.1 shows different advantages, drawbacks and key applications of the techniques previously described.

Technology	**Advantages**	**Drawback**	**Key applications**
3D Packaging	Known good die (KGD); Heterogeneous integration.	Difficult to manufacture on a large scale.	Dynamic random access memory; synchronous dynamic random-access memory; High Bandwidth Memory.
3D transistor buildup technologies	Wafer-level lithography and processing; high-density memory.	Material and Thermal limitations.	Low performance CMOS; NAND flash memory.
Monolithic 3D ICs	Low cost for high scale production; Heterogeneous integration; short TSV connections.	Design and technology complexity.	Memory; Imagers; 3D-integrated MEMS; Wireless communication; biosensor.

Table 1.1: 3D integration technologies and related applications [5, 17, 18]

Starting with multi-chip modules (MCMs) dedicated to the aerospace and Defense fields to heterogeneous integration (Figure 1.3), 3D integration technologies are still pioneering new ways to create integrated circuits. From a smartphone-dominated market in the early 20th century, continuous chip improvement has propelled new applications like AI, augmented reality, and 5G connectivity. For example, Samsung has presented a 3D technology, stacking logic and memory chips in the same package. It has also developed a package which combines an AI processing function with memory [33]. Another exemple are Chiplets. This new approach can break monolithic chips into smaller dies. With the right infrastructure, chiplet can be plugged like LEGO blocks on a standardized substrate. This futuristic path will bring more choice, affordability, interchangeability in the market of semiconductors [34, 35].

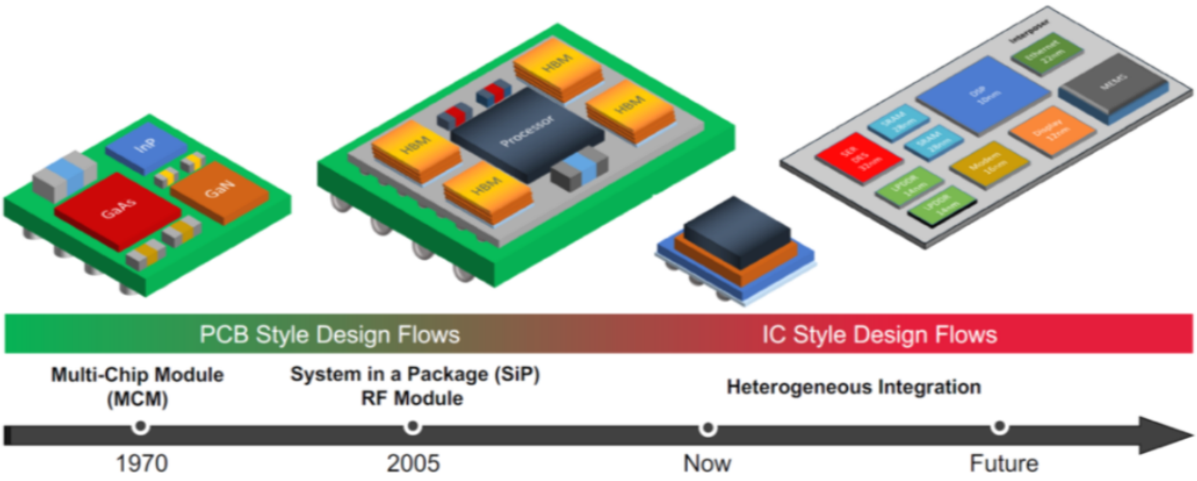

Figure 1.3: Evolution of multi-chip advanced packaging [6]

1.1.1.2 key 3D integration challenges

The key technical challenges of 3D integration are testing, operating temperature, mechanical stability, process steps including bonding strategies. Firstly, testing is a critical operation in any manufacturing process. Each chip must meet the performance requirements, hence the chip stack must therefore be inspected in the same way as conventional chips. The oblivious strategy is to test each chip separately to avoid bonding nonfunctional with functional dies. However this testing process is complicated due to the nature of dies and the differences between each layer. This issue affects Design-for-testability on 3D ICs and make it more complex. Next, the operating temperature heat created by power consumption should be dissipated otherwise the circuit temperature will increase. In a small dense volume where multiple blocks operate simultaneously, the power density increases because of the highly compact thinned and bonded chips. As a result, heat is generated causing reliability issues and leakage currents. In order to overcome this problem, the materials used must be able to dissipate heat; also layers must potentially dissipate heat through each other.

Thirdly, mechanical stress due to thinning and thermal expansion can cause damage to the structure. Since the layers are made of different materials with different expansion

coefficients, they can potentially jeopardize bonding and electrical connections. New thinned wafers can also be a major source of problems because of their extreme small thickness making them flexible. The current solution utilizes carrier wafers in others to protect them in the transfer from a process step to another. But bonding and detaching them may also create mechanical issues [28]. Lastly, 3D ICs require additional steps to be assembled. As mentioned earlier, the process steps are etching and filing TSVs, thinning and bonding. Electrical connections are made by etching holes through the substrate and filling them with conductive material. Afterwards the drilled substrate is thinned until it thickness ranges around a few micrometers. Figure 1.4 shows multiple stacked dies linked with TSV after bonding.

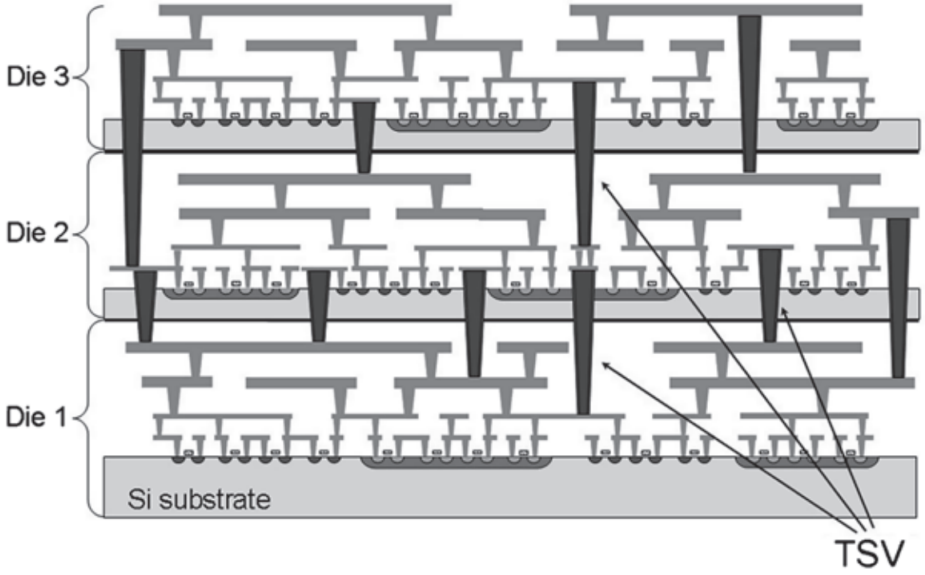

Figure 1.4: Through-silicon via providing electrical links with multiple vertically stacked die [7]

.

Now let's tackle bonding which stands at the core of this research. First, the two substrates must align carefully such that TSVs shall match to create electrical connections between the upper and lower layers. Next, the bonding should maintain the mechanical stability of the stack. Adhesive deposits were the early methods selected but rapidly limitations were noticed such as outgassing of the adhesive causing TSVs pitch [36]. Furthermore, this last solution proposes a poor stability to manufacture 3D ICs with three or more layers. This requirement led to the innovation of alternative methods such as low temperature oxide-oxide bond [37] and metal-metal thermal compression bond processes [38]. Again, these bonding techniques must respect the alignment and mechanical stability requirements of the multi-layer structure and hence not weaken the existing TSV connections.

1.1.2 Direct bonding

To avoid using adhesive, direct bonding relies on spontaneous adhesion at ambient temperature. *Lasky & al* presented the first achievable direct bonding on two semiconductor wafers in 1985 [20, 39]. It requires specific surface conditions on the two

substrates in order to achieve a high quality bond. Perfectly clean, smooth and flat substrates are this essential requirements. When these conditions are obtained with the two surfaces sufficiently close to each other, the contact is maintained due to forces such as Van der Waals forces, Hydrogen bond and capillary forces. Those forces appeared when the surfaces are hydrophilic and especially the two last ones. Direct bonding doesn't require any material input to provide a first attachment between the two substrates. At room temperature (RT), the bonding is still reversible due to insufficient number of strong bonds such as covalent bonds. To increase strong bonds an annealing process is applied making it irreversible. The separation of those bonded layers requires an amount of energy, expressed in $J.m^{-2}$, which is called **Bonding energy**.

1.1.2.1 Direct bonding application process requirements

The exigencies for direct bonding to achieve a perfectly weld substrate are a suitable morphology and clean surfaces. Experimentally, the contact of raw surfaces isn't sufficient to initiate adhesion. The three principal morphological criteria are controlled surface bow, flatness and low micro-rugosity. Each criterion addresses the roughness problem at a different scale (Figure 1.5). On the other hand, clean surfaces prevent contamination which is an important source of bonding defects.

- **Morpholigical requist for direct bonding**

On the substrate level, bow surface represents the bend deformation along the diameter of silicon wafers (Figure 1.5(1)). This first condition ensures the full contact between the two substrates since less curved surfaces allows countering the detachment linked to the bow. The detachment create an energy which goes against bonding energy, therefore it impacts the full adhesion of the layers. The bow is measured by optical profilometer. For example, two silicon wafers with a diameter of 200 mm and thickness of 725 μm require a maximum bend depth of 30 μm to maintain the bonding [40].

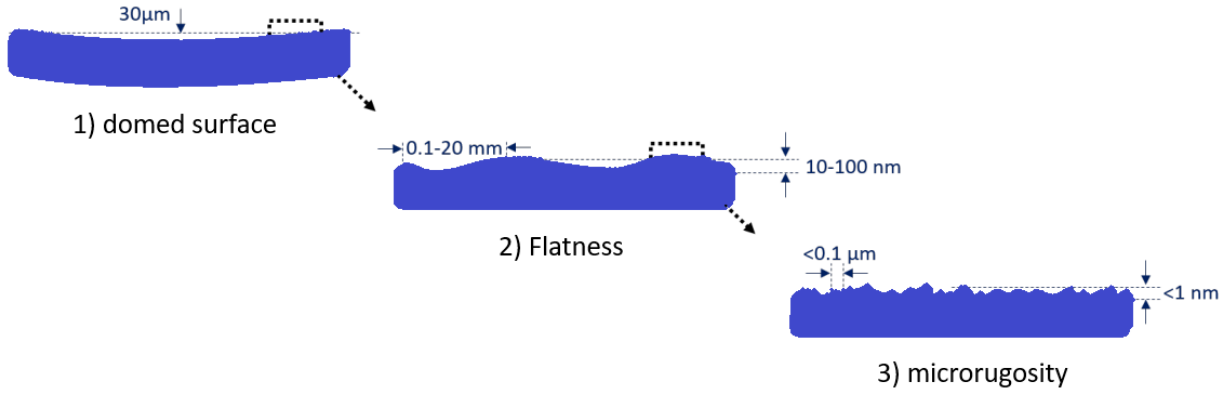

Figure 1.5: Morphological substrate criteria for bonding energy,(1) domed surface,(2) Flatness,(3) microrugosity.

The next criteria to achieve a high quality direct bonding is flatness. It is characterized by the undulation on the surface of the wafers (Figure 1.5(2)). The length

wave of those deformations varies from a few tenths of a millimeter to a few millimeters, while their amplitude range between 10 nm and 100 nm. Low surface undulation allows a better adhesion since the deformation energy will be low regarding bonding energy, while high range undulation amplitude can cause bonding defects. To overcome this constraint, a flattening step of the wafers is necessary to eliminate surface irregularities and ensure a successful bonding process.

Lastly, microrugosity is the key factor in direct bonding (Figure 1.5(3)). This parameter is measured by Atomic Force Microscopy (AFM). This very-high-resolution scanning probe is able to obtain a resolution up to a fraction of a nanometer. In order to quantify microrugosity, Root Mean Square (RMS) of surface amplitude enables the determination of the right roughness limit. For hydrophilic samples, the RMS limit value of a clean surface is 0.5 nm [41, 42]. The same applied for hydrophobic samples, the forces involved at room temperature don't tolerate roughness since RMS limit value is 0.3 nm [42].

While the control of wafer morphology comes before steps such as etching and engraving, Chemical-mechanical polishing (CMP) can be introduced to catch up on surface morphological criteria after these steps.

- **Surface contamination**

The second important criteria is surface contamination which is an important source of bonding defects. It is differentiated by two main types of pollution. Firstly, organic contamination is the deposition of organic compounds on wafer surfaces during the bonding process. This type of pollution causes microrugosity degradation of the surfaces by the absorption of organic compounds, which makes it harder for the bonding to be established [43]. During the annealing process, the formation of gases is another effect of organic contamination that is the source of bubbles at the bonding interface [44]. To address such contamination, peroxymonosulphuric acid, composed of sulfuric acid and hydrogen peroxide, is used for example to decontaminate the surfaces [45].

Despite the fact that Cleanroom provides an environment where the temperature, humidity and air quality are regulated. Particles are still likely to be deposited on the surfaces and get trapped at the bonding interface (Figure 1.6). This second form of contamination creates a void between the two bonded wafers. In the case of 1 μm diameter particle, it has been shown that a bonding defect of 5 mm diameter can be observed [46].



Figure 1.6: Example of bonding defect caused by particle contamination

On the industrial level, the tolerated particle diameter to achieve bonding stands below 0.09 μm. To tackle those particles, cleaning protocols are established to meet the requirement and gets wafers ready for first contact.

1.1.2.2 Contact at ambient temperature

Once the surfaces are flat, smooth and clean, they can be joined together. The air trapped between the two surfaces initiates a capillary phenomenon, which allows the plates to slide over each other easily. Then, a small local pressure helps the air to escape, which creates the first bonding forces and brings the plates even closer together. Normally, the wafer weight on top is sufficient to apply a minimum mechanical pressure (Figure 1.7(a)). The bonding wave propagates along the surface (Figure 1.7(b)), finally leading to the bonding of the two layers (Figure 1.7(c)). The contrast created by the bonding wave on the IR images refers to the bonded areas in bright gray, where dark gray areas indicated still separated layers. For the last image which show a full bonded stage, the camera has automatically adjust its contrast to show a dark gray even for a bonded wafer.

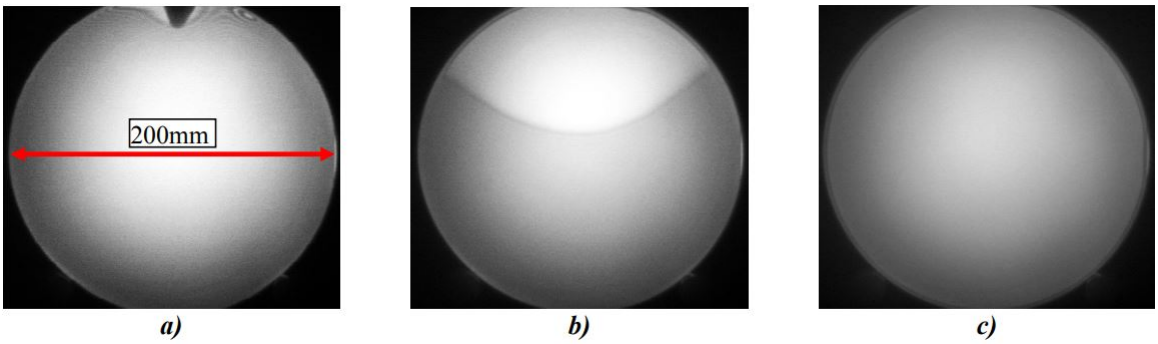

Figure 1.7: Bonding wave observed during the bonding of 200 mm silicon wafers by infrared light (IR) [8]. a) After positioning the two substrates on top of each other, contact between the two surfaces is initiated by local pressure, b) Propagation of the bonding wave, c) End of propagation, the wafers are bonded.

The observation of bonding waves by IR shows wavefront propagation shape, which is a good quality indicator of the bonding. It is also possible to use the bonding wave to quantify bonding energy by measuring the wave velocity [47].

When the wave propagation ends. The bonding depends on weak forces such as Van der Waals force to maintain the structure. As a result, bonding energy varies depending on the bonding nature between a dozen and hundreds of $mJ.m^{-2}$. To increase the bonding energy, the chemical bonds must be modified at the interface. To achieve that, annealing process can provide a switch of the molecules at the bonding interface. Yet, the bonding evolution depends on the morphological and chemical conditions in order to obtain a quality bond.

1.1.2.3 Hydrophilic and Hydrophobic bonding

Two types of direct bonding exist. They are distinguished by the nature of bonds involved in the adhesion processes. Hydrophilic and hydrophobic bonding of silicon depend on the surface's chemical affinity to water. In the case of hydrophobic bonding, the surfaces has no affinity with water and is not moistened. They are rinsed with hydrofluoric acid (HF) leading silane (Si-H) compounds to overlays the surfaces. On the other hand, hydrophilic bonding has more affinity to water due to silanol (Si-OH) compounds. This

type of compound involves the creation of a thin film of water after the cleaning and while the surface is exposed to humid atmosphere [14, 19].

Since the treatment differs between the two techniques, the bonding evolution of the two cases will also vary during the fabrication process. Van der Waals forces (W) play a key role at room temperature. *Rieutord & al* [11] measured this force using Hamaker constant A_{123} and the distance separating the silicon layers D (Equation 1.1). This last parameter was measured experimentally using X-ray reflectivity:

$$W = -\frac{A_{123}}{12.\pi.D^2}. \tag{1.1}$$

In the case of a hydrophobic silicon bonding labeled as $Si//Si$, Van der Waals force is about 7.4 $mJ.m^{-2}$ for 0.9 nm spread between the silicon layers, which shows that bonding energy is manly due to Van der Waals forces in this case [19]. In the second case of Hydrophilic bonding labeled as $SiO_x//SiO_x$ due to the presence of a thin film of silicon dioxide (SiO_2), Van der Waals force is around 0.4 $mJ.m^{-2}$ for 0.7 nm of spread. This value doesn't concord with the bonding energy of 150 to 200 $mJ.m^{-2}$ measured experimentally by *Moriceau* [48]. Therefore, the source of this energy can only come from the water trapped between the two substrates. The thin film of water ensured by the hydrogen bonds gives an extra bonding energy estimated theoretically around 144 $mJ.m^{-2}$, which is in line with the experimental value [19].

Bonding Strategy	$A_{123}(J)$	$D(nm)$	$W(mJ.m^{-2})$
Si/Air/Si (Hydrophobic)	21.10^{-20}	0.9	7.4
SiO2/bonding/SiO2 (hydrophilic)	$0.71.10^{-20}$	0.7	0.4

Table 1.2: Van der Waals energy between two substrates separated with a distance D for Hydrophobic and hydrophilic bonding [11]

Next, the annealing process allows the covalent bonds to develop. Again the chemical reactions are different between the two bonding strategies. For hydrophobic bonding, $Si-Si$ covalent bonds are created allowing the consolidation of the structure (equation 1.2):

$$Si-H+Si-H->Si-Si+H_2. \tag{1.2}$$

For hydrophilic bonding, $Si-O-Si$ covalent bonds are the one responsible of the consolidation through the condensation of $Si-OH$ bonds (equation 1.3) [14, 19]:

$$Si-OH+Si-OH->Si-O-Si+H_2O. \tag{1.3}$$

During the annealing process of hydrophilic samples, the density of $Si-O-Si$ bonds increase leading to the reinforcement of bonding energy. At room temperature, the bonding energy is around 150 to 200 $mJ.m^{-2}$. At this stage, bonding relies on few covalent bonds due to a few contact points (Figure 1.8(a)). By raising the temperature

up to 600°C, the number of covalent bonds increase between the two substrates driving the bonding energy higher than 3.5 $J.m^{-2}$ (Figure 1.8(b)). Next, the water is diffused through the bonding interface by increasing the temperature up to 1200°C, which drives backside oxidation (Figure 1.8(c)) [49, 50]. At this stage, bonding energy is between 4.5 and 5 $J.m^{-2}$. The final stage delivers a fully weld bonding interface with a bonding energy around 5 $J.m^{-2}$ (Figure 1.8(d)).

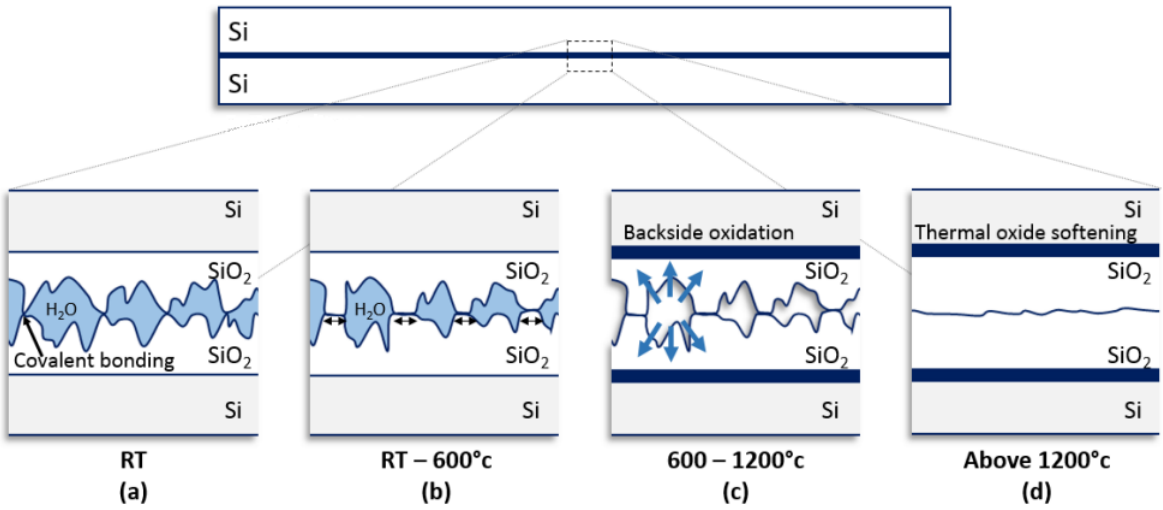

Figure 1.8: Evolution of bond interface sealing according to the annealing temperature for an hydrophilic bond [1, 9].

1.1.2.4 Impact of the annealing process

Fournel & al demonstrated the evolution of direct bonding energy under anhydrous atmosphere according to measured annealing temperature for hydrophobic and hydrophilic bonding (Figure 1.9) [10, 46]. Hydrophobic samples tend to evolve exponentially in response to annealing ([10]-*Fig* 14). On the other hand, hydrophilic samples have a first very fast evolution, then a plateau is reached before the final increase at high temperatures.

According to Figure 1.9, bonding energy remains superior for hydrophilic bonding regarding hydrophobic bonding between RT and 600°C. The main advantage of hydrophobic bonding is its ability to reach a high bonding energy value (5 $J.m^{-2}$) for a relatively low annealing temperature (600°C), where hydrophilic bonding attains this value around 1200°C. The hydrophobic increase much faster at high temperature thanks to silicon atoms mobility. This allow to close atomically the bonding interface leading to a fully bonded interface.

Nevertheless, the bonding interface for the two cases is welded perfectly at the end of the process [50, 51]. The measurement of the density and width on hydrophobic interface using X-Ray Reflectometry (XRR) allows quantifying the sealing of this bonding. It is noticed that the density of the bonding layer increases with the annealing temperature until reaching the silicon density (Figure 1.10). It is also observed that the width of the

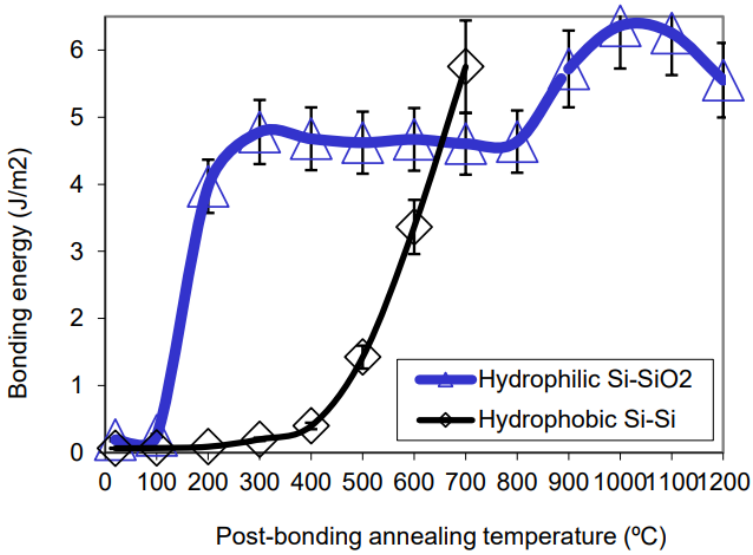

Figure 1.9: Bonding energy for hydrophilic (Blue curve) and hydrophobic (Black curve) samples according to annealing temperature in an anhydrous atmosphere [10].

interface is shrinking during the annealing process until it disappears and metamorphoses the two substrates into a single layer. This last advantage provides a good mechanical strength comparably to adhesive.

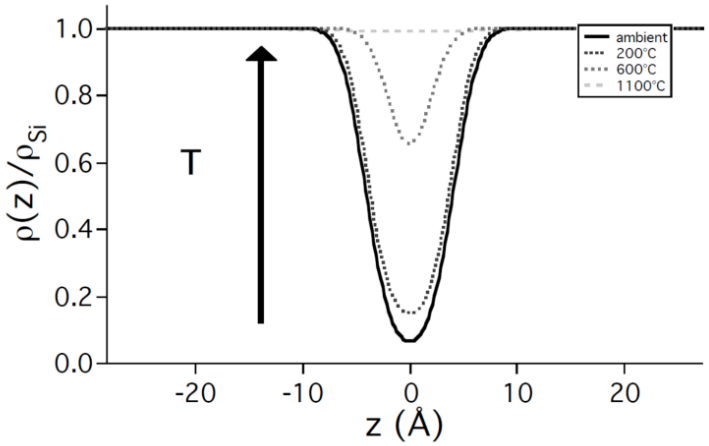

Figure 1.10: Electron density measurements with XRR of the bonding interface for a hydrophobic bond [11].

Given the advantages presented above, direct bonding stands as a robust technique to assemble silicon structures. From an industrial point of view, hydrophobic bonds are more advantageous as their bonding energy is higher at lower temperatures than hydrophilic. Lastly, direct bonding is widely used in the industry today for applications such as silicon on insulator, heterogeneous structures, and microelectromechanical systems (MEMS).

1.2 Bonding energy characterization techniques

Direct bonding is a technology with a broad range of applications. However, its deployment has some limitations such as delamination and gas formation on the bonding interface. Their negative effects on the bonding should be quantified to understand their influence on the overall quality of the newly formed substrate. Several techniques can be mentioned. Among them are transmission electron microscopy (TEM), X-ray crystallography (XRD), X-ray reflectivity (XRR), infrared spectroscopy (IR), scanning acoustic microscope (SAM) and The Double Cantilever Beam (DCB) [52]. Each technique targets a specific problem or parameter of the bonding. For example, when the XRR measures the width of an interface, the DCB test takes over the measurement of the bonding energy. In this work, the main objective is to characterize the bonding energy, which leaves us with the SAM and DCB test since they are the most widely used techniques due to their immediacy and ease of application. The next two subsections describe these techniques in order to understand the mechanism of a bonding energy measurement.

1.2.1 DCB test (Double Cantilever Beam)

Double Cantilever Beam (DCB) test represents a standard method to estimate the fracture toughness of bonded joints or fabric composites. This technique is based on the insertion of a blade into a solid material in order to cause a crack which allows the surface energy measurement (Figure 1.11).

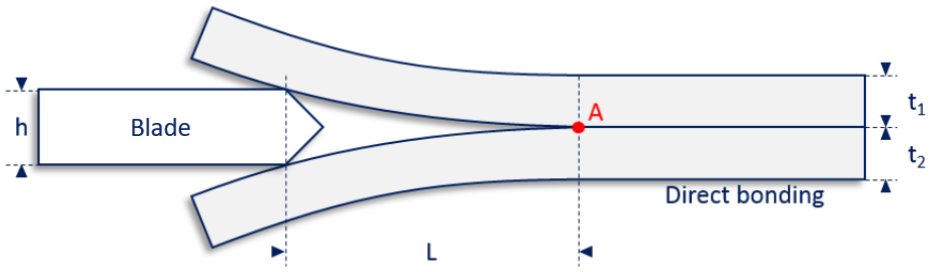

Figure 1.11: principle of the DCB test applied to direct Bonding [1, 12]

Maszara & al were the first to introduce the evolution of wafer bonding energy based on crack propagation [12]. Their studies were based on the theory developed by *Gilles & Gilman* on quantitative cleavage method for determining surface energies of solids [53–55]. This technique is widely used because it is very simple to implement and execute, since no surface preparation is required to perform a measurement. The main major drawback is its destructive character as it relies on opening the bond.

The concept of DCB test is to insert a blade to cause a crack of length L at the bonding interface, to subsequently measure the length of the crack experimentally to solve the bonding equation numerically. Several techniques can be used to measure the length of the crack. Figure 1.12 shows an infrared measurement of the disband length. This measurement can also be done by acoustic microscopy if the layers are IR opaque.

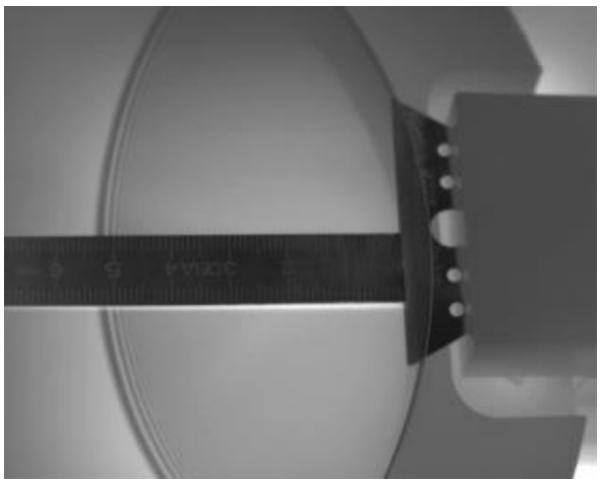

Figure 1.12: infrared visualization of the area stripped by the blade [8]

In the case of two silicon wafers of identical thickness, the numerical solution of the equation 1.4 equals the bonding energy at point A (Figure 1.11). With G the bonding energy, h the thickness of the blade, E the Young's modulus, t the thickness of the wafer and L the crack length:

$$G = \frac{3}{32}\frac{Eh^2t^3}{L^4}. \tag{1.4}$$

In a more generalized case of two non-identical plates, bonding energy equation can be described as follows:

$$G = \frac{3.h^2}{16.L^4}\frac{E_1t_1^3.E_2t_2^3}{E_1t_1^3 + E_2t_2^3}. \tag{1.5}$$

However, the above equations are based on the mechanical beam theory; thus they are not valid for circular plates and a finite width blade [8]. Several studies have shown that the use of these formulas overestimates by 10% to 30% bonding energy in the case of a beam structure made by the same materials [40, 56]. To address this challenge, they therefore recommended that the test should be performed on thin strips of beams cut from wafers or extract the interface toughness values by finite element analysis. Despite that, these practices are not conventional due to time and difficulties associated with slicing weakly bonded wafers or developing finite element models. Another observation by *Turner & al* shows that this overestimation varies and can not be corrected by a correction factor [57]. Certainly, a strict protocol makes it possible to compare measurements with each other and ensures reproducibility. This allows quality comparisons between the different levels of bonding. For hydrophilic samples, it is recommended to establish the test under anhydrous atmosphere in order to avoid corrosion [10].

1.2.2 SAM test (Scanning Acoustic Microscopy)

The first proposal to use high frequency acoustics waves imaging started with *Sokolov* in 1929 [58] at the V.I.Ulyanow Electrotechnical Institute of Leningrad. He succeeded in 1937 to setting up the first high-frequency ultrasound imaging tool for detecting defects deep in materials [59]. The device was known as Acoustic Electron-Ray Converter. It consisted of Piezoelectric Element Matrix of 1000 square elements with sides of 1 *mm*. Each element is connected to a Cathode-Ray Converter which coverts the mechanical response into an output signal that can be displayed as an image. *Sokolov* honorable work was the description of the ultrasonic microscope. He predicted that sound waves could be utilized as a new way of microscopy and recognized that sound waves with a frequency of 3 GHz would have a resolution likely to optical microscopy. During the second half of the 20th century, various projects were carried out to propose new approaches to acoustic microscopy [60, 61]. *Kessler & al* set up one of the first scanning acoustic microscopes operating at 100 MHz, capable of providing acoustic images in 1972 [62]. Two years later, *R.A.Lemons & C.F.Quate* were able to reach a lateral resolution of 10 μm operating in transmission mode (Figure 1.13(b)) using two transducers [63]. Alternatively, *Johnston & al* developed a reflection mode (Figure 1.13(a)) microscope who depends on a single transducer for transmission and reception simultaneously [64].

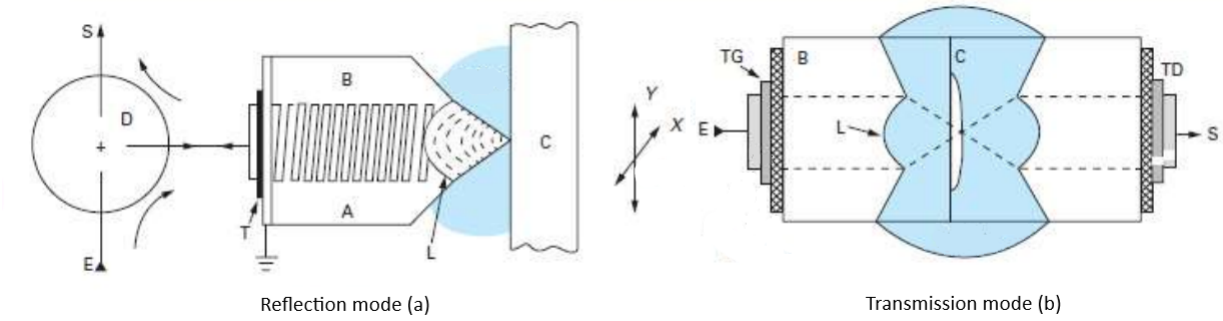

Figure 1.13: Operation diagram of the acoustic microscope (a) in reflection, (b) in transmission modes [13]. *A :acoustic beam - B: delay line - C: Samples - D: circulator - E: Input signal - L: Lens - S : Output signal - T : piezoelectric transducer - TG: generating transducer - TD: detecting transducer - In sky blue : coupling liquid.*

1.2.2.1 SAM operating procedure

Scanning Acoustic Microscopy or SAM depends on the piezoelectricity versatility to convert mechanical energy into electrical. Firstly, high-voltage impulsion stimulates the piezoelectric element to generate a mechanical reaction, which is translated by an ultrasonic acoustic wave travailing through the delay line (Figure 1.13(B)). The delay line acts as a mechanical support so that the piezoelectric element can have only one motion direction, thus making its emission more efficient. It also allows the temporal isolation of the incident and reflected signals due to the use of materials such as sapphire or silica. At the delay line extremity (Figure 1.13(L)), a lens is placed to focus the waves into the material inspected. The next step is to enable the waves to travel within the material. To do so, the coupling liquid is used to conduct the waves up to the sample since acoustic waves can not be transmitted into the air due to its low acoustic impedance (Table 1.3).

Once the wave reaches the sample, its sensitivity to every obstacle is observed in its amplitude. After propagation, it is collected rather with a detecting transducer placed in the other side of the sample in the transmission mode case (Figure 1.13(b - TD)), or with the same emitting transducer in the reflection mode (Figure 1.13(a - T)). Lastly, the piezoelectric element takes the acoustic wave and converts it into an electrical signal. It is conducted to the instrumentation chain so that the propagation history of the acoustic wave can be observed. This leads to the reconstruction of the samples in depth and allows them to be examined without being destroyed, which is the major advantage of SAM. Other significant advantages are the ability to characterize different types of materials, including optically opaque ones, regardless of whether the observations are on the surface or inside the material. The second benefit is that image contrast can also relate to the mechanical properties of the samples.

1.2.2.2 Ultrasound and applied characterization techniques

Ultrasounds refer mainly to acoustic waves beyond the audible range. The range of human hearing is between 20 Hz and 20 kHz, whereas ultrasounds cover frequencies from 20 kHz to several GHz. Like all periodic processes, the notions of frequency (f), wavelength (λ) and wavenumber (k) are the main characteristics of any ultrasonic wave:

$$f = \frac{1}{T}. \qquad \lambda = \frac{c}{f}. \qquad k = \frac{1}{\lambda}. \tag{1.6}$$

Ultrasound Non-Destructive Testing is inspired directly from the Sonar concept. Let's illustrate this principle in the case of direct bonding in Figure 1.14.

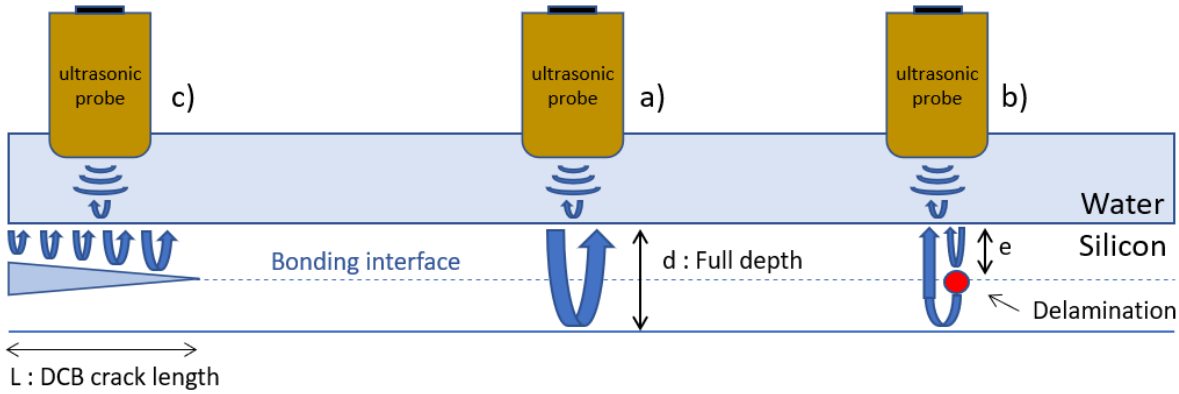

Figure 1.14: Principle of ultrasonic imaging in the case of direct bonding

Water immersion of the ultrasonic probe is the first step to ensure good coupling so that the waves reach the silicon surface. For a silicon layer of thickness d, the transducer emits an ultrasonic wave into the fluid. Part of the energy carried by this wave penetrates the silicon and the other part is reflected by the silicon surface and received later by the transducer. This first echo received by the transducer is called the interface echo (Figure 1.14 (Reflection [Water/Silicon]) & Figure 1.15). After penetration, two cases occur, the first case is when the penetrating wave doesn't encounter a defect (Figure 1.14 (a)). It propagates to the bottom of the silicon and returns to the top surface where it

is transmitted to the transducer through water. The second received echo corresponds to a round trip of the wave in the silicon and called the background echo (Figure 1.15 (Red signal)). The duration of the wave's travel ΔT is then related by the time-of-flight (ToF) equation:

$$\Delta T = \frac{2d}{c} \tag{1.7}$$

where d is the thickness of the silicon and c the speed of sound in the silicon. In the case in which a wave encounters a delamination in the form of a water bubble (Figure 1.14 (b)), this defect will act as a reflector, and an additional delamination echo is received by the transducer (Figure 1.15 (Blue signal)). Knowing the propagation speed c, a time measurement allows the prediction of the defect position e in the silicon layer.

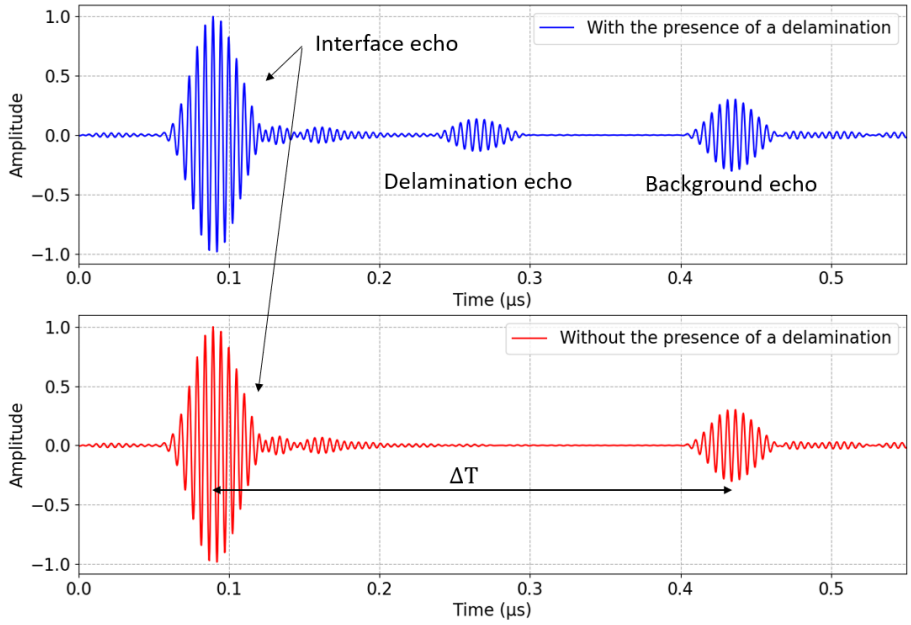

Figure 1.15: Example of A-scans showing a perfect bond and a delamination

To talk about the DCB crack length measurement (Figure 1.14 (c)), it is necessary to define the ultrasonography types which are differentiated by the signals used in the analysis. In its simplest form, it stands as the time signal obtained for one scanning position. The result is visualized in the amplitude of the echoes, depending on the time-of-flight. This makes it possible to calculate the distance between the source and the potential receivers. This type of analysis is called A-scan (Figure 1.15). By expanding the transducer mobility, it is possible to scan the material by moving the transducer along a parallel line to the sample surface. This approach is referred to as the B-Scan (Figure 1.16). By tracking the echo amplitude, the wave path can be represented as a contrast, leading to the length of the delamination.

The last and most popular type of ultrasonography is the C-scan (Figure 1.16). By moving the transducer parallel to the material surface, a depth image of the sample is formed. To select the height of the slice, a time window is applied to an area of the time signal and only the maximum of the signal is retained. Which allows the representation of the slice seen from above by several contrast based on the level of the amplitude.

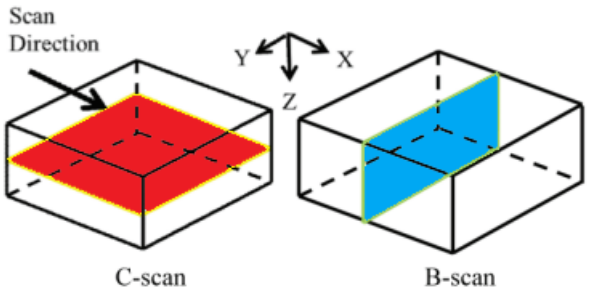

Figure 1.16: C-scan and B-scan scanning modes

Figure 1.17 is an example of C-scan ultrasound images of a wafer with a defective bonding interface. The black contrast indicates areas where the bonding is effective. The coupling between the two bonded wafers allows the wave to pass through the bonding without a change in the impedance. In contrast, the white contrast is caused by the acoustic impedance break between the poorly bonded interface and the silicon. It can be observed that the geometry and size of the unbonded areas is very well defined.

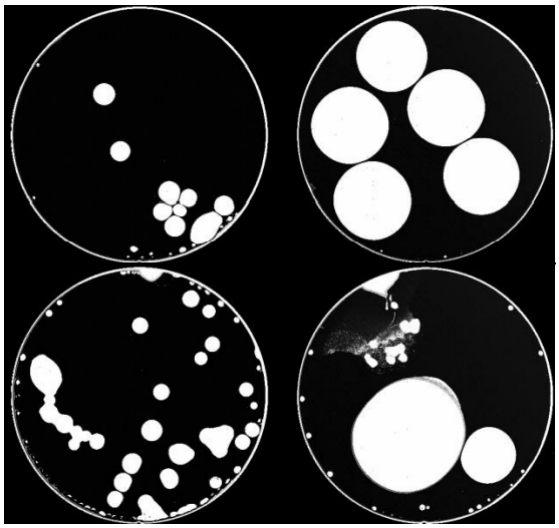

Figure 1.17: Example of C-scan applied to direct bonding [14]

1.2.2.3 Type of transducers and acoustic field

The transducer type is selected depending on the material, the geometry and the defect size. Planar and focused transducers are the most widely utilized. The planar or unfocused transducer uses waves that propagate perpendicularly to the transducer flat lens. This transducer is distinguished by an acoustic beam composed of a near field and a far field (Figure 1.18). The near field or the Fresnel zone is an area where the field is very irregular. It should be avoided because the sound field is turbulent, which makes it tough to pick up signals. For an transducer aperture D, the length of the Fresnel zone l_0 is measured by equation 1.8 (Figure 1.18). In the far field, the wave flares out and forms an angle of divergence γ. This angle corresponds to the zone range where the sound pressure is higher. Nevertheless, the -6 dB zone is the most optimal zone. It corresponds

to the area in which the amplitude returned by an obstacle is greater than half maximum amplitude at the distance l_0 , which is the position of the last maximum [65]:

$$\sin\gamma = 1.22\frac{\lambda}{D} \qquad\qquad l_0 = \frac{D^2}{4\lambda}. \tag{1.8}$$

Focused transducers increase resolution by focusing the beam on a single point (Figure 1.18). The focalization is achieved either by bending the piezoelectric, or by using an acoustic lens. The characteristics of a focused acoustic beam are the width of the focused beam R_f and its length L_f [66]

$$R_f \approx \frac{L_f\lambda}{D}. \tag{1.9}$$

The focal length depends on the material under investigation. It is very common to mention the focal distance of transducers operating in water. To adjust these distances according to the defect position, equation 1.10 can predict the new focal length inside the material:

$$W_p = F - M.\frac{c_{tm}}{c_w} \tag{1.10}$$

where W_p is the water path, M is the depth of the defect in the material inspected, F is the focal length in water. Finally, c_{tm} and c_w are the sound speed in the material and water respectively.

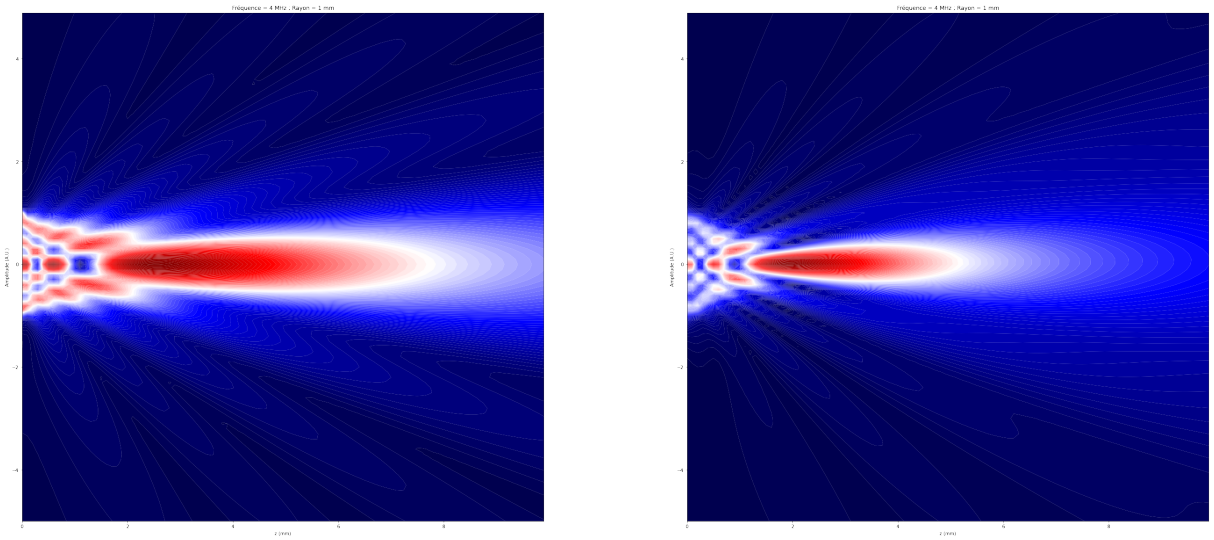

(a) (b)

Figure 1.18: Unfocused (a) and focused (b) acoustic beam

The frequency of a transducer is another important parameter. Since an object mainly reacts to a wavelength of the order of its size, the frequency choice should be based on the size of the object inspected. The transducer bandwidth is also an important point, as imaging transducers tend to favor a wide bandwidth to be able to probe any defect size and avoid resonance. A narrow bandwidth transducer will focus the energy on a defined frequency allowing certain defects to be targeted more precisely. The

influence of the frequency and focal length parameters on the C-scans can be observed in Figure 1.19. A high frequency will allow a better resolution by sacrificing the focal length since attenuation increases with frequency. In contrast, a lower frequency will allow more effective waves to penetrate the material but less resolution in return (Figure 1.19(b-c-d)). By selecting a deep focal length, it can be seen that depth details are visible since the focal zone is deeper in the sample. Nevertheless, the resolution is less optimal (Figure 1.19(a)).

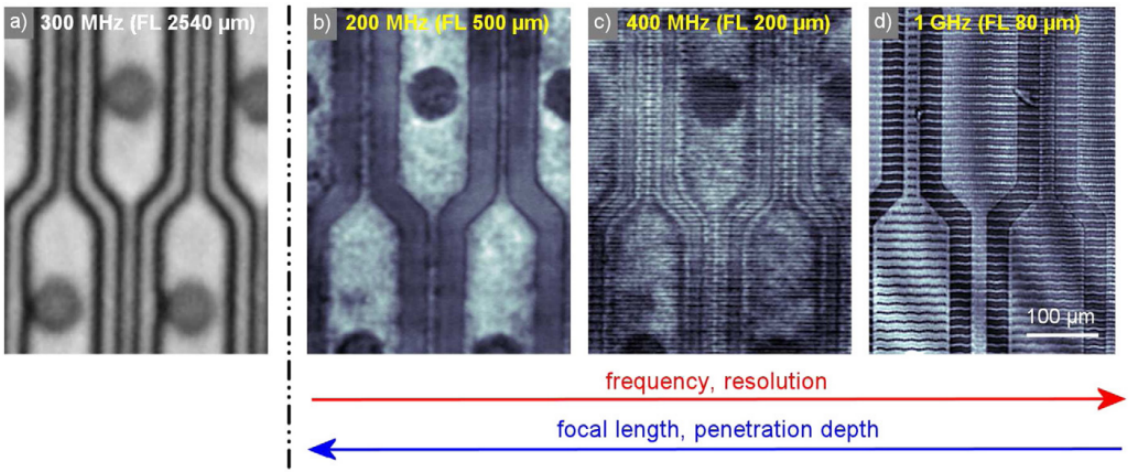

Figure 1.19: Comparison of SAM images obtain by a) 300 MHz transducer with 2.5 mm focal length, b) 200 MHz transducer with 500 μm focal length, b) 400 MHz transducer with 200 μm focal length, b) 1 GHz transducer with 80 μm focal length [15].

1.2.2.4 Ultrasonic resolution

Resolution refers to the ability of an ultrasound wave to discern two very close points in space. Two major types can be distinguished. Firstly, axial resolution is the capability to discern two points parallel to the beam path. It is strongly related to the wavelength. However, a signal with an unsuitable wave train and frequency can cause unwanted overlapping. For a resolution Δx, echoes shouldn't last longer than $\Delta t = \Delta x / c$ (Figure 1.20).

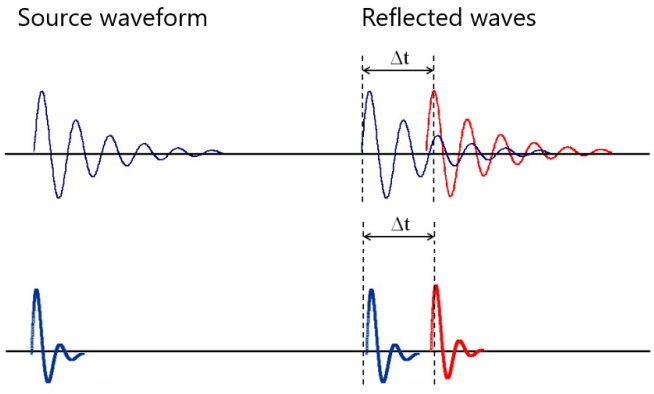

Figure 1.20: Axial resolution influence on the time signal

Secondly, lateral resolution is the capability of ultrasound waves to distinguish two points perpendicular to the beam. It is related to the beam width, length and transducer frequency. The acoustic beam calculated by the analytical solution of Rayleigh integral can be used to measure the lateral resolution [67]. Figure 1.21 shows the sound field of a 200 MHz planar and 100 MHz focused transducers, along with transverse profiles of the sound pressure amplitude showing the gain in lateral resolution at -3 dB.

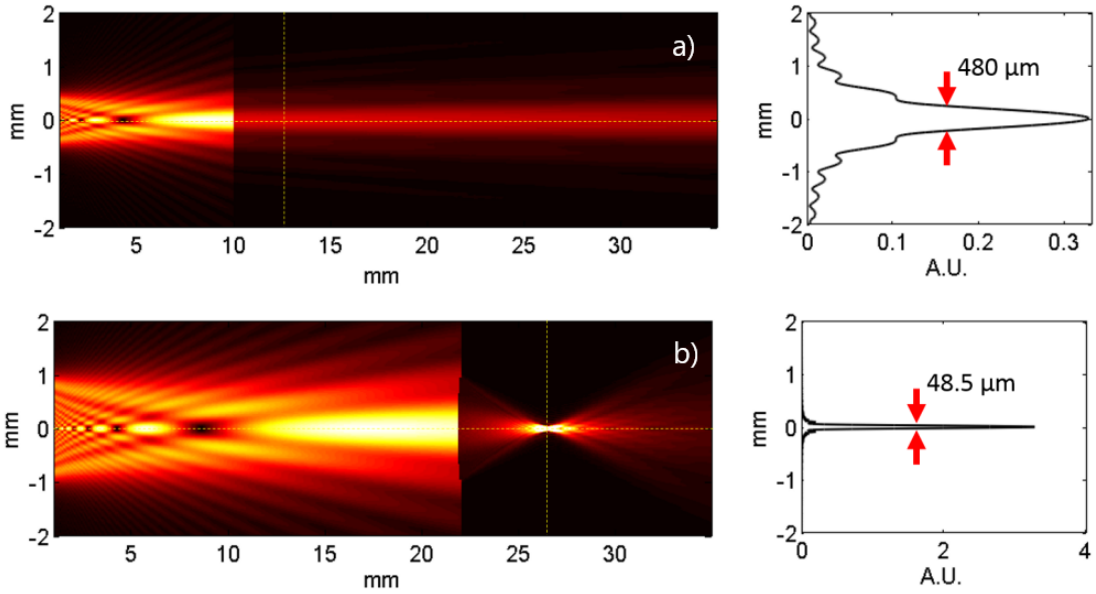

Figure 1.21: Acoustic beams of 200 MHz planar transducer with lateral resolution of 480 μm (a) and 100 MHz focused transducers with lateral resolution of 48.5 μm (b) and their respective transverse sound pressure amplitude profile [1]

1.3 Acoustic's physics

1.3.1 Acoustic impedance

From a theoretical standpoint, the shift in the acoustic impedance from one material to another is the key to understand the physics around SAM. The acoustic impedance is the resistance that a system exhibits to the acoustic flow due to an acoustic pressure. In the case of a plane wave, it is defined by the following equation:

$$Z = \rho c. \tag{1.11}$$

where Z is the acoustic impedance, ρ the volumetric mass density and c the speed of sound waves in the media. it is expressed in *Rayleigh* or *MRayl*, which is relative in SI unit to $Pa.s/m$ [68].

Media/Material	c (m/s)	ρ (Kg/m^3)	Z $(MRayl)$
Air	330	1,293	426.69
Water	1500	1000	$1.5\ 10^6$
Silicon	8430	2330	$19.6\ 10^6$

Table 1.3: Acoustic impedance of different media

Acoustic impedance (Z) is also defined as the ratio of the acoustic pressure (p) to acoustic particle velocity (v) in a media and is given by the following equation:

$$Z = p/v \tag{1.12}$$

where p is the acoustic Pressure (Pa) and v acoustic particle Velocity (m/s). To remind, these equations are only valid in plane wave case.

1.3.2 Reflection and transmission coefficients

When a wave arrives at the boundary of two media (Figure 1.22), an analogy can be made with optics where the change in the propagation media yields a transmitted and reflected wave. Acoustic waves respect the same law involving a reflection and transmission coefficient relative to the incident wave amplitude (equations 1.13). If the acoustic impedance of the media B is very low compared to A, the reflection is total due to the value of the transmission coefficient converging to 0. This explains the utility of coupling liquid to propagate the wave beyond the delay line.

Based on the acoustic impedance of the media A and B $(Z_A = \rho_A c_A; Z_B = \rho_B c_B)$, it is theoretically possible in the case of a plane wave to calculate the amplitude of the transmitted and reflected wave at normal incidence as follows:

$$r = \frac{Z_B - Z_A}{Z_B + Z_A}, \qquad t = \frac{2Z_B}{Z_B + Z_A}, \qquad t = r + 1, \tag{1.13}$$

where t is the amplitude of the transmitted wave and r the reflected wave amplitude, with a normalized incident wave amplitude [68].

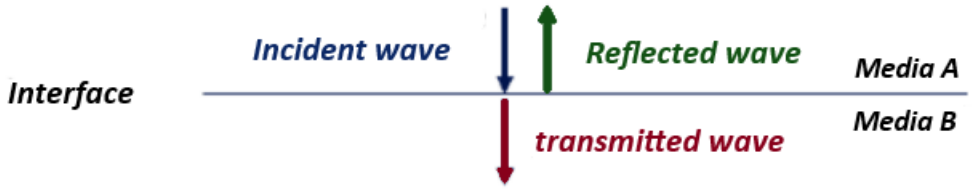

Figure 1.22: Reflection and transmission of a plane wave normally incident between two media A & B.

Reflection and transmission intensity are driven from the pressure (p) transmission and reflection coefficients since the intensity of a harmonic plane wave is $p^2/2Z$ [68]. They are described as follows :

$$R = (\frac{Z_B - Z_A}{Z_B + Z_A})^2. \qquad T = \frac{4Z_A Z_B}{(Z_B + Z_A)^2}. \qquad T + R = 1. \tag{1.14}$$

1.3.3 From Hooke law to Longitudinal and transverse waves

After a brief description of the rudimentary ambient acoustic wave physics, let's now focus on the wave itself. Acoustic waves are mechanical waves who depend on particles to propagate their energy. It can be considered as a pressure field carried by particles. The speed of these waves will then depend on the distribution of these particles in the media. The acoustic wave behavior in a media depends on it properties such as density (ρ), the Young's modulus (E) and shear modulus (G). The Young's modulus is defined as the media resistance to an compression, where the shear modulus can be described as the resistance of a media to shear deformation caused by a shear stress. It is interesting to mention that in an isotropic material, the longitudinal and transverse wave speeds depend on these two parameters since the elastic tensor is simplified and contains only these two unique elastic constants. Thus, the longitudinal and transverse wave speeds are given by:

$$v_T = \sqrt{\frac{G}{\rho}} \qquad v_L = \sqrt{\frac{E}{\rho}}. \tag{1.15}$$

However, the elastic tensor matrix of anisotropic materials introduces additional complexity relative to the direction dependence, which results in different longitudinal and transverse wave speeds in various directions of the material.

Hooke's law is the first introduction to understand the relationship between the forces and deformations present during the wave propagation. First, the representation of a deformation can not be described by a single vector since materials can be stretched, compressed and sheared along different directions. The same applied to the stresses, where they can be pushed, sheared and pulled at once. To express this complexity, two-second-order tensors must represent the stress tensor (σ_{ij}) and the strain tensor (ϵ_{kl}). In the case of linear acoustics, where only small deformation occurs, the Hooke's law for continuous media is then

$$\sigma_{ij} = c_{ijkl}\epsilon_{kl} \tag{1.16}$$

where c_{ijkl} is the fourth-order tensor also called stiffness tensor and is considered as a linear mapping between the strain tensor and the stress tensor [69]. It is composed of 81 elastic coefficients since stress and strain tensors are represented by 3 x 3 matrices. This number can be reduced to 36 elements due to the symmetries in the material. For isotropic materials, this number is reduced to two parameters, which are the stiffness tensor component c_{11} and c_{12} . This is logical since an isotropic material has the same physical properties in all directions. It is important to note that stiffness tensors are unique to each material [70, 71]. For an isotropic solid, the stiffness tensor can be expressed as follows :

$$c_{\alpha\beta} = \begin{bmatrix} c_{11} & c_{12} & c_{12} & 0 & 0 & 0 \\ c_{11} & c_{12} & c_{11} & 0 & 0 & 0 \\ c_{11} & c_{11} & c_{12} & 0 & 0 & 0 \\ 0 & 0 & 0 & \frac{c_{11}-c_{12}}{2} & 0 & 0 \\ 0 & 0 & 0 & 0 & \frac{c_{11}-c_{12}}{2} & 0 \\ 0 & 0 & 0 & 0 & 0 & \frac{c_{11}-c_{12}}{2} \end{bmatrix} \tag{1.17}$$

For an anisotropic material, the elastic tensor is represented by 6x6 matrix. The three-dimensional components of stress and strain are represented by the indices i and j which range this time from 1 to 6. For an anisotropic solid, the stiffness tensor can be expressed as follows :

$$c_{\alpha\beta} = \begin{bmatrix} c_{11} & c_{12} & c_{12} & c_{14} & c_{15} & c_{16} \\ c_{21} & c_{22} & c_{23} & c_{24} & c_{25} & c_{26} \\ c_{31} & c_{32} & c_{33} & c_{34} & c_{35} & c_{36} \\ c_{41} & c_{42} & c_{43} & c_{44} & c_{45} & c_{46} \\ c_{51} & c_{52} & c_{53} & c_{54} & c_{55} & c_{56} \\ c_{61} & c_{62} & c_{63} & c_{64} & c_{65} & c_{66} \end{bmatrix} \tag{1.18}$$

The anisotropic material tensor can also be represented in it canonical form as follows:

$$c_{\alpha\beta} = \begin{bmatrix} c_{11} & c_{12} & c_{13} & 0 & 0 & 0 \\ c_{12} & c_{22} & c_{23} & 0 & 0 & 0 \\ c_{13} & c_{23} & c_{33} & 0 & 0 & 0 \\ 0 & 0 & 0 & c_{44} & 0 & 0 \\ 0 & 0 & 0 & 0 & c_{55} & 0 \\ 0 & 0 & 0 & 0 & 0 & c_{66}. \end{bmatrix} \tag{1.19}$$

It is interesting to link each component in the matrix to it right deformation. Firstly, c_{11}, c_{22}, c_{33} coefficients are related to the compression along the principal axes, thus the longitudinal wave propagation. Secondly, c_{12}, c_{23}, c_{23} are linked to the coupling transverse deformations. Finally, c_{44}, c_{55}, c_{66} represent the shear deformations along different crystallographic directions in the material. They are responsible for transverse wave propagation.

To shake things up, the equation of motion which describes the position, velocity and acceleration of a mass body (m) through Newton's second law ($F = ma$), combined with the Hooke law allows the introduction of Christoffel formula. The idea is to find the solution of the fundamental equation of dynamics applied to a continuous isotropic solid in an infinite media. The purpose is to determine the propagation direction of the energy. For displacement due to a vibration u_i, the equation of motion is represented as follow :

$$\rho \frac{\partial^2 u_i}{\partial t^2} = c_{ijkl} \frac{\partial^2 u_l}{\partial x_j \partial x_k}. \tag{1.20}$$

The next step involves the equation 1.20 solution in the case of a plane wave which propagates perpendicularly to its wavefront in the direction defined by the unit vector $\overrightarrow{n}(n_1, n_2, n_3)$:

$$u_i(t, x) = A.P_i.e^{iw(t-\frac{nx}{V})} \tag{1.21}$$

where A is the displacement amplitude, x is the position vector, P_i is the polarization of the wave which can be explained as the relationship between the direction of the oscillation and the motion direction of the wave. Lastly, V is the phase velocity referring to the speed at which the phase of the wave propagates through the material.

The introduction of the wave solution equation (1.21) into the dynamic equation (1.20) allows expressing Christoffel formula in order to determine the phase velocity V and the polarization P_i [69]:

$$\rho.V^2.P_i = \Gamma_{il}.P_l \tag{1.22}$$

where Γ_{il} is the Christoffel tensor:

$$\Gamma_{il} = c_{ijkl}.n_j.n_k. \tag{1.23}$$

The Christoffel equation shows that polarization P_i is a Christoffel tensor eigenvector with an eigenvalue of γ=ρV^2. Thus, three solutions of the propagation equation stand. The first solution is the longitudinal wave whose polarization is parallel to the wave propagation direction. The second and third solutions are transverse waves whose polarization are perpendicular to the propagation direction [72]. In conclusion, this result shows that three acoustic wave propagation modes occur. These waves are the results of compression and shear forces associated with the acoustic wave flow. It is important to notice that these three modes have different propagation speeds (v_T,v_L) [69]. The longitudinal speed of an acoustic wave (v_L) is related to the longitudinal modulus (C_L), where the transverse speed (v_T) is related to the shear modulus (C_T).



(a) (b)

Figure 1.23: Schematic of longitudinal (a) and transverse (b) wave propagation

The velocity expressions deducted from the Christoffel tensor eigenvector , the longitudinal and transverse velocity in an isotropic media can be expressed by the mechanical parameters of the media as follows:

$$v_T = \sqrt{\frac{C_T}{\rho}} \qquad v_L = \sqrt{\frac{C_L}{\rho}}. \tag{1.24}$$

1.3.4 Rayleigh and Lamb waves generalities

In a finite media, the boundary conditions must be added to the propagation equation. The results in this condition emphasize Rayleigh and Lamb waves. Rayleigh waves travels near the surface. They include longitudinal and transverse motions whose amplitude decreases exponentially as the distance from the surface increases. The mathematical setting for the analysis is a media which occupies a half-space. The detailed analysis can be found in [73]. Rayleigh wave velocity can be measured by its characteristic equation :

$$\eta^6 - 8\eta^4 + 8\eta^2(3 - 2\zeta^2) + 16(\zeta^2 - 1) = 0 \tag{1.25}$$

where $\eta = c_R/c_T$ and $\zeta = c_T/c_L$. It can be shown that only one real root of Equation 1.25 occur, which is the Rayleigh wave velocity c_R. It is also observed that the Equation 1.25 does not depend on frequency, which means that Rayleigh waves are nondispersive.

Lamb waves are another way of looking at wave propagation in a media. They're considered as vibration modes of a plate in a vacuum, which is very interesting in the case of a wafer. These vibrations are directly related to the plate thickness and its mechanical properties. They are characterized by resonance modes linked to the plate thickness h. The analysis solution of the waves propagation in thin plates initiate the understanding of Lamb waves. The boundary conditions consider two infinite parallel planes surrounding the media. Therefore, reflections on the surfaces of the plates must be considered. The detailed analysis can be found in [74]. It is possible to establish analytically the dispersion equations which allows finding the Lamb modes. It transpires that two types of solutions exist. These two solutions represent two wave classes, one in which the displacements toward the propagation are symmetrical relative to the median plate plane and another in which the displacements are anti-symmetrical (Figure 1.24).

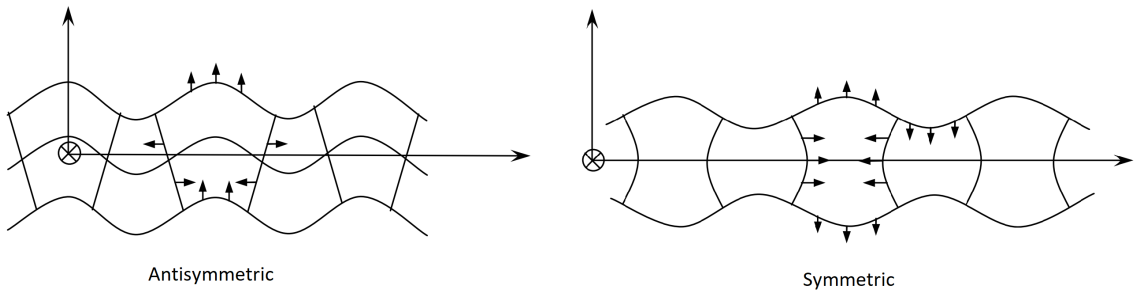

Figure 1.24: Lamb waves modes.

For the symmetrical mode the dispersion equation is:

$$\frac{tan(k_T h/2)}{tan(k_L h/2)} + \frac{4K^2 k_T k_L}{(K_T^2 - K^2)^2} = 0. \tag{1.26}$$

For the anti-symmetrical mode the dispersion equation is:

$$\frac{tan(k_T h/2)}{tan(k_L h/2)} + \frac{(K_T^2 - K^2)^2}{4K^2 k_T k_L} = 0 \tag{1.27}$$

where K is the angular wavenumber and related to the phase velocity by $V = \omega/K$, k_L is the angular wavenumber of the longitudinal wave and k_T is the transverse wave angular wavenumber. The solution of these equations leads to the angular wavenumber K, based on the frequency-thickness product, of the lamb modes that may exist in the plate. It is worth mentioning that these equations are possible only in the case of an isotropic medium.

It is important to note that each Lamb mode is associated with a cut-off frequency. In the case of anisotropic material, more complex methods have been developped to study the Lamb wave propagation. Yet, In the isotropic case, Lamb modes are a combination of longitudinal and transverse modes, their cut-off frequencies are classified as follows:

$$f_c = n\frac{c_L}{2h}; \qquad \text{with, } n = \begin{cases} 2i & \text{Anti-symmetrical mode.} \\ 2i+1 & \text{Symmetrical mode.} \end{cases} \tag{1.28}$$

$$f_c = n\frac{c_T}{2h}; \qquad \text{with, } n = \begin{cases} 2i & \text{Symmetrical mode.} \\ 2i+1 & \text{Anti-symmetrical mode.} \end{cases} \tag{1.29}$$

1.4 Acoustic characterization of direct bonding

The characterization of bonding by ultrasound is a frequent technique. The problem with most studies is that the thickness of the bonding layer is huge compared to direct bonding. XRR measurements show that this thickness varies between **2 nm and 1 nm** (Figure 1.10). This sub-chapter will look at some characterization techniques from the literature and explain the technique selected for direct bonding.

1.4.1 Overview on acoustic characterization of bonding

The elastic nature of acoustic waves allows them to interact effectively with multi-layer structures. For this reason, most studies of interface inspection use acoustic waves. Ultrasonic methods for interface control can be divided into three categories.

1.4.1.1 Time signal analysis/ Echography

The most obvious method is time signal analysis. It involves sending a pulse into the structure and analyzing the echoes relative to the acoustic impedance variations in the bonding. The scanning will locate cracks, porosity and delamination in it. A concrete example of interface control with this approach is detachment detection, which results in a time diagram discontinuity caused by acoustic impedance breakdown. In most cases, longitudinal waves are the most commonly used because of the coupling simplicity between the probe and the structure.

Another solution is to send longitudinal waves at oblique incidence to stimulate the shear stresses. Under these conditions, the wave at the interface generates longitudinal and transverse waves that can be picked up by a second transducer in what is known as the "pitch-catch" mode. However, at an oblique incidence, the waves detected are more numerous due to multiple reflections and transmissions at the interfaces, which makes echo identification difficult.

A concrete example using oblique incident on a bonded structure [Aluminum (1.6 mm)/epoxy(0.1 mm)/Aluminum (0.3 mm)] shows that some reflected echoes can differentiate between poor and good adhesion [75]. The results show an average difference of 1 dB between the interface amplitudes echoes for the area without Teflon and 7 dB for the area with it.

1.4.1.2 Resonance approach/ Spectroscopy

Spectroscopy is another way to approach bonding characterization. When the duration of the incident wave is sufficiently long, the multiple reflections by the different interfaces give a global response of the stratified layer. The frequency spectrum allows deducing the mechanical resonances of the structure. Layer resonance under normal incidence enables the observation of minima in the frequency spectrum of the reflected signal. The position of these minima is related to the observed layer thickness d, representing either an even or odd number of the half wavelength (d=n.$\frac{\lambda}{2}$). Thus, the distance between the minima is given by the following relationship which corresponds to the resonances of each layer i:

$$\Delta f_i = \frac{c_i}{2d}. \tag{1.30}$$

In the case of a three-layered structure, the resonance of each layer is observed in the periodicity of the spectrum and the gaps between the different minima (Figure 1.25).

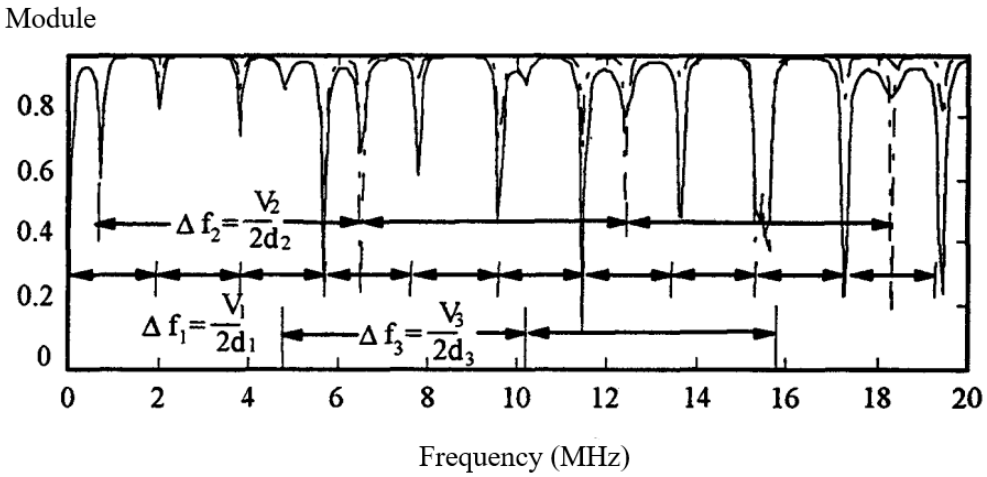

Figure 1.25: Evolution of the modulus of the reflection coefficient in the case of a three-layered structure immersed in water [16].

Most theoretical and experimental studies have shown that two parameters characterize the spectral response. They are the resonance frequency through the minima of the spectrum and the depth of the resonance. They are directly related to the thickness and elastic properties of the layer [76–78]. In the context of spectroscopy and multi-layer structures, the following studies can be quoted [79–82].

1.4.1.3 Guided wave approach

Guided wave characterization depends on the variation of the propagation speed and attenuation during their pathway. However, to be able to characterize the quality of an interface, it is necessary to have a very good knowledge of the waves behavior in the media [16]. The simulation of guided wave propagation in a multi-layer structure is discussed in [83–90]. Generally, guided waves in a multi-layer structure are characterized by dispersion curves giving the evolution of the phase velocity or wavenumber according to frequency.

The generation of guided waves can be done under oblique incidence which promotes several advantages. First, it allows mode conversion, where incident waves excite multiple guided wave modes. Secondly, oblique incidence can increase energy efficiency, resulting in stronger signals and improved sensitivity. Third, it enables guided waves to travel along multiple paths within the structure, providing better coverage and access to different inspection points... Guided waves can also be generated by the emission of a wide-band wave at any angle of incidence. Next, instead of measuring the phase velocity directly, the wave reflected by the whole structure is detected as a function of the incidence angle. For each angle, the generation of guided modes corresponds approximately to the position of the minima on the reflection coefficient. Theoretical and experimental studies using guided

wave dispersion in a bonded structure can be quoted in [91, 92]. An inverse algorithm allows determining the wave propagation speed, thickness, density or the elastic constant of the different layers [93–95].

V(z) technique could also reveal the quality of an adhesion. In certain conditions, acoustic waves generate leaky Surface Acoustic Waves (SAW), which interact with longitudinal waves. The interference produces oscillations in the signal amplitude collected along the vertical direction, called the *V(z)* response. These oscillations can be used to calculate the SAW velocity [96]. *Hyeong Sick Ju & Bernhard R. Tittmann* summarized several *V(z)* characterization for adhesive and thin layer in [97]. To summarize, Table 1.4 shows some of the techniques used to characterize bonding layers by the different approaches mentioned above.

Authors	*Pilarski & Rose* (1988) [75]	*Dekious* (2016) [1]	*Guyott & Cawley* (1988) [80]	*Nagy & Adler* (1989) [91]	*Kosbi & al* (1998) [98]
Acoustic microscopy	15 MHz oblique Focused	200 MHz Planar & 100 MHz focused	Planar (1-13 MHz)	double transmission technique (1-18 MHz)	Spherical lens ($>$ 1 GHz)
Material	Al//Al	Si//Si	Al//Al	Al//Al	Gold on glass
Film Thickness	0.1mm	1 to 2 nm	0.4 to 0.6 mm	300 μm	100 nm
Approach	Echography	Spectroscopy	Spectroscopy	Guided waves	V(z) technique
Bonding strategy	Epoxy	Direct bonding	Adhesive	adhesive	Sputtering
Parameter detected	Adhesion quality	Bonding energy measurement	thickness measurement	Adhesion quality	thickness measurement

Table 1.4: Comparison of bonding characterization researches

1.4.2 Bonding energy acoustic characterization

The method used for bonding energy characterization in this study is based on spectroscopy. To obtain the reflection coefficient, a longitudinal wave is emitted into the wafer at normal incidence. Next, a signal containing multiple reflections in the stratified structure is collected by the ultrasound probe. The reflection coefficient is calculated by the spectrum's ratio between the wave reflected by the surface and the wave penetrating the sample (Equation 1.31):

$$R_{(\omega)} = \frac{S_{R(\omega)}}{S_{I(\omega)}}. \tag{1.31}$$

The variation of the resonance peaks along the frequency axis shall be the link between the bonding energy ΔQ and the acoustic parameter Δf. This parameter shall be called **frequency distance**. Figure 1.26 resume the methodology applied. These peaks are theoretically aligned with the cut-off frequencies of the longitudinal Lamb modes (Equation 1.28) and they are characterized by symmetric and anti-symmetric peaks. Frequency distance refers to the distance between symmetric and anti-symmetric peaks in the spectrum. By probing the wafer surface along XY plane, the cartography of bonding energy is possible on any surface element of the wafer, which is a significant advantage compared to the DCB test.

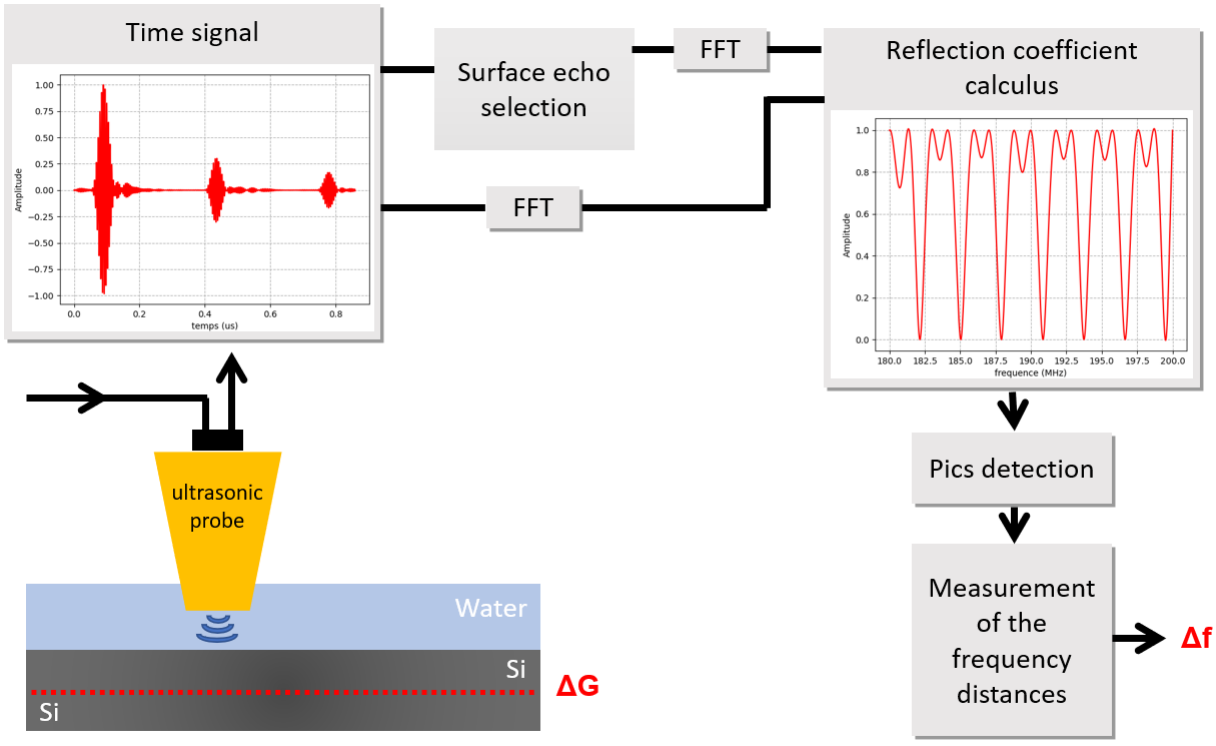

Figure 1.26: Spectroscopy measurement method for direct bonding with ΔQ is bonding energy and Δf the frequency distance

1.4.3 Main results and discussion

Dekious [1] presented theoretical results showing the evolution of the reflection coefficient peaks based on the bonding interface parameters (Figure 1.27). For a hydrophobic bonding with a 2 nm bonding thickness, the results indicate the shift of some resonance peaks according to the Young modulus of the interface. The frequency distance decreases with the Young modulus simultaneously. This shift only concerns anti-symmetrical peaks, the symmetrical peaks remaining static regarding the frequency axis. To establish the vocabulary used in this manuscript, the distance between the symmetrical and the anti-symmetrical peaks is describe as Δf.

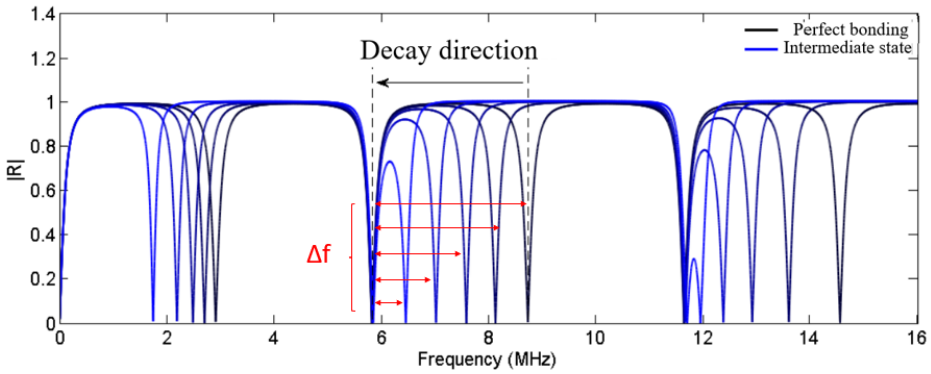

Figure 1.27: Evolution of the reflection coefficient as a function of the interface quality [1]. Young modulus values E = 130, $2.3e^{-3}$, $1e^{-3}$, $0.5e^{-3}$, $0.23e^{-3}$ Gpa.

This outcome can be discussed. First, the bandwidth of the simulation is very low compared to the established theoretical result. It can also be seen that the values of the detected Young's modulus are very low. Which raises the following questions. Is the behavior of the reflection coefficient similar at high frequencies? And is it possible to detect higher values of Young's modulus?

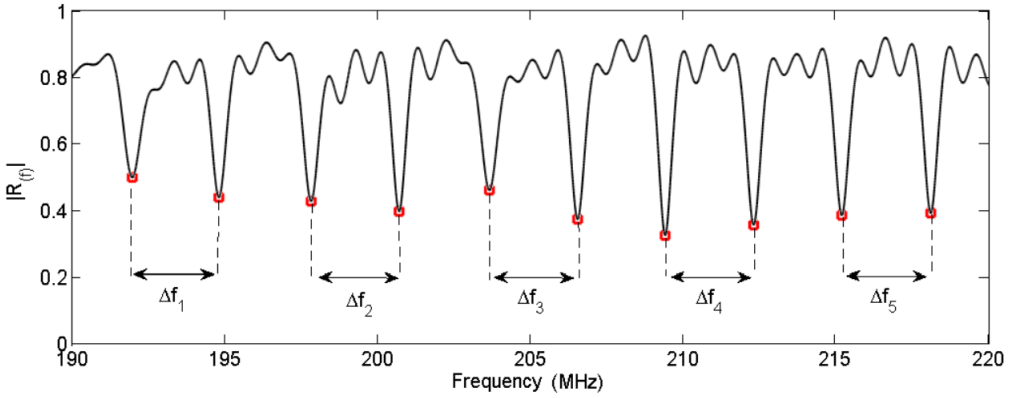

Figure 1.28: Reflection coefficient for a planar transducer [1]

From a practical standpoint, Figure 1.28 and Figure 1.29 show the reflection coefficient of a planar and a focused transducer respectively. These results indicates that a planar transducer will be more suitable considering the depth of the resonance peaks. This is logical since the energy in a focused transducer is concentrated in the focal area,

whereas to resonate the different layers, the planar transducer allows a broader beam spread in its far field. *Dekious* emphasizes the number of echoes used as an important indicator for obtaining finer peaks.

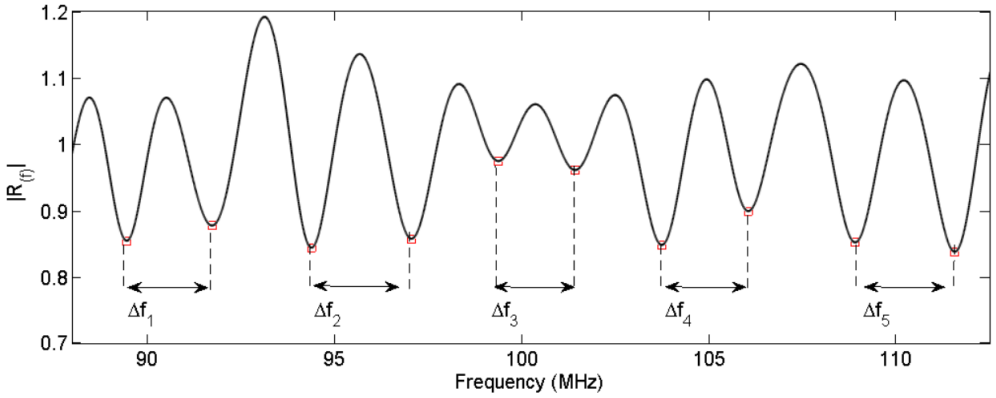

Figure 1.29: Reflection coefficient for a focused transducer [1]

The distribution of experimental results shows a gradual evolution of the distance frequencies relatively to the bonding energy of the samples tested. Figure 1.30 illustrated this evolution. It can be noticed that the sensitivity range is very short and the sensitivity curve saturates around 1 $J.m^{-2}$. *Dekious* shows that a high frequency transducer improves the sensitivity range. They also quote that the sensitivity is sufficient for the control of the bonding quality since beyond 1 $J.m^{-2}$ the bonding is considered good.

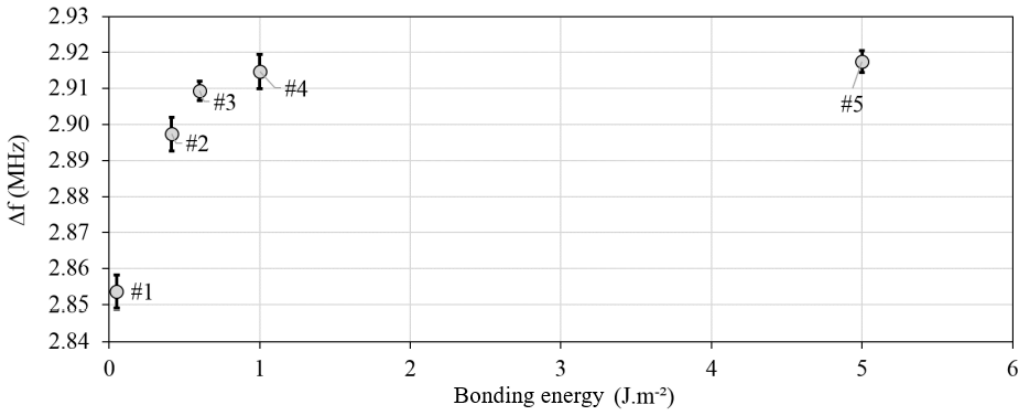

Figure 1.30: Sensitivity of the frequency distance (measured by SAM) according to the bonding energy (measured by DCB test) (1:RT / 2:100°C-400°C / 3:500°C / 4:600°C / 5:1100°C) [1]

The results on wafers shows the evolution of bonding energy clearly (Figure 1.31). The images A, B and D contrast shows that the technique can measure the bonding energy of a defect. Images C and E, with respective dimensions of 30 × 90 mm and 40 × 20 mm, shows variations in bonding energy at the DCB crack area. This result is a solid proof for an concept of non-destructive bonding energy characterization technique.

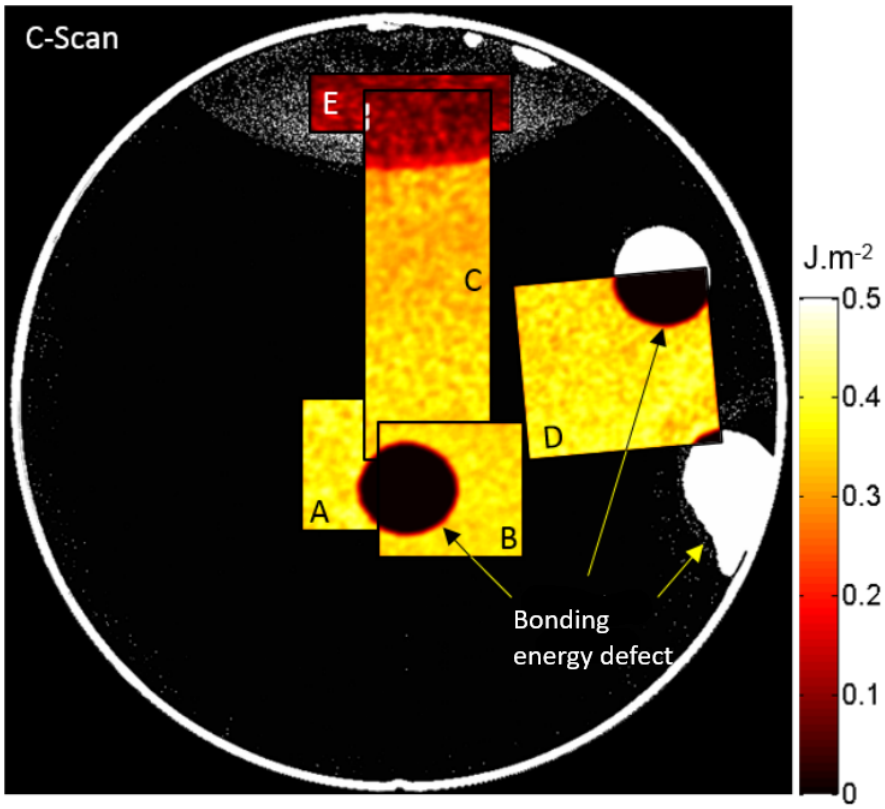

Figure 1.31: Example of a different cartography [1]

1.5 Conclusion

In conclusion, this introductory chapter summarizes the majority of the concepts used during this study. 3D integration methods has been exposed. Three major approaches are mentioned and have been linked to direct bonding. Next, the steps require to apply direct bonding are explained and hydrophobic and hydrophilic bonding are described. The difference between these two strategies relative to annealing temperature and chemical interaction are mentioned and described. The major fact of this first subsection is the different evolution of the bonding energy between hydrophilic and hydrophobic samples. It is also quoted that the thickness of the layer narrows during the annealing process. Moreover, DCB tests and SAM are described in the context of a bonding energy measurement.

Acoustic generalities are described followed by a description of the different approaches relative to ultrasonic bonding characterization. Three categories are explained and several studies have been mentioned in this context. Direct bonding characterization technique is described and results based on previous studies are discussed. The next chapters will be exclusively dedicated to the results obtained in order to put to test the proof of concept established before.

Chapter 2

Feasibility on hydrophilic and hydrophobic samples

Contents

2.1 Introduction and hypothesis 50
2.2 Description of the analytical model 50
2.3 Time signal analysis 52
2.3.1 Hydrophobic case 53
2.3.2 Hydrophilic case 56
2.4 Reflection coefficient analysis 60
2.4.1 Hydrophobic case 60
2.4.2 Hydrophilic case 63
2.5 Variation of the bonding interface condition 69
2.5.1 Distance frequency variation based on bandwidth 69
2.5.2 Thickness variation effect on the reflection coefficient 72
2.5.3 Angle variation effect on the reflection coefficient 74
2.5.4 Variation effect based on the acoustic impedance 76
2.6 Sensitivity curves 77
2.7 Conclusion 79

2.1 Introduction and hypothesis

The first hypothesis to be verified is the feasibility of the technique on hydrophilic and hydrophobic samples according to the criteria elaborated previously. The main criterion is the variation of the resonance peaks according to the quality of the bonding interface. To verify this feasibility, the analysis of the reflection coefficient will reveal the behavior of the resonance peaks based on the states of the bonding interface. The simplest way is to start with the extreme cases of direct bonding. This will allow the validation of the models used and highlight the behavior of the reflection coefficient.

This chapter will start with a description of the proven analytical model used to extract the reflection coefficients. Then, the presentation of hydrophobic and hydrophilic stacks and their response will be shown. The chronographs of the propagation on these multi-layers will be revealed in order to compare the subtle elements to highlight the variation of bonding energy. In a first part, extreme cases will be studied and later more variation will be discussed such as angle, bandwidth and Young modulus variation.

The main hypothesis of this chapter is centered around the theoretical feasibility of the technique on hydrophilic and hydrophobic samples. A first understanding of the physics related to the reflection coefficient shift allows a deep understanding of the Δf variation.

2.2 Description of the analytical model

Since the thickness of the bonding interface layer is extremely small compared to the bonded wafers, it makes element finite analysis in this case slow and obsolete regarding memory since it requires at lease 5 steps in each wavelength. To put concrete numbers on this quote, a 2 nm thickness requires at lease a 0.4 nm mesh. Then, the overall thickness of the wafers is 1.4 mm which require 3.5 billiard points!

To encounter that, Transfer Matrix Method provides the acoustic response through a multi-layer structure. To simplify the boundary conditions by considering the sample an infinite plate horizontally, the incident plane wave response related to the overall path in the multi-layer structure is then obtained. The model is based on the relation between the pressure and bulk flow in the boundary between two medias and it is expressed by matrices. By knowing the acoustical properties of each material, the continuity of the sound pressure and the velocity allows the merge of all the layers into one matrix leading to the acoustical properties of the stack.

Transfer Matrix Method (TMM) was introduced by W.T Thomson [99]. His approach regarding the continuity of stresses and particle velocities in the interface boundaries provides a method to predict acoustical properties. But, limitations were pointed due to the way the problematic is established. Hence, his equations were valid only for multiple fluid layers and solids sandwiched between fluids. In the same path, Brekhovskikh's treatment presents equations whose limitations are close to those of Thomson [100]. In this context, Haskell was the first to propose a general formulation of any multiple layer structure [101]. Moreover, the calculus of transmission and reflection

coefficients was proposed by D.L. Folds and C.D. Loggins, which are based on the analysis of Brekhovskikh's [102]. Here some honorable mention regarding the derivation of transfer matrices in the cases of multi-layers of fluids and solids [90, 103–106].

In our case, the reflection coefficient is at the core of the Δf variations. The model proposed by D.L. Folds and C.D. Loggins suits perfectly for wave propagation through a stack of wafers. It started with a plane wave originating from the bottom layer and proceeds through each layer until it emerges through the first layer. It propagate along the z axis making the last layer semi-infinite. The infinite character of the x and y axis with the incident angle of the waves lies into xz plane making the problem two dimensional (Figure 2.1). When a plane wave arrives to a layer boundary at an angle θ, normal stress and shear stress are induced in the layer giving birth to normal particle velocity and tangential particle velocity. The continuity of these parameters is ensured by the boundary conditions in each layer since for a harmonic wave the particle velocity is given by $v = i\omega u$. Thus displacement (u) continuity is similar to the particle velocities (v) continuity.

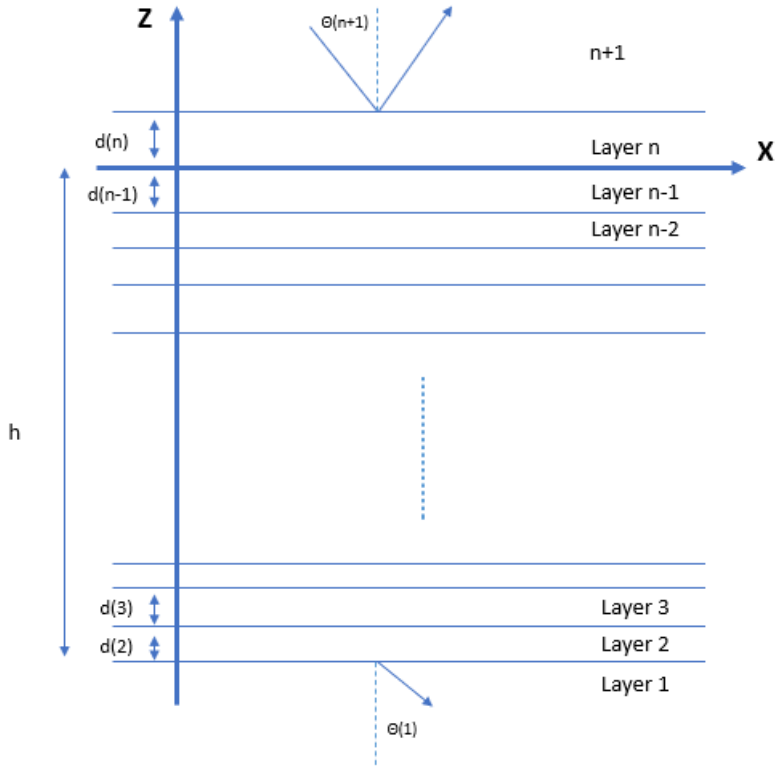

Figure 2.1: geometry of the multi-layer system

The model requirement are numerical inputs such as longitudinal and transverse velocities, density and thickness. Each layer is described by these elementary parameters. Then, the calculus of the reflection and transmission coefficients based on the velocities and stresses of each layer is possible by solving the global matrix regrouping all the amplitude coefficients. The demonstration is found in [102] and Appendix B. The results are resumed in equations 2.1 and 2.2, which predict the transmission and reflection of the sound wave incident on multi-layer setup:

$$T = \frac{2Z_1}{(M_{22} + Z_1 M_{23})Z_{n+1} + M_{32} + Z_1 M_{33}} \tag{2.1}$$

$$R = \frac{M_{32} + Z_1 M_{33} - (M_{22} + Z_1 M_{23})Z_{n+1}}{(M_{22} + Z_1 M_{23})Z_{n+1} + M_{32} + Z_1 M_{33}} \tag{2.2}$$

where Z_n are the respective impedance of the layers and M_{ij} are coefficients of the global matrix which regroup all the amplitude matrices.

The construction of the time signal by using the reflection coefficient is possible with an inverse FFT. Yet, In order to adjust the reflection coefficient, the frequency response of the impulse is required. The pulsed wave is centered on a nominal frequency. The spectrum of the impulse response is automatically centered at the same frequency. The modulation of the reflection coefficient with the impulse response provides the frequency spectrum of the multi-layer stack response. Afterward, an inverse FFT provides the time signal relative to the acoustic propagation trough all the stack.

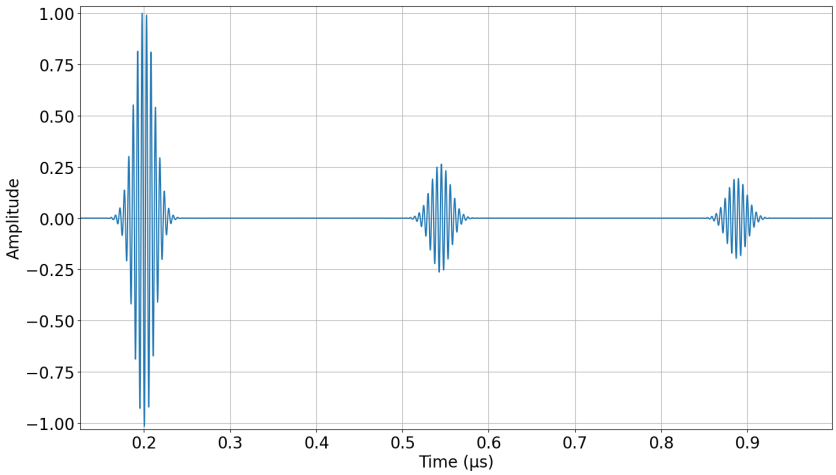

Figure 2.2: Example of time signals produced by the model

A fast checking of the model can be made by measuring the Time of Flight of the overall path by using the same parameters inserted previously in the model. For example, Figure 2.2 represents the propagation into 2 bonded wafer of 725 μm each. The speed of the wave into silica is 8430 m/s, thus the time of flight is around 0.34 μs.

2.3 Time signal analysis

After describing the model, The first attempt is to analyze the signals established by the wave propagation for hydrophilic and hydrophobic stacks. Firstly, The easiest approach is to simulate the extreme cases of the bonding. In the case of hydrophobic bonding, since water does not play a bigger role in the process, the first state of the bonding interface shall be considered air. In the case of hydrophilic bonding, water

presence is much important and thus the first states shall be consider water. According to Figure 1.10, the bonding layer merges into the silicon, thus a good bonded layer shall be considered the same as it upper and lower layer. The bonding nuance range is defined between these two limits for the both cases.

2.3.1 Hydrophobic case

To start the discussion of the time signal response regarding the different cases, Table 2.1 describes the parameters of each layer insert into the model in this case.

condition	Stack	longitudinal speed c_l	transverse speed c_t	density ρ	thickness h
unbonded	layer 1 (Silicon)	8432	5842	2329	725 μm
	Bonding layer	340	0.0001	1	2 nm
	layer 2 (Silicon)	8432	5842	2329	725 μm
bonded	layer 1 (Silicon)	8432	5842	2329	725 μm
	Bonding layer	8432	5842	2329	2 nm
	layer 2 (Silicon)	8432	5842	2329	725 μm

Table 2.1: Unbonded and bonded interface theoretical parameters of the hydrophobic case (SI//SI).

It is noticed that this first sample is characterized by a symmetric geometry. This fact will influence the way the layers resonate during the propagation. In the case of a bonded stack (Figure 2.3), the duration of each overall path corresponds to the full thickness of the bonded wafers. The time of flight relative to this propagation is 0.344 μs for a 1.450 mm full thickness (Figure 2.5). The first echo in the illustration represents the first interaction with the wafer, which is referred to as the surface echo in the first chapter. Each echo after it represents an overall path through the sample, thus the double thickness of the wafer.

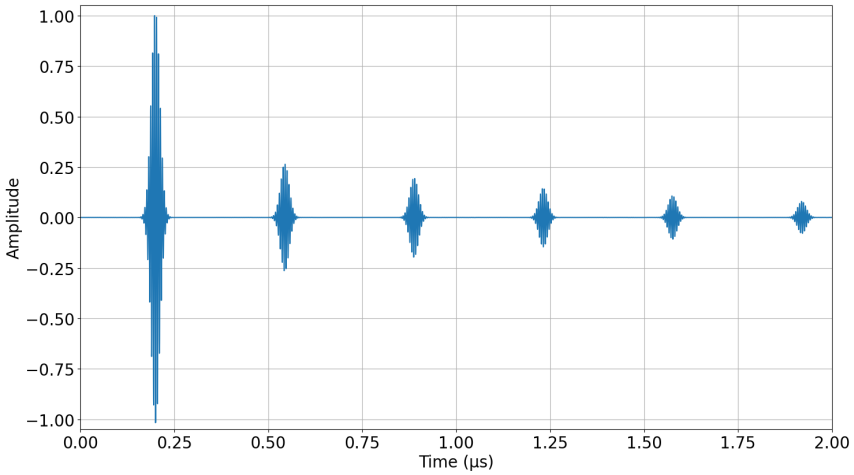

Figure 2.3: Time response of an bonded wafer in the hydrophobic case (SI//SI)

Since the bonding layer is sandwiched between two identical media, no discontinuity of the stress and displacement is present in the model, leading to a perfect crossing through the bonding. This graph could also reveal the attenuation of the wave propagation in the silicon stack. The amplitude decreasing is due to the interactions of the wave with the inner boundaries of the sample causing several reflections and transmissions in the stack.

The next figure represents the opposite of the previous case. Figure 2.4 shows the evolution of the time response when the bonding layer is replaced with air in the model. This case is interesting since it demonstrates the time response of an uncoupled wafer due to a severe disruption of impedance. The time of flight is twice shorter than in the bonded case. The stack symmetry plays a role on the perfect alignment of the echoes. Next, the amplitude decreasing caused by the reflections and transmissions in the inner structure reveals interesting facts on the Echography approach in this type of samples.

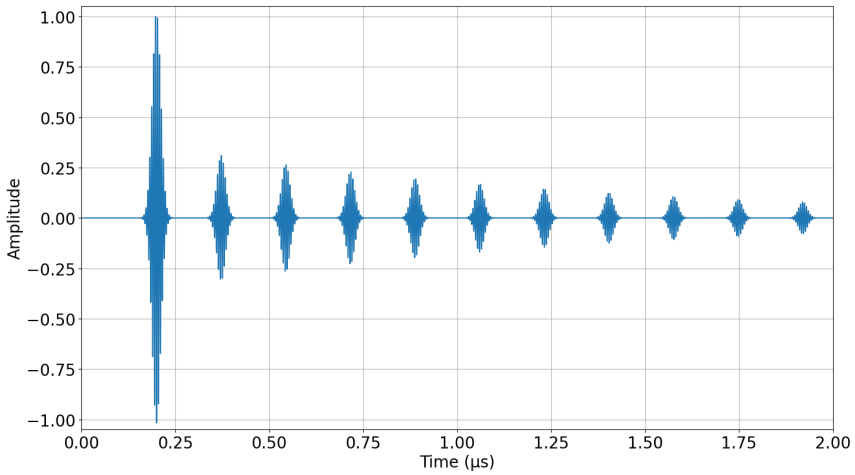

Figure 2.4: Time response of an unbonded wafer in the hydrophobic case (SI//SI)

Figure 2.5 presents the amplitude variation in 725 μm of silicon in orange, and 1.450 mm in blue. The dots represent each background echo for both unbonded and bonded output signals respectively. The normalized surface echo is used as a reference for all the dots to calculate their amplitude values in dB. Figure 2.5 displays the amplitude behavior regarding the distance and the time-of-flight a wave covered in the inner stack by looking to the amplitude of the different echoes in the time response. It is important to notice that in the model a tiny water layer is added since the wafer is immersed in water. Figure 2.5 emphasizes on the lost of energy due to the propagation in the silicon and the interaction of the wave regarding inner reflections and transmissions.

Let's describe more deeply Figure 2.5. To remind, the idea is to compare the maximum amplitude of the background echoes with the normalized surface echo. It is visible that the dots are generally aligned at the beginning based on the time-of-flight and the distance no matter the bonding condition. It is worth noticing that a shift in amplitude is occurring along the following background echoes due to the length of their path. Nevertheless, the distance and time of flight between the orange and the blue dots superpose, even if the stacks are different. The unbonded case does not allow the wave to

pass to the lower part of the sample, resulting in a thickness and time-of-flight that are two times shorter. The important observation in this case is the comon linear decrease. Yet, the behavior is similar in both cases, emphasizing the relationship between inner reflections and transmissions and the acoustic impedance of each layer. The amplitude decreasing is due to the wave interaction with the boundaries, making the thickness of the stack irrelevant to the amplitude variation. Nonetheless, the thickness is represented by the time-of-flight and the distance, which are the true elements to quantify this parameter.

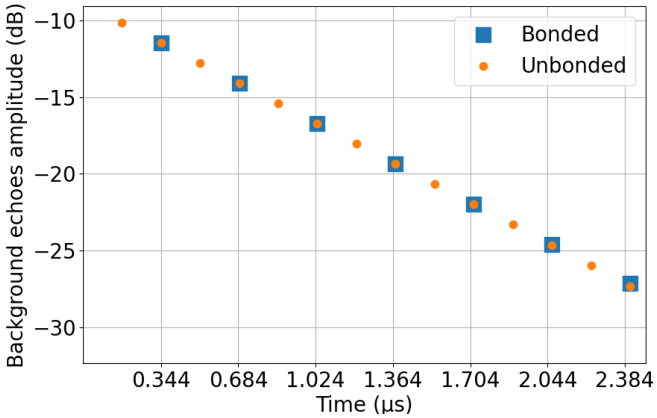

(a) Time-of-flight

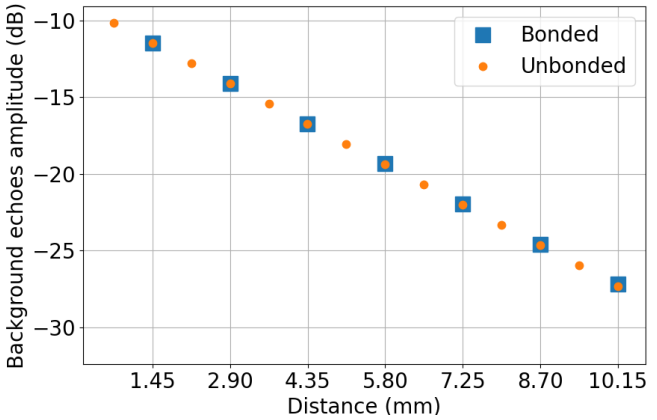

(b) Distance

Figure 2.5: Attenuation of the resonating wave in 1.450 mm of silicon (red), 0.725 mm (pink) dip in water

2.3.2 Hydrophilic case

The number of layers in hydrophilic samples is much bigger than hydrophobic. The difference between the two cases is the presence of the silicon dioxide layers. Table 2.2 describes the parameters of each layer inserted into the model in this case. In this category, two main sub-samples were selected. The main difference between them is their symmetry relative to the bonding layer.

condition	Stack	longitudinal speed c_l	transverse speed c_t	density ρ	thickness h
unbonded	layer 1 (Silicon dioxide)	5837	3558	2150	200 nm
	layer 2 (Silicon)	8432	5842	2329	725 μm
	layer 3 (Silicon dioxide)	5837	3558	2150	200 nm
	Bonding layer	1480	0.0001	1000	2 nm
	layer 4 (Silicon)	8432	5842	2329	725 μm
bonded	layer 1 (Silicon dioxide)	5837	3558	2150	200 nm
	layer 2 (Silicon)	8432	5842	2329	725 μm
	layer 3 (Silicon dioxide)	5837	3558	2150	200 nm
	Bonding layer	5837	3558	2150	2 nm
	layer 4 (Silicon)	8432	5842	2329	725 μm

Table 2.2: Unbonded and bonded interface theoretical parameters of the hydrophilic case (OX//SI)

condition	Stack	longitudinal speed c_l	transverse speed c_t	density ρ	thickness h
unbonded	layer 1 (Silicon dioxide)	5837	3558	2150	200 nm
	layer 2 (Silicon)	8432	5842	2329	725 μm
	layer 3 (Silicon dioxide)	5837	3558	2150	200 nm
	Bonding layer	1480	0.0001	1000	2 nm
	layer 4 (Silicon dioxide)	5837	3558	2150	200 nm
	layer 5 (Silicon)	8432	5842	2329	725 μm
	layer 6 (Silicon dioxide)	5837	3558	2150	200 nm
bonded	layer 1 (Silicon dioxide)	5837	3558	2150	200 nm
	layer 2 (Silicon)	8432	5842	2329	725 μm
	layer 3 (Silicon dioxide)	5837	3558	2150	200 nm
	Bonding layer	5837	3558	2150	2 nm
	layer 4 (Silicon dioxide)	5837	3558	2150	200 nm
	layer 5 (Silicon)	8432	5842	2329	725 μm
	layer 6 (Silicon dioxide)	5837	3558	2150	200 nm

Table 2.3: Unbonded and bonded interface theoretical parameters of the hydrophilic case (OX//OX)

For the first hydrophilic case (OX//SI), the time responses of an bonded and unbonded wafer are shown respectively in Figure 2.6 and Figure 2.7. Hilbert transform in red is performed to extract the amplitude and the TOF values. It is observed that the

two signals exhibit a lot of similarities except on the amplitude of the background echoes. Since the bonding layer only measures 2 nm, the response of the 200 nm dioxide layer combined with the bonding layer provides a single time signature, which is referred to by odd numbers. The even numbers represent the response of an overall path in the sample. Table 2.4 displays the TOF and amplitude values relative to the first five background echoes.

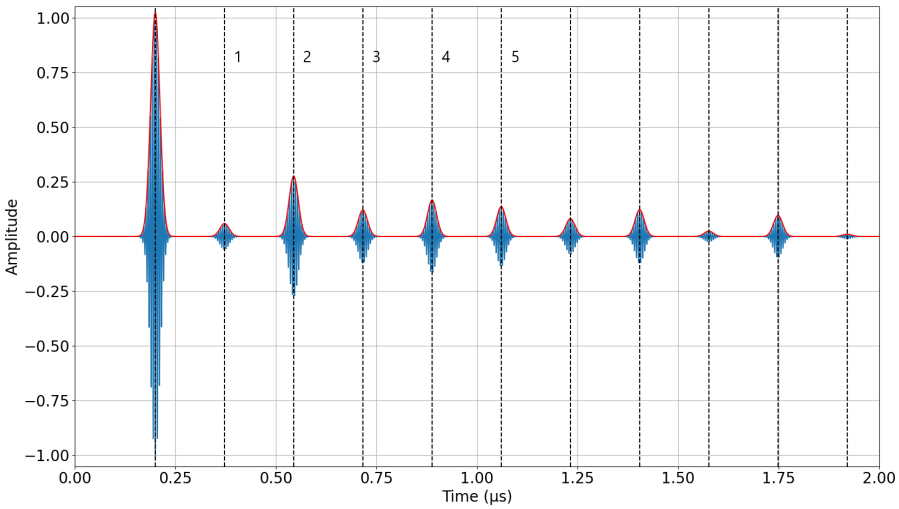

Figure 2.6: Time response of an bonded wafer in the hydrophilic case (OX//SI)

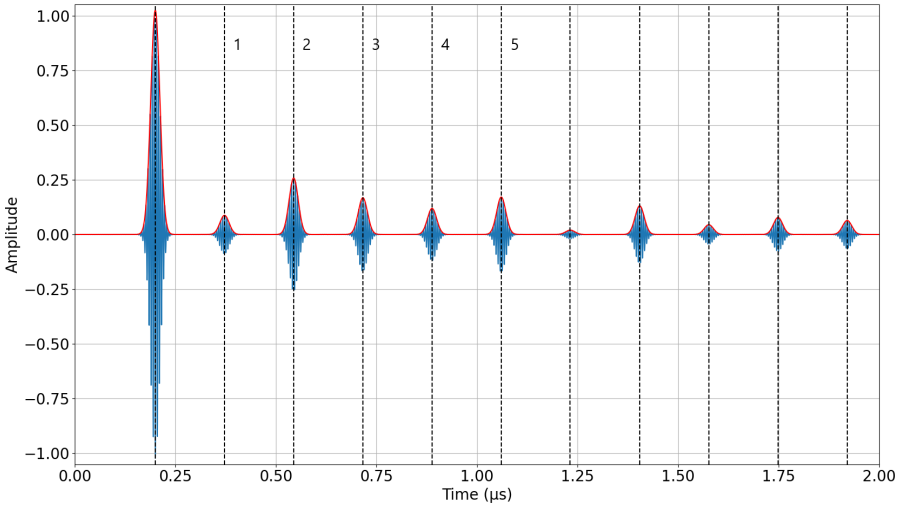

Figure 2.7: Time response of an unbonded wafer in the hydrophilic case (OX//SI)

Based on the previous elements, the influence of the bonding layer conditions on the amplitude is much important compared to the TOF. This fluctuation represents the most prominent factor to discriminate hydrophilic samples based on their bonding energy level. The time of flight (TOF) demonstrates the merging of silicon dioxide echoes with the

Background echoes index	1	2	3	4	5
Amplitude bonded case	0.0593	0.2753	0.1216	0.1657	0.1362
Amplitude unbonded case	0.087	0.258	0.1679	0.1191	0.1710
Time of flight unbonded case (μm)	0.372256	0.544258	0.716261	0.888264	1.06051
Time of flight bonded case (μm)	0.372256	0.544258	0.716261	0.888264	1.06026

Table 2.4: TOF and amplitude values of the time response of unbonded and bounded hydrophilic layers (OX//SI)

bonding layer echoes. Thus, the prediction of the bonding layer fluctuations depends on the silicon dioxide also. Another factor to consider is the amplitude level of the odd and even background echoes. Let's start with the bonded condition graphic, the amplitude of the even echoes decreases along the propagation. The odd echoes in the other hand show a more complex pattern. For example, The first background echo is smaller compared to the third and the fifth, where the fifth and the third show relatively similar amplitude values. In the unbonded case, the odd and even echoes represent the same TOF pattern. But, the amplitude fluctuation are different compared to the bonded case. Those fluctuations can be linked to the constant parameters of the silicon dioxide layer, mainly its size, which behaves as a resonator inserted between the two much bigger silicon layers.

For the third case (OX//OX), TOF values are similar until the fourth echo where a strange drop of amplitude is noticed on the unbonded time response (Figure 2.8). This raises an important question regarding the behavior of the background echoes amplitudes. Are these amplitude fluctuation more present when the bonding layer parameters change ? Are they only present on odd echoes or both background echoes ? The most important, are they reliable to extract the bonding energy level of the samples ?

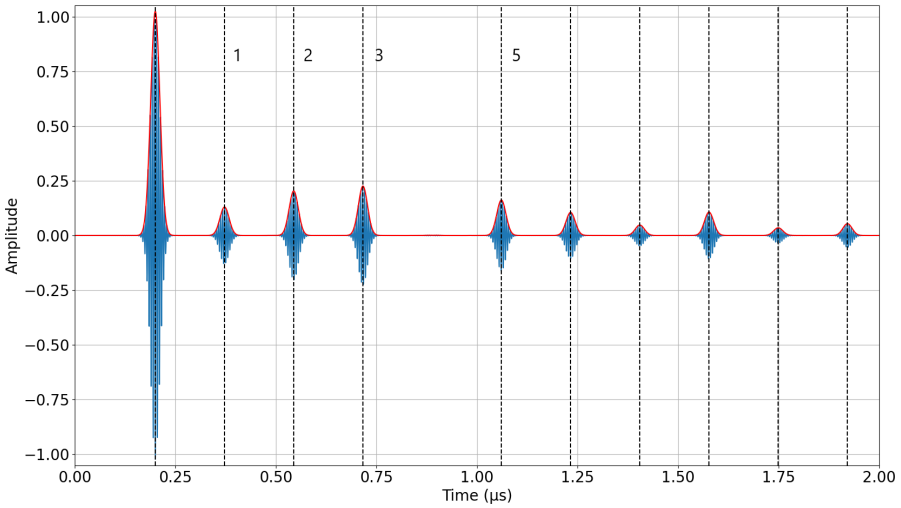

Figure 2.8: Time response of an unbonded wafer in the second hydrophilic case (OX//OX)

Table 2.5 shows again the TOF disability to separate the bonding layer and the silicon dioxide layers since the thickness of the bonding layer is much smaller. This fact

could lead to unwanted dependency linked to the superposed echoes, which saturate the response of the bonding layer by the response of the silicon dioxide. Figure 2.9 highlights the complex pattern of amplitude variation in the bonded case. In this condition, the fourth background echo is present, while the amplitude variation of the second and third background echoes shows a similar amplitude gap between the bonded and the unbonded case.

Background echoes index	1	2	3	4	5
Amplitude unbonded case	0.1302	0.2033	0.2257	-	0.1619
Amplitude bonded case	0.1049	0.2327	0.1976	0.0632	0.1751
Time of flight bonded case (μm)	0.372256	0.544508	0.716511	0.88851	1.060767
Time of flight unbonded case (μm)	0.372256	0.544508	0.716511	-	1.060767

Table 2.5: TOF and amplitude values of the time response of unbonded and bounded hydrophilic layer (OX//OX)

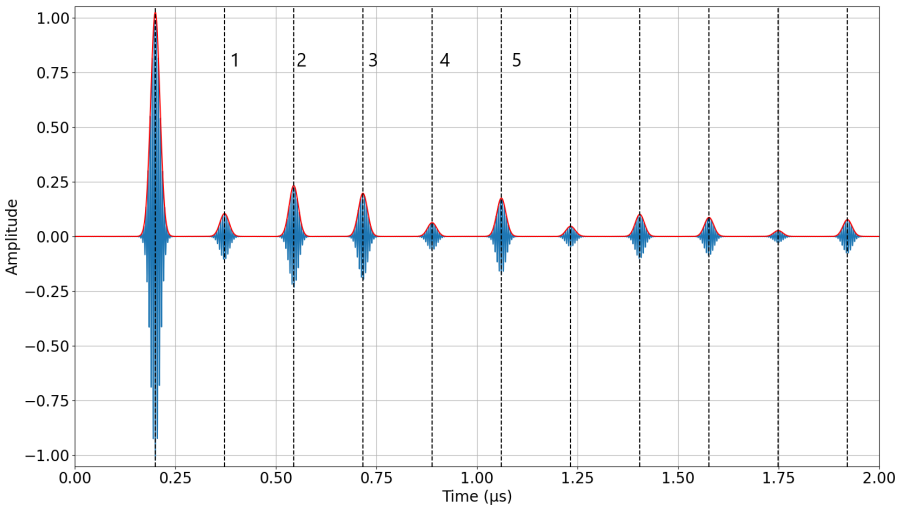

Figure 2.9: Time response of an bonded wafer in the second hydrophilic case (OX//OX)

In conclusion, the results presented in this subsection highlight the challenges of using a time signal analysis approach for bonding energy characterization. In the hydrophobic case, the bonding layer response is visible since the layer is sandwiched between two much bigger silicon layers. However, in the case of hydrophilic samples, the presence of the silicon dioxide layer hides the time interval of the bonding layer. Additionally, the silicon dioxide layers create significant resonance phenomena in the samples due to their thickness.

2.4 Reflection coefficient analysis

The reflection coefficient is an another way to view the wave propagation through the wafer stacks. The analysis in the frequency domain provides another perspective as it displays the signal energy across the bandwidth of the incident wave. In our case, the incident wave is centered around 190 MHz in the model. Again, the analysis is done on hydrophobic and hydrophilic samples. There parameters are highlighted in the tables 2.1, 2.2 and 2.3 respectively. Let's also remind the extreme conditions of the two cases. In the case of hydrophobic bonding, the first condition of the bonding interface shall be considered air. In the case of hydrophilic bonding, the first condition considers water. The second part of the interval defined the converging state of the bonding stack. According to Figure 1.10, The bonding layer merges into the silicon; thus, in the model, a good bonded layer shall be considered as a silicon layer for hydrophilic samples. For hydrophobic samples, the converging condition of a good bonding is considered as silicon dioxide. This choice is explained by the fact that a good bonding layer will not disrupt the boundary condition when the wave is crossing through it.

2.4.1 Hydrophobic case

Figure 2.10 displays the reflection coefficient pattern based on the input parameters described in Table 2.1. In the case of a perfect bonding, the continuity of velocity and displacement provides the response of an 1.45 mm silicon layer. In the second case, the air doesn't help the acoustic wave to reach the second wafer. As a consequences, the reflection coefficient response corresponds to a 725 μm silicon layer.

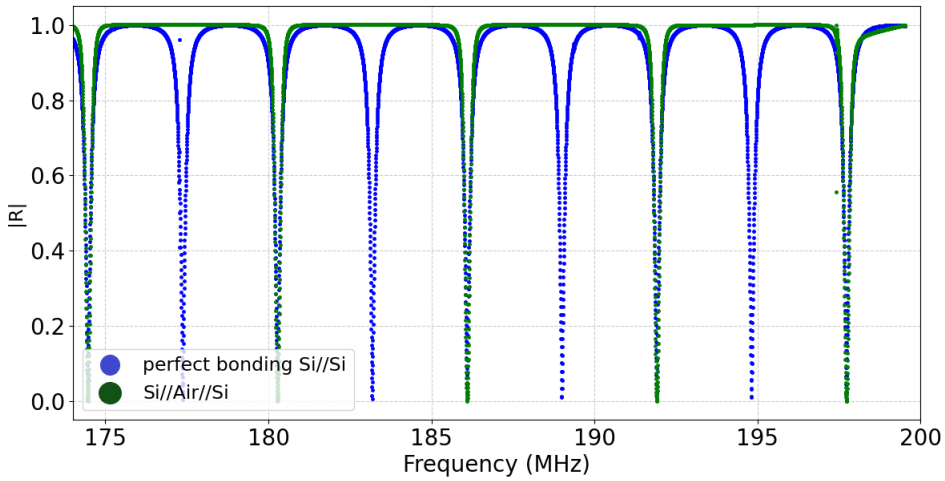

Figure 2.10: Reflection coefficient of hydrophobic extreme cases, in blue SI//SI, in green SI//Air//SI

To provide a deeper description of Figure 2.10, let's focus on the frequency value where the reflection coefficient is null. Table 2.6 shows the cutoff frequencies displayed in Figure 2.10.

Bandwidth	Idx(i)	SI//Air//SI cutoff frequency [MHz]	Idx(j)	SI//SI cutoff frequency [MHz]	$\lvert f_{c_i}$[SI//SI] - f_{c_j}[SI//Air//SI]$\rvert$
[173 MHz - 175 MHz]	1-2	174.462963	1	174.456713	6.25 kHz
[175 MHz - 178 MHz]	-	-	2	177.366044	2.903081 MHz
[178 MHz - 182 MHz]	3-4	180.278499	3	180.272249	6.25 kHz
[182 MHz - 185 MHz]	-	-	4	183.181580	2.903081 MHz
[185 MHz - 188 MHz]	5-6	186.094035	5	186.087785	6.25 kHz
[188 MHz - 190 MHz]	-	-	6	188.997116	2.903081 MHz
[190 MHz - 193 MHz]	7-8	191.909572	7	191.903322	6.25 kHz
[193 MHz - 195 MHz]	-	-	8	194.812652	2.903081 MHz

Table 2.6: Cutoff frequencies of the reflection coefficients based on Figure 2.10

On the macroscopic level, Figure 2.10 shows the difference between the two cases clearly. It reveals the double gap of the cutoff frequencies generated by the discontinuity caused by the air layer. This gap can be measured theoretically by Equation 1.30:

$$\Delta f_{SI//SI} = 2.9068 MHz, \qquad \Delta f_{SI//air//SI} = 5.8137 MHz. \tag{2.3}$$

Table 2.6 provides a microscopic view of the reflection coefficient in this cases. It also shows the positions of the cutoff frequencies based on the selected bandwidth. To dive deeper into the analysis, two types of peaks are identified. A class of peaks that does not respond to the bonding layer parameters' variation and the second who responds more effectively. The cutoff frequencies comparison between the two cases quantify this observation. Let's begin with the superposed peaks, the subtraction between bonded and unbonded cutoff frequencies in the same bandwidth correspond to 6.25 kHz. This value can be traced to the sampling frequency since each step correspond to 3.125 kHz. Thus, a shift of two points occurred between the two curves. An attempt to reduce this gap was performed, the model was compiled with a higher number of point but the gap remained the same. Another shift source could be the thickness of the unbonded layer who does not take into consideration the 2 nm bonding layer, which could be a generator of the shift since the overall thickness is not the perfect double of the unbonded case. Meaning, that the alignment of the superposed peaks depend on the symmetry of the sample exclusively. This quote will be expanded in next subsections.

The second main parameter to analyze is the gap between the superposed peaks and the new emerging peaks from the bonded case. This interval is measured as 2.903081 MHz, which corresponds to the highest value of spread possible between the two extreme cases for hydrophobic samples. A simple calculus could provide the number of cutoff frequency values possible in this spread since it is linked to the sampling frequency. For a 3.125 kHz sampling step, the number is 464 possible potential cutoff frequency values in this interval. This suggests that a higher sampling rate is highly recommended.

Let's now put a theoretical frame on this parameters, Equation 1.29 and Equation 1.28 exhibit the cutoff frequencies of the Lamb modes. The classification of longitudinal Lamb modes should theoretically align with the coefficient reflection cutoff frequencies compiled by the model. Figure 2.11 superpose these two elements in the hydrophobic case. It is important to understand that the black and the red vertical lines correspond to the symmetrical and anti-symmetrical modes respectively in the bandwidth of the chart. Their positions are linked directly to the thickness and the longitudinal and transverse speed of the overall layer, thus the modes observed in this graph correspond to a full bonded wafer. Figure 2.12 displays the corresponded modes for an unbonded case, thus for the half thickness of the stack.

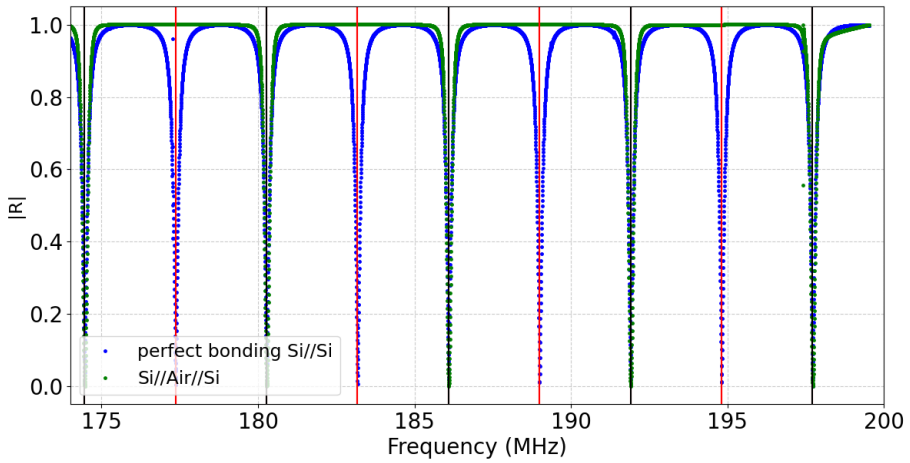

Figure 2.11: Reflection coefficient of hydrophilic extreme cases, in blue SI//SI, in green SI//Air//SI associate with symmetrical (Black) and Anti-symmetrical (Red) Lamb modes

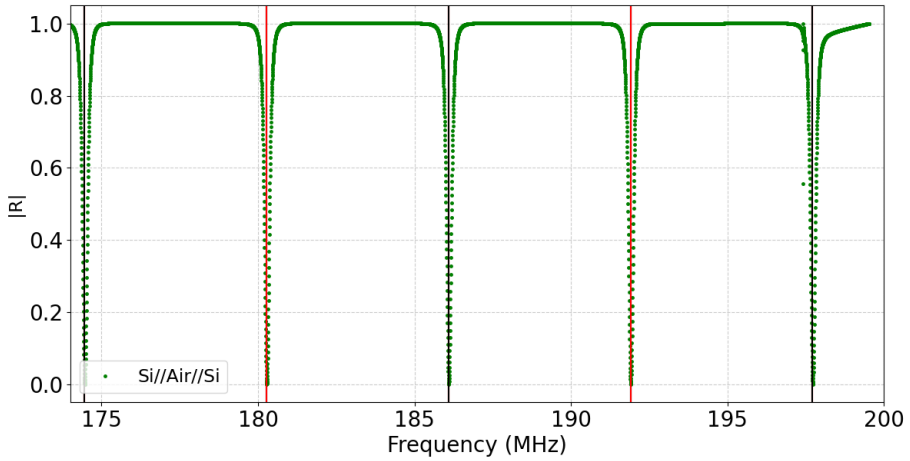

Figure 2.12: Reflection coefficient of an unbonded layer (in green SI//Air//SI) associate with symmetrical (Black) and Anti-symmetrical (Red) Lamb modes corresponding to a half thickness of the full stack 725 μm

The comparison between Figure 2.11 and Figure 2.12 reveals interesting remarks regarding the positioning of symmetrical and anti-symmetrical peaks. The flashy gap between the two curves emphasis the thickness influence on the cutoff frequency's positions. When the bonding is perfect, the resonances appear at regular frequency intervals. These intervals are divided by two when no bonding exists due to the factor two in the thickness decrease. However, we can notice that the resonances are regularly spaced. This phenomenon can be observed if and only if the wave doesn't cross to the other side of the sample. Thus, it occurs only in the case of a full unbonded condition. When the bonding or the unbonding is not perfect, the regularity of the resonances is broken.

2.4.2 Hydrophilic case

In this second case, the theoretical assumption of the unbonded layer will impose a much important interaction of the wave with all the layers. The full discontinuity observed in the hydrophilic case is not a starter point since the bonding energy in these types of stacks is much higher due to the presence of hydrogen bonds. Again, two cases were selected to analyze the reflection coefficient behavior. Table 2.2 and Table 2.3 display the parameters introduced in the model to obtain the following results for OX//OX and OX//SI samples respectively. To remind, the difference between the two hydrophilic cases is the layers anatomies engaged in the bonding. Besides, the last case presents a bonding structure using two wafers of different anatomies. This will highlight the impact of the bonding geometrical symmetry on the reflection coefficient.

Let's start by the configuration of Table 2.3. The particularity of it stands at the symmetry structure, meaning that the wafers engaged in the bonding are made up of the same layers. The question to be asked in this subsection is: Can the complexity of these samples reveal other facts about the acoustic wave response behavior observed in subsection 2.3.2, and how will this be reflected on the reflection coefficient?

Figure 2.13 represents the reflection coefficient chart for OX//OX samples. On the macroscopic view, this first configuration seems to give the same results in both ways. The shift on the bonding layer parameters doesn't affect the reflection coefficient as observed before. The cutoff frequencies values tend to show a reflection coefficient of a full bonded sample!

More deeply, Table 2.7 focuses on the cutoff frequencies positions in Figure 2.13. In the beginning, this analysis shows the proximity of all the peaks in different bandwidths around the pulse frequency (190 MHz). Nevertheless, the last column in the table provides more information about the reflection coefficient behavior. The comparison between the two extreme cases shows that these peaks are spaced by a less significant frequency distance. On top of that, the spread value on each bandwidth is different. Furthermore, it shows that bandwidths with odd indexes display smaller distances compared to bandwidths with even indexes. This behavior is similar to the symmetrical and anti-symmetrical modes seen in the hydrophobic case. Yet, an unusual pattern is observed. By focusing on the first three values of the Table 2.7 last column, one can notice the irregularity shown on the frequency spread values along the full bandwidth.

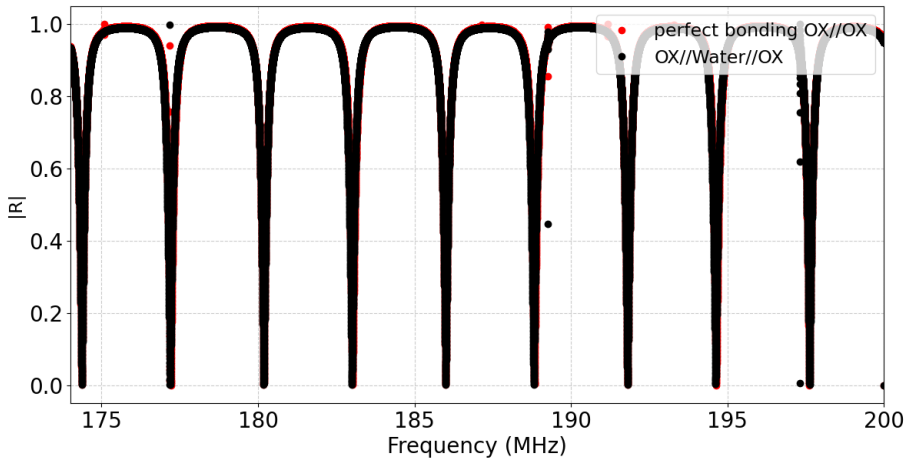

Figure 2.13: Reflection coefficient of hydrophilic extreme cases, in Red OX//OX, in Black OX//water//OX

Compared to hydrophobic samples results, the position of the cutoff frequencies doesn't respect a constant spread distance between the peaks (Table 2.6). The odd values are rising along the frequency spectrum expressing a sort of dependency. Can this last column be explained by the number of points in the simulation? A frequency sampling effect? or physical phenomenon related to the structure analyzed?

Bandwidth	Idx(i)	OX//H_2O//OX cutoff frequency [MHz]	Idx(j)	OX//OX cutoff frequency [MHz]	$\lvert f_{c_i}$[OX//OX] - f_{c_j}[OX//H_2O//OX]$\rvert$
[173 MHz - 175 MHz]	1	174.36999	1	174.36921	779.99 Hz
[175 MHz - 178 MHz]	2	177.198	2	177.212	13.999 kHz
[178 MHz - 182 MHz]	3	180.18240	3	180.18240	0 Hz
[182 MHz - 185 MHz]	4	183.00189	4	183.01986	17.969 kHz
[185 MHz - 188 MHz]	5	185.99481	5	185.99403	779.99 Hz
[188 MHz - 190 MHz]	6	188.81118	6	188.82993	18.749 kHz
[190 MHz - 193 MHz]	7	191.80644	7	191.80644	0 KHz
[193 MHz - 195 MHz]	8	194.62046	8	194.63999	19.530 kHz
[195 MHz - 198 MHz]	9	197.62042	9	197.618860	3.999 kHz

Table 2.7: Cutoff frequencies of the reflection coefficients based on Figure 2.13

Figure 2.14 displays a 10 MHz bandwidth including 4 peaks. The observation of a smaller interval shows the difference between odd and even peaks in the chart. The variation of the reflection coefficient anti-symmetrical peaks is easily seen, which emphasizes the impact of the bonding intrinsic property shifts on the reflection coefficient in this case. While the Table 2.7 displays an irregular pattern mainly caused by the signal sampling, Figure 2.14 demonstrates partially the maintaining of the hydrophobic pattern.

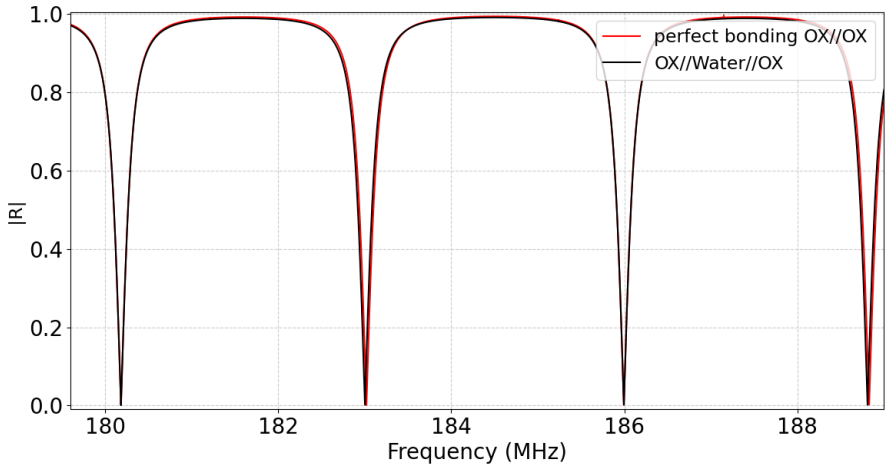

Figure 2.14: Reflection coefficient of hydrophilic extreme cases, in Red OX//OX, in Black OX//water//OX between 180 MHz and 190 MHz

Figure 2.15 and Figure 2.16 represent a zoom on the odd and even peaks. Figure 2.16 shows the symmetrical peaks stability in both extreme cases, where Figure 2.15 displays the anti-symmetric peaks shift between them. This shift is measured by the difference of the peaks position relative to the frequency axis and is equal to 17.969 kHz. It should be mentioned that this shift is unstable over all bandwidths that include anti-symmetrical peaks as seen in Table 2.7. But, if this interval is taken as a reference and knowing the frequency sampling steps, the potential frequency steps between the two extreme cases are only six. Indeed, this observation suggests that a higher sampling frequency is an important factor in order to capture more nuanced information on the bonding layer.

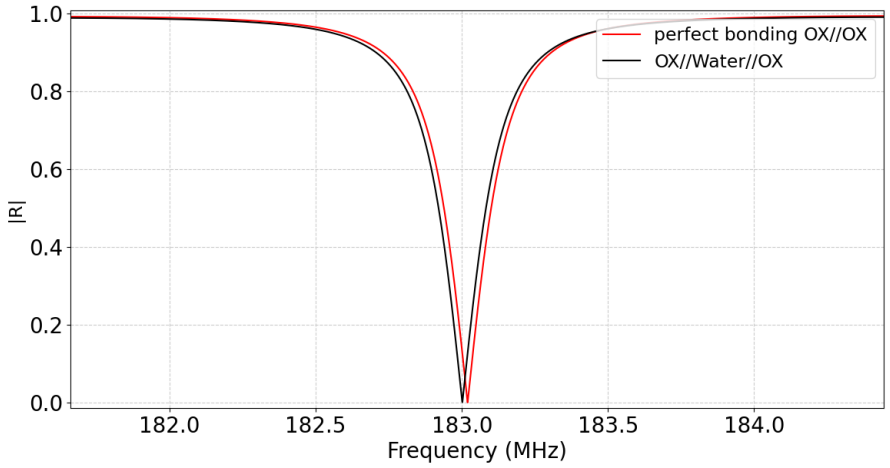

Figure 2.15: Reflection coefficient of hydrophilic extreme cases, in Red OX//OX, in Black OX//water//OX between 182 MHz and 185 MHz (Anti-symmetric)

By looking to this primary analysis, it is hard to make an analogy with hydrophobic samples. Besides, since hydrophilic samples include an extra layer of silicon dioxide on their stack, it is easy to assume that those layers affect somehow the reflection coefficient.

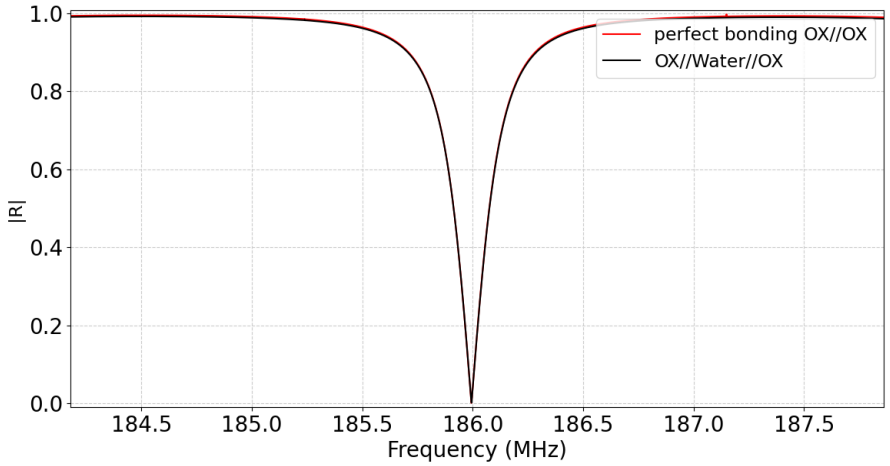

Figure 2.16: Reflection coefficient of hydrophilic extreme cases, in Red OX//OX, in Black OX//water//OX between 185 MHz and 187 MHz (symmetric)

The starter condition also plays a bigger role in the frequency distances interval shrinking. In summary, these observations highlight two major difficulties. The first is the frequency distances interval tightness. Meaning that by choosing water as starting point in the bonding modeling, the wave transmission to the sample bottom layer is more effective due to the water higher acoustic impedance, leading to the shrinking of anti-symmetric peaks gap in Figure 2.14. The second fact is the shift irregularity between the different bandwidths. The position of the peaks is somehow linked to the geometry of the stacks studied. Therefore, this two quotes will be detailed in the following sub-chapters.

Let's now focus on OX//SI samples, Figure 2.18 provides the reflection coefficient for the two extreme cases shown in Table 2.2. To remind, the difference between OX//OX and OX//SI is the presence of silicon dioxide layers in only one side of the bonding. This section highlights the influence of the 200 nm silicon dioxide layers absence in one side on the reflection coefficient. Figure 2.17 shows this anatomy disparity of these to type of samples.

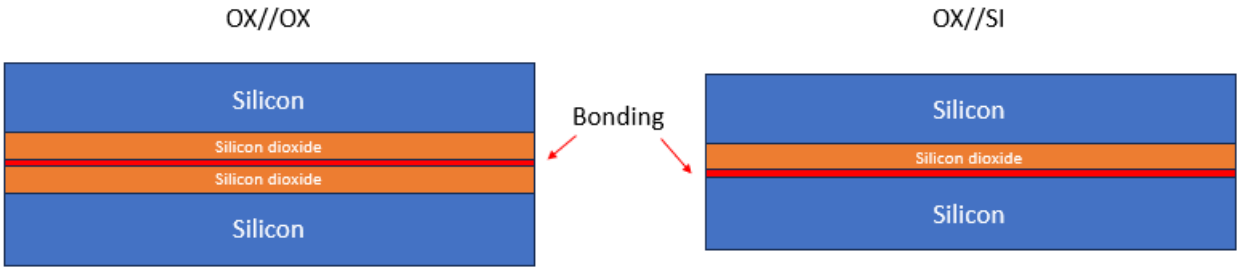

Figure 2.17: Non-scale diagram showing the anatomy of OX//OX and OX//SI samples

To begin, the curves in Figure 2.18 are superposed leading to assume that no difference is observed. Table 2.8 provides a more advanced analysis of the reflection coefficients in this case. The most oblivious note is the cutoff frequency positions between

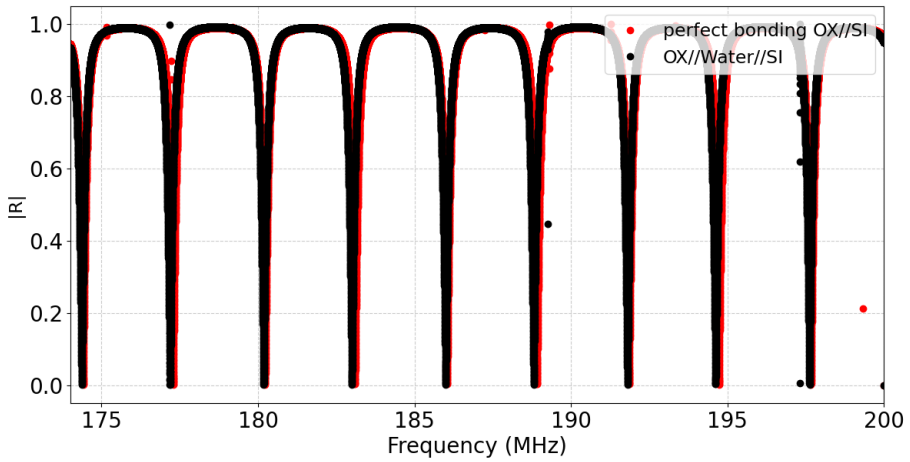

Figure 2.18: Reflection coefficient of hydrophilic extreme cases, in Red OX//SI, in Black OX//water//SI

the extreme cases in each bandwidth and their similarity with the pattern observed in the hydrophobic case.

The comparison between the peaks in each bandwidth exposes the disparity between odd and even peaks in the reflection coefficients. Yet, the distances are not similar to those found in the OX//OX results. Let's focus on the values of odd and even indexes, the even peaks display a bigger interval this time but the spread value is not stable along the bandwidth. The odd peaks are vacillating around 10 kHz spread and the values are not that stables compared to the hydrophobic case. The analogy between symmetrical and anti-symmetrical peaks is also contempt since both even and odd peaks are spaced in the two extreme cases.

Bandwidth	Idx(i)	OX//H_2O//SI cutoff frequency [MHz]	Idx(j)	OX//SI cutoff frequency [MHz]	$\lvert f_{c_i}$[OX//SI] - f_{c_j}[OX//H_2O//SI]$\rvert$
[173 MHz - 175 MHz]	1	174.36999	1	174.41374	43.7499 kHz
[175 MHz - 178 MHz]	2	177.17854	2	177.28870	11.0160 kHz
[178 MHz - 182 MHz]	3	180.18240	3	180.22771	45.310 kHz
[182 MHz - 185 MHz]	4	183.00189	4	183.10033	9.8440 kHz
[185 MHz - 188 MHz]	5	185.99481	5	186.04091	46.099 kHz
[188 MHz - 190 MHz]	6	188.81118	6	188.91274	10.1560 kHz
[190 MHz - 193 MHz]	7	191.80644	7	191.85488	48.439 kHz
[193 MHz - 195 MHz]	8	194.62046	8	194.72515	10.4690 kHz
[195 MHz - 198 MHz]	8	197.62042	8	197.66885	48.428 kHz

Table 2.8: Cutoff frequencies of the reflection coefficients based on Figure 2.18

Figure 2.19 shows this new disparity between the two extreme cases. Where in OX//OX and SI//SI cases the symmetrical peaks kept the same positions relative to the

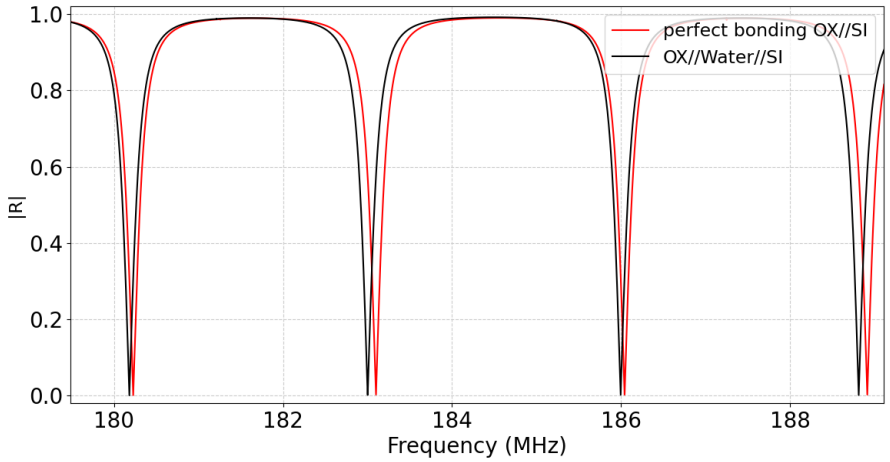

Figure 2.19: Reflection coefficient of hydrophilic extreme cases, in Red OX//SI, in Black OX//water//SI between 180 MHz and 190 MHz

frequency axis, this pattern is not respected in OX//SI samples. This result is a proof of the influence caused by the anatomy stack on the reflection coefficient. When OX//OX samples respected the stability of symmetrical peaks in the two extreme cases, OX//SI samples present a gap between all peaks, meaning that the absence of the silicon dioxide layer on one side in them will break the symmetrical behavior on the reflection coefficient. It concludes that in order to obtain the stability of symmetrical peaks, the two bonded wafers anatomy should be the same as in OX//OX and SI//SI samples.

In conclusion, subsection 2.4.2 highlights the main characteristic of the reflection coefficient in the hydrophilic cases OX//OX and OX//SI. The first observation is the shrinking of the spread between anti-symmetric peaks in the extreme cases selected for this theoretical analysis. The second note is the instability of the reflection coefficient peaks observed in Table 2.8 and Table 2.7, where SI//SI provides more stable results in Table 2.6, OX//OX and OX//SI display the peaks positions irregularities, which are based on the anatomy of the samples studied. These two essential characteristics will be the subject for more profound studies in the next subsections in order to understand the main parameters that influence the reflection coefficient behavior.

2.5 Variation of the bonding interface condition

After discussing the behavior of the reflection coefficient on the real anatomies studied, in this subsection, the main idea is to try to twist the bonding layer parameters in order to extract more information on the reflection coefficient behavior. Based on section 2.4 observations, parameters such as bandwidth, angle and thickness are tested in more extreme ways to display effectively their influence on the frequency distance shift.

2.5.1 Distance frequency variation based on bandwidth

Based on the results obtained previously, the frequency distance shift is somehow affected by the bandwidth selected. To observe the shift seen in Table 2.8 and Table 2.7, Figure 2.20 demonstrated a larger bandwidth of the reflection coefficient. Three samples with different bonding layer parameters were selected, their intrinsic properties are summarized in Table 2.9.

Samples	$c_l[m/s]$	$c_t[m/s]$	$\rho[Kg/m^3]$
SI//SI (Perfect bonding)	8432	5842	2329
SI//SI (Intermediate bonding)	2000	300	1100
SI//SI (Water interface)	1500	0.00001	1000

Table 2.9: Bonding layers intrinsic properties used in subsection 2.5.1

The first sample represents a full bonded wafer. The second and the third are a sub-variation of an unbonded wafer. More explicitly, the second sample is represented by fictional parameters representing an intermediate bonding. In the third case, the bonding layer is replaced by water. The idea here is to obtain a condition where three different gaps are possible on the anti-symmetrical peaks. SI//SI samples were selected based on their stability on previous calculus in order to avoid any variation caused by the anatomy of the sample.

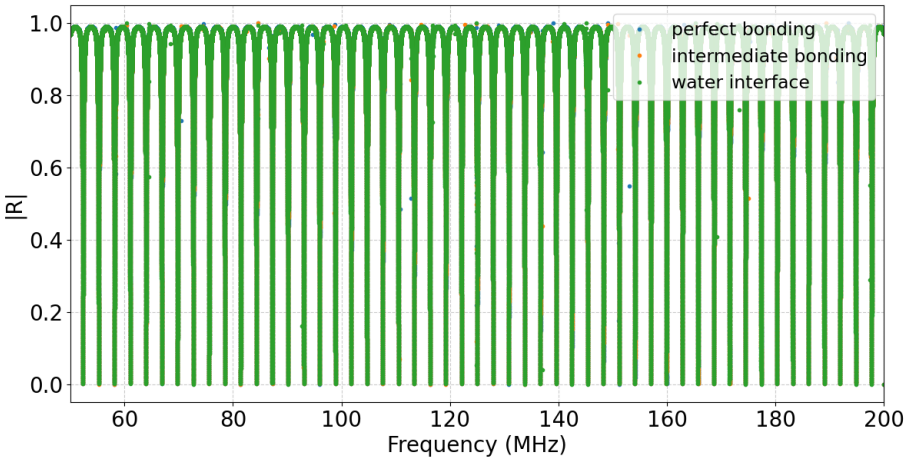

Figure 2.20: Reflection coefficient based on Table 2.9 parameters along [50 MHz - 200 MHz] bandwidth.

In Figure 2.20, the larger peaks diaspora exposed do not reveal any macroscopic shift. The peaks are aligned normally, and the three configurations are superposed, suggesting that no significant modification was established between the three charts. However, in contrast, Figure 2.21 shows the behavior of anti-symmetric peaks more precisely, zooming in on the disparity of this peak class from one configuration to another. Specifically, the perfect bonding case exhibits a wider shift compared to the other cases. This behavior is similar to what was observed in Figure 1.27, where the peaks positions shifted concurrently with the bonding layer composition.

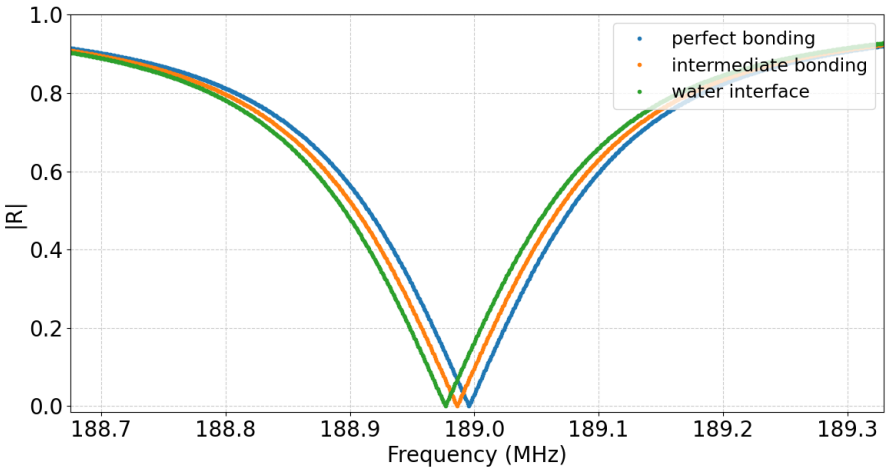

Figure 2.21: Example of Anti-symmetric peaks position for Table 2.9 configurations

On the other hand, Figure 2.22 displays symmetrical peaks. Again, their behavior is identical to previous results. The peaks superposition is maintained, which provides a great benchmark for anti-symmetric peaks. Figure 2.22 and Figure 2.21 represent two consecutive modes in the bandwidth, each of them is behaving regarding it status on the spectrum. The distance between those modes is the acoustic indicator to quantify the composition of the bonding layer.

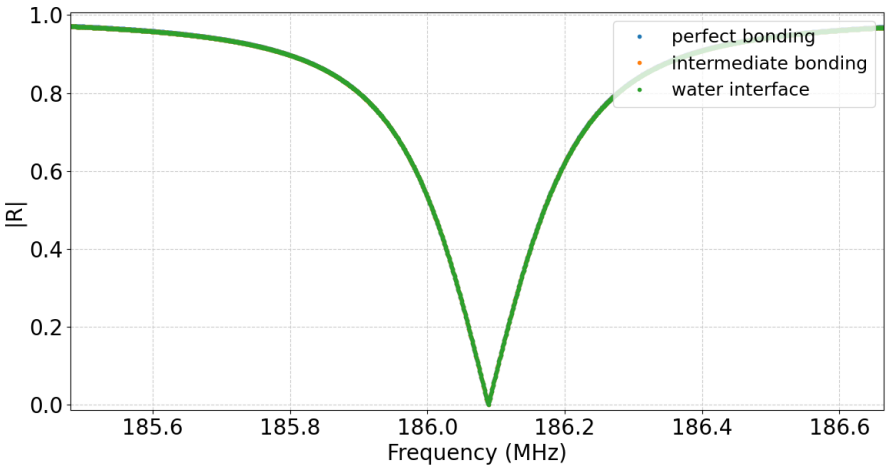

Figure 2.22: Example of symmetric peaks position for Table 2.9 configurations

Yet, in this subsection the main idea is to test the stability of frequency distances shift along a larger bandwidth. To do this, let's regroup all the frequency peaks positions in Figure 2.20 and subtract each value with the one up front of it in the spectrum. This sequence is illustrated in Figure 2.23 where each dot represent the frequency shift value between $Peak(i+1)$ and $Peak(i)$.

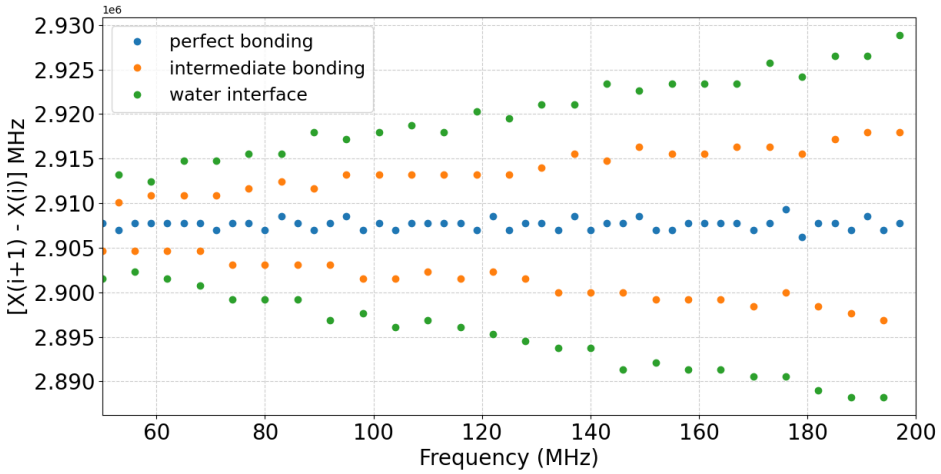

Figure 2.23: Variation of the frequency spread along a larger bandwidth for three different configurations

The main observation in Figure 2.23 is the frequency gap expansion expressed by the distance between upper and lower dots for each color. At 50 MHz, the gap between upper blue and upper green dots is around 5 kHz. This means that the higher the frenquency, the higher the sensitivity of the modes to the contact layer characteristics. In contrast, this gap is close to 23 kHz at 200 MHz. Also, it displays the frequency spread variation based on the bandwidth selected for the analysis clearly. It concludes that a higher bandwidth is more suitable for the analysis since it provides more shades of bonding, where a lower frequency bandwidth condenses the analysis spectrum.

Next, the slope of each dot group is linked to the distances disparity between odd and even peaks in Figure 2.20. Besides, the perfect bonding case presented in blue dots provides a flat result, meaning that the gap between symmetrical and anti-symmetrical peaks is relatively the same. This stability is sourced from the similarity of the bonding layer with the two bonded stacks, leading to produce a response of a single stack. For the orange and green dots, the anti-symmetrical peaks shift relative to the symmetrical ones leads to create the pattern observed above. The degree of the shift is related to the bonding stack properties as observed in Figure 2.21. Thus, the gap larger extended when the bonding is represented by a reflective layer as water. Otherwise, when the bonding layer is less reflective for an acoustic wave, the narrower is the spread.

Finally, these results highlight the effects on the reflection coefficient in a larger bandwidth. It displays a stretch effect on the positions of all the peaks in it. This stretch is more accentuated in higher frequencies which provide a larger interval between bonding shades. This emphasizes on the transducer frequency importance for the technique success in order to distinguish samples more effectively.

2.5.2 Thickness variation effect on the reflection coefficient

The bonding layer thickness influence on the reflection coefficient is a factor to be considered. Based on Figure 1.10, the bonding interface width is shrinking during the annealing process until it metamorphoses with the two substrates. In this subsection, the layer thickness variation impact on the reflection coefficient is studied. The bonding layer thickness (d_b) variation is investigated. Again, SI//SI samples were selected based on their stability on previous calculus in order to avoid any variation caused by the sample anatomy.

Table 2.10 describes the four configurations implemented in the algorithm for this part. SI//SI samples with a water interface in the middle are selected for their bonding layer higher reflectivity. The only difference between these setups is the bonding layer thickness d_b which increase by a factor of two each time. To put things in perspective, the wafer layers proportions are similar to those used previously (Table 2.1).

Samples	$c_l[m/s]$	$c_t[m/s]$	$\rho[Kg/m^3]$	$d_b[m]$
SI//SI (Water interface)	1500	0.00001	1000	$2e^{-9}$
SI//SI (Water interface)	1500	0.00001	1000	$4e^{-9}$
SI//SI (Water interface)	1500	0.00001	1000	$8e^{-9}$
SI//SI (Water interface)	1500	0.00001	1000	$16e^{-9}$

Table 2.10: Bonding layers intrinsic properties used in subsection 2.5.2 first part.

Figure 2.24 displays the reflection coefficient for the four cases projected in Table 2.10. The macroscopic view of it provides a first interpretation of the behavior of symmetrical and anti-symmetrical peaks under these conditions.

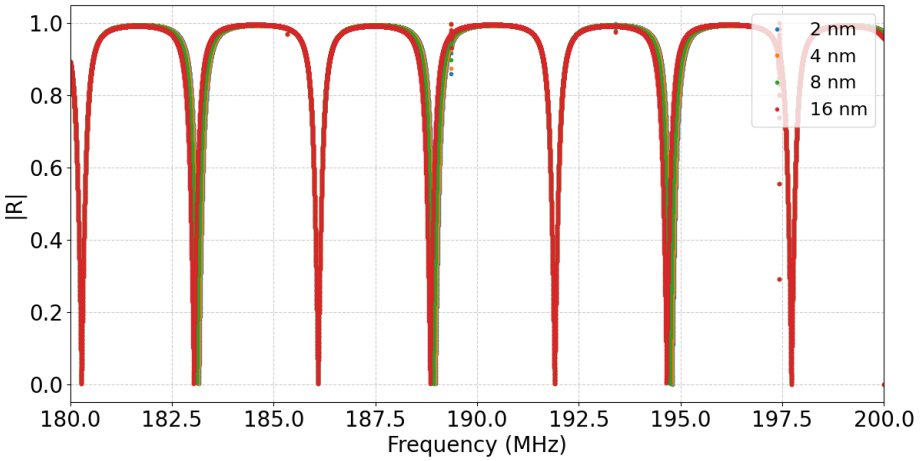

Figure 2.24: Reflection coefficient of four different bonding layer thickness based on Table 2.10.

On a first hand, the symmetrical peaks are aligned on the same frequency for the four cases, while anti-symmetric peaks are sensitive to the bonding layer thickness variation. Figure 2.25 and Figure 2.26 validates this statement.

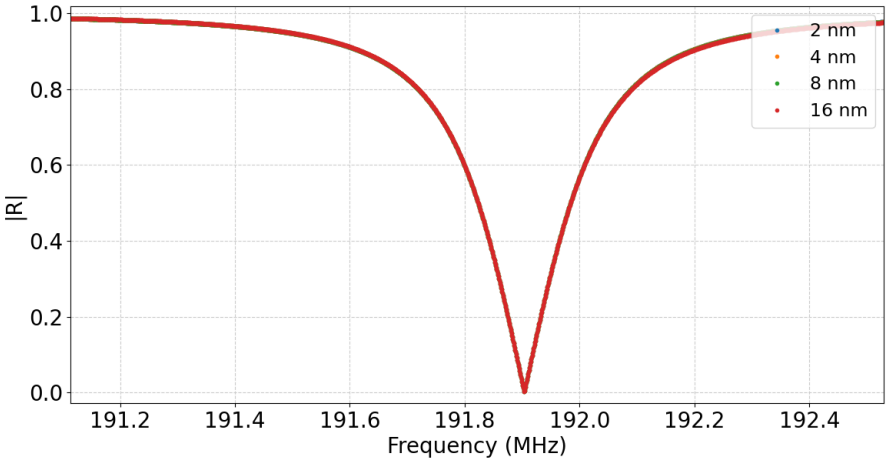

Figure 2.25: Symmetrical peaks of four different bonding layer thickness based on Table 2.10.

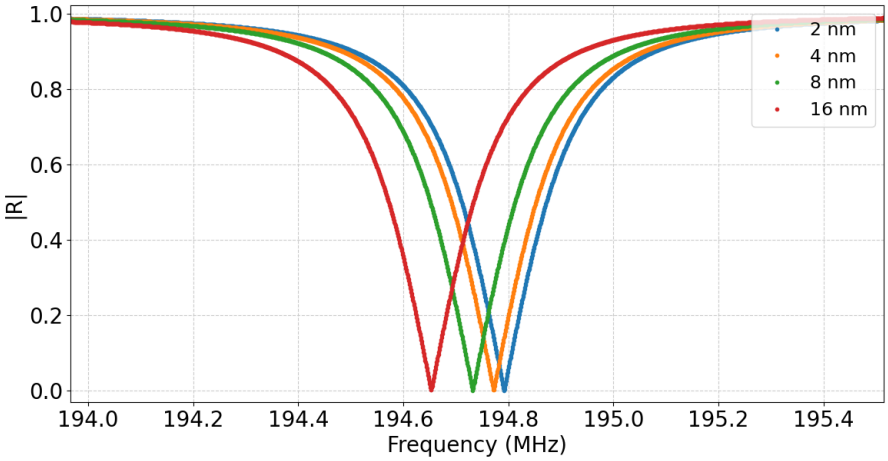

Figure 2.26: Anti-symmetrical peaks of four different bonding layer thickness based on Table 2.10.

Figure 2.26 shows that the reflection coefficient is not sensitive only to the layer properties but also to an nanometric thickness variation. Theoretically, since the bonding layer shrinks during the annealing process, the anti-symmetrical peaks shift is highly occurring. The good note is that the shift direction concords with the quality of the bonding. Meaning that when the bonding is thinner, the spread is larger between symmetrical and anti-symmetrical peaks, which is similar when the bonding intrinsic properties are varied since a fully bonded stack is always represented with the largest spread between symmetrical and anti-symmetrical peaks.

Having shown that the shift is sensitive to the thickness, the only problem is the difficulty to perceive the source of the spread. Both intrinsic properties and thickness are impacting the anti-symmetrical peaks in the same way. So, it is important to be sure that the variation of the acoustical parameters is unique to the bonding state.

2.5.3 Angle variation effect on the reflection coefficient

The incident wave angle attack is among the parameters that impact the reflection coefficient. The particularity of this parameter is its independence from the sample examined. In this subsection, the attack angle influence on anti-symmetrical and symmetrical peaks is studied in order to understand its effects on the frequency shift Δf. For this analysis, SI//SI samples are used for their rudimentary, stability and geometrical symmetry.

Table 2.1 parameters are introduced in the model for several angle positions. Figure 2.27 represents the reflection coefficient evolution for a bonded and unbonded case between a range of 0° and 4°.

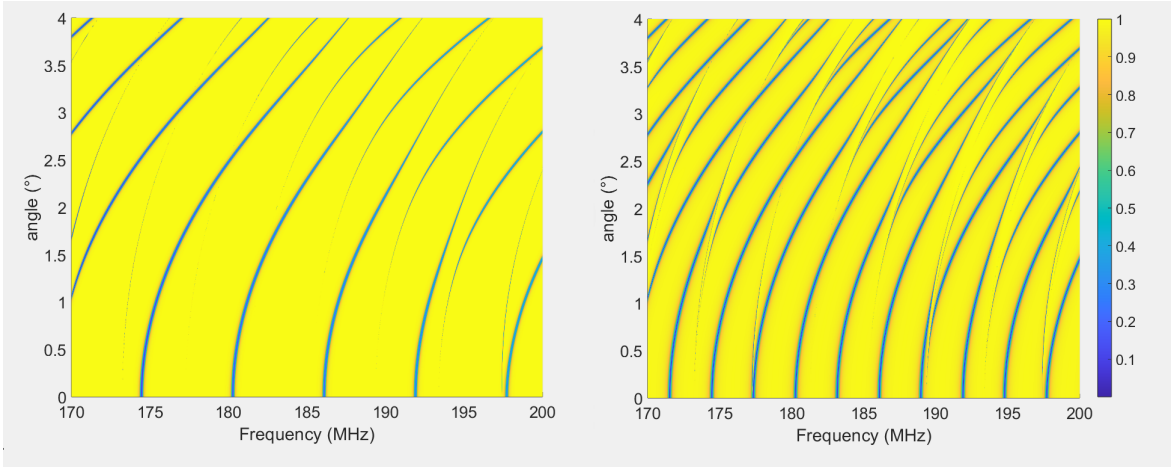

Figure 2.27: Reflection coefficient evolution for an SI//SI bonded (Right) and SI//SI unbonded (Left) case between a range of 0° and 4°

Firstly, let's explain each variable in Figure 2.27. The X and Y axis represent the frequency and the angle respectively, the normalized reflection coefficient is represented by the color mapping above. In our case, the reflection coefficient null values are brought to interest and they are represented by the blue shades.

Previously, Figure 2.10 treated the reflection coefficient behavior on normal incident, which represents the bottom line in both illustrations on Figure 2.27. It is easy to make the analogy between the two figures by focusing on the double gap created by the unbonded case. The main observation this time will be the variation of the null positions on the reflection coefficient based on the angle chosen. It is observed that the position of the peaks is shifting relative to the angle. This shift is observed on both symmetrical and anti-symmetrical peaks. The outline drawn by the reflection coefficient indicates that the unbonded pattern is twice as thin as the bonded one. As a result, we observe a spectrum corresponding to twice the frequency. Yet, the pattern is stretched due mostly to the uncoupled wave with the full stack. Besides, the peaks in both cases show discontinuities which disrupt the familiar pattern, this implies the appearance of a peak doubling in the transitional areas which can be detrimental to the measurement.

Since our characterization technique is applied in a normal incident, the angle shift could be an unwanted output on the reflection coefficient. Yet, the transducer parallelism with the sample is not often guaranteed easily. Besides, it is difficult to ensure the same angle conditions for each sample examined. Figure 2.28 and Figure 2.29 emphasize this difficulty by comparing the reflection coefficient for four smaller angle shifts.

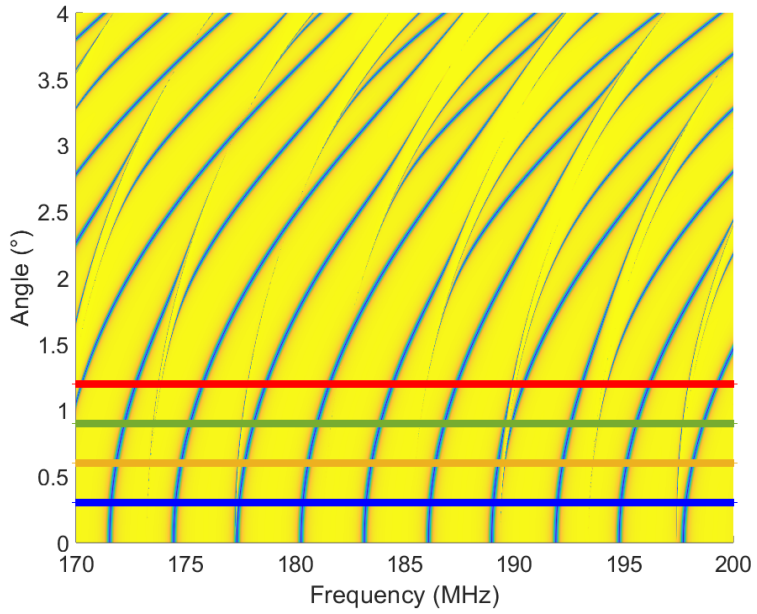

Figure 2.28: Reflection coefficient evolution for an SI//SI bonded case between a range of 0° and 4° with the projection on 0.3° in blue, 0.6° in orange, 0.9° in green and 1.2° in red

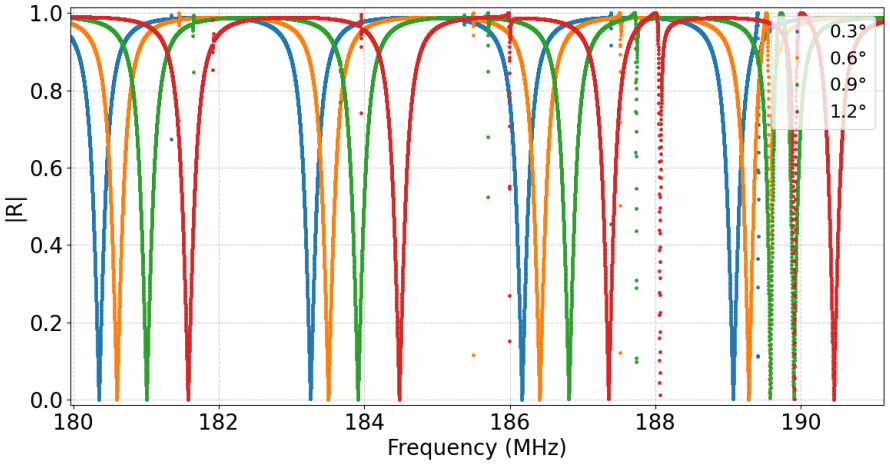

Figure 2.29: Classical representation of the reflection coefficient for 0.3° in blue, 0.6° in orange, 0.9° in green and 1.2° in red

The two figures are complementary since each of them shows the reflection coefficient from a different perspective. The classical approach focuses on the shift between the four

different angles. Figure 2.29 proves that an angle shift of 1.2° could offset the overall curve by 1.3 MHz relative to the selected bandwidth. In addition, the angle rising increases the chance of stumbling upon peak doubling interval, which distorts the calculation of the frequency shift Δf. In conclusion, the angle's influence on the reflection coefficient is pictured in the overall shift of the spectrum and the appearance of peak doubling due to the discontinuities observed on the reflection coefficient. This last parameter is more pronounced for higher angles, emphasizing the importance of angle control for the technique. Having said that, it is important to give credit to the stability of the spectrum peaks since the shift is applied to the overall spectrum. So, based on this stability, very small angle variations can be tolerated and corrected indirectly.

2.5.4 Variation effect based on the acoustic impedance

The fourth category to be studied is the bonding layer intrinsic properties. Again, their influence on anti-symmetrical peaks are analyzed. To put that into perspective, one hundred fictional bonding states are generated based on the variation percentage (b_s) of silicon parameters. Table 2.11 summarizes this new setup.

Samples	$c_l[m/s]$	$c_t[m/s]$	$\rho[Kg/m^3]$	$d_b[m]$
SI//SI (Layer index b_s)	8432*(b_s%/100)	5842*(b_s%/100)	2329*(b_s%/100)	$2e^{-9}$

Table 2.11: Bonding layers intrinsic properties used in subsection 2.5.4

The second element in this analysis is the introduction of the acoustic impedance, which can be linked to the intrinsic properties of the bonding layer with the following equation:

$$Z = \rho c \tag{2.4}$$

where Z is acoustic impedance of the bonding layer, ρ is density and c is the longitudinal speed in the media. This equation provides a link between the speed which is an acoustic parameter and the bonding layer.

Figure 2.30 synthesis the results of the elements described above. Four curves were selected based on the positions of the anti-symmetrical peaks in each case, thus the cutoff frequencies shift Δf difference between them. Each curve is linked to an acoustic impedance calculation based on Equation 2.4. It provides an indicator to link the peaks shift with the physical properties of the bonding. Besides, since one hundred theoretical simulations were performed, the percentage of convergence into a perfect bonding is another indicator that reveals the shade iteration based on the peaks shift evolution. To discuss Figure 2.30, it is important to put the spotlight on symmetrical peak positions on the left of the curve, their stable positions provide the benchmark for the anti-symmetrical peaks on the right. Furthermore, the red curve represents the larger shift possible since it shows the perfect bonding state. The acoustic impedance value calculated in this case is 0.610 MRy. In contrast, the three other cases emphasize lower values of acoustic impedance. The blue and the green curves represent 3% and 5% of convergence into a perfect bonding respectively. The values of the acoustic impedance are very low in both cases. Conversely, the shift variation is very rapid between these two cases. The

last case is the red curve, the value of the acoustic impedance is around 0.61 MRy in this case. The particularity of this state is the anti-symmetrical peak superposition with the perfect bonding state causing saturation on the cutoff frequencies shift for previous shades. Lastly, the black curve represents a bonding layer made of silicon, indicating a fully bonded state with an acoustic impedance of 19.25 MRy.

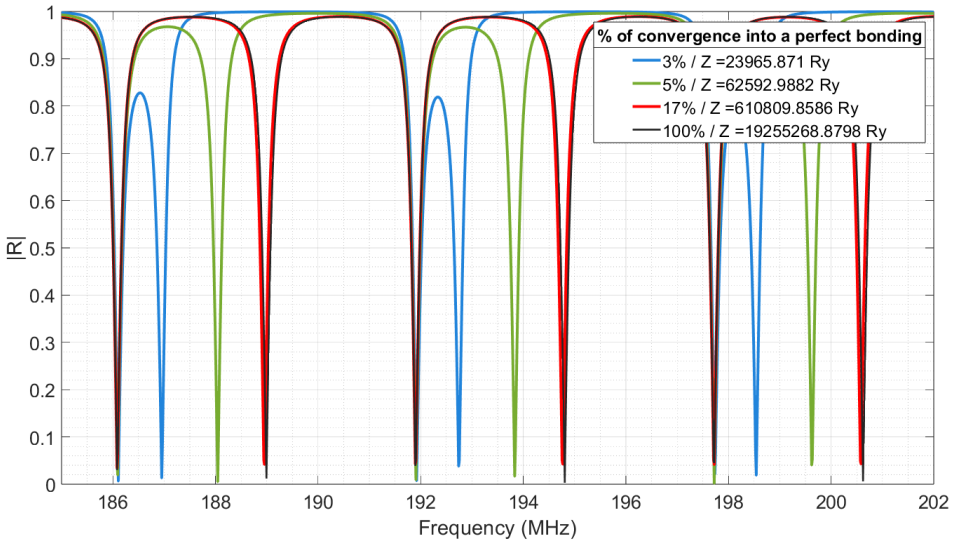

Figure 2.30: Reflection coefficient evolution based on the acoustic impedance and the convergence percentage to a perfect bonding

The description of Figure 2.30 shows the frequency spread limitations. The main limitation is the cutoff frequencies rapid variation of the frequency shift for low impedance values that my cause a limitaiton in the method sensitivity. This burden could limit drastically the potential of the technique.

2.6 Sensitivity curves

To understand this burden, Figure 2.31 displays the cut-off frequency shift evolution based on the acoustic impedance. This disposition provides the sensitivity curve since it shows the acoustical parameter evolution relative to the properties of the bonding layer. By observing this curve, two distinct zones can be identified. The first zone is defined by a good sensitivity. However, the second zone is characterized by a saturated sensitivity above 1 GPa. The curve also displays this evolution for four other samples. This diversity does not affect the pattern but it superposes the four curves in hydrophobic or hydrophilic cases. Otherwise, the converging points for the both cases are not the same since a perfect bonding ensure a full transit of the wave, and the bonding state in the two cases is not the same based on their anatomy. Lastly, fewer shades in the non-saturated zone are observed comparably to the saturated zone. This can be linked to the frequency sampling step of the model, yet the saturated zone regroups a larger number of simulations shades.

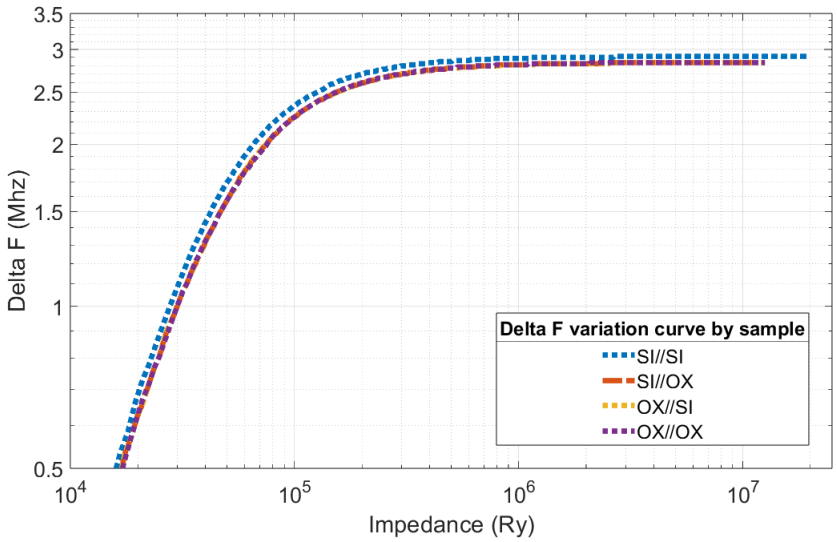

Figure 2.31: Sensitivity curves according to the sample type.

The next question to be asked is how to extend the non-saturated zone. Figure 2.32 exposes the sensitivity curve of SI//SI samples for four incident wave frequencies utilized in the model. The improvement is observed clearly between the four cases where each curve provides more shades of cutoff frequencies shift. In conclusion, this is a result that proves the incident wave frequency importance to improve the sensitivity range of the technique.

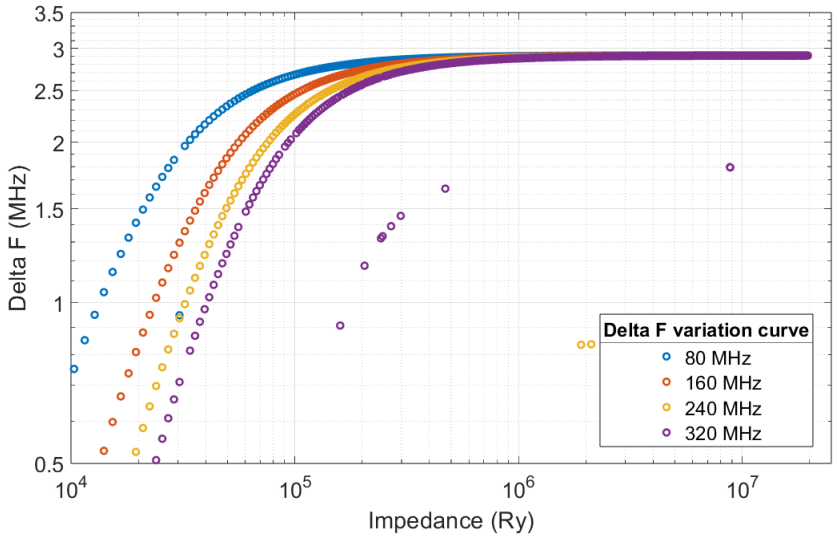

Figure 2.32: Sensitivity curves according to the incident wave frequency

2.7 Conclusion

In conclusion, chapter 2 outlines the theoretical aspect of the technique's feasibility on hydrophilic and hydrophobic samples. This attempt to understand the frequency shift Δf started by describing the model used and its output results as a time chronograph or frequency spectrum. These two elements were tested in extreme ways in order to compare the most relevant parameters. Firstly, the time signal on the hydrophobic and hydrophilic cases were exposed. Yet for each category, the sample anatomy was described. For the hydrophobic case, SI//SI time signal and reflection coefficient output were analyzed and discussed. The main points established in this analysis is the relationship between inner reflections and transmissions and the acoustic impedance of the layers, leading to the amplitude decrease of background echoes due to the wave interaction with the boundaries. Besides, the symmetrical and anti-symmetrical peaks are introduced and linked to the modes on each state of the bonding selected. Next, the hydrophilic cases are dispatched to two cases which are SI//OX and OX//OX. These two anatomies were studied and their new constrains provide a new angle regarding the anti-symmetrical peaks. The differences between hydrophilic and hydrophobic cases are established and connected to the hypothesis frame establish in each case. The analysis shows the extreme reduction of the frequency spread for the hydrophilic case due to the nature of the bonding. In contrary, the hydrophobic case provides a larger spread due to the starting condition which is a full unbounded case.

The second part of this chapter focuses on the main parameters that could shift the symmetrical and anti-symmetrical peaks. The first parameter studied was the bandwidth. Its effect on the frequency spread was shown in Figure 2.23. It concludes that a higher bandwidth is more suitable for the analysis since it provides more shades of bonding. The second parameter was the thickness and its impact on the frequency spread. It has been shown that the reflection coefficient is not sensitive only to the layer properties but also to the thickness through the variation of the anti-symmetrical peaks. Figure 2.26 displays the frequency gap expansion relative to the thickness shift and highlights the relation between a higher bonding state and a thinner thickness. The third parameter was the incident wave angle, it has been shown that the angle influence on the reflection coefficient is present on the full spectrum (Figure 2.29 & Figure 2.28). It concludes that this parameter could be tolerated and corrected for smaller angles and should be taken into consideration for a larger angle of incidence due to the modification of the reflection coefficient pattern. Subsequently, Figure 2.30 synthesizes the changes in the bonding layer's intrinsic properties on the anti-symmetrical peaks. The acoustic impedance is introduced to provide a link between the acoustic parameter and the bonding layer's structure. This curve shows the fast saturation of the anti-symmetrical peaks and their inability to represent more shades of bonding. Moreover, Figure 2.31 and Figure 2.32 are the extension of this analysis in order to understand the saturation burden observed. This disposition provides the sensitivity curve since it shows the acoustical parameter evolution relative to the properties of the bonding layer. By observing this curve, two distinct zones can be identified. The first zone is defined by a good sensitivity. However, the second zone is characterized by a saturated sensitivity above 0.610 MRy. The curve also displays this evolution for four other samples. This diversity does not affect the pattern but it superposes the four curves rather in hydrophobic or hydrophilic cases. The

last important observation is related to the incident wave frequency utilized and its impact on the unsaturated zone, meaning that the frequency is the only parameter that provides a healthy interval that could represent all the possible shades.

Figure 2.33 enters in this analogy. It displays the Δf variation regarding the acoustic impedance of the bonding layer. This variation is performed under several frequencies. Again, the major observation is the improvement of the sensitivity range for higher frequencies. The difference in this case is the X-axis parameter selected. Acoustical impedance provides a more realistic approach to distinguish between bonding shades.

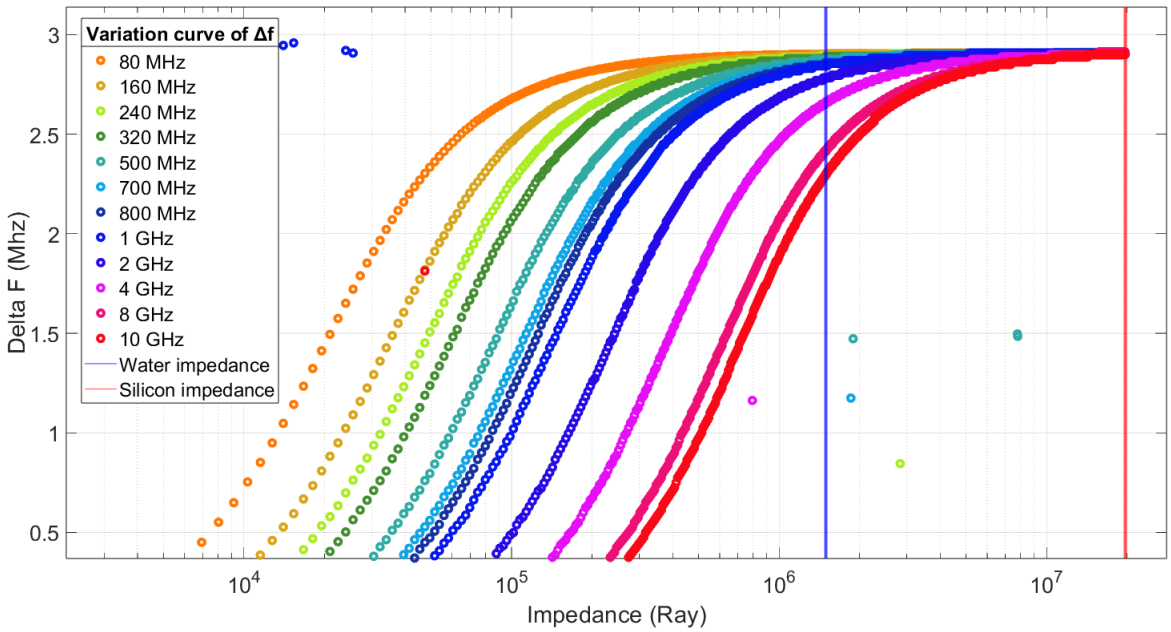

Figure 2.33: Sensitivity curves of Δf variation relative to acoustic impedance of the nanometric bonding layer

The thick vertical lines represent two extreme potential bonding states which are water and silicon. Those new lines provide another perspective since it highlights the interval where the technique is expected to nuance between the different shades. By observing this smaller window, the theoretical frequencies where the technique is effective are above 1 GHz. This statement challenges the experimental results found by Dekious [1].

Chapter 3

Experimental results and measurement constraints

Contents

3.1 Introduction and hypothesis 82

3.2 Experimental protocol 82

3.3 Transducer and measurement constraints 88

3.3.1 Transducer characteristics 88

3.3.2 Empty time window position based on the transducer reflection echoes 90

3.4 Reflection coefficient for an bonded and unbonded conditions 92

3.4.1 Experimental results 92

3.4.2 Theoretical and experimental results comparison 93

3.4.3 Noise impact on the cutoff frequency positions 97

3.5 Experimental results 102

3.5.1 A-scan results on hydrophobic samples 102

3.5.2 C-scan results on hydrophobic samples 104

3.5.3 A-scan along the wafer diameter for hydrophobic samples . . . 106

3.6 Conclusion 106

3.1 Introduction and hypothesis

Experimental results encompass all outputs obtained from conducting a scientific experiment. These results are used to either support or refute a hypothesis or theory. However, measurement constraints can affect the accuracy and precision of experimental measurements. These constraints can be due to various factors, including measuring instrument limitations, environmental factors, and human errors. It is essential to consider these constraints when designing experiments and interpreting results since they can affect the reliability and validity of the experimental outcomes. Acknowledging these constraints can help researchers make appropriate adjustments to their methods and analyses to enhance the accuracy and precision of their measurements.

This elaborated definition provides the vocabulary of chapter 3. While the previous chapter treated the theoretical aspect of the elements that distinguish the bonding shades, this part tested the reflection coefficient reliability and validity in experimental conditions. To start this chapter, the protocol utilized is described. Next, measurement constraints linked to the test overall environment are discussed and their impact on the results is elaborated. Then, experimental results of the bonding energy characterization are displayed such A-scan and C-scan. Their output is discussed and analyzed in order to validate the observation seen in theoretical results. The major observation to look for is the bonding layer influence on the anti-symmetrical modes. Their stability between each measurement campaign is primordial to validate the technique. If it is the opposite, the constraint causing the limitation should be put in spotlight.

The first questioning in this chapter will focus on the reflection coefficient ability to nuance between different bonding levels. This major hypothesis is based primarily on the work done previously [1] and the conclusions made in chapter 2. A 190 MHz planar transducer is used in all the experiments conducted since an higher frequency is more suitable for the technique. The planar transducer choice is more worthy based on the results established in Figure 1.29 and Figure 1.28. They exhibit that a planar transducer provides a more pronounced reflection coefficient. This results is linked to the beam nature. Meaning that, the planar transducer projects a broader beam leading to target all the layers of the inspected sample. It is important also to emphasis on the transducer bandwidth, in this case a narrower spectrum is desirable, which makes it more sensitive to the symmetrical and anti-symmetrical modes in the bandwidth of choice. The second questioning is related to the disparity between hydrophobic and hydrophilic samples seen in the theoretical results. The hypothesis in this case is based on the time signal differences and the coefficient reflection pattern observed based on the sample anatomy. In this chapter, these results will be tested on real samples in order to validate the assumptions based on the conditions assumed in chapter 2.

3.2 Experimental protocol

To validate these hypotheses, an experimental protocol is adjusted based on the infrastructure elaborated previously in IES. In order to apply the theoretical results, a test bench based on a research acoustic microscope is established. As mentioned previously, A 190 MHz planar ultrasound transducer is chosen for its highest sensitivity. The sensor's

parallelism with the sample is taken into account since the reflection coefficient is very sensitive to the angle. To ensure normal incidence, the microscope is equipped with 5 micrometric angle adjusters for several parts (Figure 3.1).

- Micrometer bolt to manually control the height of the sensor.
- Goniometer (Y axis of the sensor).
- 360° rotation plate (X axis of the sensor),
- Goniometer to rotate the plate on the Y axis.
- Goniometer to rotate the plate on the X axis.

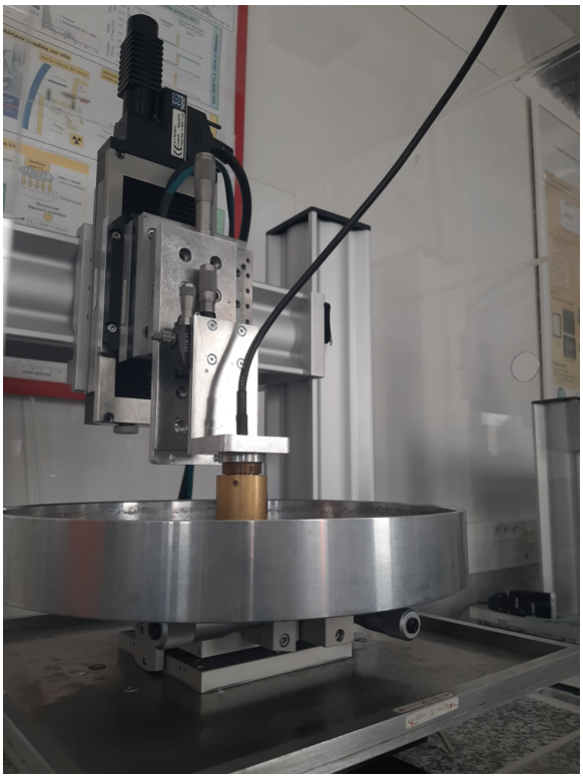

Figure 3.1: Test bench setup with the five goniometers to adjust the transducer angle attack.

The sample is installed on a motorized table with a micrometric precision, allowing precise positioning. With this setup, a C-scan will provide a surf on any position on the sample which is required to produce the frequency distance cartographies. The ultrasonic transducer is connected to a dual Pulser/Receiver DPR500 (JSR Ultrasonics) and excited by an electrical pulse with 3 μJ energy per pulse, 200 Hz pulse repetition (PRF), and 50 Ω damping factor. The acoustic response is received and digitized by a M9211A **10-bit 3-GHz** data acquisition board (Agilent). The calculus used to obtain the cartographies is elaborated in **Python**, the last result is resumed as an experimental report that incorporates all the test details (Appendix C).

The samples used in this experimental chapter are similar to the ones described in chapter 2. Table 2.1, Table 2.2 and Table 2.3 provide the anatomies of the hydrophobic and hydrophilic samples. In order to nuance between the wafers, five annealing temperatures were selected for each bonding type. Figure 3.2 displays the bonding energy values estimated by the DCB test joined with the opposite notch detachment length caused by the blade.

Bonding type	Bonding energy (J/m²)						
	RT	200°C	300°C	L100-400	500°C	600°C	1100°C
	23	200	300	400	500	600	1100
Ox/ox	118	296	565		1813		4194
Ox/Si	194	706	2311		3192		5000
Si/Si	20			415	973	2061	5000

Bonding type	Opp-notch detachment (mm)						
	RT	200°C	300°C	L100-400	500°C	600°C	1100°C
	23	200	300	400	500	600	1100
Ox/ox	55	45	40		30		25
Ox/Si	50	40	30		25		
Si/Si	50			23	19	15	5

Figure 3.2: Bonding energy value and their respective opposite notch detachment for hydrophobic and hydrophilic samples [CEA]

To start an experiment, the wafer is placed on the sample holder which is fixed to the motorized table. The first step is to adjust the sensor parallelism with the micrometric angle adjusters. A valid alignment can be determined by examining the phase of the signal along the X and Y axis scan dimensions. If the sample holder is tilted, it can cause a time shift of the time signal and generate a phase variation along the track. Figure 3.3 demonstrates the phase difference between a good alignment on the right and a poor alignment on the left. The phase stability along a displacement is detrimental to avoid any mismatch between each measurement. The unphased signal ensures the adjustment repeatability between each measurement.

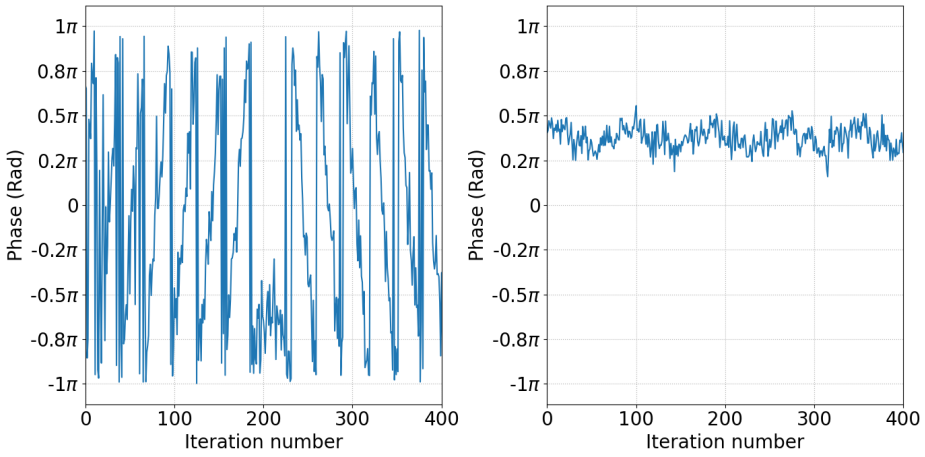

Figure 3.3: Phase indicator for a tilted (left) and parallel (right) transducer in regard to the sample.

Next, the scanned surface dimensions are selected based on the number of point and the step length for each axis. The output of the measurement provides the signals for each dot on the mesh. Figure 3.4 displays an example of a time signal extracted by the bench test. They are stored to keep a trace of each measurement. It is important to mention the presence of band-pass butterworth order 3 filter with a frequency range between 175 MHz and 200 MHz. It provides a maximally flat response around the transducer frequency range leading avoiding any ripple or distortion in the treatment bandwidth.

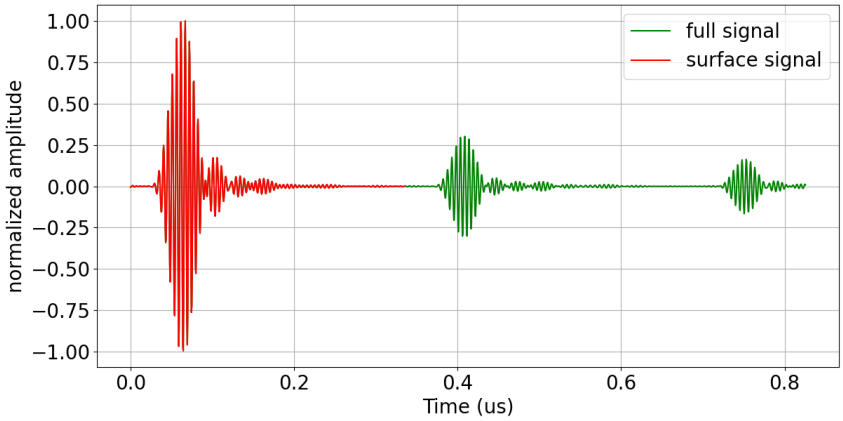

Figure 3.4: Example of an experimental time signal promoting the sample surface echo in red and the full background echoes in green.

Based on the patent developed previously [107], the time signals provide the elements to construct the reflection coefficient experimentally. The reflection coefficient is calculated by taking the spectrum's ratio between the wave reflected by the surface and the wave penetrating the sample. subsection 1.4.2 summarizes the approach. The first step is to calculate the Fourier transform of the full signal (green + red) and the interface echo (red). Figure 3.5 displays the two spectrum's of the wafer surface echo in red and the full echo in green.

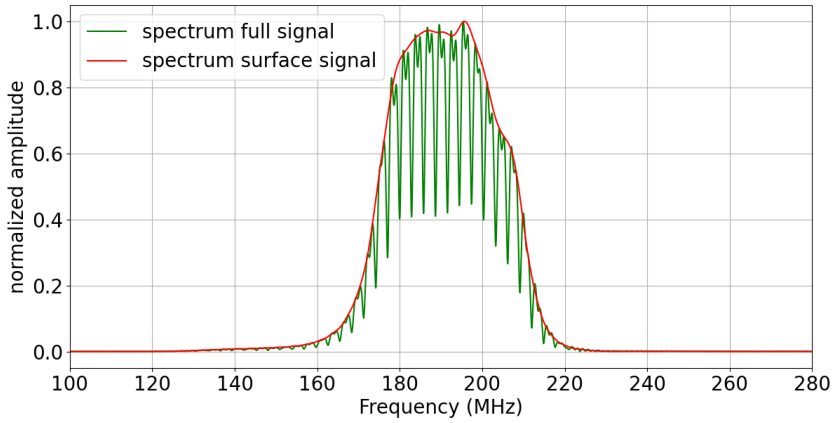

Figure 3.5: Example of an experimental spectrum's promoting the sample surface echo FFT in red and the full background echoes FFT in green for 190 MHz ultrasonic transducer.

The obvious ascertainment is the red spectrum envelopment of the overall response represented in green. This pattern is due to the redundant nature of the signal. The spacing between the minima observed in the green spectrum is fundamentally linked to the spacing imposed on the time signal, thus the time of flight. The minima depth on the full signal FFT are linked to the number of background echoes on the time signal and slightly to their amplitude. The third element of the full signal spectrum to discuss is the shape of the maxima and the minima. First the minima, their finesse is exclusively linked to the number of background echoes present on the time signal. On the other hand, the maxima are similarly sensitive to the number of background echoes. The more echoes are selected, the flatter the upper side of the curve responses, an example is displayed lately to validate this quote.

Another effect that can be mentioned is the amplitude mismatch between the interface echo spectrum and its full signal counterpart. This small variation will impose an down or upper shift of the ratio between the wave reflected by the surface and the wave penetrating the sample. Figure 3.6 exhibits this ratio result and emphasis on the minima pattern misalignment by the red horizontal line which represents the threshold to pickup the minima. In consequences, the wavy pattern of the minima could cause an unwanted lost of the peaks values based on the threshold imposed.

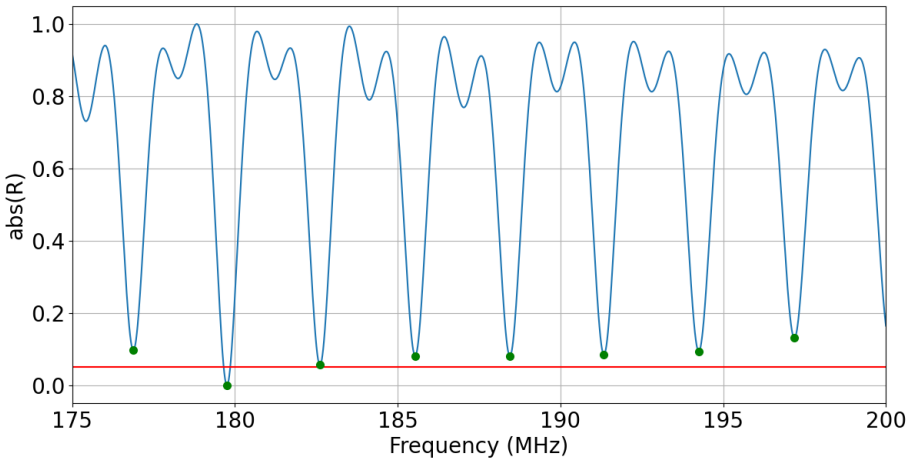

Figure 3.6: Example of an experimental normalized reflection coefficient (Blue) and the threshold applied to extract the minima (Red)

To handle this problem, a correction is applied to the reflection coefficient minima in order to stretch the amplitude values to zero. This operation does not change the landing frequencies values of the curve and provides the condition to ensure the pick up of all the minima. Figure 3.7 displays the final result of the reflection coefficient stretch.

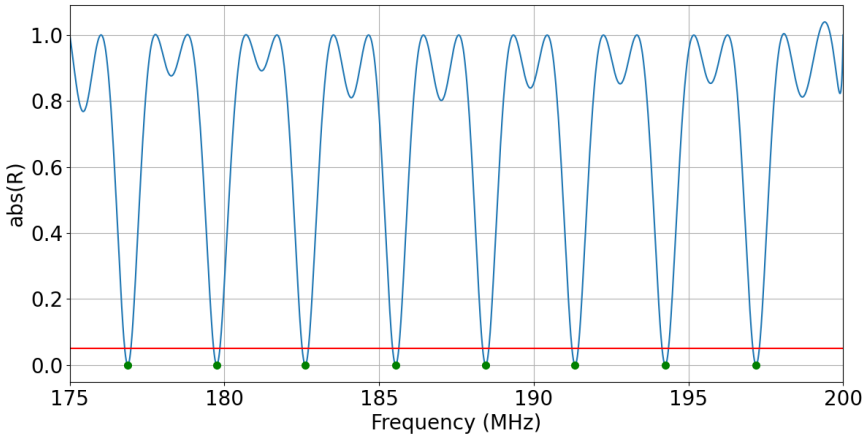

Figure 3.7: Example of an reflection coefficient after a full stretching

Thereafter, the distances between all the peaks relative to the frequency axis are calculated and divided to odd and even distances. The mean of each group is calculated and compared in order to define the symmetrical and the anti-symmetrical peaks. If the mean of the odd distances is bigger than the mean of the even, the representative frequency distance of this set is the mean of the even distances. If it is the opposite, the frequency distance is the mean of the odd distances. In chapter 4, many results present experimental configurations where the frequency distances vary heavily. They are the proof to validate this procedure.

Finally and after affecting each signal to an Δf value, the next step is to plot a colormap of all the values based on the dimensions selected for the scan. Sometimes, the microscope browses the odd and the even lines on opposite directions, Attention must be paid to the orientation of the data with respect to the scan direction. Appendix C provides an example of cartographies.

The experimental report approach enables the evaluation of the methodology constantly, allowing to exploit the work in future research. This is important because scientific progress depends on the ability to replicate and build on previous research. In addition to communicating results, experimental reports also serve several other purposes such accountability and documentation promoting transparency.

3.3 Transducer and measurement constraints

The transducer plays the most crucial role in the test bench, thus it is important to detail its technical characteristics, also its pros and cons. Generally, transducers are the elements who convert an energy to an other. Pressure, temperature, or distance are common examples that can be measured by an electrical output via various sensors. Nevertheless, they can introduce measurement constraints that impact the precision and the accuracy of the output. Environmental factors, non-linearity, hysteresis, sensitivity and frequency response are among the most prevalent factors that affect sensor performance.

In the case of this study, the most influential are sensitivity and the bandwidth selected frequency response. The transducer frequency used is around 200 MHz, which corresponds to a wavelength of 42.15 μm for an acoustic wave propagating in silicon. Since the bonding layer thickness corresponds to only a few nanometers, its impact on the wavelength is insignificant. All bets in this case are placed on the resonance phenomenon seen previously. Therefore, a study is conducted to exhibit the transducer major parameters such as SNR ratio and bandwidth.

3.3.1 Transducer characteristics

The transducer output is displayed in Figure 3.8 and could enrich the discussion. This chronograph exhibits all the reflections generated by the transducer inner structure. The first information that could be extracted from it is the delay line size. Figure 3.9 shows the frequency spectrum of the first lens echo. The central frequency is 194 MHz with full width at half maximum bandwidth between 182 MHz and 202 MHz.

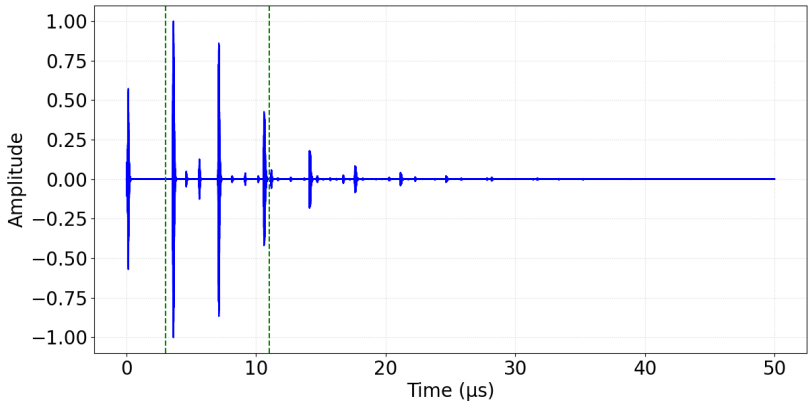

Figure 3.8: Transducer chronograph

Additionally, the chronograph also displays multiple secondary reflections placed between the lens echoes. The amplitudes and positions of these reflections are still under investigation since their presence poses a challenge in picking up a larger number of background echoes. Knowing that the time of flight of a bonded wafer is equal to 0.34 μs, the empty time intervals selected for the treatment should provide a good SNR ratio and be able to hold a big number of background echoes.

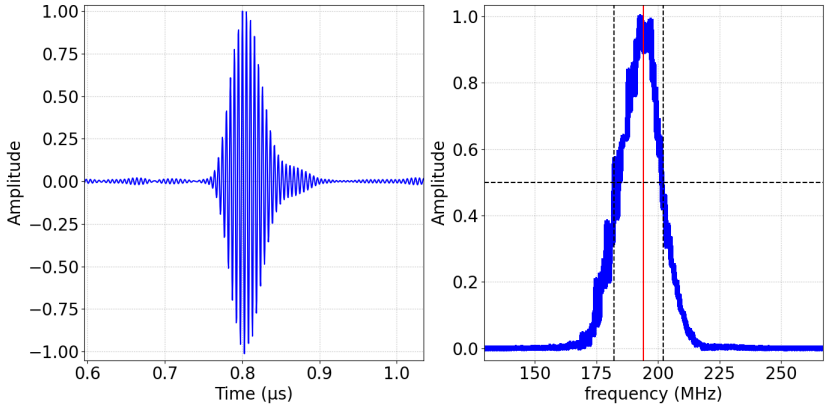

Figure 3.9: Transducer lens echo joined with its frequency spectrum

Figure 3.10 displays a zoomed-in view of the region where the first and second lens echoes are located. The region is framed by the vertical green lines in all the graphs shown in this subsection. The red and black vertical lines in the figure project the spotlight on the two potential zones that could host the treatment echoes. However, their time window is limited, which affects the number of echoes that they could hold. The two time windows are separated by an transducer inner reflection causing the reduction of the time window of the treatment. The first placement is fenced with black vertical lines providing a 0.9 μs window, whereas the placement in red gives a larger second window of 1.3 μs. The distance between the transducer and the sample in the first case will be equal to 0.825 mm, where is the second case this distance is equal to 1.58 mm.

Figure 3.11 shows the power in dB of the signal displayed in Figure 3.10. This graph provides an information on the noise level relatively to the lens echoes. It show a 60 dB difference between the max value of amplitude and the ambiance noise. This value can be linked to the quantification level, as the resolution ratio of an 10-bit ADC (Analog-to-digital converter) is estimated at 61.94 dB.

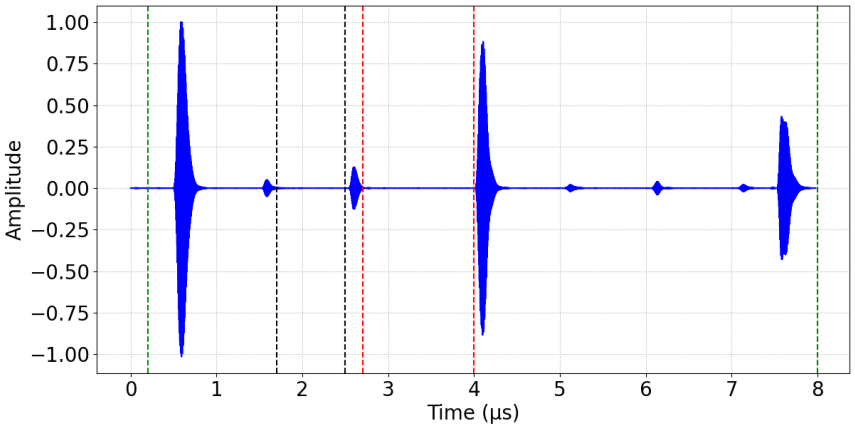

Figure 3.10: Transducer chronograph zoomed on the first and the second lens echoes

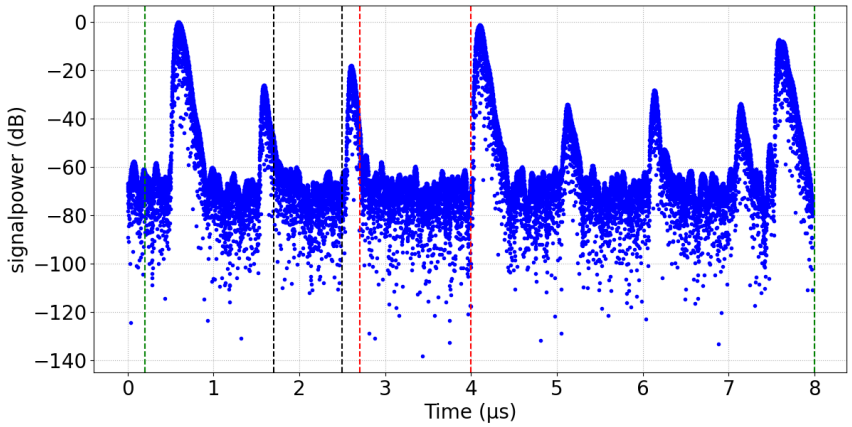

Figure 3.11: Transducer signalpower chronograph in dB zoomed on the first and the second lens echoes

3.3.2 Empty time window position based on the transducer reflection echoes

To start simple, this subsection focuses on the time windows available for the treatment relative to the transducer's inner reflections. The first window can hold three echoes, whether the second provides a time frame for four. The main goal in this subsection is to choose the right window for the treatment. It is true that a higher number of echoes provides a more refined reflection coefficient, but the signal-to-noise ratio (SNR) is an essential parameter to ensure a good quality signal. A choice must be made to select the right window based on the advantages and drawbacks of each.

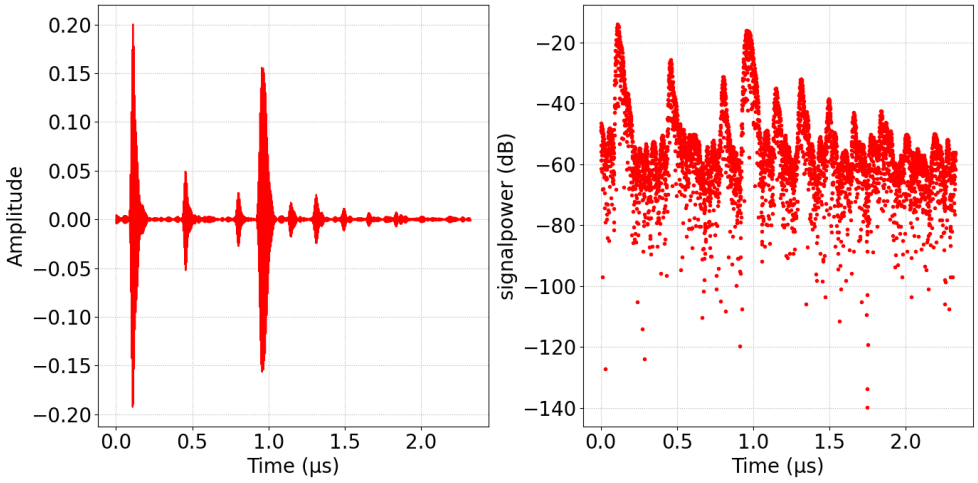

Figure 3.12: Time window and its signal power of the first time fragment relative to a distance between the transducer and the sample of 0.825 mm

Figure 3.12 and Figure 3.13 provide a cut of the time windows where sample echoes are present. This two fragments are separated by a transducer inner reflection echo. Figure 3.12 presents the first window and its signal power. The SNR value on the three first echoes time fragment equal to 24.65 dB. Figure 3.13 presents the second window and

its signal power. The SNR value on the sample echoes only equal to 15.90 dB. The noise signal used for this calculation is the empty time window on the blue signal before the transducer inner reflection echo in Figure 3.13. The difference observed between the two signals means that the power of the three echoes' window is 9 dB higher than the power of the four echoes' window. Mathematically, this corresponds to a power ratio of 8:1, since each 3 dB difference represents a doubling or halving of power.

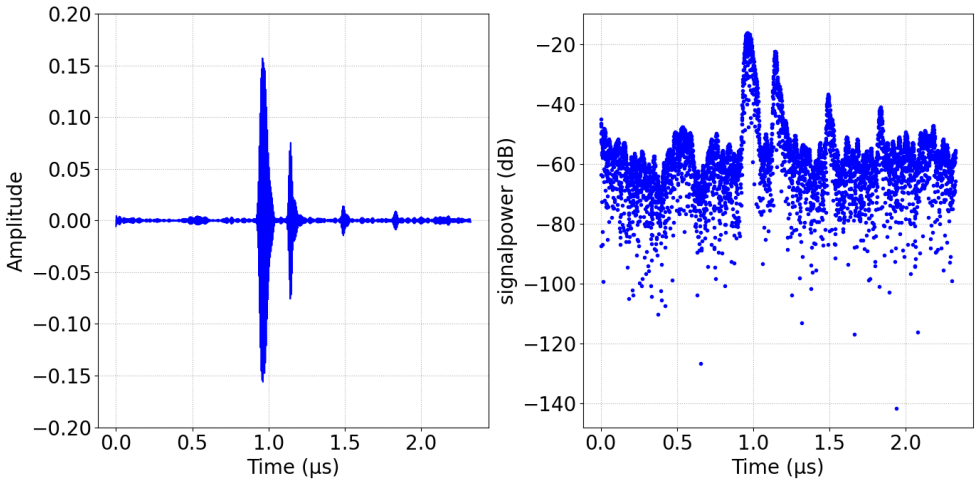

Figure 3.13: Time window and its signal power of the second time fragment relative to a distance between the transducer and the sample of 1.58 mm

The superposition of the two signal power graphs in Figure 3.14 clearly shows the difference in signal quality between both cases. While the first window provides three clean reflections, the second fragment barely provides the same output. Although the fourth echo is the main advantage of using this time fragment, it is hardly distinguishable. This result proves that the smaller window is more suitable for the treatment based on the SNR ratio and the signal power representation. These elements are unique to the transducer used for this study.

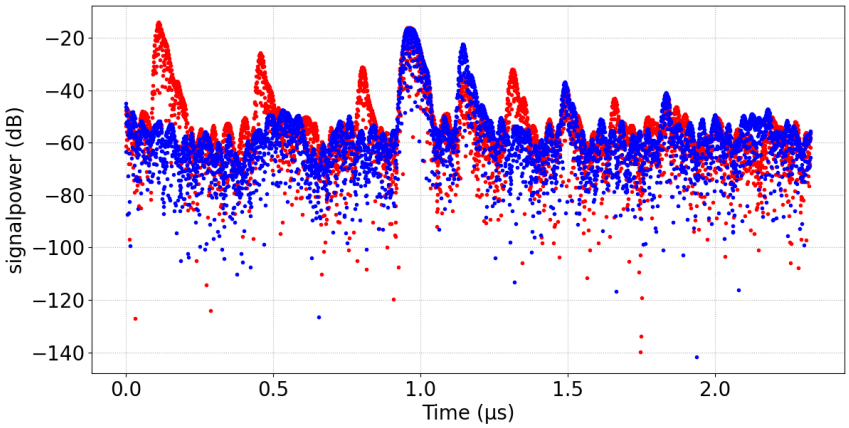

Figure 3.14: Figure 3.12 and Figure 3.13 signal power superposition representing a three echoes' time fragments and four echoes' time fragments respectively, using the same color code.

3.4 Reflection coefficient for an bonded and unbonded conditions

3.4.1 Experimental results

The first attempt to validate the hypothesis observed in the previous chapter started with analyzing the extreme cases. As in subsection 2.3.1, the element utilized to construct the reflection coefficient in both cases are compared to their theoretical counterpart.

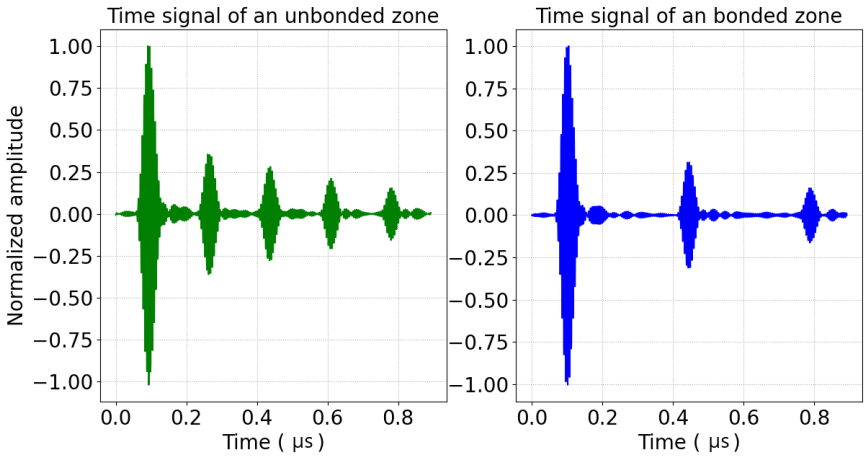

Figure 3.15: Normalized time signal of an unbonded (green) and an bonded (blue) zone for SI//SI sample in experimental conditions

Figure 3.15 displays the time signals of a bonded (blue) and unbonded zone (green). Figure 2.3 and Figure 2.4 represent the identical equivalent on the theoretical side. The time of flight difference is linked to the wave path in both cases. This means that the green signal only propagates on the upper half of the sample, while the blue signal crosses the bonding layer until it reaches the sample bottom. The time of flight values validate this in both graphs.

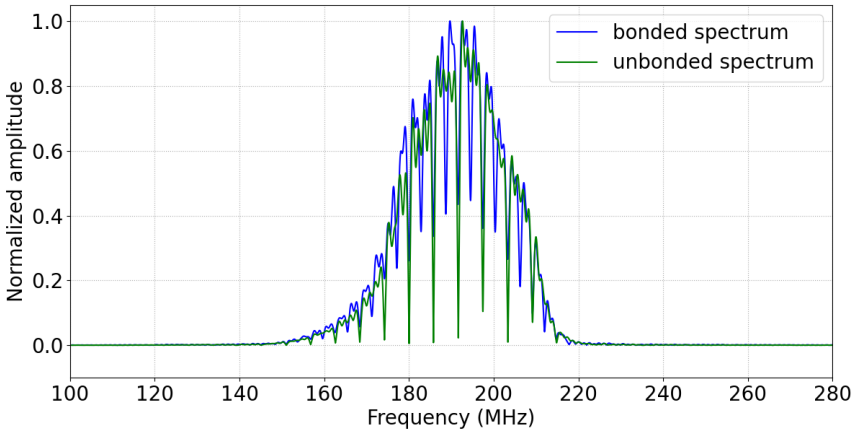

Figure 3.16: Normalized FFT spectrum of an unbonded (green) and an bonded (blue) zone for SI//SI sample in experimental conditions

The spectrum of these two conditions can provide an answer on the background echoes influence on the minima and maxima of the full signal spectrum. Figure 3.16 displays a normalized FFT spectrum of an unbonded (green) and an bonded (blue) zone for an SI//SI sample in experimental conditions. First, the minima depth is more pronounced when the number of the echoes is higher. Moreover, the maxima shape is smoother compared to the bonded case. This result emphasizes on the background echoes' impact on the spectrum and their influence on the maxima and minima.

The next step is the reflection coefficient calculus. Figure 3.17 presents a normalized and corrected reflection coefficient of an unbonded (green) and bonded (blue) zone for an SI//SI sample in experimental condition. This result is similar to its theoretical counterpart Figure 2.11.

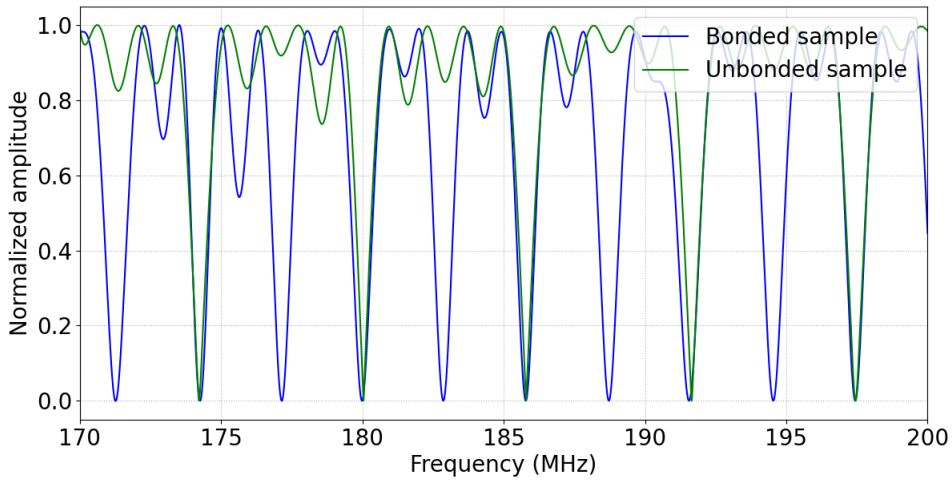

Figure 3.17: Normalized and corrected reflection coefficient of an unbonded (green) and an bonded (blue) zone for SI//SI sample in experimental conditions

Before pushing the analysis deeper, the impact of the angle adjusters is significantly visible on the reflection coefficients. The alignment of the symmetrical peaks in both cases is astonishing compared to primary experiments without the adjusters. These results demonstrate the stability provided by the goniometers and the phase indicator, which allow very precise alignment. But, how accurate are they?

3.4.2 Theoretical and experimental results comparison

Table 3.1 displays the cutoff frequencies of an unbonded and bonded case, where Table 3.2 and Table 3.3 compare the cutoff frequencies in experimental and theoretical conditions. The comparison of unbonded and bonded experimental cutoff frequencies shows the peak gaps located on the same bandwidths. This observation puts the spotlight on tiny variations between the two curves' minima, which are quantified at the last column of the Table 3.1. The most important factor to consider in this table is the symmetrical peaks' positions for both cases, marked on green. Since these peaks are the benchmarks for the anti-symmetrical peaks, it is important that they maintain the same position for each measurement or at least show a small and stable variation. In this case, it is observed that cutoff frequencies present a random offset in each bandwidth, resulting

in the values presented in the last column of Table 3.1. In contrast, the quality of the alignment is clearly evident in the Figure 3.17, which leads to the following question. Is this small random offsets tolerable, giving the dimension of the bonding layer, which does not exceed 2 nm? Or, are the bonding layer intrinsic properties sufficient to generate a gap beyond the offset in the five experimental cases?

Bandwidth	Idx(i)	Unbonded case [MHz]	Idx(j)	Bonded case [MHz]	$\|f_{c_i}$[bonded] - f_{c_j}[unbonded]$\|$
[173 MHz - 175 MHz]	1-2	174.22294617	1	174.25918579	36.23 kHz
[175 MHz - 178 MHz]	-	-	2	177.14881897	2.925872 MHz
[178 MHz - 182 MHz]	3-4	180.0403595	3	179.98695374	50.40 kHz
[182 MHz - 185 MHz]	-	-	4	182.86323547	2.8228 MHz
[185 MHz - 188 MHz]	5-6	185.79101562	5	185.78147888	9.5 kHz
[188 MHz - 190 MHz]	-	-	6	188.72070312	2.92968 MHz
[190 MHz - 193 MHz]	7-8	191.65229797	7	191.55693054	95.36 kHz
[193 MHz - 195 MHz]	-	-	8	194.53811646	2.8858 MHz

Table 3.1: Cutoff frequencies of the reflection coefficients based on Figure 3.17

On the other hand, the comparison of theoretical and experimental data provides an optimistic outlook on the offset seen previously. Table 3.2 presents the cutoff frequencies of a bonded case in theoretical and experimental conditions. First, the experimental data is compiled with only 2 background echoes, where in theoretical condition this number is much higher. Yet, the gap between the theoretical and the experimental cutoff frequencies is really small compared to any conventional measurements, which demonstrates the accuracy obtained by the bench test developed. The larger offset value observed is 148.87 kHz. This value is obtained by subtracting the maximum and the minimum values of the last column in Table 3.2, which gives a proportion of the biggest offset seen in this case between theoretical and experimental results in a bonded case. As a reminder, the overall bandwidth is 20 MHz.

Bandwidth	Idx(i)	Bonded Theoretical [MHz]	Idx(j)	Bonded Experimental [MHz]	$\|f_{c_i}$[T] - f_{c_j}[E]$\|$
[173 MHz - 175 MHz]	1	174.456713	1	174.25918579	197.52 kHz
[175 MHz - 178 MHz]	2	177.366044	2	177.14881897	217.22 kHz
[178 MHz - 182 MHz]	3	180.272249	3	179.98695374	285.29 kHz
[182 MHz - 185 MHz]	4	183.181580	4	182.86323547	318.34 kHz
[185 MHz - 188 MHz]	5	186.087785	5	185.78147888	306.30 kHz
[188 MHz - 190 MHz]	6	188.997116	6	188.72070312	276.41 kHz
[190 MHz - 193 MHz]	7	191.903322	7	191.55693054	346.39 kHz
[193 MHz - 195 MHz]	8	194.812652	8	194.53811646	274.53 kHz

Table 3.2: Cutoff frequencies of an bonded case in theoretical and experimental conditions

Table 3.3 shows cutoff frequencies of an unbonded case in theoretical and experimental conditions. The facts remain the same. Again, the gap between the theoretical and the experimental cutoff frequencies is small, which shows the precision

obtained by the bench test developed. These results demonstrate the level of precision that the bonding characterization require in order to nuance between the different samples. If any offset is present on the experimental results, it could be fatal to the technique accuracy. So, the cutoff frequencies shift source should be quantify.

Bandwidth	Idx(i)	Unbonded Theoretical [MHz]	Idx(j)	Unbonded Experimental [MHz]	$\|f_{c_i}$[T] - f_{c_j}[E]$\|$
[173 MHz - 175 MHz]	1	174.462963	1	174.25918579	203.77 kHz
[175 MHz - 178 MHz]	-	-	-	-	-
[178 MHz - 182 MHz]	3	180.278499	3	179.98695374	291.54 kHz
[182 MHz - 185 MHz]	-	-	-	-	-
[185 MHz - 188 MHz]	5	186.094035	5	185.78147888	312.55 kHz
[188 MHz - 190 MHz]	-	-	-	-	-
[190 MHz - 193 MHz]	7	191.909572	7	191.55693054	352.64 kHz
[193 MHz - 195 MHz]	-	-	-	-	-

Table 3.3: Cutoff frequencies of an unbonded case in theoretical and experimental conditions

In this case, drawing a conclusion on the source of the offset based on the previous comparisons is challenging. To make a statement, the theoretical reflection coefficients are calculated in five cases with a different number of background echoes (Figure 3.18). The cutoff frequencies positions are not impacted by the number of background echoes selected for the treatment.

based on this observation, the background echoes' number is not the only factor that disturbs the precise alignment of the cutoff frequencies. Figure 3.19 displays a narrower spectrum to emphasis on the prefect alignment of the cutoff frequencies for all the conditions and also their shape. The convex geometry of the peaks is another factor to consider in order to understand the misalignment observed in the experimental setup, which results in the random shift. The epigraph shrinking relative to the number of background echoes is the real element that provides stability. Yes, its width is linked directly to the background echoes, but somehow there is something missing in this analysis. This quote is validated based on the perfect alignment of the cutoff frequencies for the different time signal lengths used. Figure 3.19 also demonstrates the echoes' influence on the upper side of the reflection coefficients. The stability and the oscillations maxima can be easily attributed to the number of echoes.

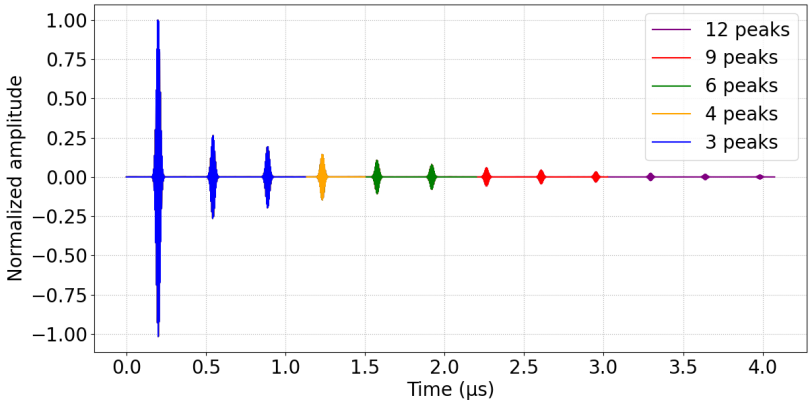

(a)

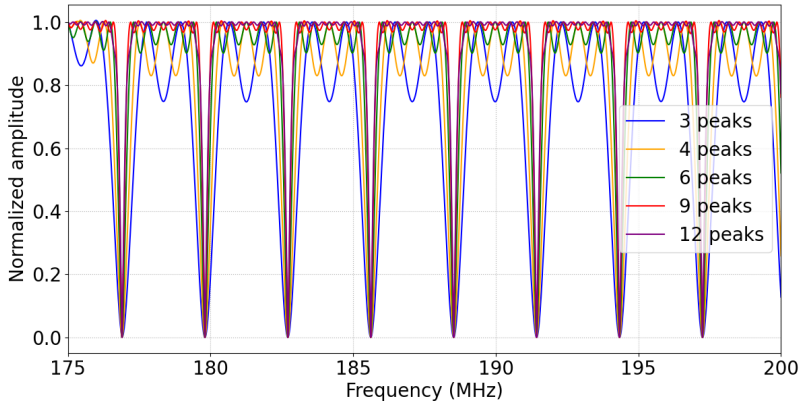

(b)

Figure 3.18: Time signals (a) and their respective reflection coefficients (b) for five different time signal window

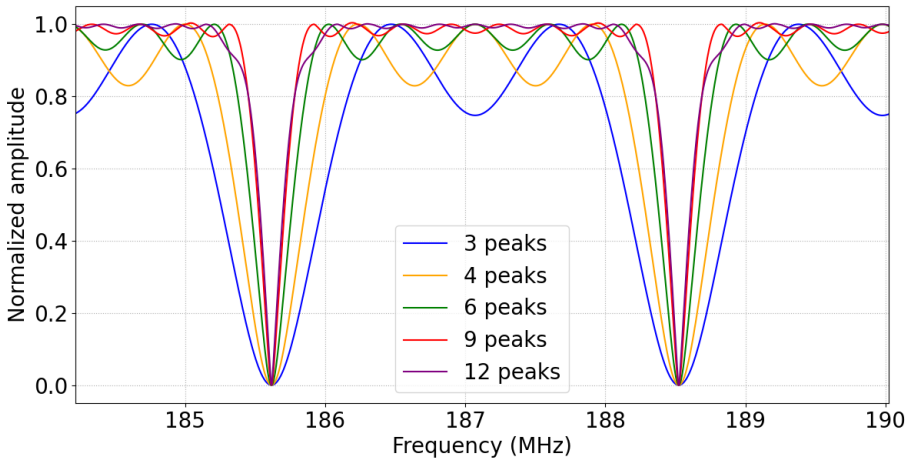

Figure 3.19: Screenshot based on Figure 3.18 emphasizing on the epigraph of the cutoff frequencies for different number of echoes

3.4.3 Noise impact on the cutoff frequency positions

Let's delve deeply and apply noise to the theoretical signals used in Figure 3.18. Figure 3.20 represent the twelve peaks time frame with three signal-to-noise ratio (SNR) levels. The purpose here is to add white noise to the signal and inspect the cutoff frequencies positions. This study is also conducted with three various time signal lengths to investigate any potential correlation between the SNR ratio and the number of background echoes. The reflection coefficient relative to each SNR ratio are exhibit in Appendix E.

The main goal is to provide a comparison between intact theoretical reflection coefficient cutoff frequencies and their noised versions. For each SNR value, three signals with different number of background echoes are noised and injected on the algorithm to detect the positions of the cutoff frequencies. Again, the offset is extracted by subtracting the smallest gap from the biggest in order to align the distorted cutoff frequencies with their clean counterpart. To remind, the motivation of this analysis is to understand the random offset observed in the experimental results.

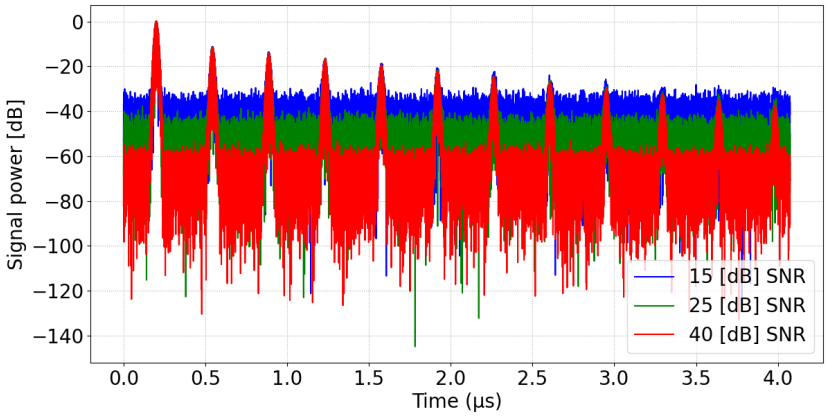

Figure 3.20: Theoretical signals of a bonded case noised with white noise for three different SNR ratio levels.

The random element of the analysis imposes several outcomes. In this case, one hundred noised signals are generated and their cutoff frequencies are extracted in each bandwidth for different time length and SNR. Table D.1 provides the comparison between intact theoretical reflection coefficient cutoff frequencies ($f_{c_i}[\mathrm{T}]$) and their noised versions ($f_{c_j}[T_{Noised}]$) for each bandwidth in the different configurations. The columns represent the configurations selected for the study, while the rows represent the offset mean found in the different bandwidths. For each signal-to-noise ratio (SNR), three different time signal lengths are selected based on the number of echoes present in each of them. The last column in the second table is the value of the difference between the smallest offset and the biggest found. This value indicates the remaining offset if a correction using the smallest offset is performed. To recap, the value obtained in the experimental result was around 100 kHz, which is significantly larger than the offsets found in all the cases studied here.

Furthermore, Table 3.4 summaries Table D.1 by providing the offsets means and

standard deviations of each configuration. It is observed that the noised signals generate an offset in all the cases, proving evidence that the background echoes are not the main parameter that shift the cutoff frequencies. In Table 3.4, the impact of the SNR ratio and the number of background echoes is now visible. Let's start by the 40 dB setup, the offsets means and standard deviations are decreasing relatively to the number of background echoes (N° of peaks). For 25 dB, the tendency is the same but the offset value mean and standard deviation are rising proving elements that the SNR ratio is an important factor to consider for the stability of the cutoff frequencies. The last setup at 15 dB validate this quote and emphasis on the instability caused by an high noised signal.

The second element to consider in this result is the background echoes impact on the stability of the cutoff frequencies. Yes, a high number of background echoes indeed provide an more stable reflection coefficient. It is observed that the offset means and standard deviation are decreasing for the three SNR ratios. But, the detail to consider is the global impact of the SNR on the signal making the number of background echoes insufficient to provide an more stable spectrum. For example, it is more suitable to use three background echoes at 40 dB than twelve at 15 dB. To resume, indeed the background echoes are important to ensure the stability of the cutoff frequencies. Yet, SNR ratio impact is more pronounced at this aspect. Table 3.4 second table summaries Table D.1 to conclude that the SNR ratio is the dominant factor responsible for the offsets seen in the reflection coefficient bandwidths.

SNR	N° of peaks	Mean($Offset_{100}$)	Std($Offset_{100}$)
40 dB	3	5.67036 kHz	2.01638 kHz
40 dB	4	3.54713 kHz	1.1318 kHz
40 dB	6	3.41866 kHz	0.96113 kHz
40 dB	9	3.34177 kHz	0.95206 kHz
40 dB	12	3.57245 kHz	0.96073 kHz
25 dB	3	12.10924 kHz	4.59702 kHz
25 dB	4	7.34528 kHz	2.45866 kHz
25 dB	6	5.96597 kHz	1.98772 kHz
25 dB	9	4.81251 kHz	1.37773 kHz
25 dB	12	4.6071 kHz	1.21633 kHz
15 dB	3	33.44001 kHz	13.74165 kHz
15 dB	4	22.01682 kHz	8.31551 kHz
15 dB	6	13.80047 kHz	5.52014 kHz
15 dB	9	10.32344 kHz	4.00531 kHz
15 dB	12	8.54102 kHz	3.05581 kHz

SNR	Mean(Mean($Offset_{100}$))	Std(Mean($Offset_{100}$))
40 dB	3.91007 kHz	0.88416 kHz
25 dB	6.96802 kHz	2.7495 kHz
15 dB	17.62435 kHz	9.16363 kHz

Table 3.4: White noise impact on cutoff frequencies position analysis

However, the experimental offset is equal to 148 kHz which is higher than the values found in the analysis made by the white noise. To remember, the main motivation in this subsection is to find the origin of the offsets. To do so, the noise injected in the theoretical signals is replaced by an modelized experimental setup noise. To understand its nature, Figure 3.21 and Figure 3.22 display the new noise with the three SNR ratio values used previously. The noise generated resemble to the noise found in the bench test (Figure 3.15). Its main characteristics is its shape and frequency. To generate the noise, parameters such as amplitude, period and placement were produced randomly for each signal. The origin of this noise pattern is the Crosstalk occurring between the different component interfering in the bench test which leads to signal degradation. Figure 3.23 displays the full theoretical signals noised for three different SNR ratio levels, the comparison could be made with Figure 3.20, where white noise provides a flat response on the noise plateau, the new modelized noised signal is providing a wavy pattern leading to a more realistic representation.

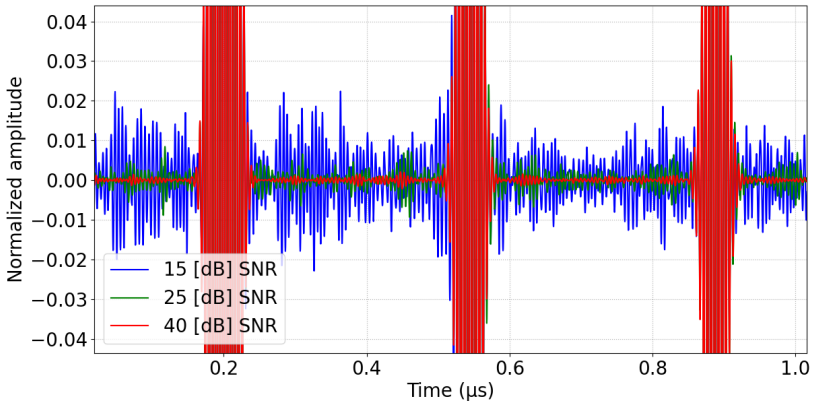

Figure 3.21: Theoretical signal with a modelized experimental setup noise

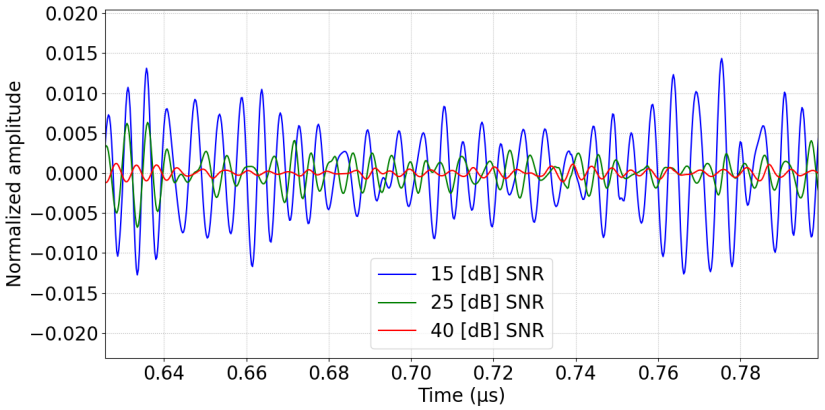

Figure 3.22: Zoom screenshot on the modelized experimental setup noise

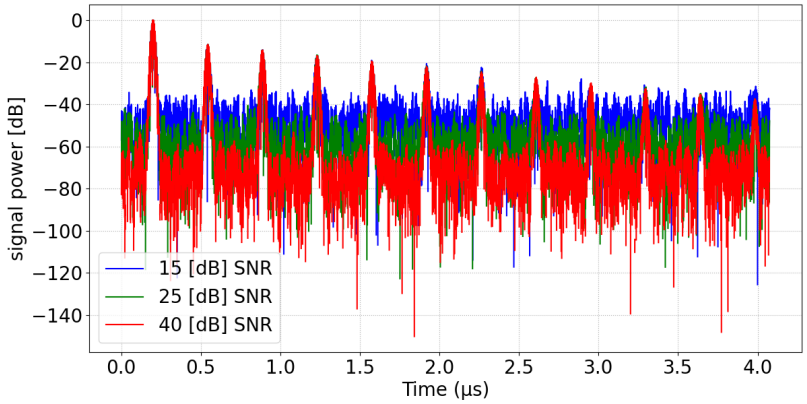

Figure 3.23: Theoretical signal of a bonded case noised with an modelized experimental setup noise for three different SNR ratio levels.

The noised signal, relative to the desired SNR ratio level, is added to the theoretical signal. A new type of noise is used which is centered on the signal bandwidth and similar to the signal seen in the experimental signal. The noise signal is defined as follows:

$$\text{Noised signal}(t) = A \cdot \exp\left(-\frac{(w \cdot (t - t_d))^2}{2 \cdot s^2}\right) \cdot \sin(\omega t) \tag{3.1}$$

where A represents a random value for the amplitude of the envelope, t_d denotes the random value of the time delay or the phase shift of the envelope and lastly s represents an random value for the standard deviation of the Gaussian distribution controlling the width of the envelope.

Table 3.5 resumes the cutoff frequencies behavior on this new setup. Table D.2 provides more details on the cutoff frequencies offsets on each bandwidth. The first observation is the higher offsets displayed in the table. Their means and standard deviations decreasing tendency is similar to the previous case, which shows that the SNR ratio plays the biggest role to ensure the reflection coefficient stability. The wavy pattern created artificially is able to produce offsets with the same proportions as seen in the experimental setup (Red value at 25 dB).

To conclude, this result proves that the nature of the Crosstalk could be detrimental to the measurement causing important variation on the cutoff frequencies positions. But, the main question to ask is: are the intrinsic properties of the bonding layer sufficient to generate a gap beyond these offset values?

SNR	N° of peaks	Mean($Offset_{100}$)	Std($Offset_{100}$)
40 dB	3	17.26888 kHz	5.86381 kHz
40 dB	4	10.13228 kHz	3.17665 kHz
40 dB	6	6.0959 kHz	1.940 kHz
40 dB	9	4.8263 kHz	1.5154 kHz
40 dB	12	4.17092 kHz	1.2117 kHz
25 dB	3	87.30103 kHz	32.77188 kHz
25 dB	4	48.69358 kHz	17.7252 kHz
25 dB	6	25.07293 kHz	8.358 kHz
25 dB	9	14.60862 kHz	5.2686 kHz
25 dB	12	12.22235 kHz	4.7159 kHz
15 dB	3	3.10487 MHz	1.6585 MHz
15 dB	4	1.5604 MHz	1.3664 MHz
15 dB	6	311.798 kHz	776.0417 kHz
15 dB	9	46.37372 kHz	15.8033 kHz
15 dB	12	34.76712 kHz	12.7695 kHz

SNR	Mean(Mean($Offset_{100}$))	Std(Mean($Offset_{100}$))
40 dB	8.49887 kHz	4.8492 kHz
25 dB	37.5797 kHz	28.01 kHz
15 dB	1.0116 MHz	1.1881 MHz

Table 3.5: Modelized experimental noise impact on cutoff frequencies position analysis

3.5 Experimental results

This subsection discusses the real conditions results conducted on hydrophobic samples. The data used in this analysis derive from the center of the wafers except in the last part. A cleaning process is established, and the wafer is placed on the bench test. The first element to adjust is the transducer height so that the echoes are placed in the suitable window. The sample holder parallelism with the transducer is performed until the phase on both X and Y axis are smooth and stable. Next, the gain on the receiver is adjusted to 25 dB. This value is chosen based on empirical observation. A higher gain will saturate the signals, where a lower will not be able to provide enough energy on the bandwidth. An order 3 Butterworth filter is applied to the signals to avoid any distortion on the narrower bandwidth which ranges between 175MHz and 200MHz. For this analysis typically, the number of signals picked up from each manipulation is 400 signals each of them is 25 time averaged. They are stored in CSV format files and all care was put to have the most digit numbers on the data, This is important because a fewer number of digits will smooth and hoax the data. Empirical observation on the nature of noise must be taken into consideration, sometimes the bench test noise is not stable and causes a heavy distortion on the signal. Attention must be paid to such phenomenon so that all data sets that contain any atypical empirical observation are removed. This approach is organized to give the same odds to all the samples in the different configurations.

3.5.1 A-scan results on hydrophobic samples

To ensure a perfect bonding, the wafers are heated after being set in contact. Figure 3.24 presents, for five different heating temperatures, ten measurements of the frequency shifts measured at the center of the samples. They were obtained on a single point, without using the set-up motorization and with no averaging. This first configuration should allow to characterize the capability of the DAQ to ensure the frequency shift estimation.

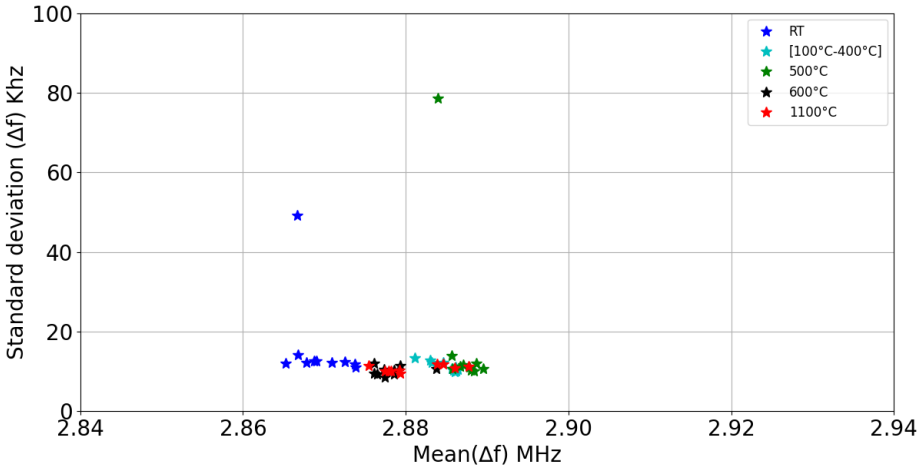

Figure 3.24: Ten experimental results for the five samples [RT - 100°C-400°C - 500°C - 600°C - 1100°C] represented in stars with previous experimental results displayed in vertical lines [1] using no motorization and no averaging.

Before starting the analysis, let's explain the graphic. The stars represent the experimental results found by the recent bench test. The Y axis stands for the frequency gap Δf standard deviation of a 400 measurement pile represented by the stars, where the X axis stands for their mean value. This first configuration demonstrates that the RT (Room temperature) sample is distinguishable from the other wafers, which were bonded at higher temperatures. These latter are grouped in a small region that may lead to difficulties in their identification.

The next major observation is the compact character of the Δf mean for the four higher annealing temperatures. Another observation pertains to the width of the measurement interval between the reference and experimental data. Table 3.6 summarized Figure 3.24 by providing the mean, standard deviation and the mean absolute error of the ten experiments for the five annealing temperature. The absolute error is calculated based on the new experimental results and the previous ones displayed by the vertical lines.

Parameter	RT	[100°C-400°C]	500°C	600°C	1100°C
Mean (MHz)	2.8695	2.8848	2.8871	2.8782	2.8809
Std (kHz)	2.9180	1.6981	1.5955	2.1364	3.9809
MAE (kHz)	16.5309	-12.1866	-21.8679	-35.7041	-36.0287

Table 3.6: Mean, standard deviation and mean average error for the no motorization and no averaging setup

Figure 3.25 displays the same experiment, but this time with 25 signal averages taken for each signal.

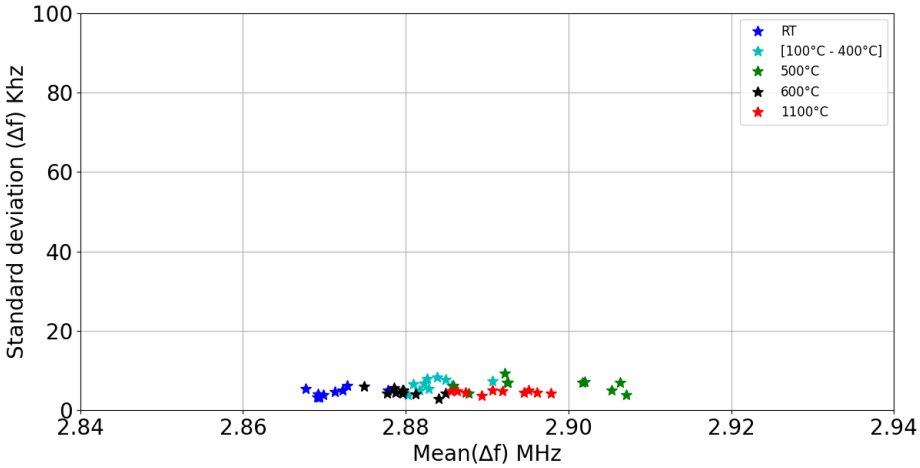

Figure 3.25: Ten experimental results for the five samples [RT - 100°C-400°C - 500°C - 600°C - 1100°C] represented in stars with previous experimental results displayed in vertical lines [1] using no motorization and with averaging [25 sample].

The main observation is the stretching of the mean Δf interval leading to conclude that the averaging adds an extra stability to the measurement. Even so, the compact

character of the output remains the same, where RT samples stand easily from the crowd, the four other samples are hardly distinguishable. Another remark to address is the reference mean Δf interval which is very large compared to the two results shown until now. This observation concludes that the reference results are found by using a very high number of averaging.

The standard deviation variation is also another parameter that differs between Figure 3.25 and Figure 3.24. The standard deviation plateau is lower for the measurement using averaging, indicating another advantage of averaging, which is the normalization of the noise and the production of a more refined output. Again, Table 3.7 summarized Figure 3.25 by providing the mean, standard deviation and the mean absolute error of the ten experiments for the five annealing temperature.

Parameter	RT	[100°C-400°C]	500°C	600°C	1100°C
Mean (MHz)	2.8708	2.8835	2.8973	2.8799	2.8914
Std (kHz)	2.7483	2.8509	7.6158	2.7763	4.1002
MAE (kHz)	17.8896	-13.4436	-11.6757	-34.0885	-25.5281

Table 3.7: Mean, standard deviation and mean average error for the no motorization and with averaging setup

3.5.2 C-scan results on hydrophobic samples

In this subsection, the motorization is used in order to quantify its effects on the measurement. The scanned surface measure **2** cm^2. Figure 3.26 displays ten experimental results for the five samples used previously. The graphic representation remains the same as before. In this setup, the motorization is used without signal averaging.

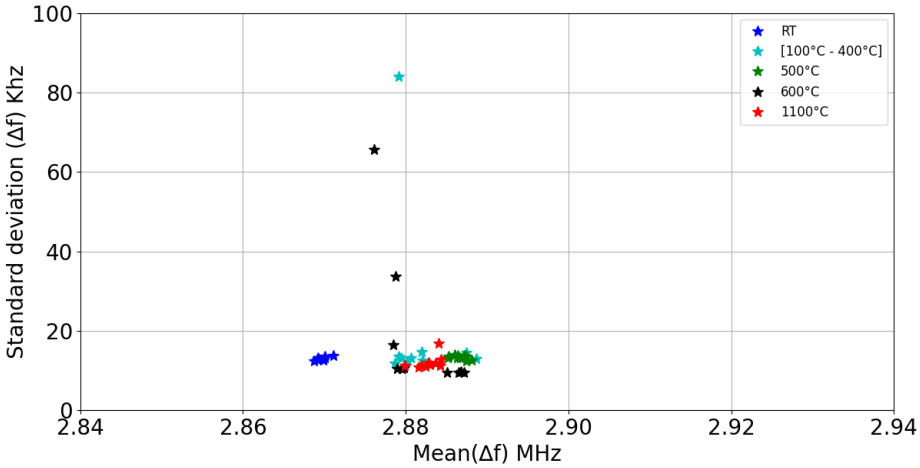

Figure 3.26: Ten experimental results for the five samples [RT - 100°C-400°C - 500°C - 600°C - 1100°C] represented in stars with previous experimental results displayed in vertical lines [1] using motorization and no averaging.

As previously, the sample bonded at room temperature (RT) is differentiated from the other four samples. The standard deviation plateau is in the same standards as previously with some diverging points. Again, the width of the mean Δf interval is not comparable to the previous results.

Parameters	RT	[100°C-400°C]	500°C	600°C	1100°C
Mean (MHz)	2.8697	2.8817	2.8866	2.8816	2.8827
Std (kHz)	0.6691	3.3531	0.9211	3.9545	1.3184
MAE (kHz)	16.7776	-15.2696	-22.3842	-32.3008	-34.2072

Table 3.8: Mean, standard deviation and mean average error for the with motorization and no averaging setup

Figure 3.27 displays the last configuration utilizing motorization and averaging. The statements drawn previously could be applied to this case as well. These results provide the answer to the question about the capability of the technique to generate an Δf gaps beyond the offsets. By observing the last four curves, it becomes evident that the technique has limitations in generating distinct Δf gaps. Therefore, achieving significant gaps beyond the offsets may require additional considerations or modifications to the technique.

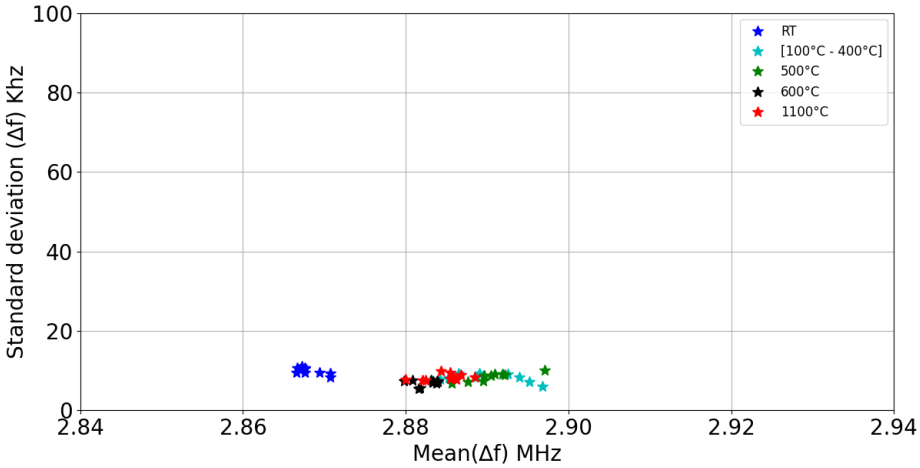

Figure 3.27: Ten experimental results for the five samples [RT - 100°C-400°C - 500°C - 600°C - 1100°C] represented in stars with previous experimental results displayed in vertical lines [1] using motorization and with averaging [25 samples].

Parameter	RT	[100°C-400°C]	500°C	600°C	1100°C
Mean (MHz)	2.8681	2.8895	2.8904	2.8825	2.4182
Std (kHz)	1.5761	4.5763	2.8675	1.3616	2.8847
MAE (kHz)	15.3495	-7.4539	-18.5377	-31.4831	-32.2973

Table 3.9: Mean, standard deviation and mean average error for the with motorization and with averaging setup

3.5.3 A-scan along the wafer diameter for hydrophobic samples

To further advance the analysis, a measurement along the diameter of the samples was performed this time. The Δf evolution along the diameter for four different samples is shown in Figure 3.28. This result is presented by the percentage variation of Δf relative to the anti-symmetric peaks. This gives us percentages ranging from 50 % (well bonded) to 100 % (poorly bonded). This representation makes it possible to avoid the experimental variability of cutoff frequencies.

It is observed that the RT sample stood out similarly to the previous subsections. This can be explained by its poor bonding. However, the other samples are very close to each others. This suggests that the RT sample may fall within the unsaturated sensitivity curve interval (Figure 2.33). The clustering of the other values may be due to the plateau of the sensitivity curve. Admittedly, the [100°C-400°C] sample separates itself slightly from the 500°C and 1100°C samples. Otherwise, these curves show the uncertainty of the measurements, which is around 0.1 % variation of Δf.

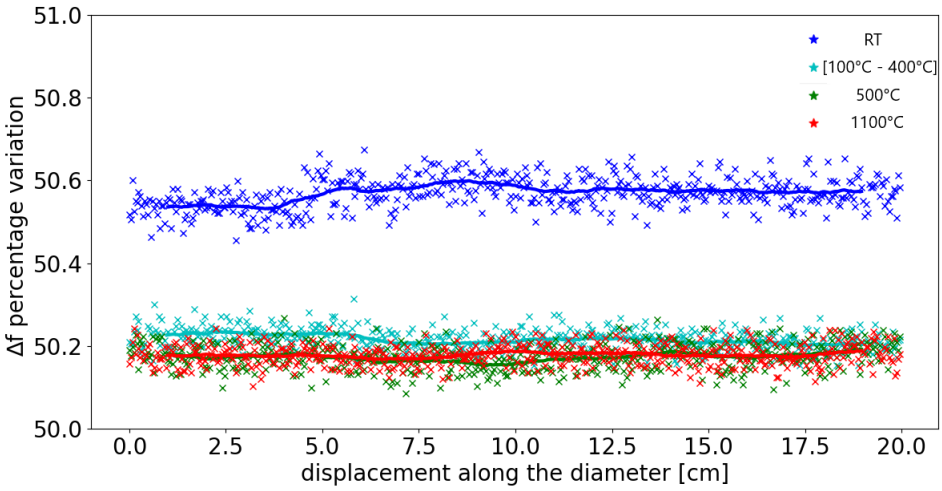

Figure 3.28: Percentage variation curves of ΔF for RT (blue), [100°C-400°C] (cyan), 500°C (green) and 1100°C (red) over a diameter of 20 cm. [ELC]

3.6 Conclusion

In conclusion, the experimental attempts to replicate the observations seen in chapter 2 have been unsuccessful. Although the room temperature sample is distinguishable, it is not sufficient to construct the experimental sensitivity curve. It is worth noting that Dekious [1] drew his sensitivity curve using 400 averaging with a four background echoes configuration. In an attempt to replicate this result, Figure 3.29 employed the same setup, but no significant findings were observed. It appears that the three background echoes' configuration combined with 400 averaging provides a wider interval, but the changes in Δf were not as pronounced as expected.

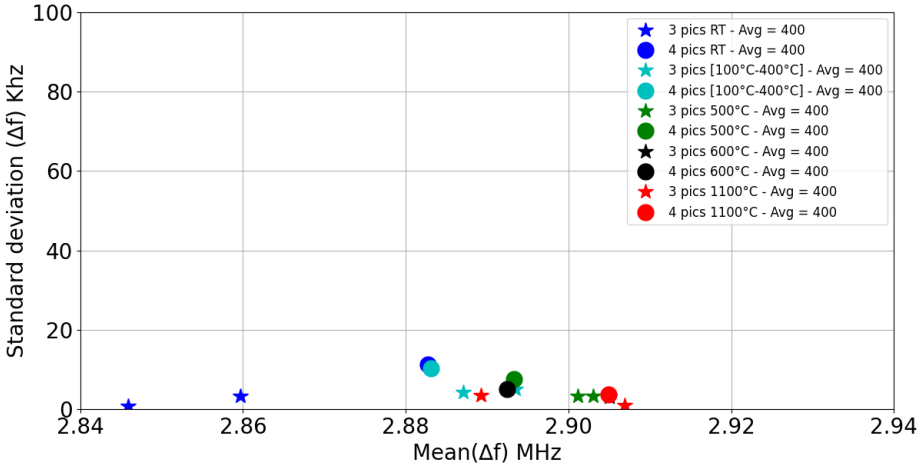

Figure 3.29: Experimental results for the five samples [RT - [100°C-400°C] - 500°C - 600°C - 1100°C] with three background echoes represented in stars and four in circles using 400 averaged samples.

This chapter summarizes the experimental protocol used to calculate anti-symmetrical peaks variations. The new bench test is equipped with five manual angle adjusters in order to ensure the sensor parallelism with the sample. The phase indicator is another tool that provides an information on the quality of the alignment leading to high precise parallelism. Additionally, a step has been added to the protocol which involves normalizing the reflection coefficient to ensure the selection of all minima on the curve. Finally, the results obtained from these manipulations are summarized in an experimental report.

The next subsection treated the transducer characteristics. The transducer inner reflections were analyzed and an empty time window were set for the treatment based on the SNR ratio and the quality of the signal used in each placement. The shorter window was privileged based on it is higher SNR ratio and the signal quality.

Subsequently, the reflection coefficient for an bonded and unbonded conditions were displayed and analyzed. The results obtained from this subsection emphasized on the quality of the alignment, leading to further discussions regarding the precision of the cutoff frequencies positions. Afterward, the theoretical and experimental reflection coefficients were compared concentrating on the offsets between the different cutoff frequencies for each bandwidth. To understand this shift, the theoretical signals are noised to observe the cutoff frequencies shift. This simulation was conducted with several SNR ratios and number of background echoes. It was concluded that a higher SNR ratio guarantees a stable reflection coefficient. The number of background echoes' impact is secondary but visible for the three SNR configuration used.

To improve SNR ratio, averaging was proposed to provide more stability to the reflection coefficient. The averaging impact on the SNR is proportional to the square root of the number of signal samples averaged. A result demonstrating the capability of this technique was propose and discussed.

Finally, results on hydrophobic samples were discussed. The main observation were the shrinking of the measurement interval and the standard deviation influence regarding averaging. Furthermore, the results presented in the last subsection shared the same outlook, it concludes that RT sample stood out in all the experiments. This can be explained by its poor bonding. However, the other samples were randomly grouped. This suggests that the RT sample may fall within the unsaturated sensitivity curve interval. Whether, the clustering of the other samples may be due to the plateau of the sensitivity curve. Other manipulations were conducted in this study, including notable ones such as Δf correction using the time of flight, experimental protocol on an industrial SAM, and measurements on hydrophilic samples. These additional experiments output were not different from the results seen previously.

Chapter 4

Time signal behavior based on the reflection coefficient variation

Contents

4.1 Introduction and hypothesis 110
4.2 Infrared and acoustic images of the opposite notch 111
4.3 Δf variation in the opposite notch 112
4.3.1 Opposite notch variation based on the scan position 112
4.3.2 Opposite notch variation for RT - [100°C-400°C] - 500°C samples 113
4.3.3 Zone B study for RT - [100°C-400°C] - 500°C samples 115
4.3.4 Time signal analysis in the opposite notch 116
4.4 Theoretical similarity based on the opposite notch variation . 119
4.5 Amplitude variation study based on the acoustic parameters 123
4.6 Conclusion 128

4.1 Introduction and hypothesis

According to the elements cited previously in chapter 3, it seems that other factors are impacting the reflection coefficient and specially the anti-symmetric peaks shift. In chapter 2, the resonance impact is seen in the signals emphasizing on the time signal influence on the reflection coefficient. Based on the knowledge established previously by Dekious [1], the analysis is focus on the frequency domain. Hence, the time signal impact on the reflection coefficient is analyzed deeply in chapter 4. The motivation of this chapter is to link the reflection coefficient variations to the time signal, making it more explicit.

In order to establish the experimental needs of this chapter, the main outlook to analyze is a heavy variation of the anti-symmetrical peaks. Based on Figure 1.31, an important variation of the acoustic parameter Δf could be exploited to understand the reflection coefficient behavior.

The opposite notch area represents the surface where the DCB test was conducted. This experiment is performed to know the bonding energy of the samples. Figure 3.2 synthesis the output of this test and displayed the length of the crack and the estimated bonding energy. The scar caused by the DCB test is an interesting zone since it provides an opening of the bonding. This zone could potentially provide several bonding variations since at room temperature the bonding is also effective. So, the output will represent three zones, the unbonded zone, the transitory zone and the third zone represented by the center of the wafer were results are more homogeneous.

The major hypothesis to focus on in this chapter is the time signal behavior regarding a nanometric layer sandwiched between two minimetric layers. The objective is to understand how the signal is affected by the different variations of the nanometric layer intrinsic properties. By addressing this question, the limitation of the bench test will become easy to determine based on the characteristics of the experimental output signal.

The second question revolves around the sensitivity curve and its capability to expand the technique range at higher frequencies (Figure 2.33). The aim is to explore ways to display this improvement differently and emphasis on the relationship between the time signal and the reflection coefficient on higher frequencies. By addressing this question, it will be possible to propose modifications in order to improve the capabilities of the method and potentially uncover more detailed information about the material under study.

4.2 Infrared and acoustic images of the opposite notch

Firstly, let's put the spotlight on the opposite notch and explain more precisely this authentic zone in the samples. Figure 4.1 displays infrared images on three different hydrophobic samples bonded at various temperatures. The wafers are represented by the blue zones, their environment being represented between orange and red. The first observation emphasizes on the crack size relative to the various samples, which decreases for higher temperatures. This area is represented by the dark blue spot at the edge of the sample represented with a deeper blue. This is related to the test nature, the crack size refers to the blade resistance to the bonding. If the bonding energy is higher the blade resistance is higher, the opposite is true leading to a bigger spot on the images in this second case. The advantage to use the infrared FLIR camera is the immediacy of the experiment. The opposite notch zones are rapidly localized.

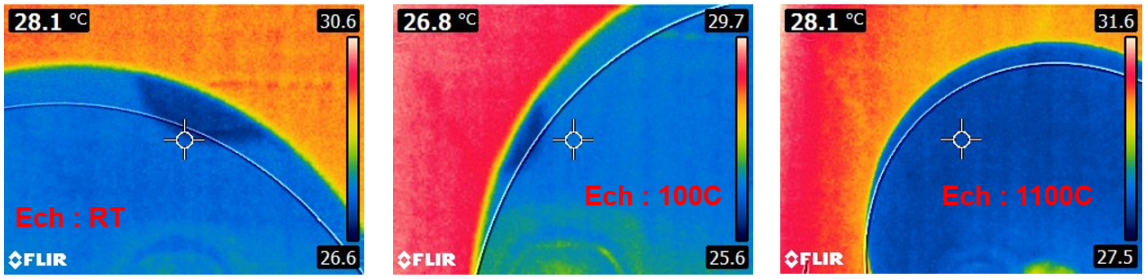

Figure 4.1: Infrared images on three different hydrophobic samples bonded at various temperature (Left : Room temperature, Center : [100°C-400°C], Right : 1100°C)

Their counterpart images using SAM are displayed in Figure 4.2. The contrast represent the Δf evolution in the opposite notch. In this case, more implicit details are extracted than the infrared images. Where infrared images provide a broader perspective, SAM emphasis more on the details providing more information about the opposite notch zone. Here, the idea is to focus on the transition zones between the blueish zones on the IR images.

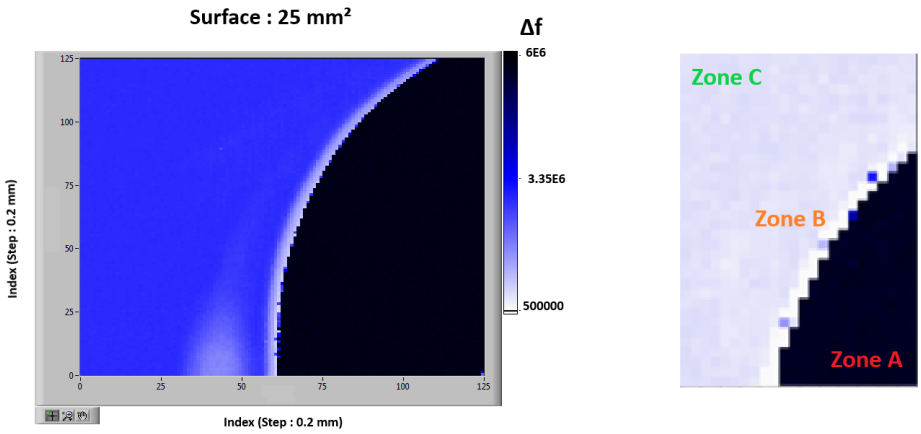

Figure 4.2: 25 mm² SAM image on the opposite notch emphasizing on the unbonded zone (zone A), the bonded zone (zone C) and the transitory zone (zone B)

This representation clarifies the reflection coefficient behavior by exposing three zones. The first zone represented in black referring to the unbonded zone (Zone A). The second zone representing a heavy drop of the Δf variation represented by a tiny white line on the border of the black spot (Zone B), and finally a third zone were the Δf displayed represent a clear homogeneous contrast proportional to a full bonded result (Zone C). This can be valid also for the black zone were the Δf value is proportional to the thickness of an unbonded case in this position.

Empirical observation on the bench test demonstrate that the signal in zone A and zone C is stable. The zone B shows heavy turbulence on the signal amplitudes. More on this topic will be discussed in the following subsections, providing further insights and analysis.

4.3 Δf variation in the opposite notch

The variation of the anti-symmetrical peaks on the opposite notch could bring a new perspective to the conversation. In this analysis, the three zones described previously will be analyzed deeply in order to understand the real motive of the Δf variation.

4.3.1 Opposite notch variation based on the scan position

In Figure 4.3, three attempts to observe the Δf variation experimentally are performed on the same sample bonded at room temperature [RT].

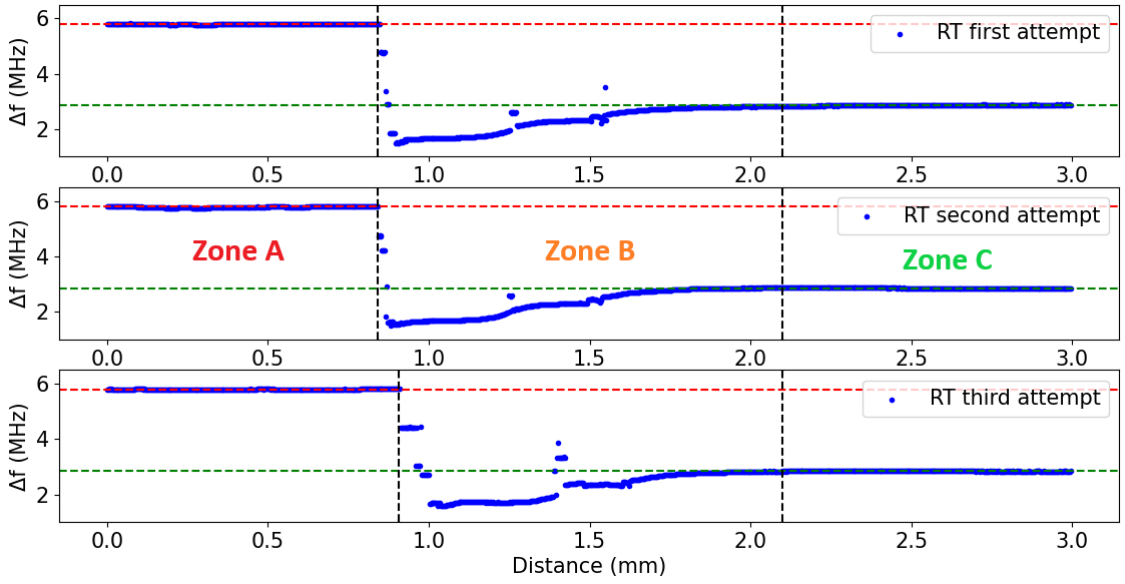

Figure 4.3: Variation of the Δf for three attempt on room temperature [RT] samples

In the three graphs, the pattern of the Δf variation is conserved across the three experiments. This first observation validates the experimental protocol and concludes that the Δf variation on the opposite notch is reproducible. This figure represents the variation along 3 mm, starting from the edge of the sample and moving towards the center.

Figure 4.3 emphasis on the three zones observed on Figure 4.2. First, the zone A represented by the values on the 6 MHz plateau. Those values are found on an unbonded zone, thus explain the interval doubling since the wave in this case used only the upper side of the sample to propagate. Afterward, a heavy drop of Δf is seen, the wave is making a first contact with the sample lower side. The zone B starts from this position, the curve represents a clean variation making a valid observation of the Δf shift. In this case the variation origin can not be cited easily since it is very likely that this pattern is influenced heavily by the thickness variation caused by the crack. Finally, zone C represents the moment where the ultrasound wave enters the bonded zone. This observation is possible since the scale of the variation is indeed much bigger. Yet, The flat character of this zone demonstrates the fragility of the technique. The fact that this zone does not show any shift confirms that the setup used would not be able to surpass this plateau. But, the end of the zone B could be an interesting way to look to the problem.

Another factor to consider is the length of the three zones. The zone A interval shows the distance where the sample is unbonded, which is equal to 0.94 mm. This value should be taken with caution as it is possible that the starting point of the measurement does not precisely align with the edge. The distance in zone C is not that interesting since the phenomenon observed in this plateau is the same along the sample. The most important zone in this graph is the transitory zone B. The length distance where the variation is effective is equal to 1.17 mm. Interestingly, the zone is divided into two transitional regions, which can be differentiated by their slopes. At the beginning, the variation in zone B exhibits a more pronounced slope compared to the end of the curve, suggesting that this region may be associated with variations of thickness. On the other hand, the latest part of the curve may correspond to variations in the intrinsic properties of the bonding, making this zone an interesting starting point for further analysis.

4.3.2 Opposite notch variation for RT - [100°C-400°C] - 500°C samples

This subsection highlights the Δf variation for three wafers with various bonding energies. The samples chosen for this analysis are RT - [100°C-400°C] - 500°C. Since the bonding energy is not equal for the three samples, the Δf variation could potentially vary based on the crack length.

Figure 4.4 presents the results of these experiments. The first experiment conducted with RT sample is discussed previously. The second with the [100°C-400°C] sample was expected to exhibit a more pronounced variation of Δf compared to the room temperature (RT) sample, considering its higher bonding energy. However, contrary to expectations, the observed Δf variation in this case does not follow this expectation. In fact, the shrinking of the variation interval is reveling another problem. The DCB mechanical test nature assumes that the crack anatomy are hardly repeatable. Yet, the bonding energy estimation is proven to be correct but if the acoustic variation represented by Δf does not match the expected crack length. Thus, it will be hard to draw a conclusion. This reveals a question about the nature of zone B variations. Are they linked only to the crack length, or do the intrinsic properties of the samples play a role in this anomalies.

The 500°C sample exhibits a more natural behavior compared to the previous result discussed. The length of zone B is wider in this case. This result is expected because the sample is bonded at a higher temperature, and it is likely that the crack opening in zone B is bonded at room temperature until it enters zone C, where the bonding is associated with a 500°C annealing temperature.

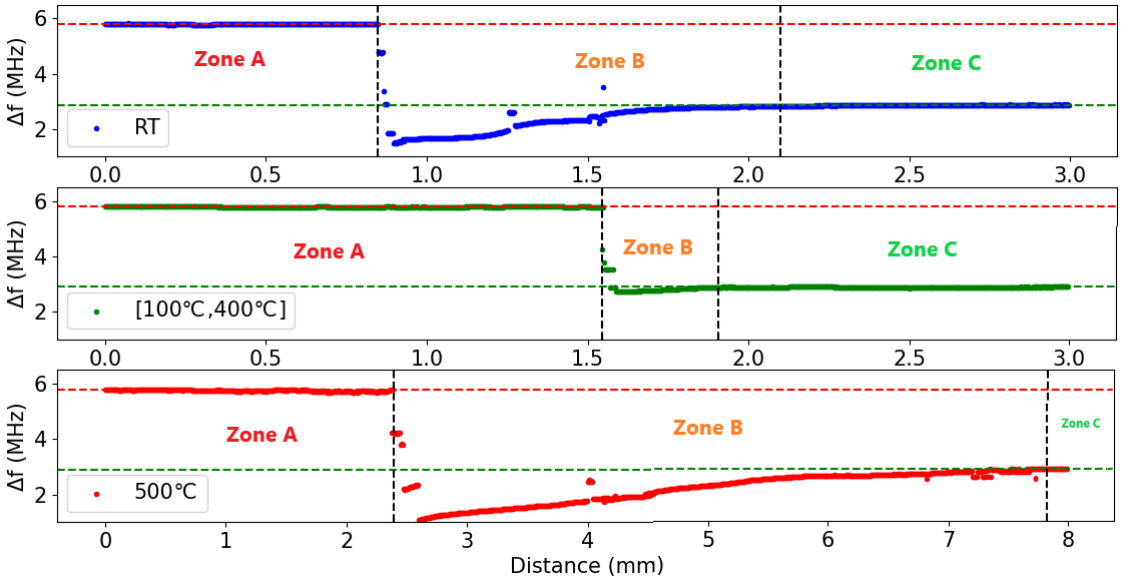

Figure 4.4: Variation of the Δf for three samples (RT in blue - [100°C-400°C] in green - 500°C in red)

The next table provide information about the parameters of the test :

Sample	N° of points	sampling step (mm)	length (mm)
RT	1000	0.003	3
[100°C-400°C]	1000	0.003	3
500°C	1000	0.008	8

Table 4.1: Opposite notch scan test parameters of the three experiments displayed in Figure 4.4

These three results show that while the bonding energy is different between the three samples, the zone B does not follow the tendency of the bonding energy. Another factor to consider is the size of the unbonded zones (Zone A + Zone B) for the three samples. If they are compared to the results in Figure 3.2, these distances are very small in comparison to the ones found in the DCB test, thus it concludes that the variation in zone B does not represent the full length crack. For example, The 500°C sample DCB crack length is equal to 19 mm, where in this experiment the transitory zone is only equal to 5.3 mm. In the RT sample, this is worse, the crack length found by the DCB test is equal to 50 mm, where its counterpart using Δf does not exceed 1.17 mm!

To conclude this subsection, the results represented above are unmatched with the DCB test crack length in Figure 3.2. Yet, the three zones are represented for the three samples. The length of the zone B and zone A combine where the detachment exist does not express the tendency expected, meaning that for lower annealing temperatures the crack length should be longer than observed.

4.3.3 Zone B study for RT - [100°C-400°C] - 500°C samples

Since no lead was found in the last two subsections, let's focus more on the zone B. Figure 4.5 represents only the zone B in Figure 4.4. The outlook to be found is a pattern that follows the annealing temperatures of the three samples.

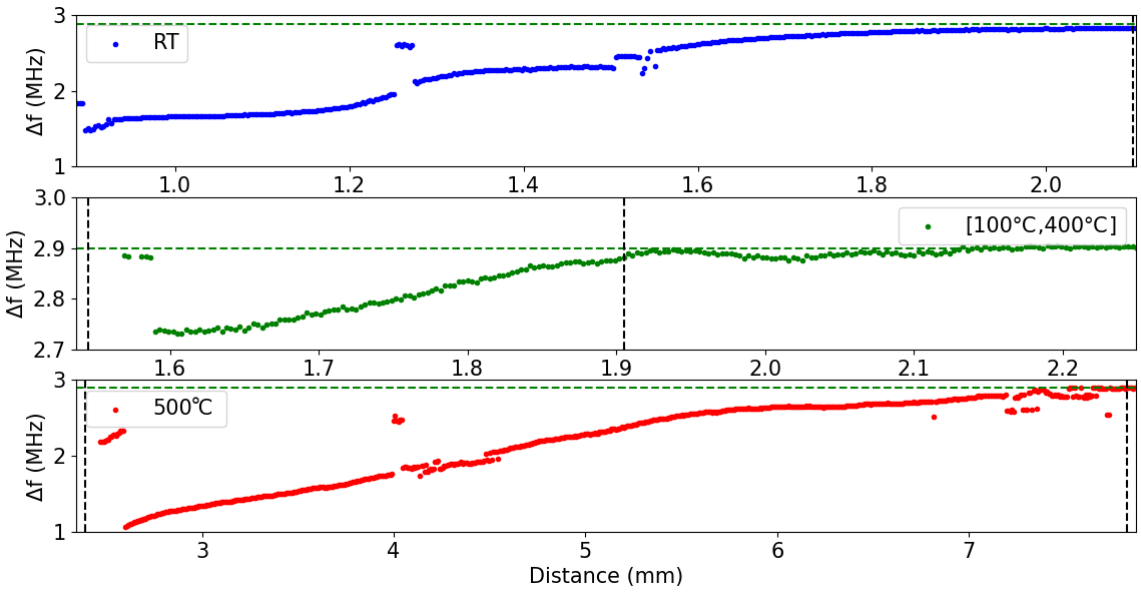

Figure 4.5: Zone B variation of the Δf for three samples (RT in blue - [100°C-400°C] in green - 500°C in red)

In this cases the length of the transition does not show any significant information. Meanwhile, the slope of the curves could potentially hold some information about the source of such variations. First, the RT sample represents a steady slope in the transitory zone making the crossing to the bonded zone smoother. This is due to the nature of the bonding in this case since the crack will be bonded after the test a second time at room temperature. In this case, the observation is unique to the thickness variation of the bonding layer. The second curve in green represents the Δf variation for a [100°C-400°C] sample. The Y axis emphasizes on a smaller range compared to the other curves since the variation in this case is not that deeper. By zooming on the curve, it is noticed that the slope variation is more pronounced in this case and shorter. The first transition could potentially represents the thickness variation. Moreover and after the 1.9 mm line, this zone represents some turbulence on the Δf values making an assumption that these variations could represent an intrinsic property shift of the bonding layer. But, in the two cases these variations are happening on a shorter distance.

Lastly, 500°C shows the same tendencies as the [100°C-400°C] sample. The exception in this case is the length of the variation which is tolerable since this sample will represent more shades of bonding energy. But, the length of the first slope that ends at 5.7 mm is too long compared to the rest of the curve. This observation assumes that all this entire phase represents a thickness variation of the bonding layer. In this case, since the bonding energy is higher, the blade will face more resistance from the bonding, making the crack shorter. Logically, the larger portion of the variation should be the second zone after the 5.7 mm checkpoint. However, this is not the case making even more challenging to understand the opposite notch variation. By addressing all these facts on the Δf variation, there are other elements that are still missing in order to obtain the full picture.

4.3.4 Time signal analysis in the opposite notch

Let's focus on the time signal. For this subsection, a second [100°C-400°C] sample was used to extract the signals relative to the opposite notch area. The result in Figure 4.6 was selected based on the quality of the Δf variation pattern. The assumption made until now states that the slope in zone B could be related to the two potential sources of Δf variation. The transitory zone B is potentially represented in this case by the two potential sources of anti-symmetric peak variations which are the thickness and the intrinsic properties.

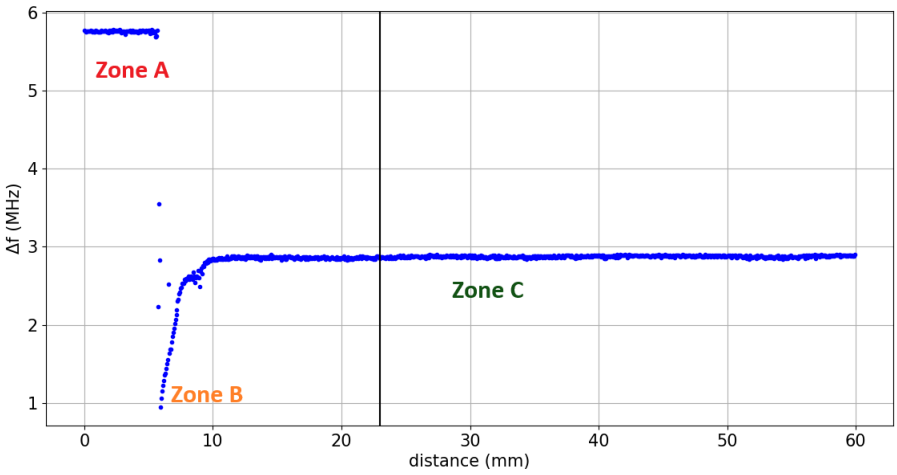

Figure 4.6: Δf variation in the opposite notch for [100°C-400°C] sample used in subsection 4.3.4 experiment

Otherwise, these results also demonstrate the crack anatomy differences between the various samples. When the first [100°C-400°C] sample in Figure 4.4 couldn't reach a deeper variation, Figure 4.6 displays the opposite.

Figure 4.7 represents the time signal used in order to obtain Figure 4.6 results. First, let's explain the curve parameters. The X axis represents the time of flight, the vertical lines in purple are the background echoes for one thousand signals along the 60 mm diagonal crossing the opposite notch zone. The intensity of the echoes is dropping regarding the wave path leading to a significant change of contrast. The signal power in decibels effectively emphasizes on the echoes behavior. The Y axis on the other hand represents the location where the signal is operating according to the opposite notch. In order to obtain a smoother observation, Hilbert transform was applied to the signals before the signal power calculus.

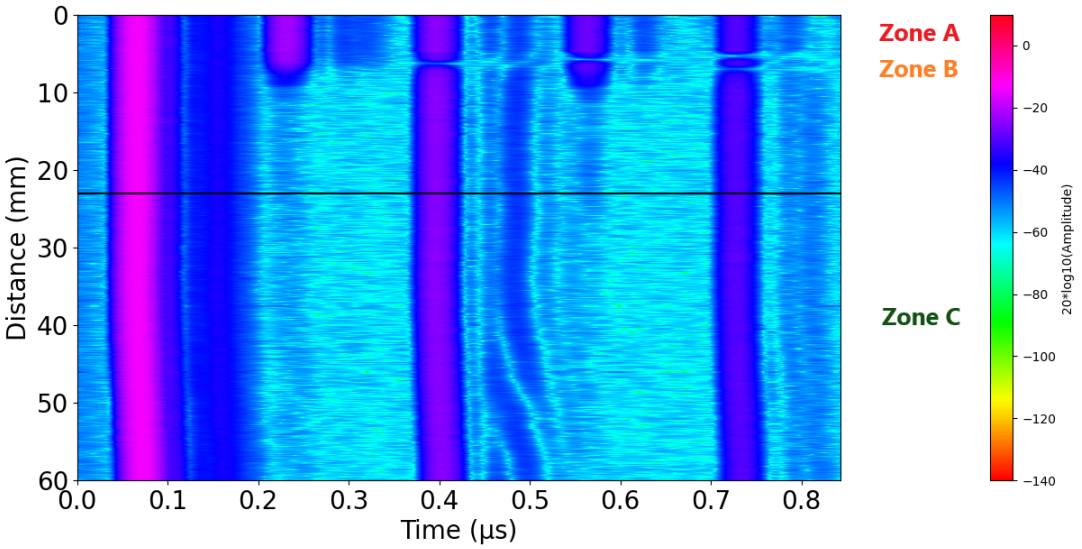

Figure 4.7: Signal behavior on the opposite notch

The amplitude variation regarding the zones established in the previous subsections is visible. First, the zone A is represented by six vertical echoes emphasizing on the unbonded condition. The time of flight is respected and could be compared to zone C where the sample is bonded. The time of flight values concord in the two cases with the sample anatomy. Before engaging on zone B discussion, the contrast of the ambient noise is around 60 dB which is relative to the signal to noise ratio of the acquisition system used in the bench test. This observation is really important because it is the key to understand the limitation of the technique. Another observation regarding the background echoes width could be cited. The decibel representation allows the observation of the real response of the major echoes and emphasis on the signal real impact on the time window. But, the echoes width is not the same for the three background echoes making this issue unique to the surface echoes where a blue wider zone is observed after the main signal in purple. The two background echoes represent less significant broad shape but the impact of the surface signal pattern is visible on both echoes.

To understand Figure 4.7, let's remind that zone C and zone A represent a constant Δf contrast. Now, let's focus on zone B where the shift is operating. Firstly, the zone B distance width is again uncorrelated with the data collected by the DCB test in Figure 3.2. The black horizontal line represents the limit where the bonding is supposed to be ineffective. Yet, the signals do not interact fully with the transitory area.

Figure 4.8 represents zone B exclusively. In this observation, the time signal impact is clearly related to the various signals variations. They are different between the fourth echoes. To be more specific, the second echo on the picture which represents the first interaction with the bonding layer displays a steady decreasing variation tending toward the zone C. The third echo which represents the first background echo shows a severe dump of amplitude, where the fifth echo is represented by two dumps. These variations are the source of the Δf shift, each amplitude combination of the five echoes is responsible of the smooth ascendant Δf variation in Figure 4.6. This result displays the essence of Δf shift making it clear that without a clear resonance of the multi layer, the anti-symmetric variation is ineffective. The second and fourth echoes represent another interesting fact relative to the amplitude decreasing along the path toward zone C. The tops of the echoes patterns show faded shades of blue, emphasizing the last signals making contact with the bonding layer. These gradual disappearances of the echoes could be indicative of the bonding layer.

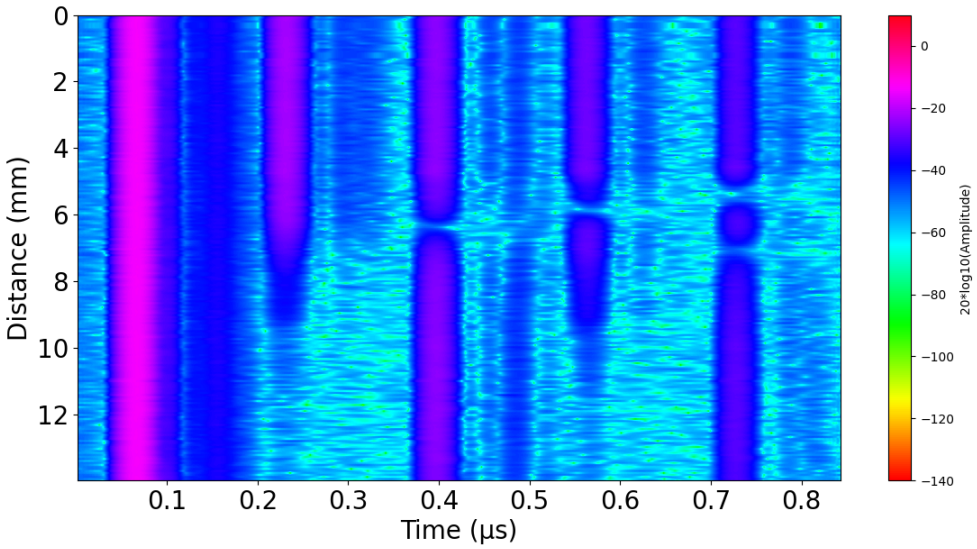

Figure 4.8: Signal behavior in zone B on the opposite notch

Figure 4.9 validates this quote by showing the reflection coefficient relative to the signals extracted in the opposite notch area in Figure 4.7. The constant behavior of zone A and zone C is also visible on the reflection coefficients. The anti-symmetric peak variations are observed in zone B making an evidence that zone B is a key region to study the bonding property variations.

Figure 4.9 psychedelic representation displays one thousand reflection coefficient along the 60 mm diagonal crossing the opposite notch area. The colormap can be hard to visualize if the reflection coefficient pattern is not remembered. The several modes that shape the reflection coefficient are expressed by multiple local minimums. To correlate this previous representation with Figure 4.9, the red lines border with the green and blue lines are the symmetrical and the anti-symmetrical peaks, where the rest of the contrast represent the reflection coefficient higher plateau. An indicator to verify this result is the distance between the modes relative to the state of the bonding. Zone A represents an unbonded state making the mode spread to times higher then the zone C where the

bonding is effective. Otherwise, this representation also emphasis on the rapid transition displayed in zone B.

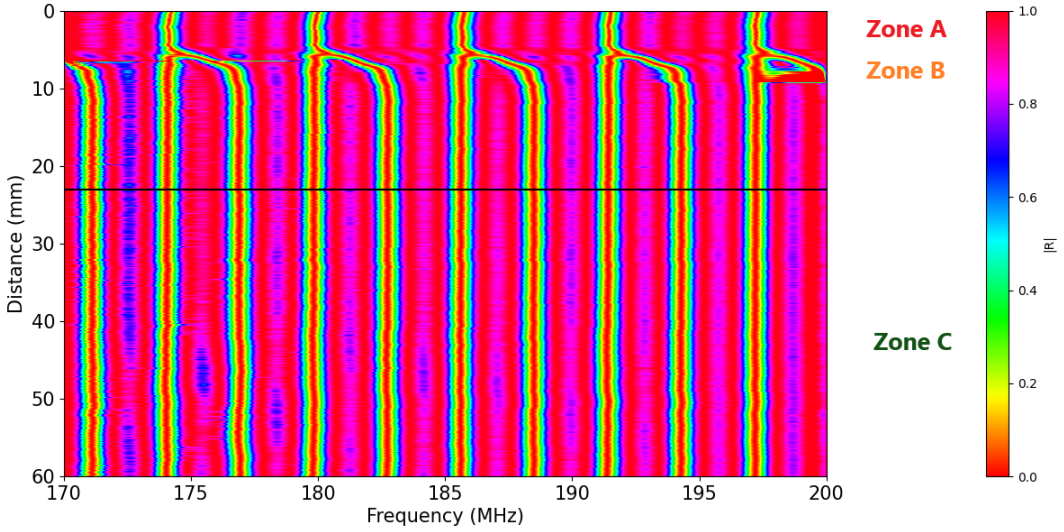

Figure 4.9: Reflection coefficient result of the opposite notch area relative to the signals in Figure 4.7

To conclude, the faculty to observe the time signal and the reflection coefficient side to side provide interesting outlook on the anti-symmetric peaks variations. If Figure 4.7 and Figure 4.9 are observed simultaneously, it is evident that the resonance pattern observed in the time signal is responsible of the Δf variation in the reflection coefficient making zone B a promising area for further studies.

4.4 Theoretical similarity based on the opposite notch variation

Since the opposite notch could not provide a specific region where only the intrinsic properties of the bonding layer are changing, it suggests that the theoretical approach should be utilized to understand how the time signal would interact with a bonding layer at different acoustic impedance's.

To gain a deeper understanding of the impact of intrinsic properties on the time signal in the case of a direct bonding, the analytical model used in chapter 2 can provide valuable insights. By varying the acoustic impedance of the bonding layer in the simulation, it is possible to generate signals corresponding to different impedance values. The range can span from an unbonded state, which is represented by a null impedance value and where the wave does not cross the lower side of the sample. The silicon acoustic impedance represents the final bonding state, assuming that the molecular bonding merges the two layers. By varying the impedance within this range, we can simulate signals corresponding to different stages of bonding and analyze their characteristics. This approach allows us to explore how changes in impedance influence the

time signal. Furthermore, this approach allows us to study the behavior of the time signal for different impedance values and assess how changes in the bonding layer properties impact the signal's features. This can help in identifying specific patterns or trends that may correspond to variations in the intrinsic properties of the bonding layer.

In Figure 4.10, the time signal is displayed along with the labeling of all the echoes. The first echo, known as the surface echo (SE), is not expected to change with the variations of acoustic impedance. The second group of echoes corresponds to the bonding layer echoes (BLE), and it is anticipated that the amplitude of these echoes will vary with the acoustic impedance change. The third and final group of echoes represent the background echoes (BL), and it is very likely that their amplitudes will also exhibit some variations. The question to be addressed is whether the background echoes variations will resemble those relative to the bonding layer echoes. It is worth mentioning that the state exhibited in Figure 4.10 is the starting signal of the model. The X axis in this graph is preserved, and the echoes in Figure 4.11 are labeled accordingly.

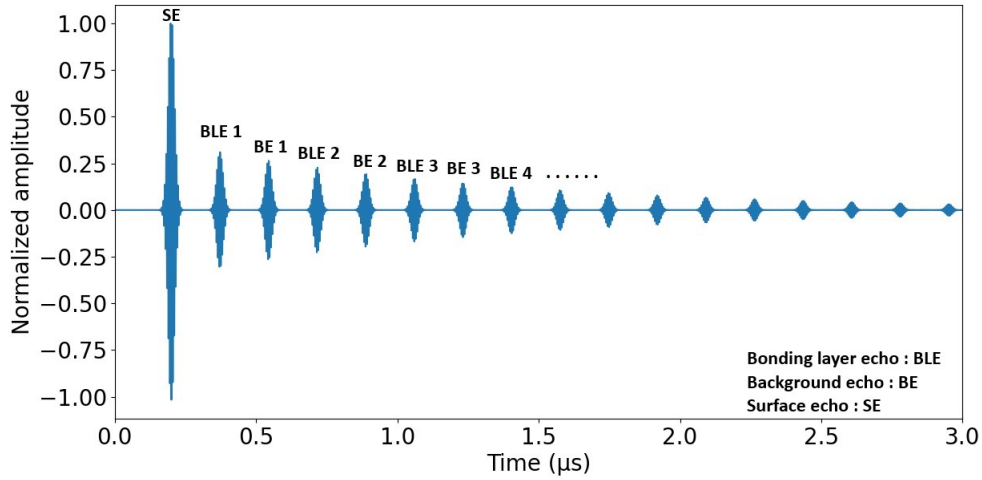

Figure 4.10: Time signal of an SI//SI unbonded state with a labeling of the different echoes

Figure 4.11 synthesizes the time signal variation according to the bonding layer's acoustic impedance. As mentioned before, the X axis is similar to the one in Figure 4.10. Thus, the first vertical line represents all the surface echoes (SE). The second vertical line represents all the first bonding layer echoes (BLE1) and the third represents all the first background echoes (BE1)...

Figure 4.11 illustrates the range of acoustic wave observations possible while crossing a SI/SI wafer. The bonding energy started from none and increases until the silicon state where the bonding is fully complete and the wave crosses the nanometric layer with ease. The Y axis represents this parameter as the acoustic impedance of the bonding layer. Next, the colormap represents the signal power variation in dB. The reddish the color the more the signal is pronounced. The green shade displays very low values of amplitude emphasizing on the time of flight between the echoes.

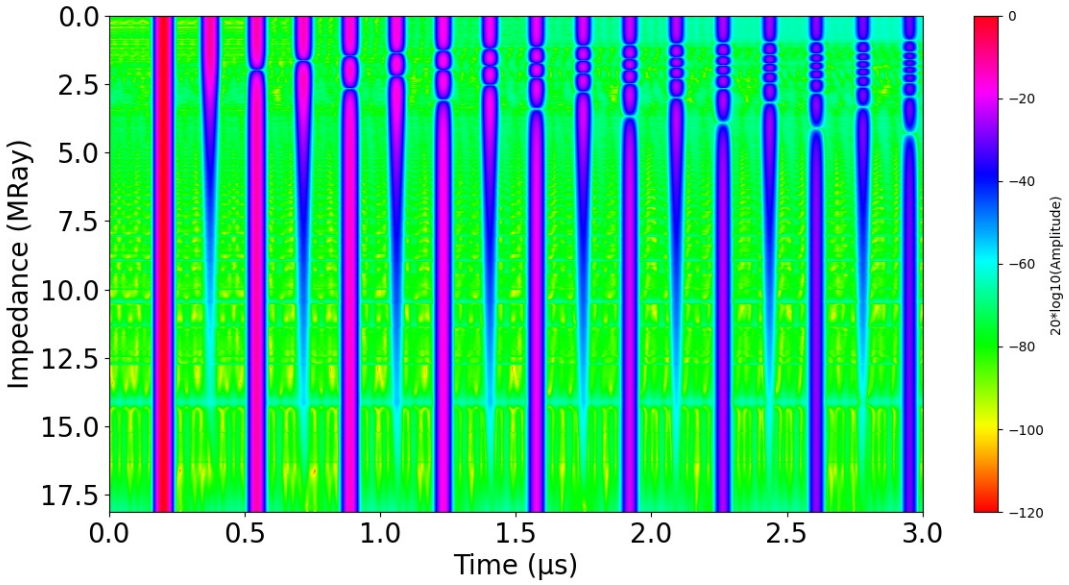

Figure 4.11: Time signal behavior relative to the acoustic impedance variation of the nanometric bonding layer

Let's now analyze the curve. The time of flight is the first noticeable indicator of the transition from a bonded state to an unbonded state, which provides insights about the constant changes of the time signal relative to an acoustic impedance gradient. At low acoustic impedance values, the time of flight corresponds to the thickness of only one wafer. As the acoustic impedance increases, the time of flight doubles, indicating that the acoustic wave is now able to travel through the bonding layer and interacts with the entire bonded structure. The time of flight remains unchanged since the bonding layer thickness is smaller compared to the wafers. If the opposite were true, the time signal changes would not only be vertical but also horizontal, resulting in a more complex pattern. The following quote is supported by the fact that a wave will takes more time to cross a bonding layer that is proportional to the wafers thicknesses, leading to a horizontal shift in the BLE echoes. In our case, the BLE echoes remain vertical, indicating no significant change in the time of flight since the bonding layer measure only 2 nm.

Moreover, the colormap shades of the signals respected the evolution observed on Figure 4.10. The first surface signal SE started at 0 dB since it is the reference for all the other amplitude values. The transition from red to deep purple displays it very clearly.

Let's describe the pattern of the signals. The surface signal (SE) represents the same observation on the thousand cases simulated. This is logical, since it only interacts with the surface and no change are expected in this case. The first BLE echo is the only echo in the illustration that responds decrescendo, making it an excellent candidate for characterizing the bonding energy. However, its reach is limited at 14 MRay, where the other BLE echoes can reach more further values suggesting that they are excellent candidate to detect higher impedance's. Moving on to the first BE echo, this time a strange drop of power is observed. This first irregularity is occurring since the bonding layer will effectively reflect an amount of energy in the opposite direction of the outgoing wave. This flow opposition allows phase cancellation. On top of that, the position of this drop along the Y-axis is also an important aspect to consider. This pattern suggests that only few observations can be described in this case. This is a first statement that proves that no macro information is visible on the background echoes (BE) since these type of echoes represents a flat response along the most values of the Y axis, which corresponds to the acoustic impedance.

The second BLE echo also exhibits this phase opposition pattern. But, its position along the Y-axis is different than the first BE. This suggests that the intrinsic properties of the bonding layer affect the wave phase opposition. The resonance pattern horizontally is shifting regarding the echo observed which provides proves to the following statement. To shift the anti-symmetric peaks, the time signal should capture the elements that describe this change, namely the phase opposition patterns. Furthermore, the reach of the second BLE echo is higher which indicates that in order to detect a high impedance values, it is worthwhile to detect and analyze the smallest amplitude variations specially at higher impedance value. This suggests that the detection and measurement of subtle changes in amplitude can provide valuable insights on the bonding layer characteristics.

At the second BE echo, things start to become clearer. The phase cancellation occurs twice, indicating the number of reflections made by the layer structure in the opposite direction of the flow towards the transducer. The positions of the phase cancellation are completely different than the previous echoes. Additionally, the position of the first amplitude drop is slightly ahead compared to the previous echo. Again, this observation shows that the information obtained from the background echoes is limited, since this class of echoes only responds to certain acoustic impedance values.

Next, the third BLE echo emphasizes on the importance of the number of background echoes in order to obtain a deeper range of acoustic impedance's. The vertical length comparison of BLE 1, BLE 2, BLE 3 and BLE 4 demonstrates that the range of earlier echoes is restrained compared to the latest ones. This observation validates the importance of strong and clear BLE echoes in order to succeed the bonding characterization technique. The ability to accurately detect and analyze these echoes at higher acoustic impedance's is crucial for obtaining reliable information about the bonding process and the associated impedance variations.

The third BE echo shows a more refined observation regarding the spacing between the phase cancellation periods. This could be applied to all the BE echoes. The pattern of phase cancellation contains two length patterns, with one of its main characteristics being

that the longest patterns are relatively twice the length of the smallest. Let's remind that the Y-axis represents the acoustic impedance and this phenomena is not related to the time axis based on Figure 4.11. If the observation is objective to all the BE and BLE echoes, the longest pattern is always at the end of the resonance. The complexity of the analysis starts by knowing that the phase cancellation periods are asymmetrical to acoustical impedance represented by the Y-axis, making each echo in the series important at lower impedance. At higher impedance, the amplitude decrease of BLE echoes provides a natural indicator but the reach of the echoes isn't that convincing. Yet, the BLE class of echoes is the one holding information at higher acoustic impedance's.

To sum up, The phase cancellation periods are more pronounced for echoes that are farther away, and the number of cancellations represents the path taken by the acoustic wave in each moment. There length and placement indicate how the acoustic wave is interacting with the bonding layer. It is important to note that the Y-axis should not be confused with the time axis. Each point on the Y-axis corresponds to the acoustic impedance value, and the amplitude variations within each vertical bar represent the response at that impedance. The vertical pattern of phase cancellation is not a variation over time, but rather a response of the layer's at each stage. The resonance pattern of all the echoes is visible along the horizontal lines, creating a unique resonance pattern for each impedance value horizontally.

4.5 Amplitude variation study based on the acoustic parameters

In the previous subsection, the representation of the time signals relative to intrinsic properties provided valuable insights into the main factors impacting the bonding characterization technique. One observation was the neutrality of the background echoes across various impedance values, indicated by their constant amplitude. On the other hand, the echoes from the bonding layer showed potential for exploitation in the bonding characterization context. In this subsection, the focus remains the same, but the representation is different.

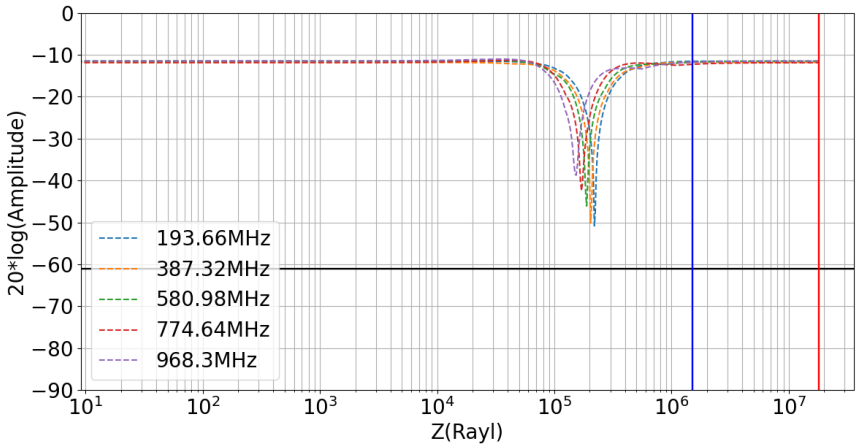

Figure 4.12: Magnitude variation in dB for BE 1

Figure 4.12 presents a new way to display the echoes. In this graph, the X-axis represents the variation in intrinsic properties, while the Y-axis represents the power, or more precisely, the magnitude in dB.

Three lines are drawn in the graph, they are the references that can provide an insight on the limitation of the technique. Two vertical lines are shown, the blue line represents water acoustic impedance and the red the silicon. Nonetheless, it is important to note that all the acoustic impedance values possible are represented in the graph. Besides, it is noticeable that the red line coincides with the last observation made by the model making it the convergence state. Meanwhile, the horizontal line in the graph represents the limitation of the data acquisition system (DAQ) in quantifying the signal, which in turn affects the signal-to-noise ratio (SNR). In the experimental setup, a 10-bit acquisition board is used, resulting in a SNR ratio of 61.2 dB. In consequence, all the signals below this line are impossible to reach with the actual setup.

Figure 4.12 represents the BE 1 echo variation along all the possible acoustic impedance nuance. The pattern of the layer resonance is present in a form of a magnitude drop. The rest of the curve represents a flat line expressing no significant change on the signal amplitude. In consequence, the impact of the BE 1 echo is restrained to a narrower range of acoustic impedance's, as the magnitude variation is limited to specific impedance values around the resonance area where a drop in amplitude is observed.

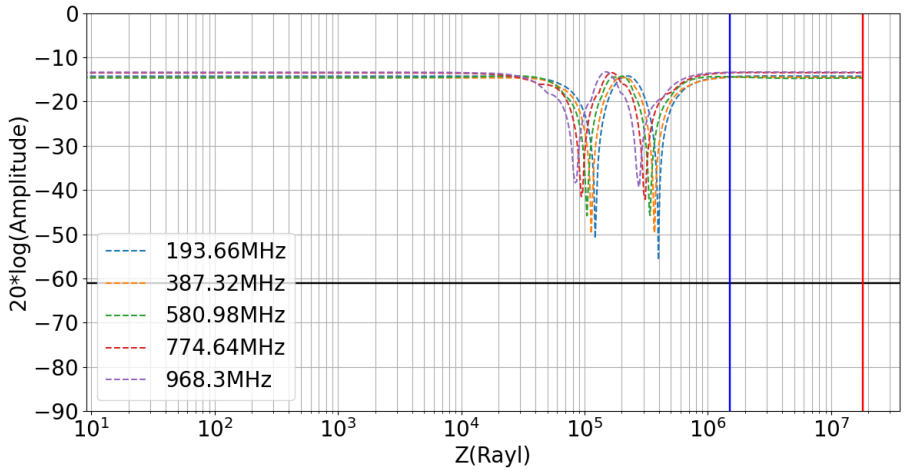

Figure 4.13: Magnitude variation in dB for BE 2

Figure 4.13 generalizes this observation. The flat line is still omnipresent on the pattern of the BE 2 echo. Yet, the phase cancellation drop is occurring twice which expresses the number of interactions the wave had with the sample font. Figure 4.14 is the BE 3 echo behavior regarding the acoustic impedance shift. The flat shape is always predominant which is expected. The main outlook is the lack of information in the BE echoes in order to make a difference in the anti-symmetric peaks shift. The only part where this class of echoes influences the reflection coefficient is at the phase cancellation periods. Furthermore, These phases occur before the water impedance blue line, which makes it clear that these patterns happen at an unbonded stage. These elements lead to the conclusion that using only the BE echoes for the purpose of bonding

energy characterization is challenging, and any attempt to use only them to characterize the bonding is likely to fail. Because, the information resides in the BLE echoes, as the next curves demonstrate.

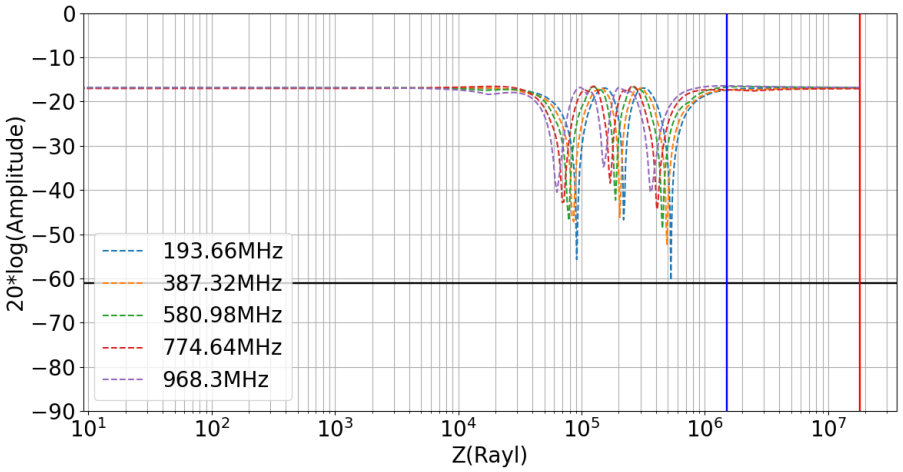

Figure 4.14: Magnitude variation in dB for BE 3

Figure 4.15 describes the amplitude variation of the BLE 1 echo along the different acoustic impedance values. It is worth emphasizing on the magnitude value regarding the water acoustic impedance which is equal to -36.7 dB at 193.66 MHz. The horizontal ADC (Analog-to-digital converter) limitation indicate that some of the magnitude values are impossible to reach with the actual setup. Most of the values are located between the blue and the red vertical lines which very likely represents the interval where the direct bonding nuance may exist.

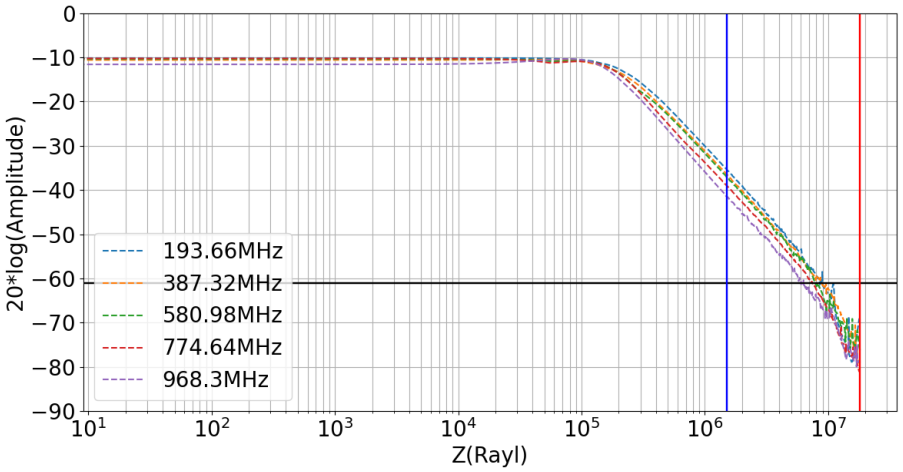

Figure 4.15: Magnitude variation in dB for BLE 1

Otherwise, the graph is composed in two phases. At lower impedance values, the magnitude remains the same. However, this first stage is not worth analyzing as the impedance values are very low. The second phase is represented by a decrease in magnitude values as the acoustic impedance increases. The decrescendo observation on

the BLE 1 echo is the proof that the bonding characterization success is linked to these minuscule signals at the BLE 1 time zone in Figure 4.10. This statement is further reinforced when considering the magnitudes after the blue vertical line, as it provides additional context.

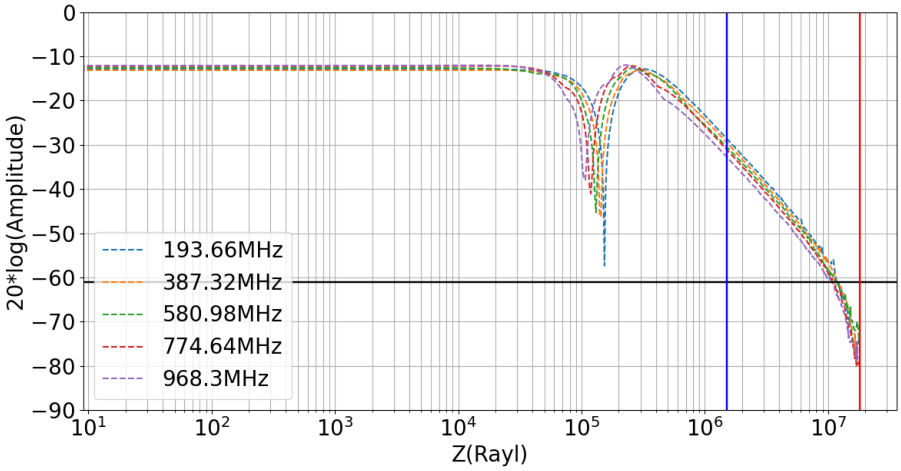

Figure 4.16: Magnitude variation in dB for BLE 2

Figure 4.16 represents the second BLE echo. This group of echoes is characterized by a single phase cancellation pattern, since the wave path interacts with opposite wave flow towards the transducer, resulting in a sever drop in magnitude. The curve overall pattern is now differentiated to three part. The first at lower impedance is the flat part where the magnitude is constant. The second part represents the drop and the third is the decreasing part of the curve. It is worth noticing that the magnitude drop occurs before the water impedance blue line which suggests that such phenomenon is occurring at an unbonded stage.

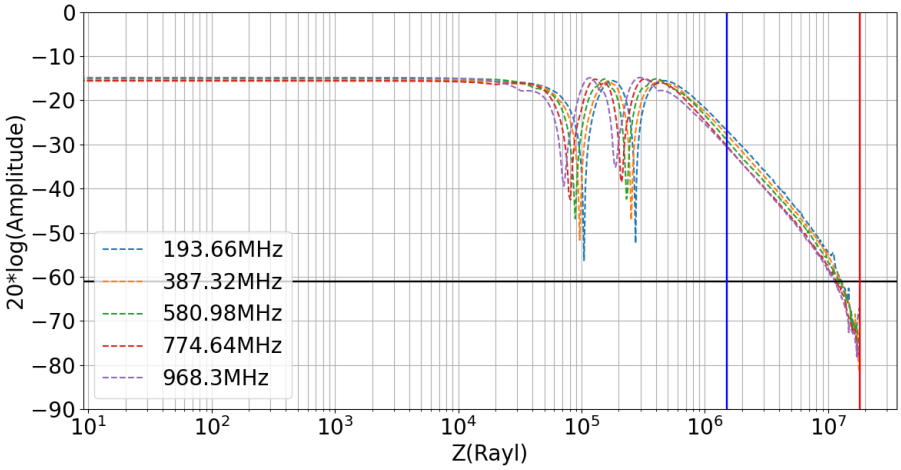

Figure 4.17: Magnitude variation in dB for BLE 3

This analysis joins the experimental results found in Figure 4.8 where the time signal shift is only happening in zone B. This suggests that the pattern observed in the opposite notch area may potentially represent intrinsic properties variations. Figure 4.17 display the BLE 3 echos pattern. The phase cancellation happens twice and always before the blue vertical line representing the water acoustic impedance. This observation validates the previous argument. Finally, the region between the vertical blue and red lines represents the area where the bonding could potentially be responsive. Thus, the inability of the acquisition system on the current setup to ensure the detection of all the echoes in this interval explains the limitation of the technique today. If this barrier is improved by changing the acquisition system, the results could be further improved, and this improvement could be observed in Zone B in further analysis.

4.6 Conclusion

The elements described in chapter 4 prove that the spectroscopy is the right technique to characterize the bonding energy. Firstly, The opposite notch area represent an interesting insight on the anti symmetric peaks shift, which emphasizes for the first time on a true reflection coefficient variation. It is observed that the opposite notch area contains three distinct zones. The first zone represents the unbonded region, labeled as Zone A. The second zone corresponds to a sharp drop in the Δf variation (Zone B). Finally, there is a third zone where the Δf variation remains stable and proportional to a fully bonded structure (Zone C) (Figure 4.2), it is concluded that Zone B was the right area to study in order to detect any bonding energy variation, since it is the only zone where the anti-symmetric peaks shifted relatively to the bonding layer anatomy. Furthermore, this variation was related to two main elements that could potentially impact the reflection coefficient, which are the intrinsic properties of the bonding layer and its thickness. Based on the results obtain in Figure 4.5, it is hard to conclude whether the variation came from the intrinsic properties or the thickness. An hypothesis suggests that the variation of the slope could potentially be the distinctive pattern between these two potential sources of the anti-symmetric peaks variation. Next, Zone B length was a subject of interrogation since no observation correlated with the crack length proposed by the DCB test was found.

The time signal analysis is another factor to consider in order to understand the reflection coefficient behavior. Figure 4.7 represent a time signal evolution at the opposite notch. The separated zones observed on the Δf variation curve are also present at the time signal. Elements such the time of flight and attenuation which are unique to the time axis are preserved. Yet, the variation along the opposite notch area which is represented by the distance in the Y-axis, shows the impact of zone B on the time signal. The reflection coefficient also displays this rapid transition at zone B in Figure 4.9.

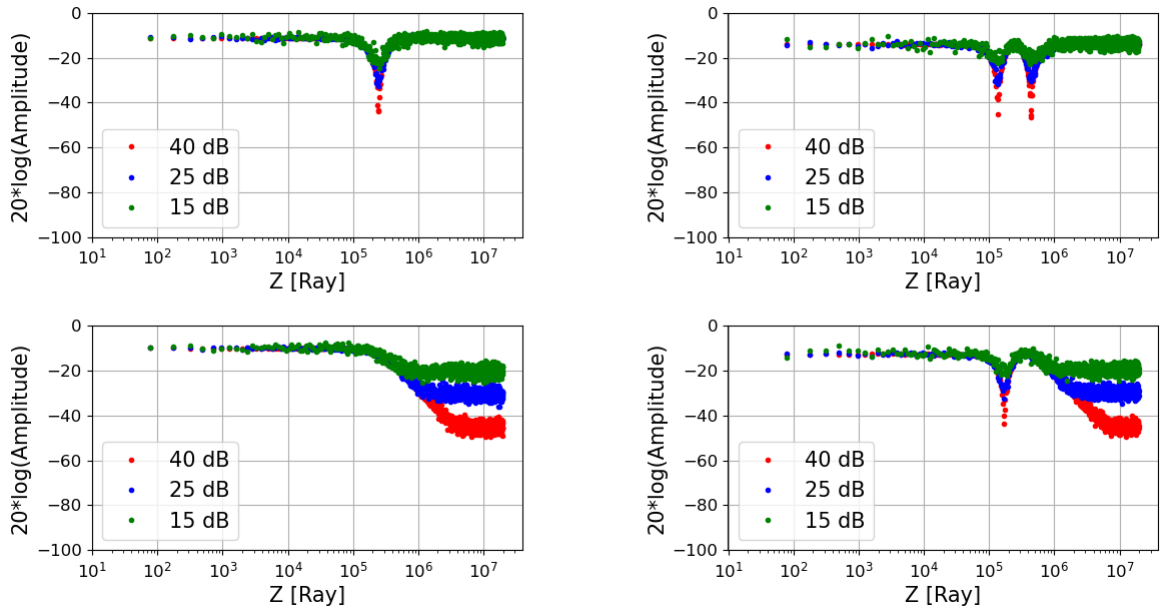

Figure 4.18: Magnitude variation of noised BE and BLE (Green : 15 dB SNR - Blue : 25 dB SNR - Red : 40 dB SNR)

Figure 4.18 displays the true evidence that the actual setup is not matching the physics of the bonding characterization technique. In the experimental setup, the SNR ratio is equal to 25 dB which limit the BLE echoes at -37 dB of magnitude. The SNR ratio distorts the amplitude of both BE and BLE which limits the number of time signal nuance possible. Figure 4.18 demonstrate that a higher SNR ratio is recommended to reach higher impedances, which are correlated with lower amplitude values. This observation can also be seen when comparing Figure 4.11 and Figure 4.7. In the experimental results, the ambient noise value is represented in sky blue, while the theoretical ambient noise is shown in light green. This difference indicates that the theoretical setup can reach a magnitude of -80 dB, whereas the experimental setup can only achieve -40 dB. This is truly the fact that hold the bonding characterization technique to be effective today.

On the whole, the capability of the bonding characterization technique to detect and analyze minuscule signals, such as the decrescendo pattern observed in the BLE echoes, is what makes it an effective and valuable tool in the field of materials analysis and bonding characterization. This sensitivity to subtle variations in the acoustic wave response allows to gain valuable insights on the intrinsic properties of the bonding layer. With the ability to detect and analyze such delicate signals, the technique becomes a powerful asset in understanding and optimizing bonding procedures in various applications.

General Conclusion

At last, this work provides immense information on the interaction af an high frequency wave with a multi-layer structure. The study presented today put the spotlight on the bonding characterization technique and its potential to nuance bonding layers with different acoustic impedance's. Each chapter tackled an unique aspects of the technique, providing valuable outlook into its feasibility, sensitivity, and limitations.

chapter 2 focused on the theoretical aspects of the technique and its applicability to hydrophilic and hydrophobic samples. The time signal and reflection coefficient outputs were analyzed for different bonding states. The observation of symmetrical and anti-symmetrical peaks provided important information on the bonding energy and layer properties. The study highlighted the impact of bandwidth, thickness, incident wave angle, and intrinsic properties on the sensitivity of the technique. The results demonstrated the potential of the technique to distinguish between different bonding shades and the importance of selecting appropriate parameters such as frequency and angle in order to achieve accurate measurements.

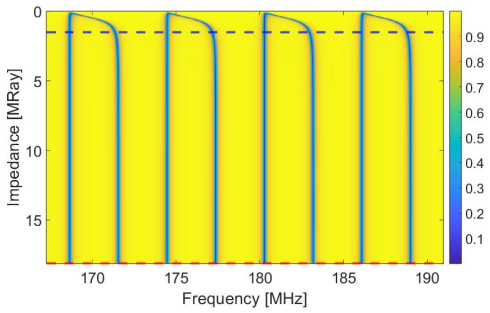

(a) R at 193 MHz

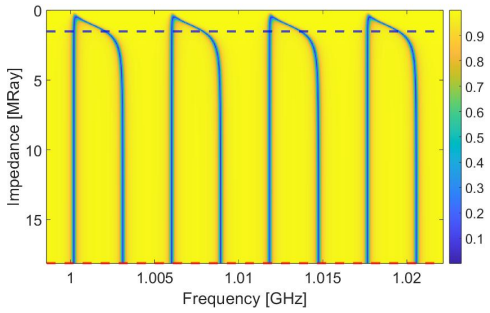

(b) R at 1 GHz

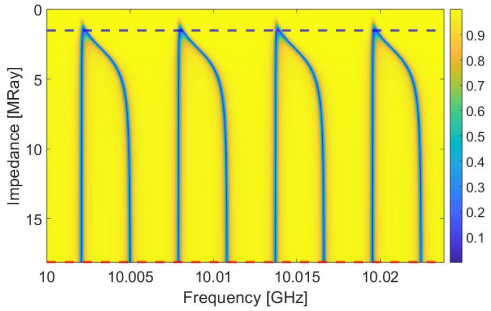

(c) R at 10 GHz

Figure 4.19: Reflection coefficient for three different frequencies

Figure 4.19 summarizes this perspective by illustrating how the reflection coefficient can be influenced by the frequency used in the analysis. This curve highlights the limited capability of the reflection coefficient to distinguish between different impedances. Even at 10 GHz, which is not a realistic frequency, the differentiation of impedances is not substantial, as the curve saturates around 10 MRy. This suggests that relying only on the variation of anti-symmetrical peaks is not a suitable approach for characterizing the bonding energy, considering the reflection coefficient limited ability to nuance between samples, and knowing that most of the information is condensed at higher impedances.

Next, chapter 3 presented the experimental attempts to replicate the observations seen in chapter 2. The room temperature (RT) samples showed distinguishable and reliable results. Hence, the overall sensitivity curve for the other samples did not match the experimental expectations based on the previous research [1]. The experiments highlighted the challenges in obtaining precise measurements, especially with limited SNR ratios. This quote is validate by the noise study, which emphasizes the influence of the SNR ratio and the number of background echoes on the measurement quality. Despite the efforts made to improve the setup, the results suggested that the technique's effectiveness is impacted by its ability to detect and analyze minuscule time signals. Figure 4.20 presents the first real-time signal representing an RT sample, where a BLE2 echo is clearly visible. This signal was captured in the center of the sample, highlighting that with the appropriate SNR ratio and acquisition system setup, it is possible to distinguish the signals coming from different samples.

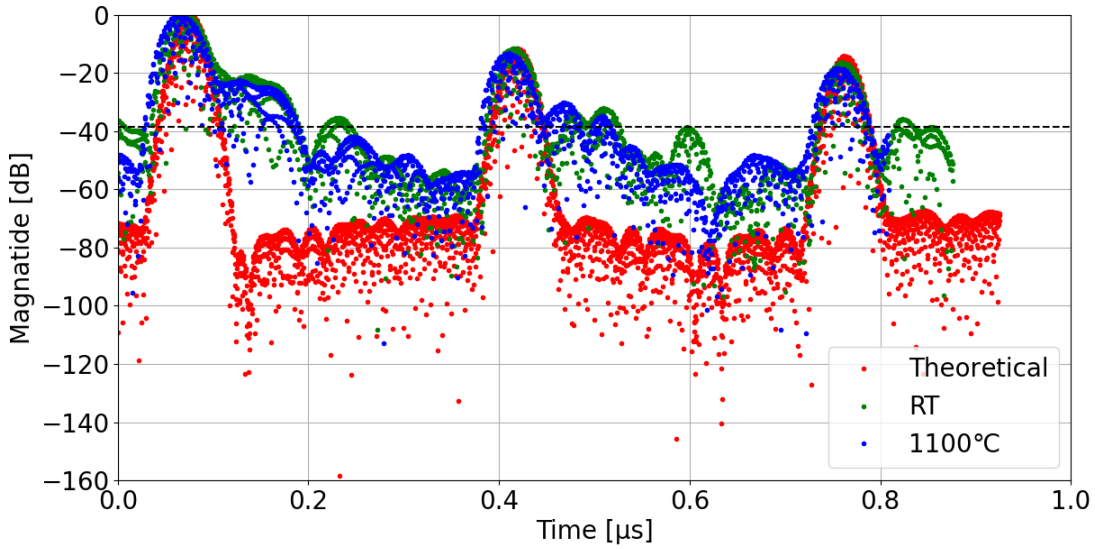

Figure 4.20: Time signal comparison of two experimental [RT - 1100°C] and a theoretical results emphasizing on the difference between the two extreme samples

By looking further and using Figure 4.21, the magnitude found in Figure 4.20 can be linked to an acoustic impedance value, giving a methodology of how the bonding characterization technique could be effectively applied. The time signal approach is more interesting because in order to obtain a useful unsaturated reflection coefficient pattern, the frequency should be very high. Yet, if we could obtain the time signal BLE echoes

with the right tools, which are a big number of background echoes and a higher SNR ratio, the frequency would not matter and the analysis would be based on their magnitude.

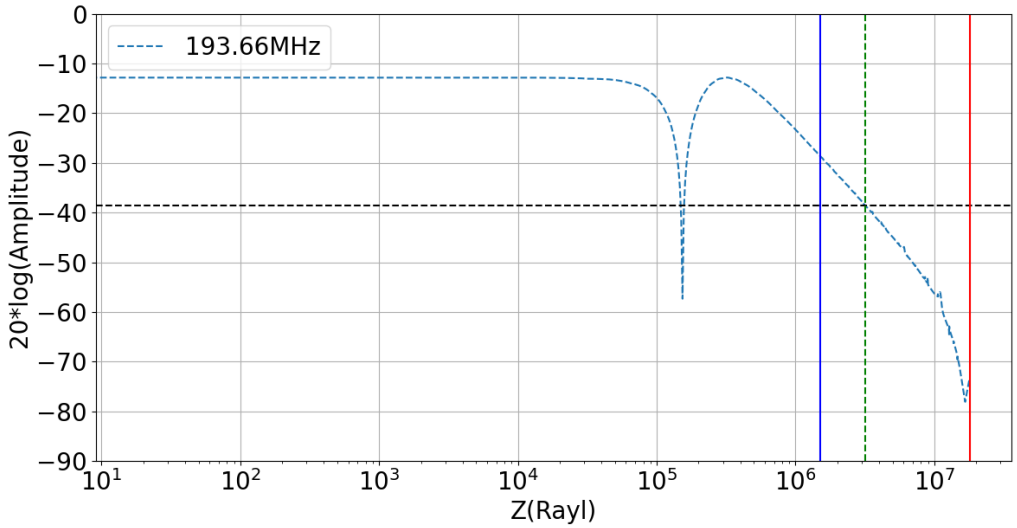

Figure 4.21: RT time signal BLE 2 magnitude related to it acoustic impedance

In chapter 4, further information on the time signal behavior and it paralleled reflection coefficient counterpart were provided. The opposite notch area analysis revealed distinct zones that emphasized the impact of the bonding layer anatomy and intrinsic properties on the anti-symmetric peaks shift.

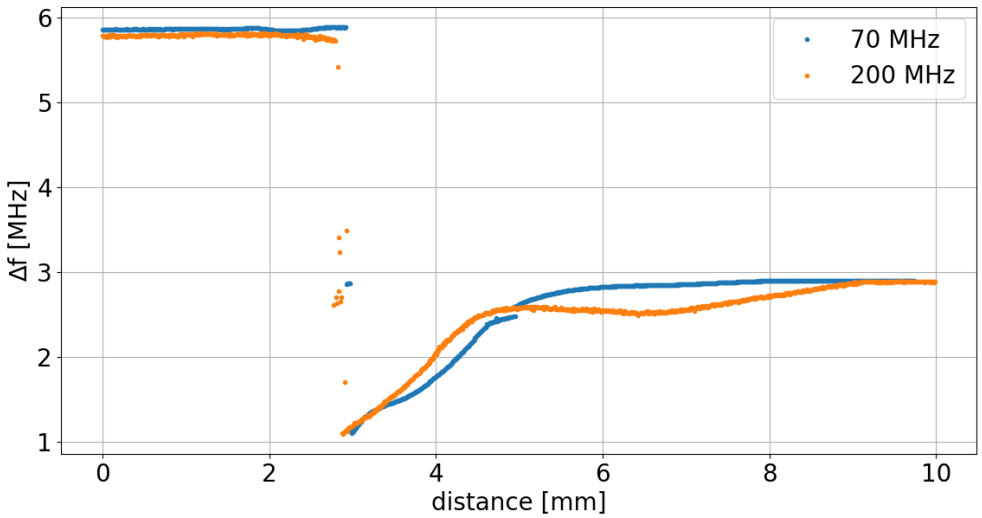

Figure 4.22: Δf variation at 200 MHz and 70 MHz for the same area

Figure 4.22 shows two different measurements of the same opposite notch area, using two different frequencies. These results validate the previously established statement, indicating that the two slopes correspond to two distinct variations originating from the

intrinsic properties and the thickness of the bonding layer. The 200 MHz measurement shows more detailed information at a longer interval, while the 70 MHz measurement represents a saturated curve at the same spot. This suggest that the first part represented by the first slope and which the two frequencies produced the same outcome is related to the thickness variation, where the second interval is related to the intrinsic properties of the material since a higher frequency show a wider interval of variation. It's important to note that these measurements are less repeatable, but they are mentioned here to propose a potential avenue for comprehending the reflection coefficient variations in the opposite notch area.

In chapter 4, the theoretical time signal analysis exposed new features on the link between the bonding layer acoustic impedance and the time signal resonance. The observation of phase cancellation periods was particularly intriguing, although their influence on the measurement is constrained due to their association with lower values of acoustic impedance. On the other hand, The BLE echoes show a tremendous potential based on the decrescendo pattern seen in the results. These category of echoes is proven to be the most suitable to any calibrated and precise measurement.

Lastly, Figure 4.23, Figure 4.24, Figure 4.25 represent the time signal behavior according to the acoustic impedance variation of 10 nm, 20 nm and 40 nm bonding layer respectively. This result is the essence of this thesis since it shows the behavior of the acoustic wave in a multi-layer stack featuring a nanometric bonding layer. Again, it is important to note that the Y-axis should not be confused with the time axis. Each point on the Y-axis corresponds to the acoustic impedance value, and the amplitude variations within each vertical bar represent the response at that impedance. The vertical pattern of phase cancellation is not a variation over time, but rather a response of the layer's at each stage. The resonance pattern of all the echoes is visible along the horizontal lines, creating a unique resonance pattern for each impedance value horizontally.

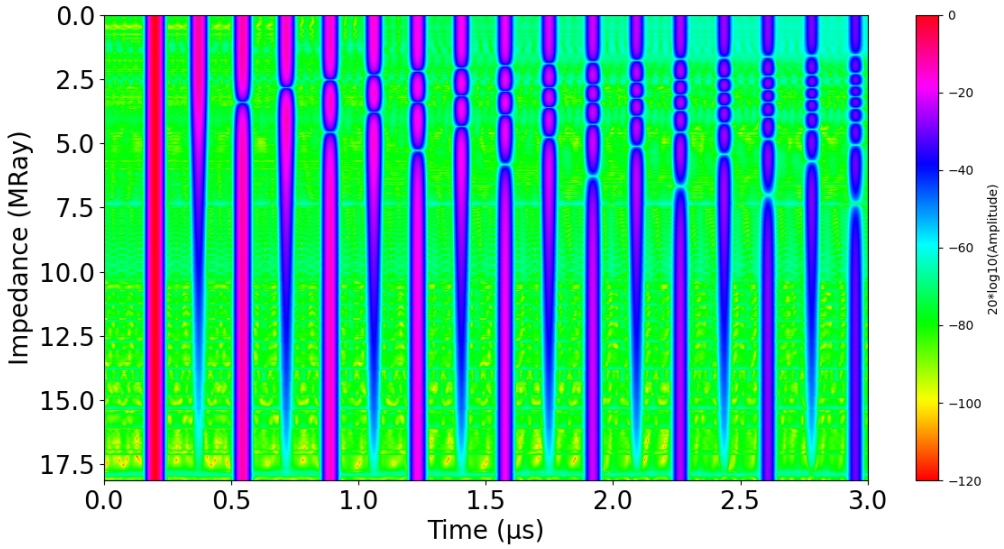

Figure 4.23: Time signal behavior relative to the acoustic impedance variation of the 10 nm SI//SI bonding layer

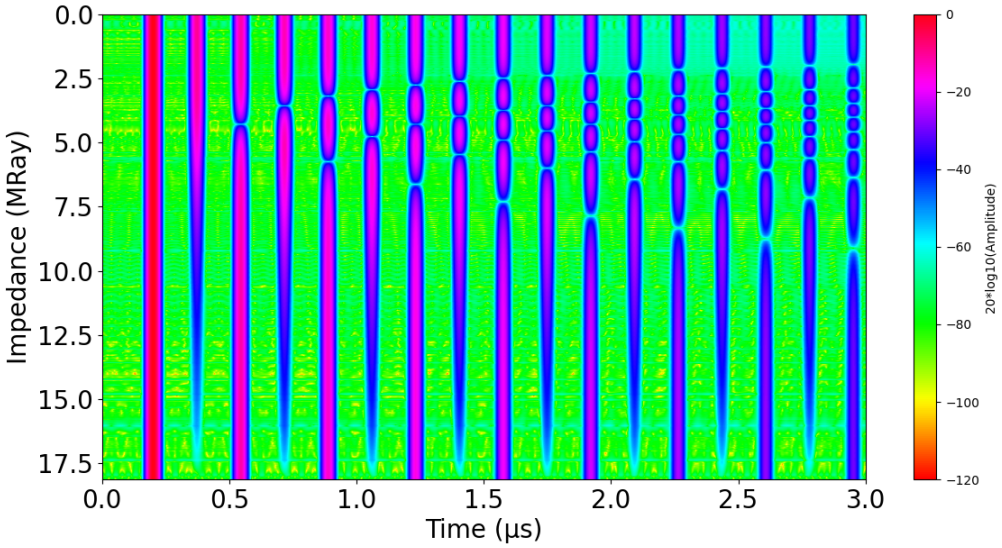

Figure 4.24: Time signal behavior relative to the acoustic impedance variation of the 20 nm SI//SI bonding layer

The primary distinction among the three curves lies in the extension of the resonance pattern corresponding to the thickness of the bonding layer. A thicker layer results in a more elongated pattern. The most insightful notion when scrutinizing these graphs is that, given the nanometric dimensions of the bonding layer, no alterations in time of flight are observed. However, the remarkable observation is the alteration in the overall resonance pattern of the time signal, which in turn affects the pattern's appearance based on impedance variations. This empirical observation summarizes the behavior of a high frequency acoustic wave interaction with a multi-layer structure containing a nanometric bonding layer.

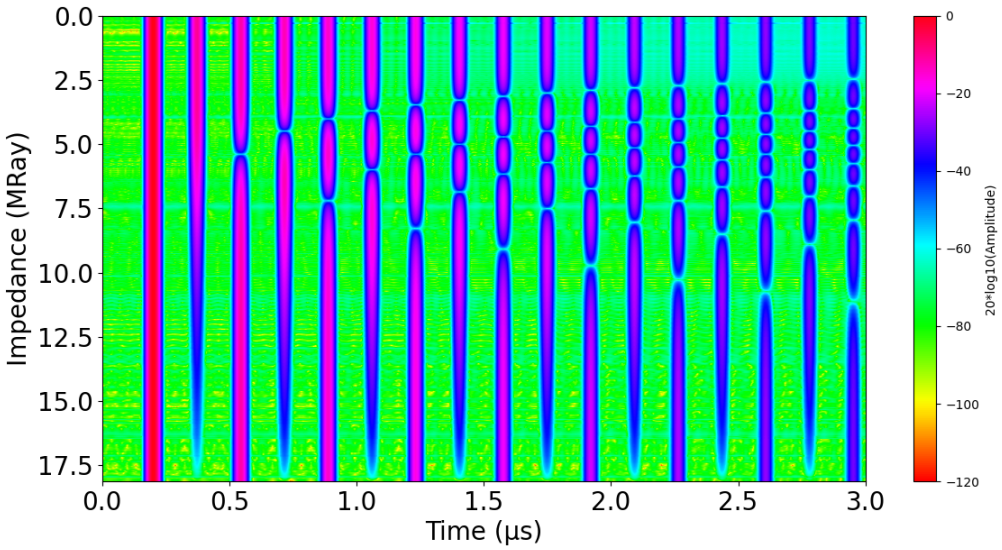

Figure 4.25: Time signal behavior relative to the acoustic impedance variation of the 40 nm SI//SI bonding layer

Figure 4.26 shows the time signal when both the impedance and the thickness of the bonding layer vary simultaneously. In this example, a starting thickness of 20 nm is used, with the layer thickness gradually decreasing to 0 nm at the final declared impedance relative to silicon. Comparing this curve to Figure 4.24 underscores how the reduction in thickness, alongside an increase in the impedance of the bonding layer, affects the behavior of the time signal.

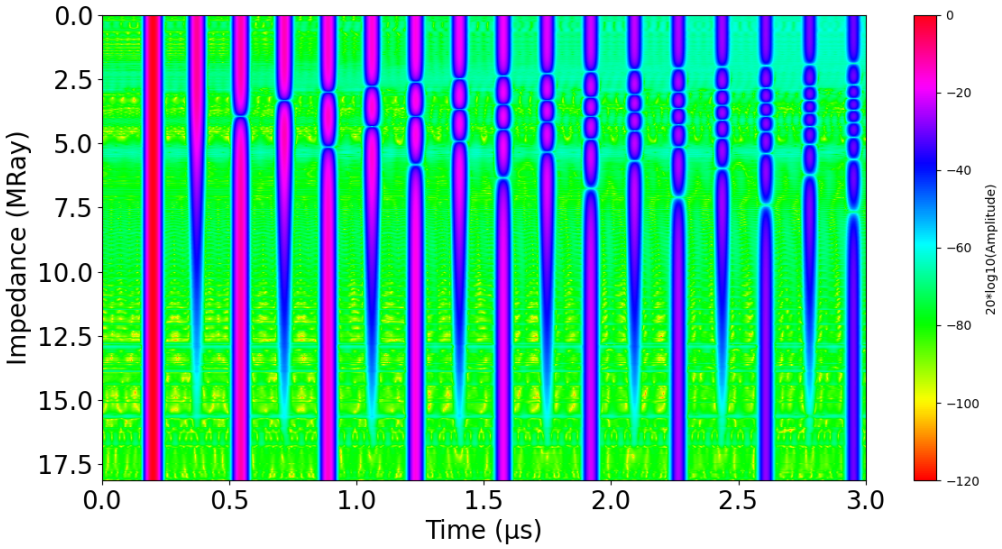

Figure 4.26: Time signal behavior relative to a simultaneous variation of the acoustic impedance [0 MRay,18 MRay] and the thikness [20 nm, 0 nm] of an SI//SI bonding layer

In conclusion, the bonding characterization technique has shown great promise as a powerful tool for materials analysis and bonding characterization. It has the potential to provide valuable insights into the intrinsic properties of bonding layers. However, the technique's effectiveness is highly dependent on factors such as SNR ratios and frequency range. Future improvements in experimental setups and data processing techniques may further enhance the technique's capabilities and broaden its applications in the field of materials science and engineering.

Appendix A

Amplitude variation based on the thickness of an semi infinite plate

A. Iklil and E. Le Clezio

The degree of difficulty in characterizing the bonding energy lies in the thickness (e) of the bonding layer, which is only few nanometers. The wavelength (λ) associated with an ultrasonic wave with a frequency of 200 MHz propagating in silicon (V_l = 8433 m/s) is 420 nm. Considering that ultrasonic waves interact with objects the size of their wavelengths, the amplitude of the echo generated by the bonding interface is generally too small to be extracted from the signals.

For a theoretical medium consisting of water interface, silicon, and silicon oxide (Figure A.1), it is observed that the surface wave depends on the reflection coefficient of the first Water/Si interface ($R_{H2O/Si}$). Meanwhile, the acoustic wave originating from the silicon oxide interface undergoes three impedance changes. Firstly, there is a Water/Si transmission ($T_{H2O/Si}$), followed by a Si/SiO2 reflection ($R_{Si/SiO2}$), and finally, a Si/Water transmission ($T_{Si/H2O}$). The interface echo amplitudes of an semi-infinite three-layer medium can be expressed in decibels (dB) as follows:

$$A_{\mathrm{H2O/Si}} = 20 \cdot \log\left(R_{\mathrm{H2O/Si}}\right) = -1.3\,\mathrm{dB} \tag{A.1}$$

$$A_{\mathrm{Si/SiO2}} = 20 \cdot \log\left(T_{\mathrm{H2O/Si}} \cdot R_{\mathrm{Si/SiO2}} \cdot T_{\mathrm{Si/H2O}}\right) = -24.82\,\mathrm{dB} \tag{A.2}$$

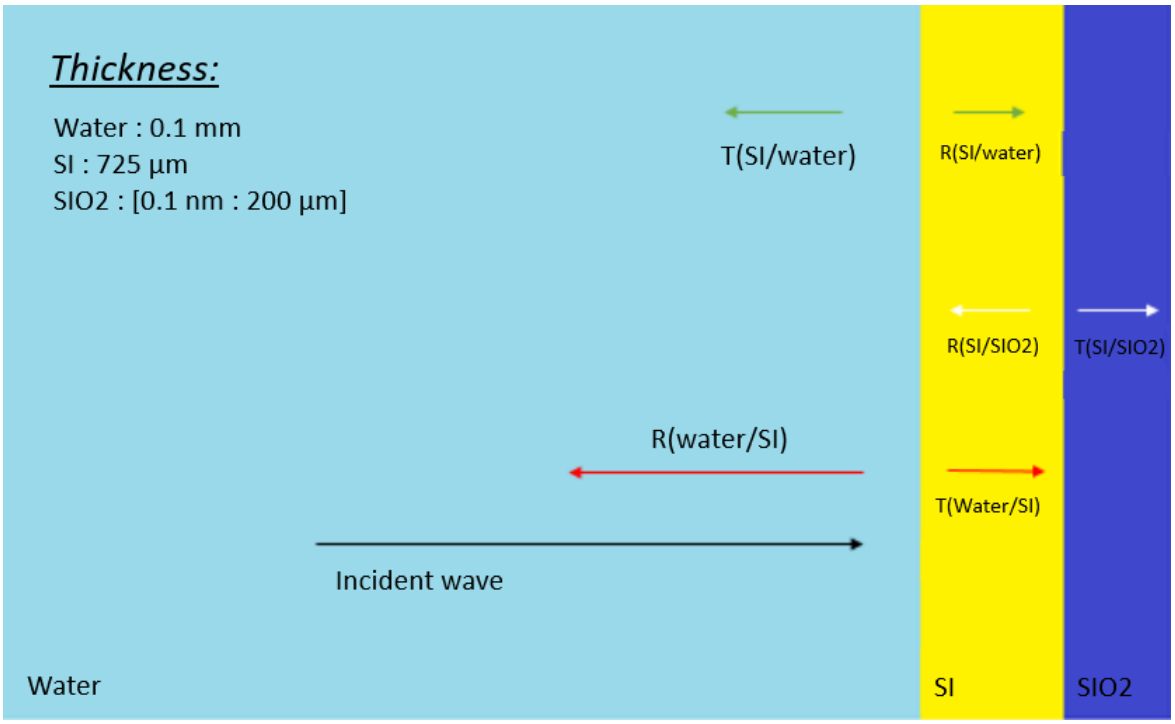

Figure A.1: Schematic diagram of reflection and transmission of the propagation of an ultrasonic wave in a theoretical three-layer made up of a layer of water, silicon and a semi-infinite medium of silicon oxide.

The analytical model described in Appendix B allows the representation of amplitude fluctuations relative to the thickness variation (Thickness interval: [0.1 nm : 200 µm]) of the semi infinite oxide layer. In the case of this simulation, the result is dependent to wavelength, the curve in Figure A.2 is presented as a function of the

thickness to wavelength ratio, making it applicable to all frequencies. To calculate the amplitude ratio in decibels (dB) on the Y-axis, the amplitude of the interaction with the silicon oxide layer is compared to the reference amplitude obtained from the surface echo reflected by the silicon yellow layer .

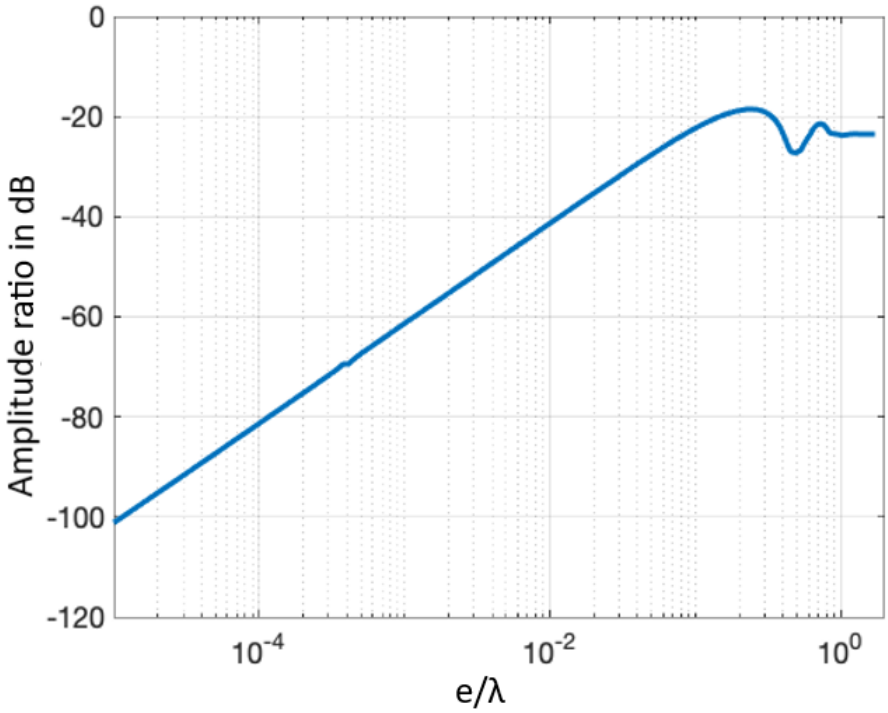

Figure A.2: Numerical evolution of the comparison between the surface echo of the silicon layer and the echo reflected by the oxide surface as a function of the thickness wavelength ratio

The results of these simulations exhibit three distinct zones. The stable zone corresponds to the area where the material is semi-infinite around -24 dB, which aligns with the theoretical value (A.2). The oscillation zone is the second zone around the wavelength and the decay zone, which indicate amplitude reduction when the thickness is much smaller than the wavelength.

Appendix B

Transmission and reflection of ultrasonic waves in layered media

D. L. Folds and C. D. Loggin

In this model, a plane acoustic wave is assumed to enter in contact with the multilayers materials as shown in Figure 2.1. In our case, the reflection coefficient is at the core of the Δf variations. The model proposed by D.L. Folds and C.D. Loggins suits perfectly for wave propagation through a stack of wafers. It started with a plane wave originating from the bottom layer and proceeds through each layer until it emerges through the first layer. It propagates along the z axis making the last layer semi-infinite. The infinite character of the x and y axis with the incident angle of the waves lies into xz plane making the problem two dimensional (Figure 2.1). When a plane wave arrives to a layer boundary at an angle θ, normal stress and shear stress are induced in the layer giving birth to normal particle velocity and tangential particle velocity. The continuity of these parameters is ensured by the boundary conditions in each layer since for a harmonic wave the particle velocity is given by $v = i\omega u$. Thus displacement (u) continuity is similar to the particle velocities (v) continuity.

The model calculates the reflection and transmission coefficients based on the velocities and stresses in layers. Thus, the velocities and stresses can be expressed in any layer by the following potential functions:

$$\phi_l = [A_l \exp(i\alpha_l z) + B_l \exp(-i\alpha_l z)] \exp[(i(\sigma x - \omega t))], \tag{B.1}$$

$$\Psi_l = [C_l \exp(i\beta_l z) + D_l \exp(-i\beta_l z)] \exp[(i(\sigma x - \omega t))], \tag{B.2}$$

where $\beta_l = (K_l^2 - \sigma^2)^{1/2}$, $\alpha_l = (k_l^2 - \sigma^2)^{1/2}$ and $\sigma = k_l \sin\theta_l$. The function ϕ_l, is the potential function for longitudinal waves and Ψ_l is the potential function for transverse waves. The quantity ρ_n is the density of the material of the layer n, ω is related to the signal frequency, and σ is the component of the wave vector, such as:

$$\sigma = k_1 \sin\theta_1 = k_2 \sin\theta_2 = \cdots = k_{n+1} \sin\theta_{n+1} \tag{B.3}$$

where θ_i are the incidence angles. The quantities k and K are given by:

$$K_n = \frac{\omega}{b_n} \qquad \text{and} \quad k_n = \frac{\omega}{c_n}$$

where b_n is the complex transverse velocity and c_n is the complex longitudinal velocity.

Let's introduce the velocities and stresses expressions at any point inside or on the boundaries of layer l:

$$v_x^{(l)} = \frac{\partial \phi_l}{\partial x} - \frac{\partial \psi_l}{\partial z}, \tag{B.4}$$

$$v_z^{(l)} = \frac{\partial \phi_l}{\partial x} + \frac{\partial \psi_l}{\partial z}, \tag{B.5}$$

$$Z_z^{(l)} = i[\lambda(\frac{\partial v_x^{(l)}}{\partial x}) + (\frac{\partial v_z^{(l)}}{\partial z}) + 2\mu(\frac{\partial v_z^{(l)}}{\partial z})]/\omega, \tag{B.6}$$

$$Z_x^{(l)} = i\mu[(\frac{\partial v_x^{(l)}}{\partial z}) + (\frac{\partial v_z^{(l)}}{\partial x})]/\omega, \tag{B.7}$$

where λ and μ represent the bulk and shear moduli.

The velocities and stresses at the uppermost interface are obtained by substituting B.5 and B.4 into B.6 and B.7 and using $l = n$, $z = d_n$. This yields to:

$$\begin{bmatrix} v_x^{(n)} \\ v_z^{(n)} \\ Z_z^{(n)} \\ Z_x^{(n)} \end{bmatrix} = \begin{bmatrix} i\sigma\cos P_n & -\sigma\sin P_n & -i\beta_n\cos Q_n & \beta_n\sin Q_n \\ -\alpha_n\sin P_n & i\alpha_n\cos P_n & -\sigma\sin Q_n & i\sigma\cos Q_n \\ -ie_n\cos P_n & e_n\sin P_n & -ig_n\beta_n\cos Q_n & g_n\beta_n\sin Q_n \\ g_n\alpha_n\sin P_n & -ig_n\alpha_n\cos P_n & -e_n\sin Q_n & ie_n\cos Q_n \end{bmatrix} \begin{bmatrix} A_n + B_n \\ A_n - B_n \\ C_n - D_n \\ C_n + D_n \end{bmatrix} \tag{B.8}$$

where $P_n = \alpha_n d_n$, $Q_n = \beta d_n$, $g_n = 2\mu_n\sigma/\omega$ and $e_n = (\lambda_n k_n^2 + 2\mu_n\alpha_n^2)/\omega$.

Next, the velocities and stresses inside the second interface are given by:

$$\begin{bmatrix} v_x^{(n-1)} \\ v_z^{(n-1)} \\ Z_z^{(n-1)} \\ Z_x^{(n-1)} \end{bmatrix} = \begin{bmatrix} i\sigma & 0 & -i\beta_n & 0 \\ 0 & i\alpha_n & 0 & i\sigma \\ -ie_n & 0 & -ig_n\beta_n & 0 \\ 0 & -ig_n\alpha_n & 0 & ie_n \end{bmatrix} \begin{bmatrix} A_n + B_n \\ A_n - B_n \\ C_n - D_n \\ C_n + D_n \end{bmatrix} = L_2 \begin{bmatrix} A_n + B_n \\ A_n - B_n \\ C_n - D_n \\ C_n + D_n \end{bmatrix} \tag{B.9}$$

These values were obtained by substituting z =0 and l =n in B.4 and B.7.

By resolving the matrix of amplitude coefficients and substituting in B.8 yields:

$$\begin{bmatrix} v_x^{(n)} \\ v_z^{(n)} \\ Z_z^{(n)} \\ Z_x^{(n)} \end{bmatrix} = L_1 L_2^{-1} \begin{bmatrix} v_x^{(n-1)} \\ v_z^{(n-1)} \\ Z_z^{(n-1)} \\ Z_x^{(n-1)} \end{bmatrix} = \begin{bmatrix} a_{11}^n & a_{12}^n & a_{13}^n & a_{14}^n \\ a_{21}^n & a_{22}^n & a_{23}^n & a_{24}^n \\ a_{31}^n & a_{32}^n & a_{33}^n & a_{34}^n \\ a_{41}^n & a_{42}^n & a_{43}^n & a_{44}^n \end{bmatrix} \begin{bmatrix} v_x^{(n-1)} \\ v_z^{(n-1)} \\ Z_z^{(n-1)} \\ Z_x^{(n-1)} \end{bmatrix} \tag{B.10}$$

The coefficients a_{ij}^n in B.27 are given below:

$$a_{11}^n = G_n \cos P_n + (1 - G_n) \cos Q_n, \tag{B.11}$$

$$a_{12}^n = i \left[\frac{(1 - G_n) \sin P_n}{E_n} \right] - iF_n G_n \sin Q_n, \tag{B.12}$$

$$a_{13}^n = -\frac{1}{H_n} (\cos P_n - \cos Q_n), \tag{B.13}$$

$$a_{14}^n = -\frac{i}{H_n} \left[\frac{\sin P_n}{E_n} + F_n \sin Q_n \right], \tag{B.14}$$

$$a_{21}^n = iE_n G_n \sin P_n - i \left[\frac{(1 - G_n) \sin Q_n}{F_n} \right], \tag{B.15}$$

$$a_{22}^n = (1 - G_n) \cos P_n + G_n \cos Q_n, \tag{B.16}$$

$$a_{23}^n = -\frac{i}{H_n} \left(E_n \sin P_n + \frac{\sin Q_n}{F_n} \right), \tag{B.17}$$

$$a_{24}^n = a_{13}(n), \tag{B.18}$$

$$a_{31}^n = -H_n G_n (1 - G_n) (\cos P_n - \cos Q_n), \tag{B.19}$$

$$a_{32}^n = -iH_n \left[\frac{(1 - G_n)^2 \sin P_n}{E_n} + F_n G_n^2 \sin Q_n \right], \tag{B.20}$$

$$a_{33}^n = a_{22}(n), \tag{B.21}$$

$$a_{34}^n = a_{12}(n), \tag{B.22}$$

$$a_{41}^n = -iH_n \left[E_n G_n^2 \sin P_n + \frac{(1 - G_n)^2 \sin Q_n}{F_n} \right], \tag{B.23}$$

$$a_{42}^n = a_{31}(n), \tag{B.24}$$

$$a_{43}^n = a_{21}(n), \tag{B.25}$$

$$a_{44}^n = a_{11}(n). \tag{B.26}$$

where $C_n = [a_{ij}^n]$ representing the elementary transfer matrix of a layer.

The application of the boundary condition at z=0 equates the velocities and stresses in layer n with those in layer n-1 at the interface. By repeating the same process for each n-1 layers between layers n+1 and 1, the global transfer matrix [C] of the structure can be obtained from the product of all elementary transfer matrices $[C_i]$ of each layer:

$$\begin{bmatrix} v_x^{(n)} \\ v_z^{(n)} \\ Z_z^{(n)} \\ Z_x^{(n)} \end{bmatrix} = C_n C_{n-1} \ldots . C_2 \begin{bmatrix} v_x^{(1)} \\ v_z^{(1)} \\ Z_z^{(1)} \\ Z_x^{(1)} \end{bmatrix} = \begin{bmatrix} A_{11}^n & A_{12}^n & A_{13}^n & A_{14}^n \\ A_{21}^n & A_{22}^n & A_{23}^n & A_{24}^n \\ A_{31}^n & A_{32}^n & A_{33}^n & A_{34}^n \\ A_{41}^n & A_{42}^n & A_{43}^n & A_{44}^n \end{bmatrix} \begin{bmatrix} v_x^{(1)} \\ v_z^{(1)} \\ Z_z^{(1)} \\ Z_x^{(1)} \end{bmatrix} \tag{B.27}$$

In the experimental work, both layers n+1 and 1 were water, so that $Z_x^n = Z_x^1 = 0$, since the shear stress is zero for liquids. But from B.27,

$$Z_x^n = A_{41} v_x^1 + A_{42} v_z^1 + A_{43} Z_z^1 + A_{44} Z_x^1, \tag{B.28}$$

and substitution of $Z_x^n = Z_x^1 = 0$ in B.27 gives

$$v_x^1 = -(A_{42}/A_{41}) v_z^1 - -(A_{43}/A_{41}) Z_z^1, \tag{B.29}$$

By using B.29 and knowing that $Z_x^n = Z_x^1 = 0$, v_z^n and Z_z^n can be written solely according to v_z^1 and Z_z^1.

$$v_z^n = M_2 2 v_z^1 + M_2 3 v_z^1, \tag{B.30}$$

$$Z_z^n = M_3 2 v_z^1 + M_3 3 v_z^1, \tag{B.31}$$

where

$$M_{22} = A_{22} - A_{21}A_{42}/A_{41} \tag{B.32}$$
$$M_{23} = A_{23} - A_{21}A_{43}/A_{41} \tag{B.33}$$
$$M_{32} = A_{32} - A_{31}A_{42}/A_{41} \tag{B.34}$$
$$M_{33} = A_{33} - A_{31}A_{43}/A_{41} \tag{B.35}$$
$$\tag{B.36}$$

Reflection and transmission coefficients are expressed according to:

$$T = \sigma_1 B_1/(\sigma_{n+1} B_{n+1}) \tag{B.37}$$

$$R = A_{n+1}/B_{n+1} \tag{B.38}$$

where A and B are the incident and reflected wave amplitudes.

Knowing that $\phi_{n+1} = \phi_1 = 0$, the velocities and stresses expressions can be express as following:

$$v_z^n = i\alpha_{n+1}(A_{n+1} + B_{n+1}), \tag{B.39}$$

$$Z_z^n = -i\rho_{n+1}(A_{n+1} + B_{n+1}), \tag{B.40}$$

with

$$v_z^1 = i\alpha_1 B_1 \tag{B.41}$$

$$Z_z^1 = -i\rho_1 \omega B_1 \tag{B.42}$$

The expression of the reflection and transmission coefficient are found by combining the last equations with B.31 and B.30:

$$T = \frac{2Z_1}{(M_{22} + Z_1 M_{23})Z_{n+1} + M_{32} + Z_1 M_{33}} \tag{B.43}$$

$$R = \frac{M_{32} + Z_1 M_{33} - (M_{22} + Z_1 M_{23})Z_{n+1}}{(M_{22} + Z_1 M_{23})Z_{n+1} + M_{32} + Z_1 M_{33}} \tag{B.44}$$

where $Z_1 = \rho_1\omega/\alpha_1$ and $Z_{n+1} = \rho_{n+1}\omega/\alpha_{n+1}$, are the impedances of layers 1 and n+1, respectively. The output of B.43 and B.44 is displayed in Figure B.1. The layers used for this example are taken from the bonded case at Table 2.1.

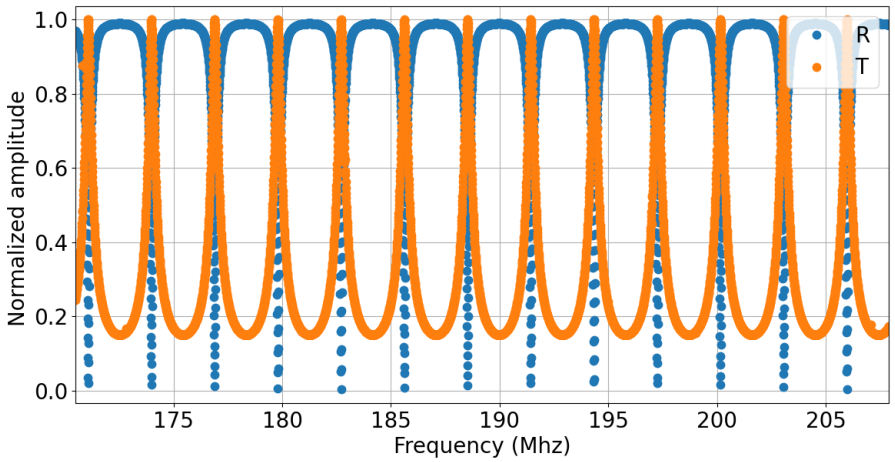

Figure B.1: Reflection and transmission coefficient output based on the analytical model of an bonded SI/SI wafer

Now, The construction of the time signal using the reflection coefficient is possible with an inverse FFT. Yet, In order to adjust the reflection coefficient (R), the frequency response of the impulse is required. The pulsed wave is centered on a nominal frequency. The spectrum of the impulse response is automatically centered at the same frequency. The modulation of the reflection coefficient with the impulse response provides the frequency spectrum of the multi-layer stack response (Figure B.2). Afterward, an inverse FFT provides the time signal relative to the acoustic propagation trough all the stack (Figure 2.2).

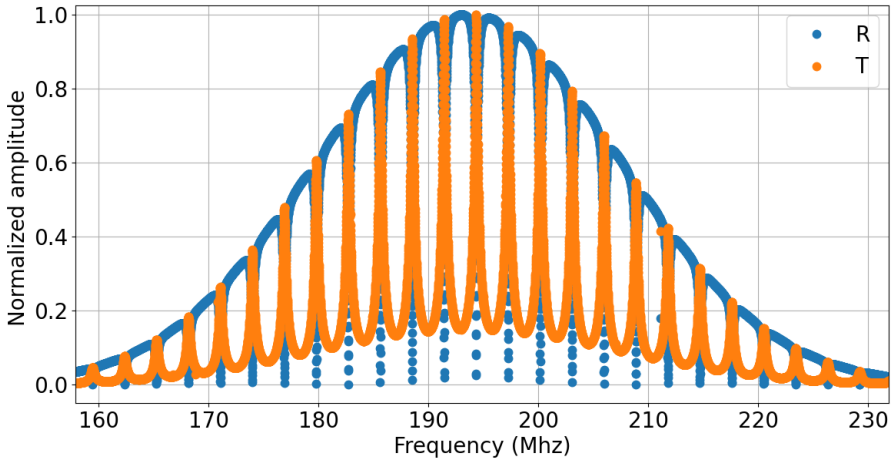

Figure B.2: Modulation of the reflection and transmission coefficient output based on the analytical model of an bonded SI/SI wafer

Appendix C

Experimental report

A. Iklil and G. Despaux

Experience report

Type of experience :Characterization of bonding energy Date:24-10-2022

Manipulator : Amine IKLIL

1.Manipulation parameter

setting	Value or designation
Sample	RT
Transducer	193 MHz
bandwith	[175 MHz,200MHz]
Filtre	Butterworth ordre 3
Gain in dB	25 dB
scan dimension	2cm²
steps_X_axis	20 points
steps_Y_axis	20 points
delta_t	5E-10
delta_f	2G
NFFT	65536 points
Mean signals	400 signals
PRF	1 kHz
number of points	1652points

2.Time signal

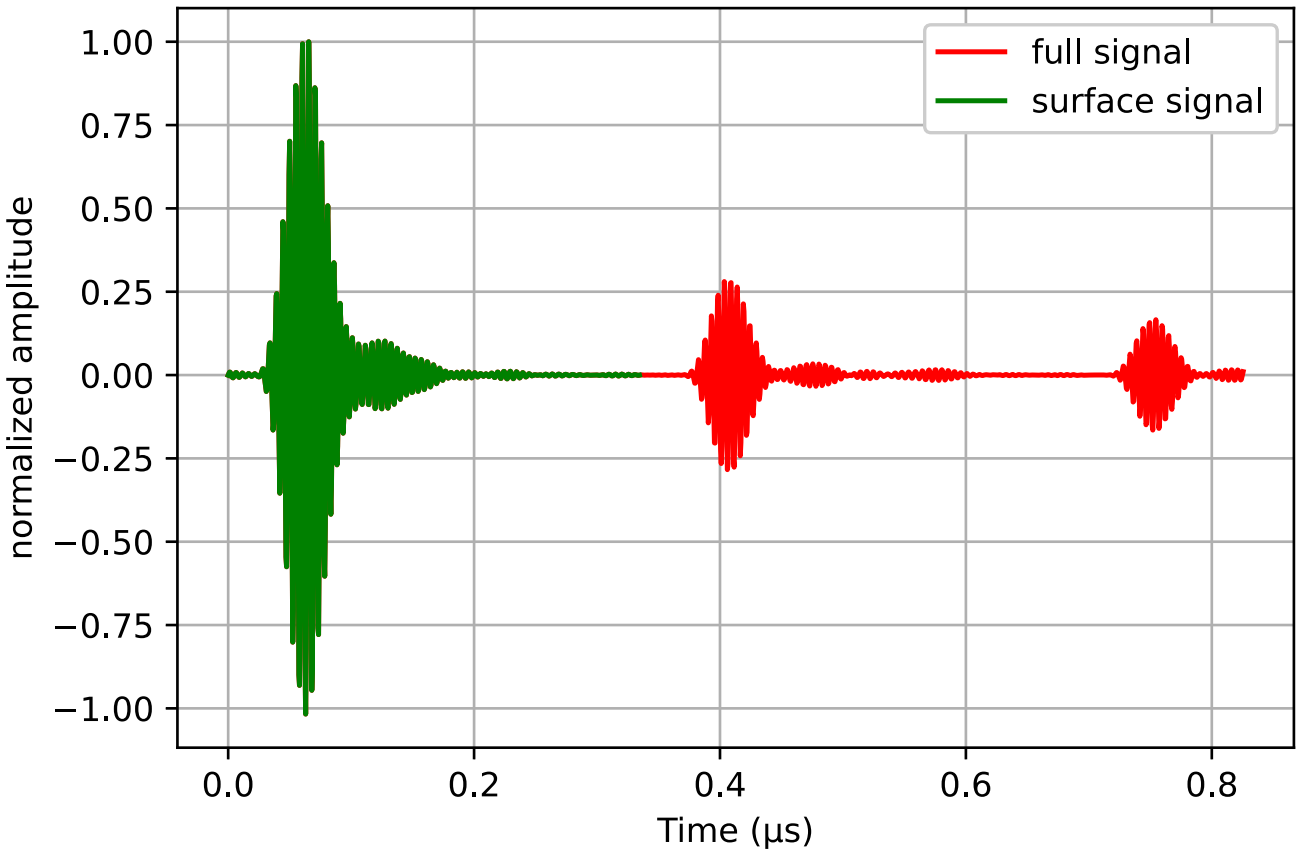

3.FFT

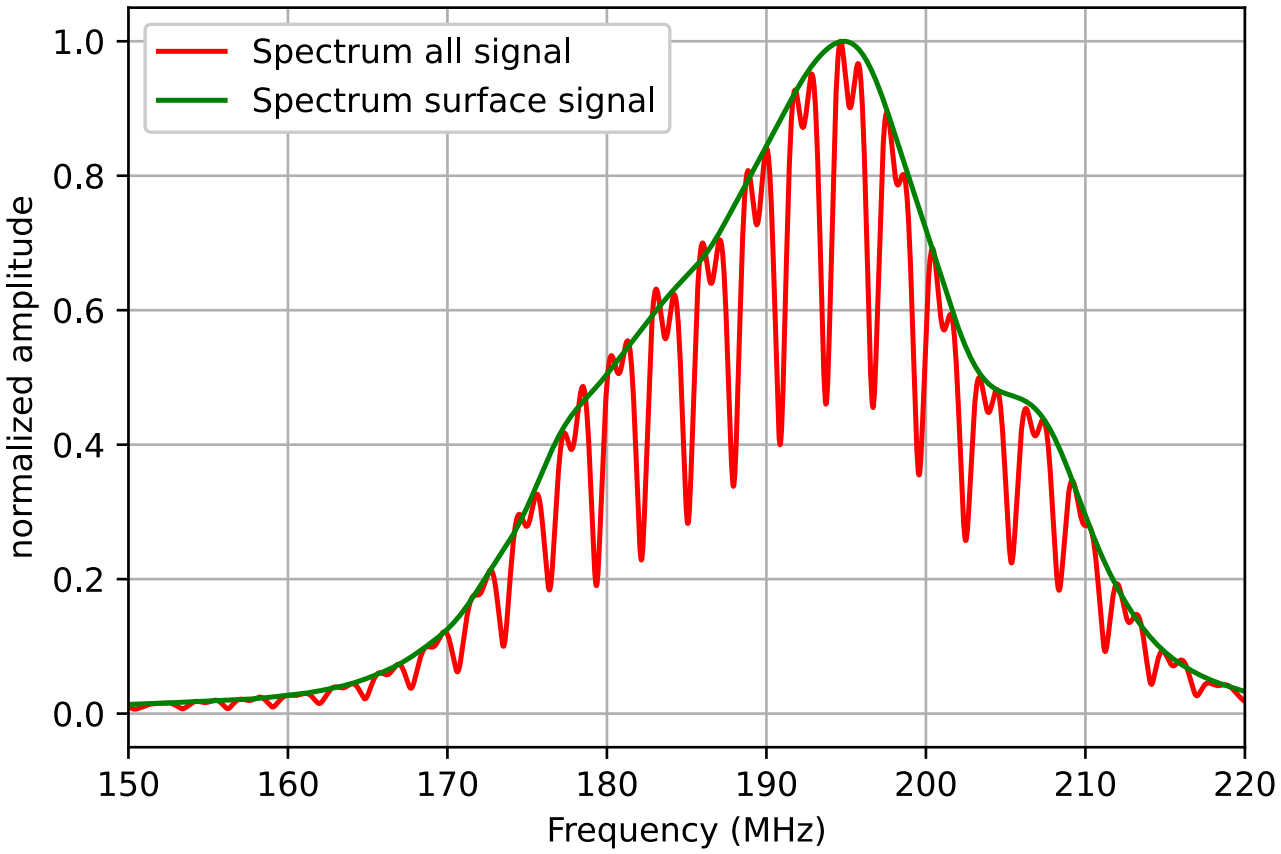

4.Reflection coefficient

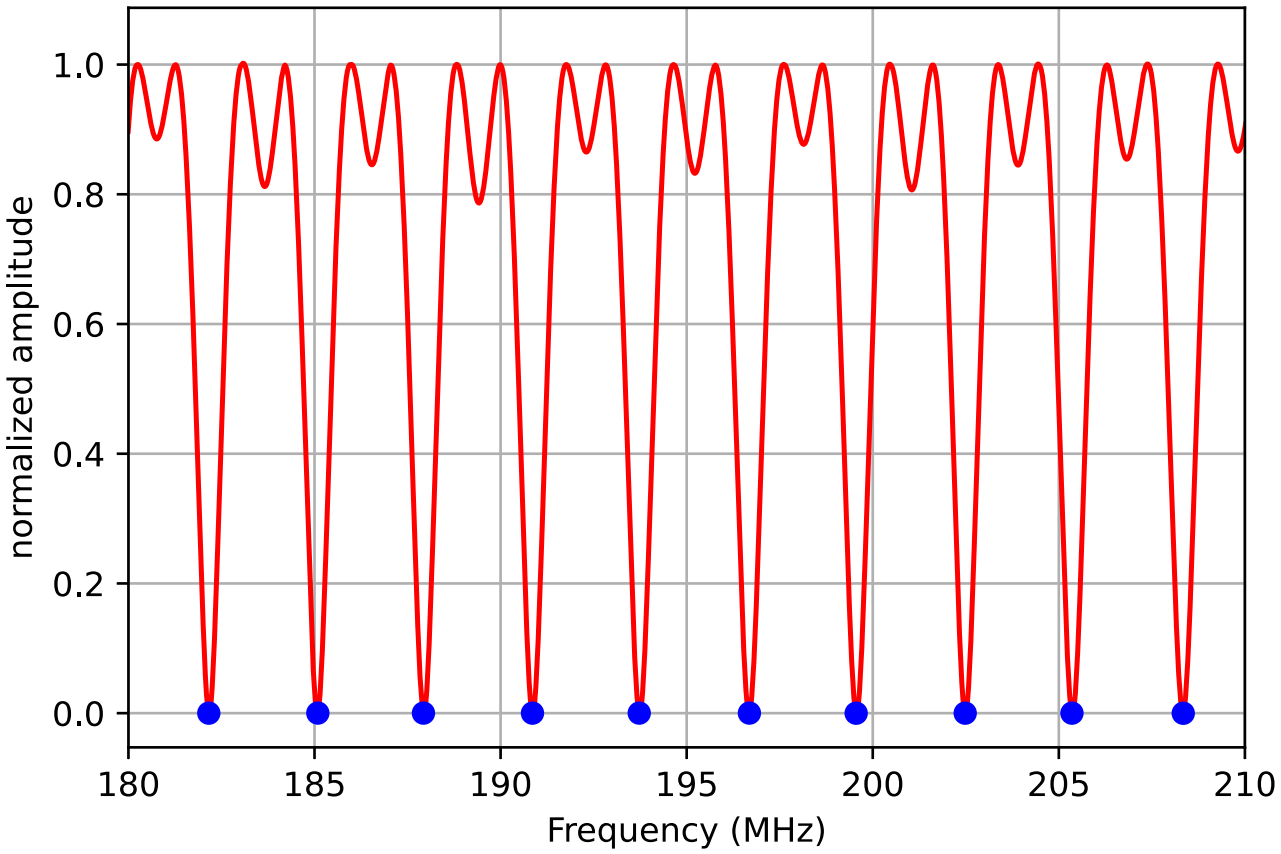

5.Cartography

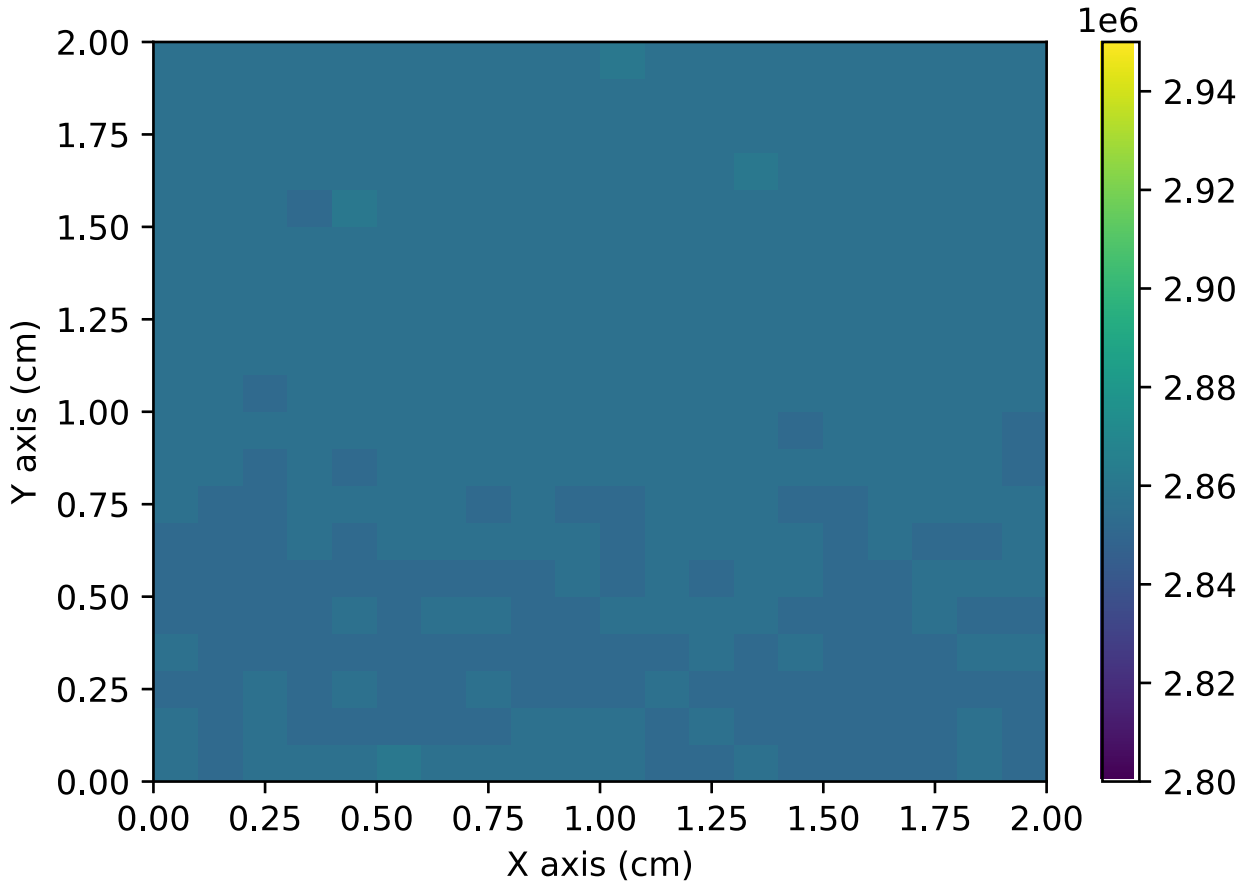

Mean Δf = 2.85454 MHz

Median Δf = 2.85557 MHz

Std Δf = 1.95502 kHz

Experience report

Type of experience :Characterization of bonding energy Date:24-10-2022

Manipulator : Amine IKLIL

1.Manipulation parameter

setting	Value or designation
Sample	[100°C - 400°C]
Transducer	193 MHz
bandwith	[175 MHz,200MHz]
Filtre	Butterworth ordre 3
Gain in dB	25 dB
scan dimension	2cm²
steps_X_axis	20 points
steps_Y_axis	20 points
delta_t	5E-10
delta_f	2G
NFFT	65536 points
Mean signals	400 signals
PRF	1 kHz
number of points	1618points

2.Time signal

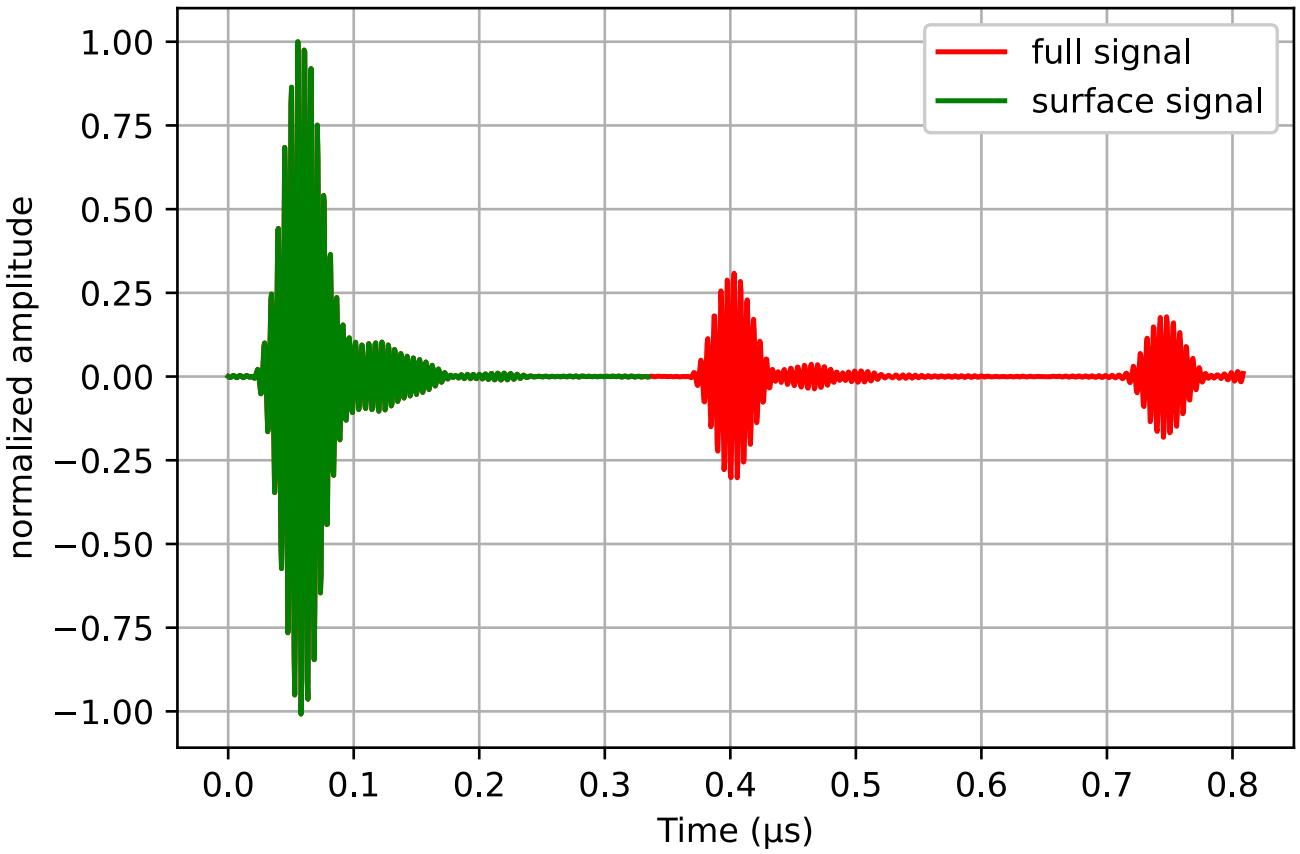

3.FFT

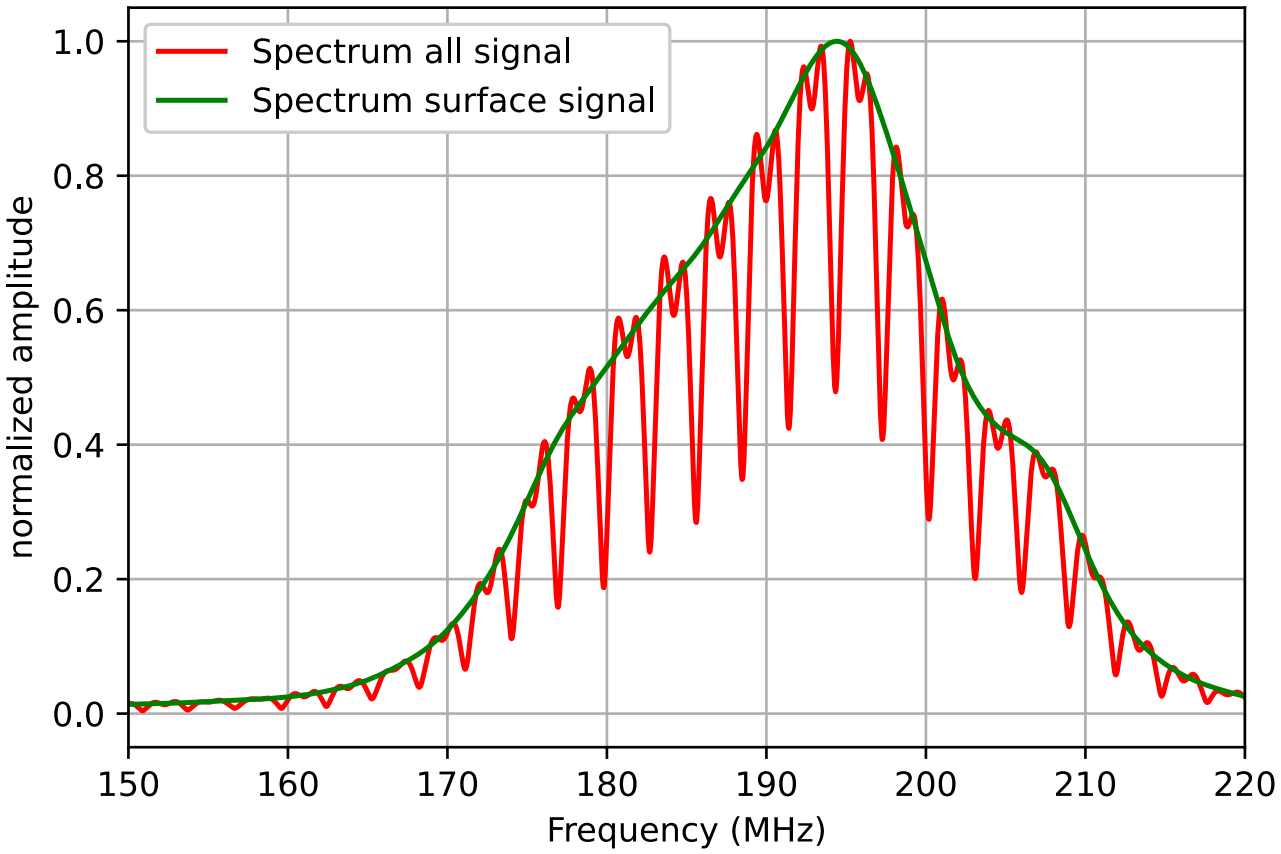

4.Reflection coefficient

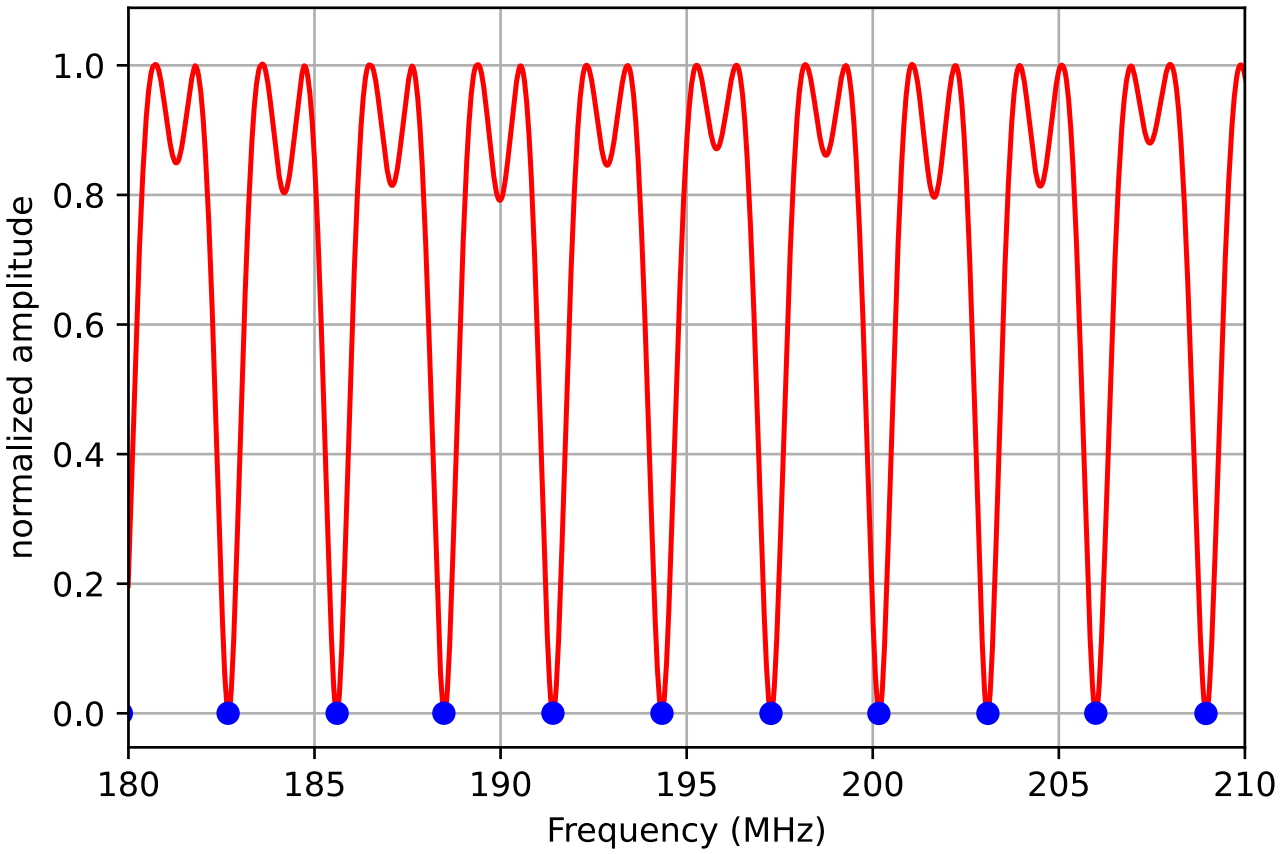

5.Cartography

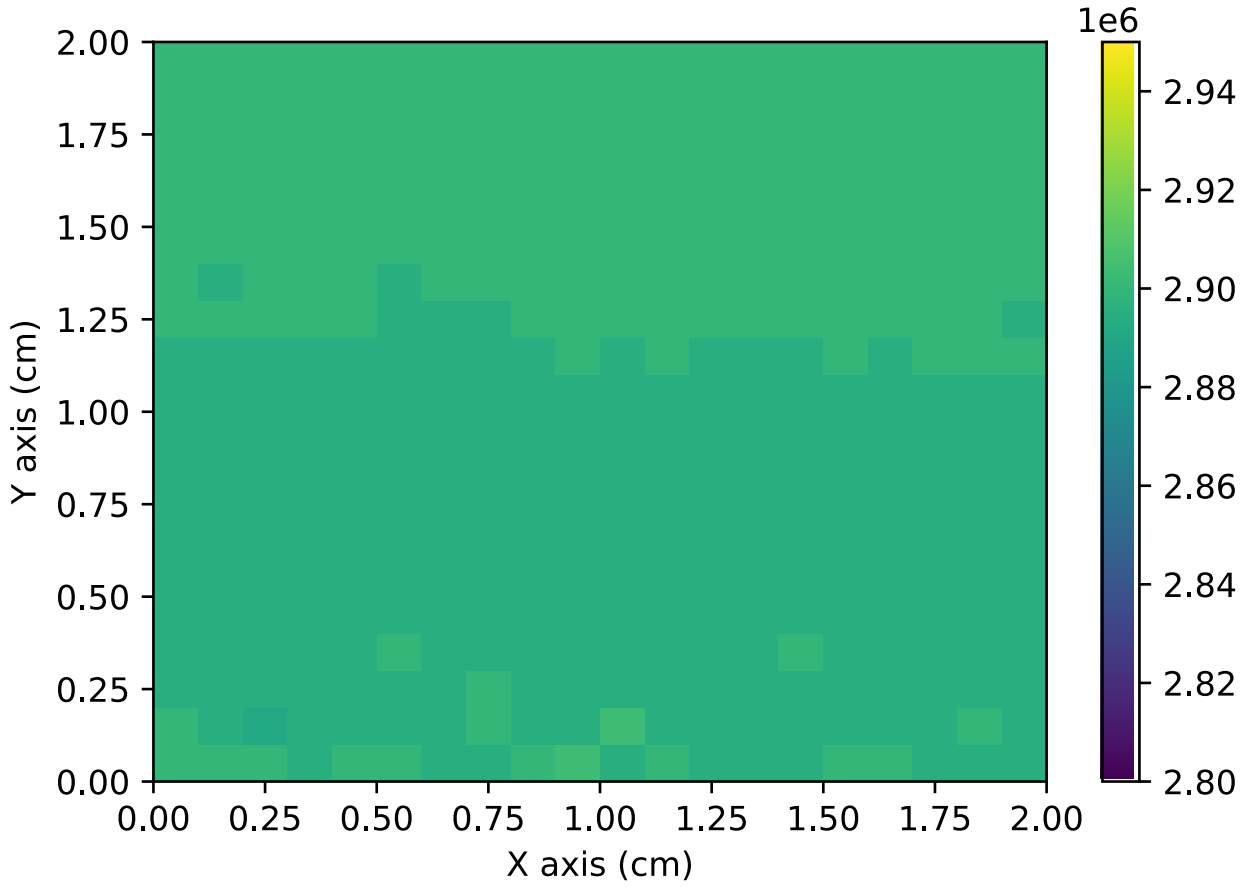

Mean Δf = 2.89675 MHz

Median Δf = 2.89481 MHz

Std Δf = 2.23142 kHz

Experience report

Type of experience :Characterization of bonding energy Date:24-10-2022

Manipulator : Amine IKLIL

1.Manipulation parameter

setting	Value or designation
Sample	500°C
Transducer	193 MHz
bandwith	[175 MHz,200MHz]
Filtre	Butterworth ordre 3
Gain in dB	25 dB
scan dimension	2cm²
steps_X_axis	20 points
steps_Y_axis	20 points
delta_t	5E-10
delta_f	2G
NFFT	65536 points
Mean signals	400 signals
PRF	1 kHz
number of points	1618points

2.Time signal

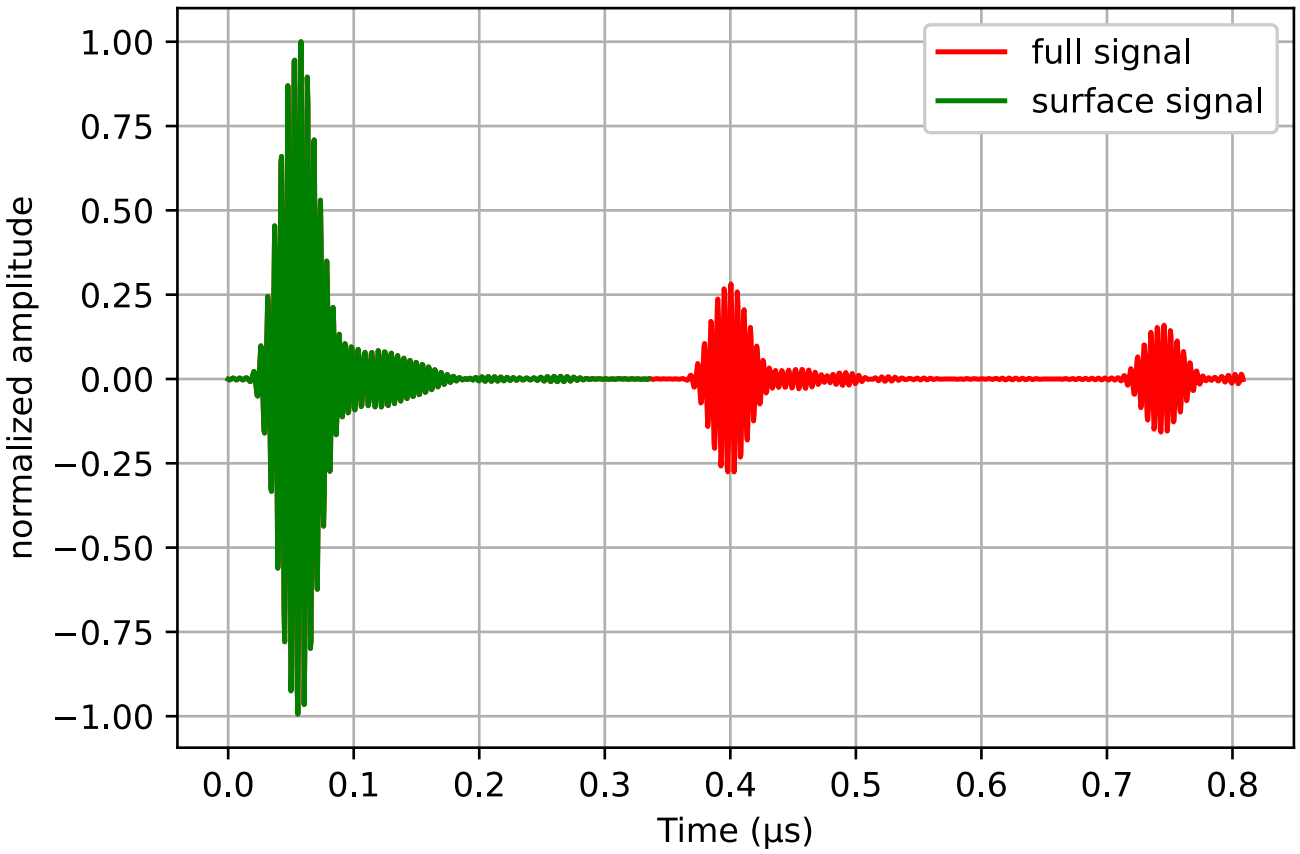

3.FFT

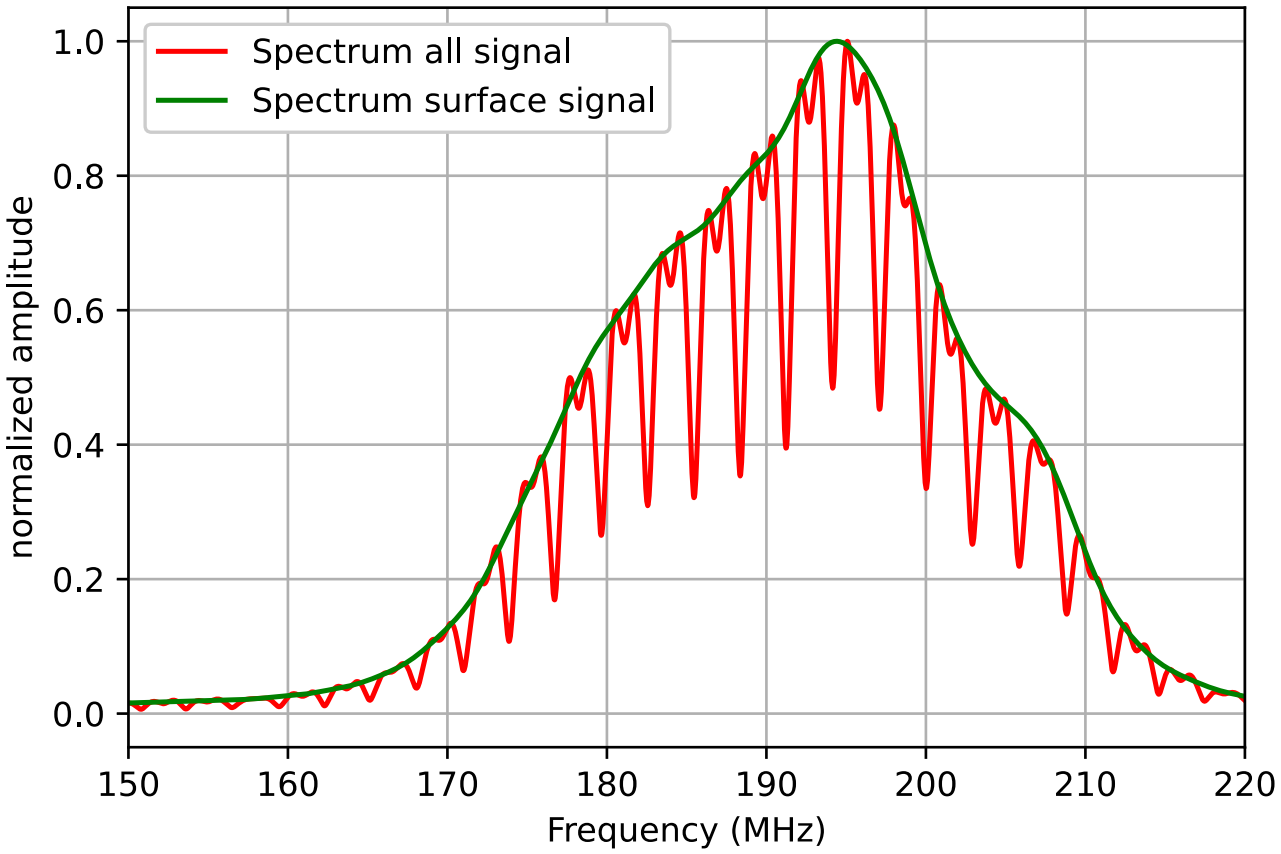

4.Reflection coefficient

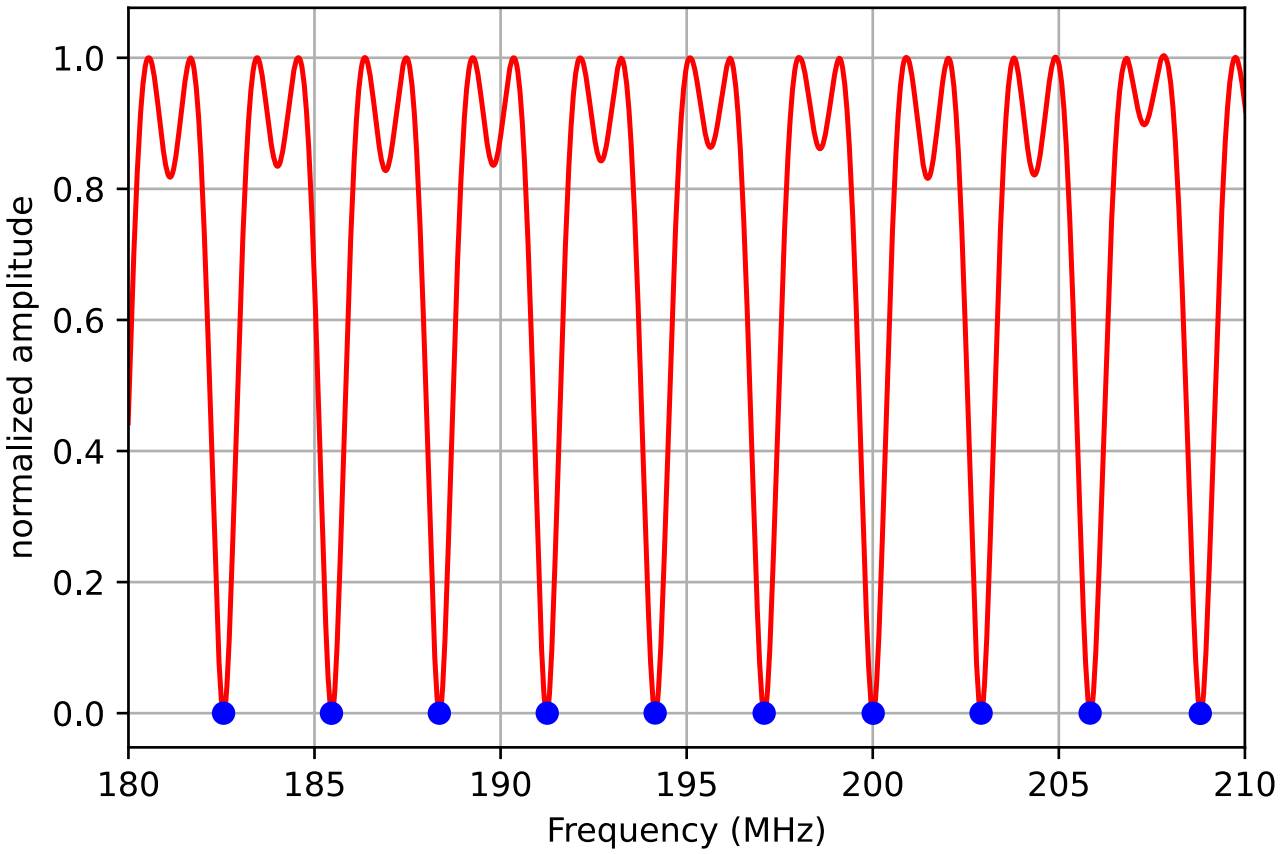

5.Cartography

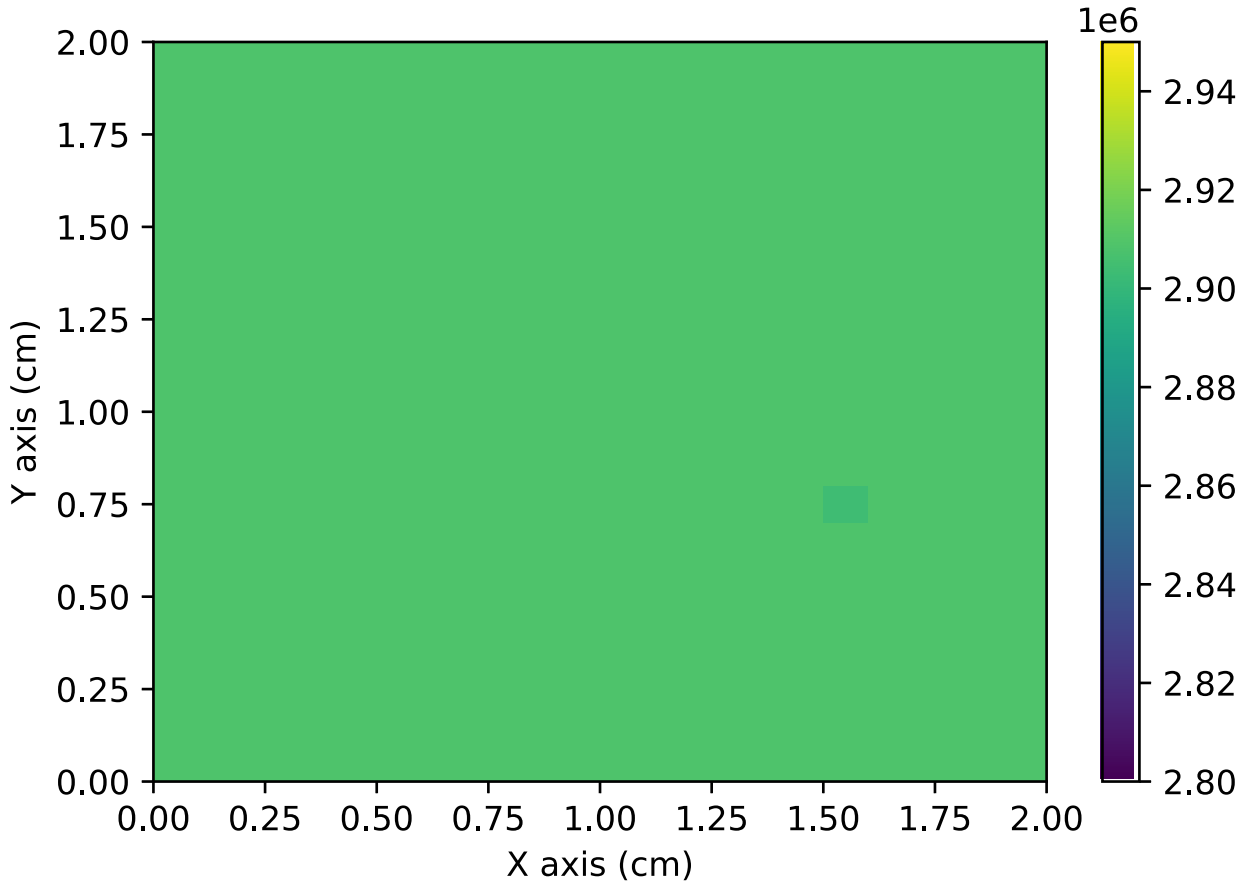

Mean Δf = 2.90788 MHz

Median Δf = 2.90789 MHz

Std Δf = 0.21771 kHz

Experience report

Type of experience :Characterization of bonding energy Date:24-10-2022

Manipulator : Amine IKLIL

1.Manipulation parameter

setting	Value or designation
Sample	600°C
Transducer	193 MHz
bandwith	[175 MHz,200MHz]
Filtre	Butterworth ordre 3
Gain in dB	25 dB
scan dimension	2cm²
steps_X_axis	20 points
steps_Y_axis	20 points
delta_t	5E-10
delta_f	2G
NFFT	65536 points
Mean signals	400 signals
PRF	1 kHz
number of points	1652points

2.Time signal

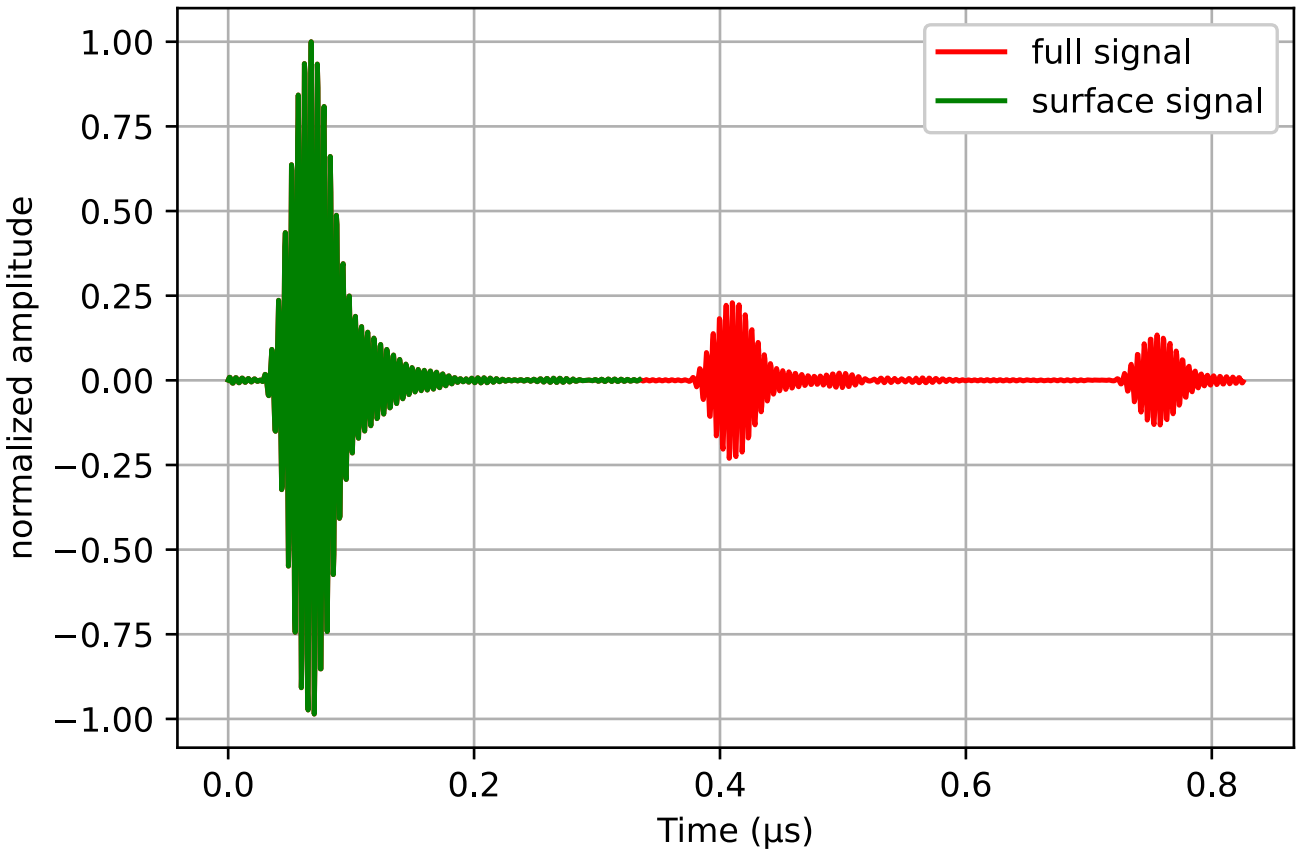

3.FFT

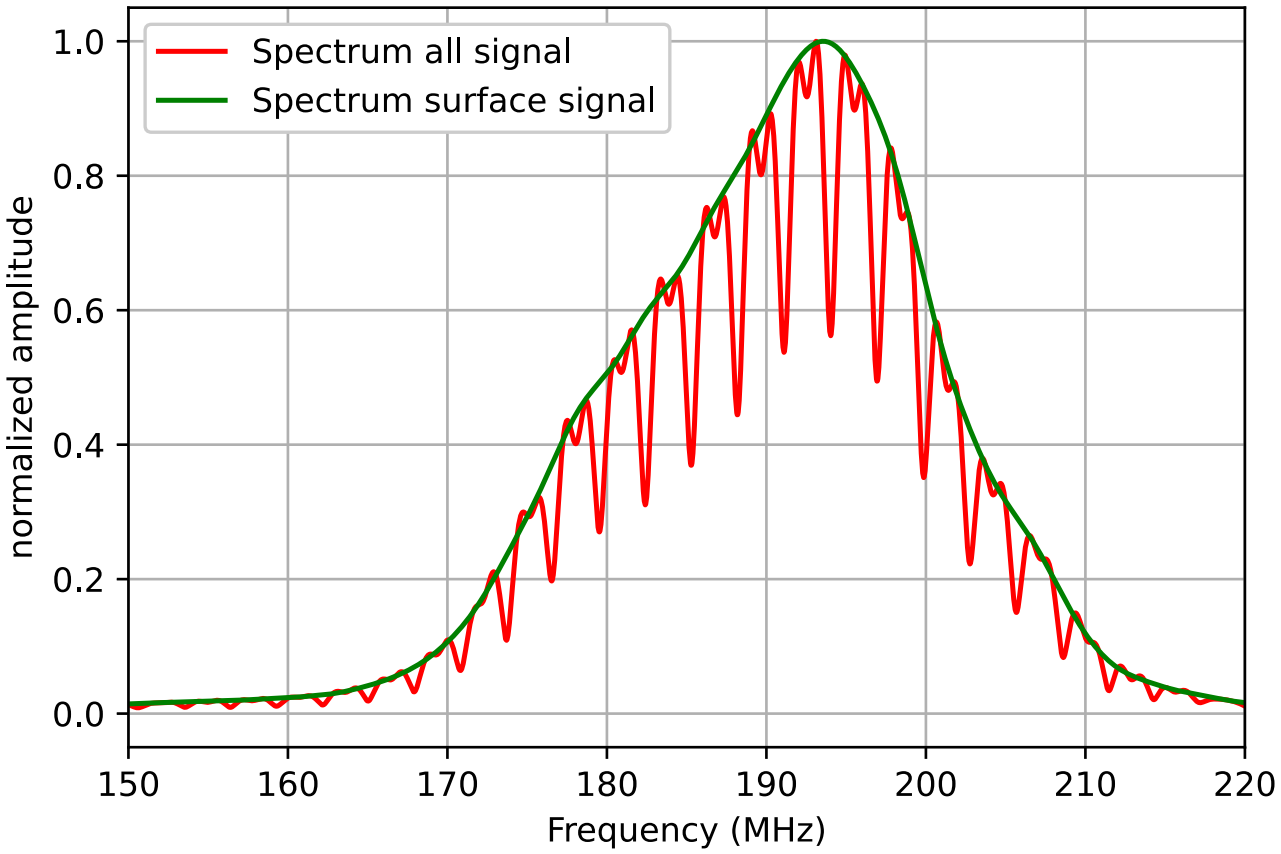

4.Reflection coefficient

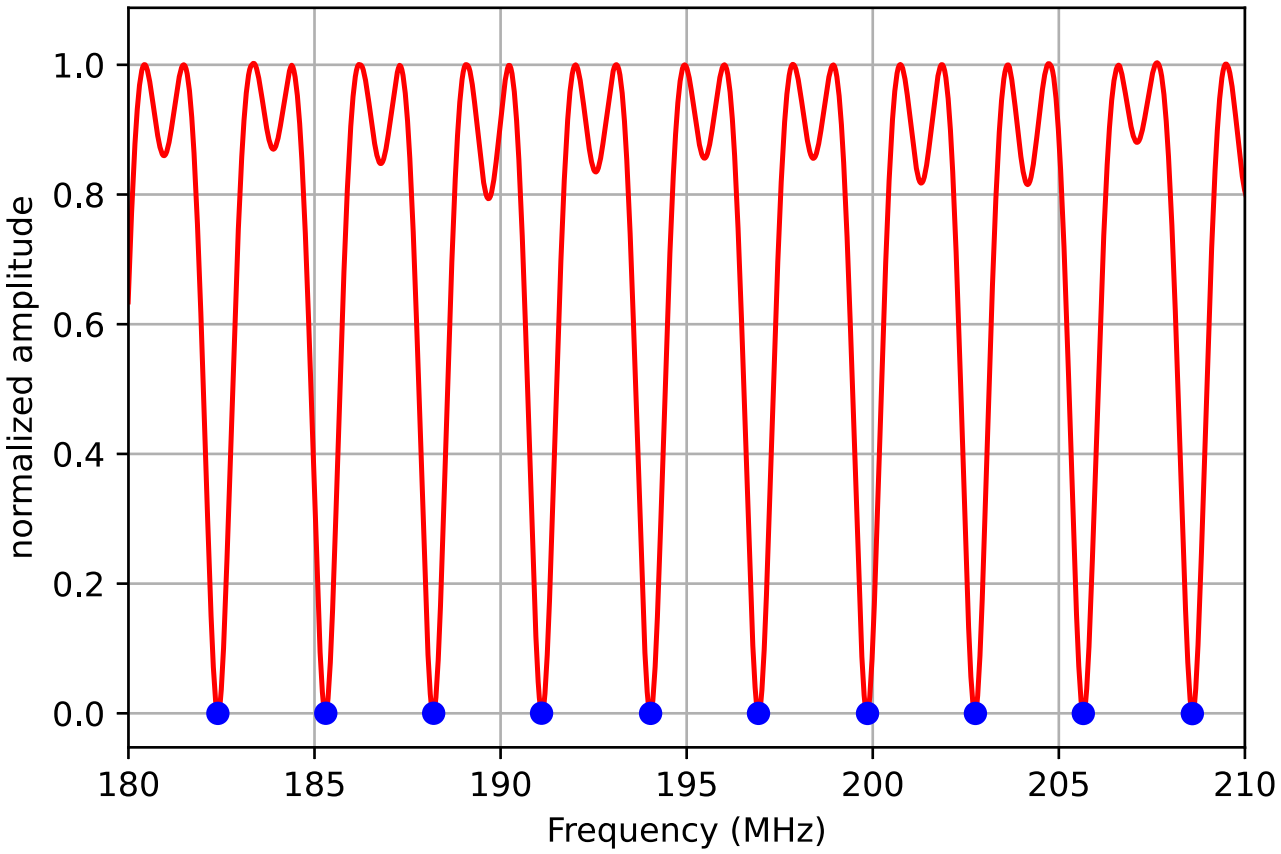

5.Cartography

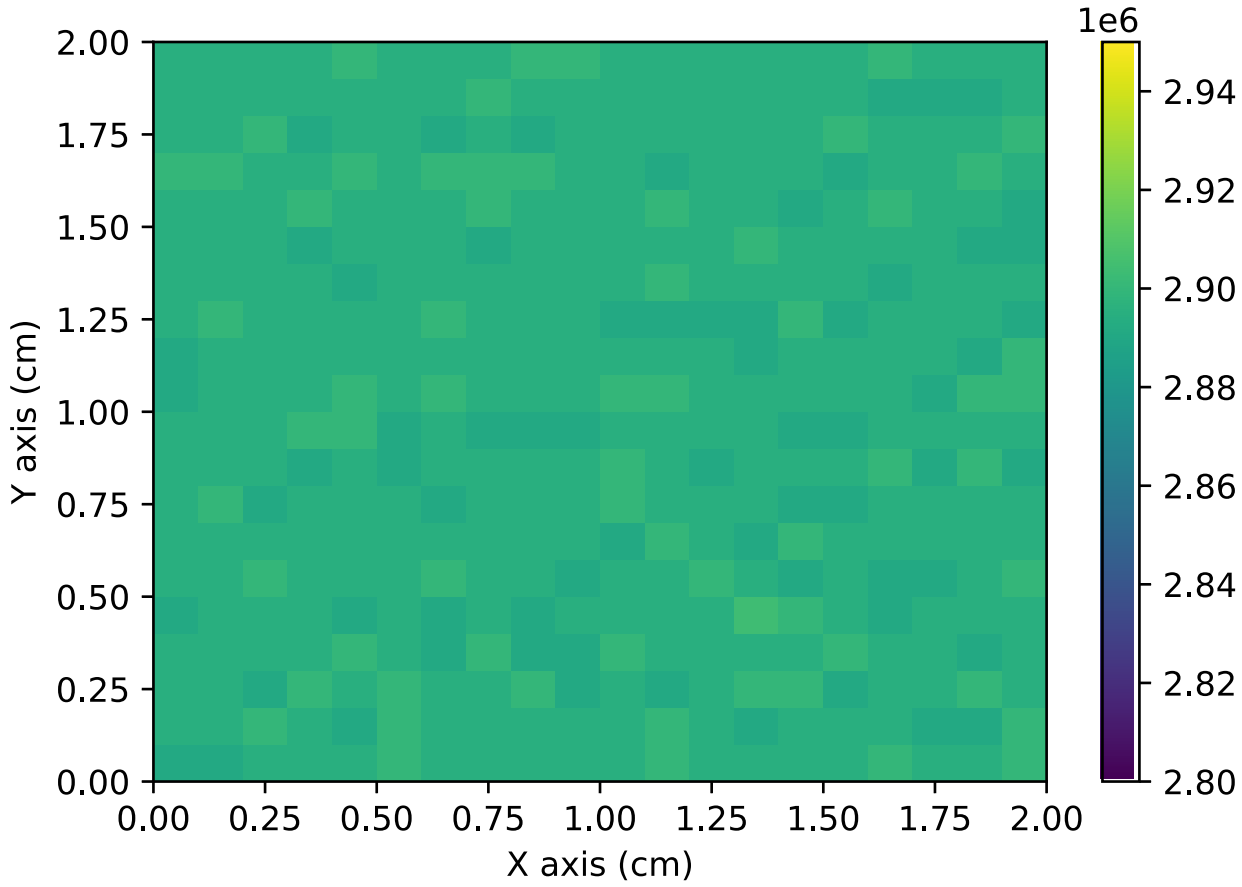

Mean Δf = 2.89479 MHz

Median Δf = 2.89481 MHz

Std Δf = 2.52324 kHz

Experience report

Type of experience :Characterization of bonding energy Date:24-10-2022

Manipulator : Amine IKLIL

1.Manipulation parameter

setting	Value or designation
Sample	1100°C
Transducer	193 MHz
bandwith	[175 MHz,200MHz]
Filtre	Butterworth ordre 3
Gain in dB	25 dB
scan dimension	2cm²
steps_X_axis	20 points
steps_Y_axis	20 points
delta_t	5E-10
delta_f	2G
NFFT	65536 points
Mean signals	400 signals
PRF	1 kHz
number of points	1618points

2.Time signal

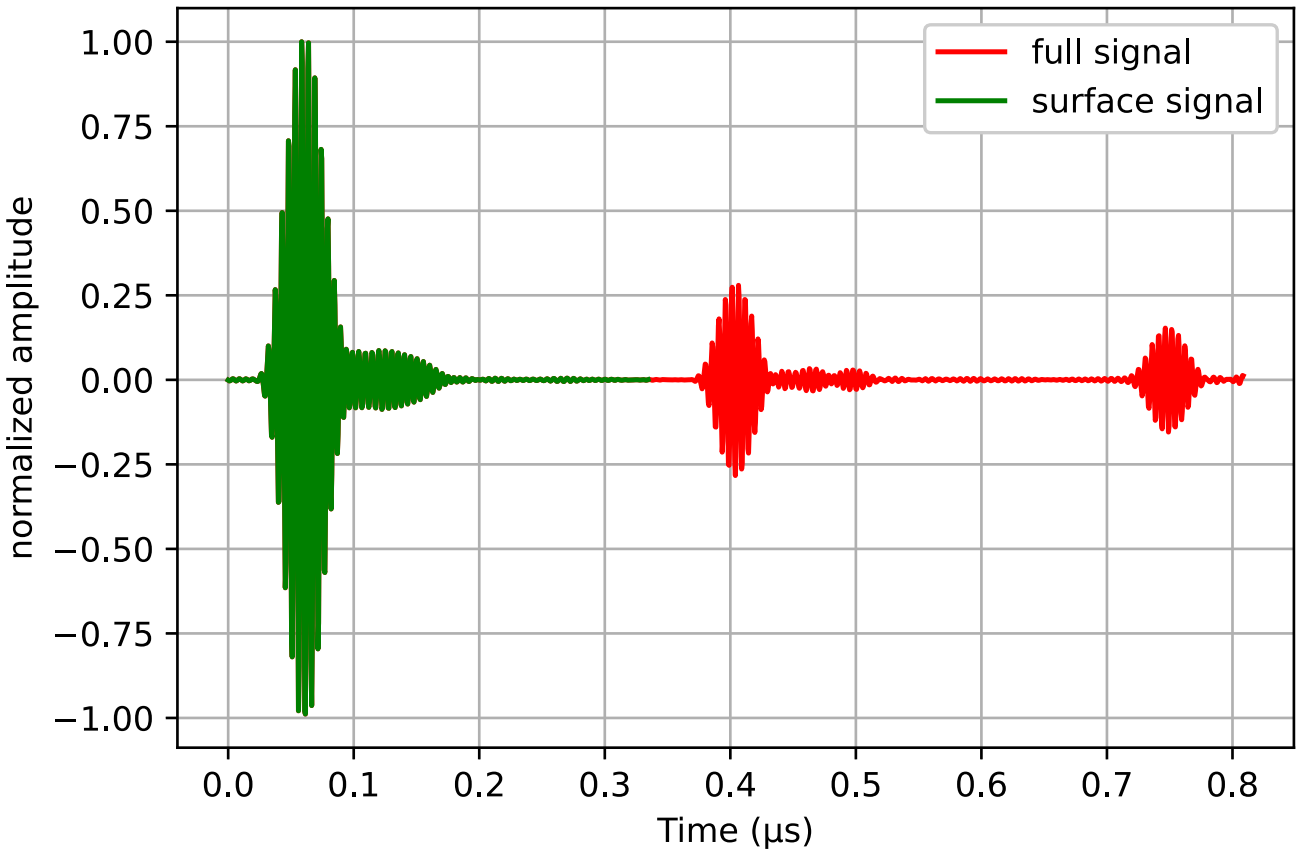

3.FFT

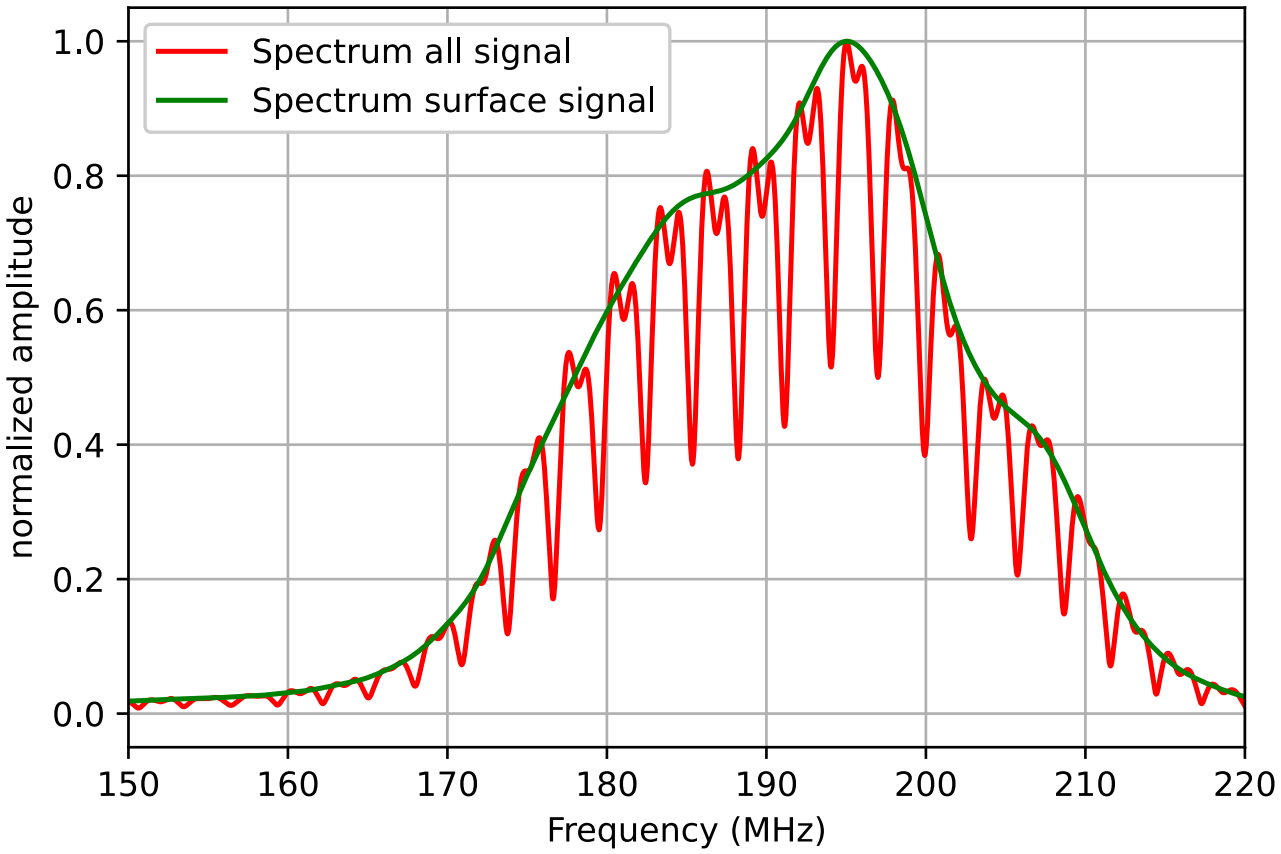

4.Reflection coefficient

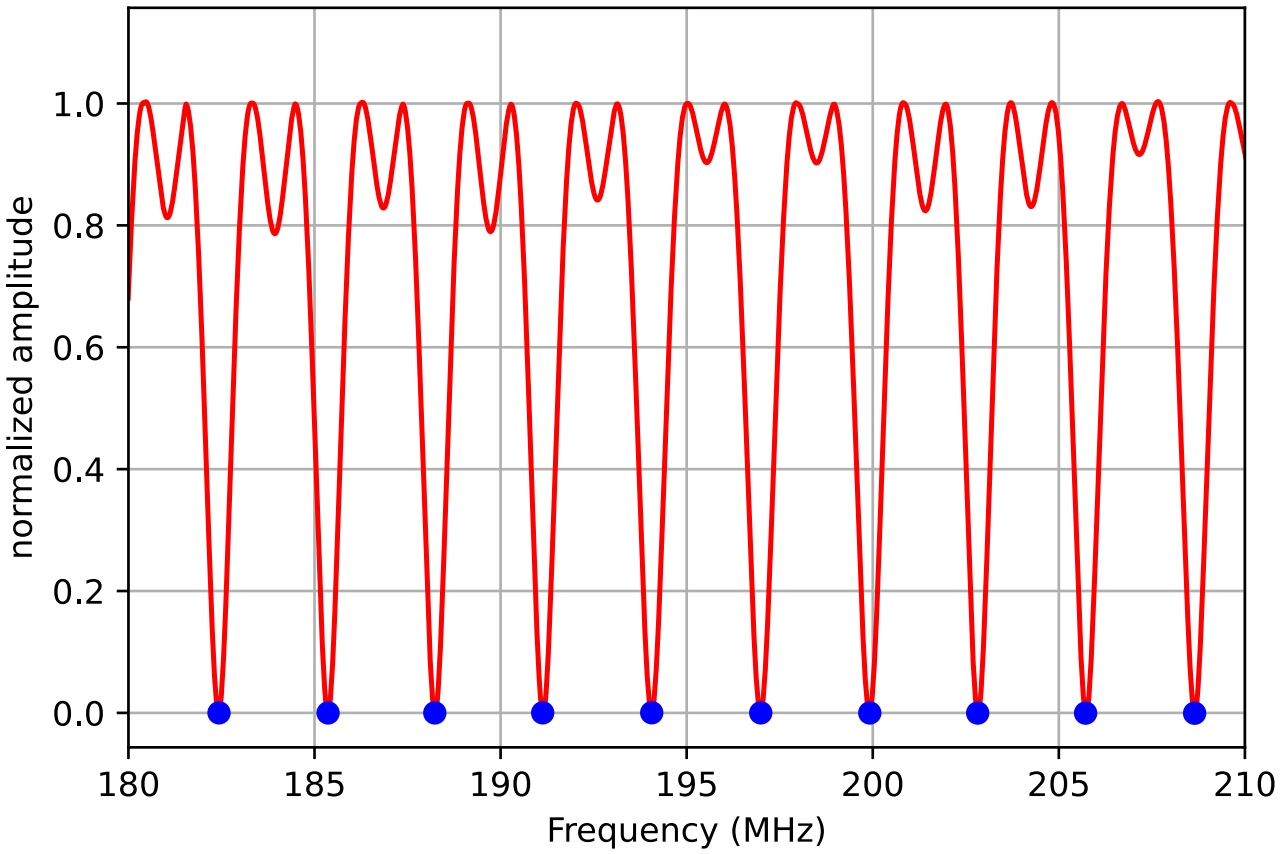

5.Cartography

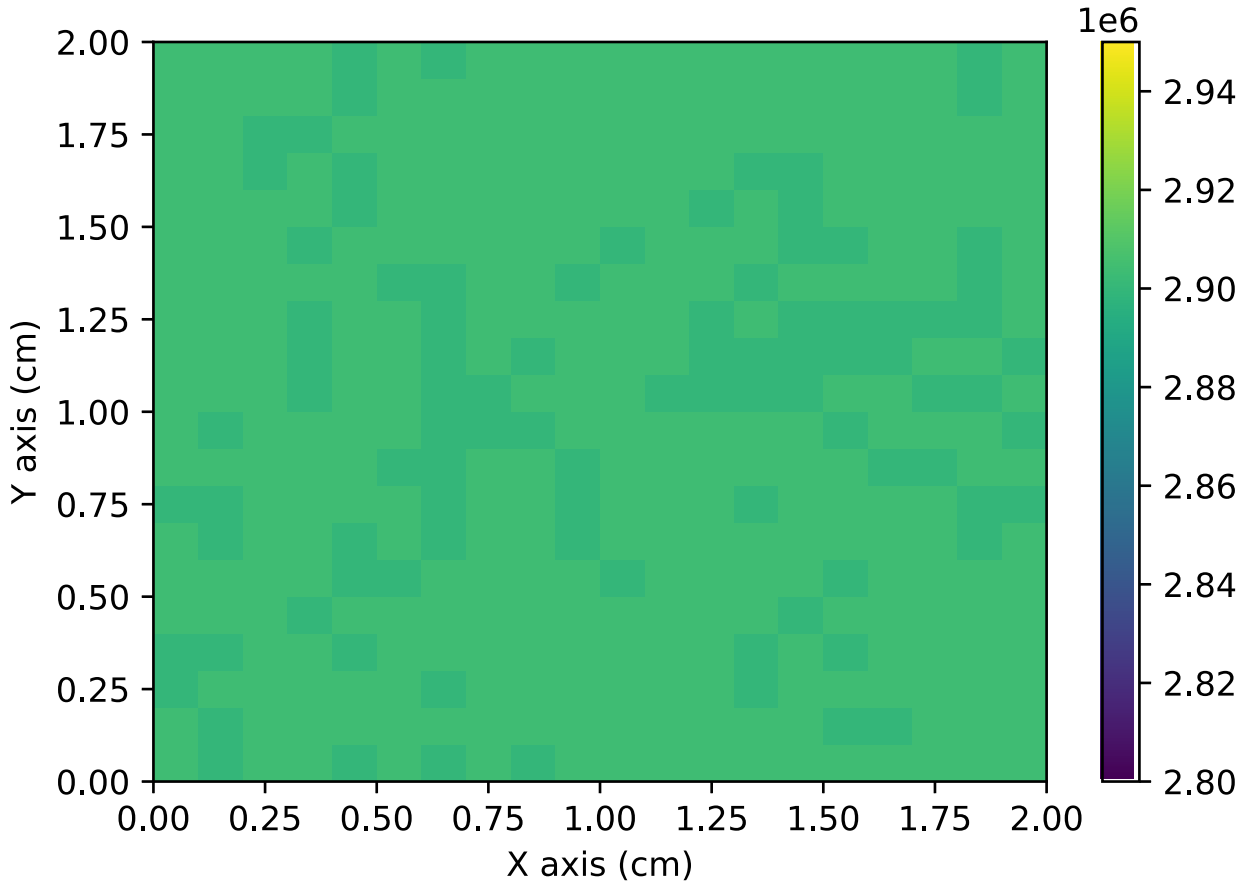

Mean Δf = 2.90251 MHz

Median Δf = 2.90353 MHz

Std Δf = 1.84849 kHz

Appendix D

Noise analysis results

SNR	N° of peaks	[175 MHz-178 MHz] $Mean_{100}(\lvert f_{c_i}[\mathrm{T}] - f_{c_j}[T_{Noised}]\rvert)$	[178 MHz-182 MHz] $Mean_{100}(\lvert f_{c_i}[\mathrm{T}] - f_{c_j}[T_{Noised}]\rvert)$	[182 MHz-185 MHz] $Mean_{100}(\lvert f_{c_i}[\mathrm{T}] - f_{c_j}[T_{Noised}]\rvert)$
40 dB	3	468.72802 kHz	470.46066 kHz	473.06864 kHz
40 dB	4	471.01683 kHz	470.34622 kHz	472.87791 kHz
40 dB	6	471.28386 kHz	470.30808 kHz	472.83976 kHz
40 dB	9	471.20757 kHz	470.30808 kHz	472.83976 kHz
40 dB	12	471.36016 kHz	470.30808 kHz	472.83976 kHz
25 dB	3	467.54546 kHz	471.26175 kHz	473.06864 kHz
25 dB	4	471.66533 kHz	471.64322 kHz	473.41197 kHz
25 dB	6	472.58086 kHz	470.57511 kHz	473.79343 kHz
25 dB	9	472.61901 kHz	470.99472 kHz	473.25938 kHz
25 dB	12	472.42827 kHz	470.99472 kHz	473.18308 kHz
15 dB	3	469.79613 kHz	474.16092 kHz	472.91605 kHz
15 dB	4	470.90239 kHz	470.99472 kHz	472.91605 kHz
15 dB	6	472.58086 kHz	470.30808 kHz	473.75529 kHz
15 dB	9	471.85607 kHz	471.52878 kHz	473.33567 kHz
15 dB	12	473.15306 kHz	471.14731 kHz	473.48826 kHz

[185 MHz-188 MHz] $Mean_{100}(\lvert f_{c_i}[\mathrm{T}] - f_{c_j}[T_{Noised}]\rvert)$	[188 MHz-190 MHz] $Mean_{100}(\lvert f_{c_i}[\mathrm{T}] - f_{c_j}[T_{Noised}]\rvert)$	[190 MHz-192 MHz] $Mean_{100}(\lvert f_{c_i}[\mathrm{T}] - f_{c_j}[T_{Noised}]\rvert)$	Offset
471.67324 kHz	472.90793 kHz	470.48356 kHz	4.34062 kHz
472.09286 kHz	472.6409 kHz	470.36911 kHz	2.53168 kHz
472.24544 kHz	472.45016 kHz	470.36911 kHz	2.53167 kHz
472.24544 kHz	472.33572 kHz	470.36911 kHz	2.53167 kHz
472.24544 kHz	472.67904 kHz	470.36911 kHz	2.53167 kHz
471.21548 kHz	473.13681 kHz	471.66611 kHz	5.59145 kHz
471.17733 kHz	472.98422 kHz	471.58982 kHz	2.23464 kHz
471.13918 kHz	473.02237 kHz	471.28464 kHz	3.21832 kHz
471.32992 kHz	472.45016 kHz	470.67429 kHz	2.58509 kHz
471.63509 kHz	472.86978 kHz	470.86502 kHz	2.31806 kHz
470.75771 kHz	473.06051 kHz	471.51352 kHz	4.36478 kHz
470.49068 kHz	473.48013 kHz	472.08573 kHz	2.98944 kHz
470.75771 kHz	473.06051 kHz	471.08573 kHz	3.4472 kHz
471.44436 kHz	473.09866 kHz	470.90317 kHz	2.4325 kHz
471.13918 kHz	472.37387 kHz	471.55167 kHz	2.34908 kHz

Table D.1: White noise impact on cutoff frequencies position analysis

SNR	N° of peaks	[175 MHz-178 MHz] $Mean_{100}(\lvert f_{c_i}[\mathrm{T}] - f_{c_j}[T_{Noised}]\rvert)$	[178 MHz-182 MHz] $Mean_{100}(\lvert f_{c_i}[\mathrm{T}] - f_{c_j}[T_{Noised}]\rvert)$	[182 MHz-185 MHz] $Mean_{100}(\lvert f_{c_i}[\mathrm{T}] - f_{c_j}[T_{Noised}]\rvert)$
40 dB	3	468.72802 kHz	472.06284 kHz	473.83158 kHz
40 dB	4	469.91057 kHz	471.49063 kHz	473.45011 kHz
40 dB	6	472.19939 kHz	470.84213 kHz	473.45011 kHz
40 dB	9	472.0468 kHz	470.91843 kHz	473.33567 kHz
40 dB	12	472.1231 kHz	470.61325 kHz	473.0305 kHz
25 dB	3	471.02545 kHz	463.66312 kHz	468.77895 kHz
25 dB	4	474.34033 kHz	471.81512 kHz	475.14742 kHz
25 dB	6	473.27152 kHz	470.99071 kHz	471.99651 kHz
25 dB	9	471.7858 kHz	470.62931 kHz	472.87992 kHz
25 dB	12	470.74509 kHz	470.54404 kHz	474.3735 kHz
15 dB	3	547.83212 kHz	1.2942 MHz	938.44475 kHz
15 dB	4	694.17438 kHz	1.4711 MHz	1.2193 MHz
15 dB	6	244.76714 kHz	335.11521 kHz	367.7067 kHz
15 dB	9	473.31168 kHz	466.19338 kHz	474.0444 kHz
15 dB	12	474.90783 kHz	474.12277 kHz	472.64903 kHz

[185 MHz-188 MHz] $Mean_{100}(\lvert f_{c_i}[\mathrm{T}] - f_{c_j}[T_{Noised}]\rvert)$	[188 MHz-190 MHz] $Mean_{100}(\lvert f_{c_i}[\mathrm{T}] - f_{c_j}[T_{Noised}]\rvert)$	[190 MHz-192 MHz] $Mean_{100}(\lvert f_{c_i}[\mathrm{T}] - f_{c_j}[T_{Noised}]\rvert)$	Offset
471.74953 kHz	473.48013 kHz	472.23832 kHz	5.10355 kHz
470.87215 kHz	472.6409 kHz	471.66611 kHz	3.5953 kHz
471.13918 kHz	472.86978 kHz	470.94132 kHz	2.60797 kHz
471.25362 kHz	472.79349 kHz	471.05576 kHz	2.41723 kHz
471.86397 kHz	472.71719 kHz	470.86502 kHz	2.41725 kHz
476.67542 kHz	471.08549 kHz	476.33727 kHz	13.0122 kHz
472.90477 kHz	471.81014 kHz	471.59358 kHz	3.55384 kHz
471.4825 kHz	472.12692 kHz	470.93128 kHz	2.34023 kHz
471.20142 kHz	473.45202 kHz	471.41314 kHz	2.82271 kHz
471.49824 kHz	473.36136 kHz	471.31296 kHz	3.82945 kHz
1.0306 MHz	1.4314 MHz	818.14235 kHz	883.57 kHz
993.737 kHz	624.89668 kHz	464.08608 kHz	1.007 MHz
349.86996 kHz	385.51321 kHz	466.85959 kHz	222.092 kHz
476.86324 kHz	474.57635 kHz	466.15287 kHz	10.710 kHz
470.52883 kHz	471.15317 kHz	473.0394 kHz	4.3789 kHz

Table D.2: Modelized experimental noise impact on cutoff frequencies position analysis

Appendix E

Git repository

https://github.com/Amineiklil123/AI_PhD_appendix

Video

Video 1 : `Without_noise.mp4`
Video 2 : `15db_signal_BR.mp4`
Video 3 : `25db_signal_BR.mp4`
Video 4 : `40db_signal_BR.mp4`
Video 5 : `15db_signal_BM.mp4`
Video 6 : `25db_signal_BM.mp4`
Video 7 : `40db_signal_BM.mp4`
Video 8 : `R_15db_signal_BR.mp4`
Video 9 : `R_25db_signal_BR.mp4`
Video 10 : `R_40db_signal_BR.mp4`
Video 11 : `R_15db_signal_BM.mp4`
Video 12 : `R_25db_signal_BM.mp4`
Video 13 : `R_40db_signal_BM.mp4`

N.B : White noise : BR / Experimental setup noise : BM

Bibliography

[1] A. Dekious, "Etude de la réponse acoustique des collages directs et temporaires," Ph.D. dissertation, Theses, Université de Montpellier, 2016.

[2] M. Koyanagi, T. Fukushima, and T. Tanaka, "Three-dimensional integration technology and integrated systems," in *2009 Asia and South Pacific Design Automation Conference*. IEEE, 2009, pp. 409–415.

[3] K. R. Jian-Qiang Lu, "3d integration: Why, what, who, when?" 2007.

[4] A. Shinde, S. Budhgaon, R. Patil, and Y. Patil, "3d vlsi technology."

[5] J.-Q. Lu, "3-d hyperintegration and packaging technologies for micro-nano systems," *Proceedings of the IEEE*, vol. 97, no. 1, pp. 18–30, 2009.

[6] B. BAILEY, "Speeding up 3d design," *Semiconductor Engineering / Source : Cadence*, 2019.

[7] G. K. Michele Stucchi and D. Velenis, *Three dimensional system integration: IC stacking process and design / Chapter 3 : TSV Characterization and Modeling*. Springer Science & Business Media, 2010.

[8] F. Fournel, *HDR : Applications de l'adhésion moléculaire*. Univ Grenoble 1 - Joseph Fourier, 2009.

[9] F. Fournel, C. Martin-Cocher, D. Radisson, V. Larrey, E. Beche, C. Morales, P. Delean, F. Rieutord, and H. Moriceau, "Water stress corrosion in bonded structures," *ECS Journal of Solid State Science and Technology*, vol. 4, no. 5, p. P124, 2015.

[10] F. Fournel, L. Continni, C. Morales, J. Da Fonseca, H. Moriceau, C. M. Cocher, F. Rieutord, A. Barthelemy, and I. Radu, "Direct bonding energy in anhydrous atmosphere," *ECS Transactions*, vol. 50, no. 7, p. 3, 2013.

[11] F. Rieutord, H. Moriceau, R. Beneyton, L. Capello, C. Morales, and A.-M. Charvet, "Rough surface adhesion mechanisms for wafer bonding," *ECS Transactions*, vol. 3, no. 6, p. 205, 2006.

[12] W. Maszara, G. Goetz, A. Caviglia, and J. McKitterick, "Bonding of silicon wafers for silicon-on-insulator," *Journal of Applied Physics*, vol. 64, no. 10, pp. 4943–4950, 1988.

[13] T. MONNIER, "Microscopie acoustique," *Techniques de l'ingénieur Techniques d'analyse*, vol. base documentaire : TIP630WEB., no. ref. article : r1402, 2014, fre. [Online]. Available: https://www.techniques-ingenieur.fr/base-documentaire/mesures-analyses-th1/techniques-d-analyse-par-imagerie-42387210/microscopie-acoustique-r1402/

[14] J. Desomberg, "Etude de l'influence des propriétés mécaniques des surfaces sur l'énergie de collage direct," Theses, Université Grenoble Alpes, Oct. 2018. [Online]. Available: https://tel.archives-ouvertes.fr/tel-02047929

[15] G. Vogg, T. Heidmann, and S. Brand, "Scanning acoustic ghz-microscopy versus conventional sam for advanced assessment of ball bond and metal interfaces in microelectronic devices," *Microelectronics Reliability*, vol. 55, no. 9-10, pp. 1554–1558, 2015.

[16] W. J. Xu, "Etude par ondes acoustiques de la qualité des interfaces dans une structure multicouche," Ph.D. dissertation, Valenciennes, 1995.

[17] C. L. Bertin, L.-S. Su, and J. Van Horn, "Known Good Die (KGD)," in *Area Array Interconnection Handbook*, K. J. Puttlitz and P. A. Totta, Eds. Boston, MA: Springer US, 2001, pp. 149–200. [Online]. Available: https://doi.org/10.1007/978-1-4615-1389-6_4

[18] P. Garrou, M. Koyanagi, and P. Ramm, *Handbook of 3D Integration, Volume 3: 3D Process Technology*. John Wiley & Sons, 2014.

[19] E. Beche, "Etude des collages directs hydrophiles mettant en jeu des couches diélectriques," Theses, Université Grenoble Alpes, Oct. 2017. [Online]. Available: https://tel.archives-ouvertes.fr/tel-01755507

[20] J. Lasky, "Wafer bonding for silicon-on-insulator technologies," *Applied Physics Letters*, vol. 48, no. 1, pp. 78–80, 1986.

[21] Y. Benelmostafa, J. De Belleval, N. Mercier, and I. Molinero, "MODÉLISATION NUMÉRIQUE DE LA PROPAGATION DES ULTRASONS DANS UN MILIEU MULTICOUCHE. APPLICATION AUX COLLAGES," *Journal de Physique Colloques*, vol. 51, no. C2, pp. C2–1257–C2–1260, 1990. [Online]. Available: https://hal.archives-ouvertes.fr/jpa-00230629

[22] E. Siryabe, "Evaluation non destructive par ultrasons de l'adhésion aux interfaces de joints collés," Theses, Université de Bordeaux, Dec. 2016. [Online]. Available: https://tel.archives-ouvertes.fr/tel-01476164

[23] A. I. Lavrentyev and S. I. Rokhlin, "Determination of elastic moduli, density, attenuation, and thickness of a layer using ultrasonic spectroscopy at two angles," *The Journal of the Acoustical Society of America*, vol. 102, no. 6, pp. 3467–3477, 1997.

[24] E. W. M. Robert W Haisty, Rowland E Johnson. Us3613226a : Three-dimensional integrated circuits and methods of making same. [Online]. Available: https://patents.google.com/patent/US3613226

[25] M. Reber and R. Tielert, "Benefits of vertically stacked integrated circuits for sequential logic," in *1996 IEEE International Symposium on Circuits and Systems. Circuits and Systems Connecting the World. ISCAS 96*, vol. 4. IEEE, 1996, pp. 121–124.

[26] Y. Akasaka, "Three-dimensional ic trends," *Proceedings of the IEEE*, vol. 74, no. 12, pp. 1703–1714, 1986.

[27] E. Rymaszewski, J. Walsh, and G. Leehan, "Semiconductor logic technology in ibm," *IBM Journal of Research and Development*, vol. 25, no. 5, pp. 603–616, 1981.

[28] A. Papanikolaou, D. Soudris, and R. Radojcic, *Three dimensional system integration: IC stacking process and design.* Springer Science & Business Media, 2010.

[29] V. Subramanian and K. C. Saraswat, "High-performance germanium-seeded laterally crystallized tfts for vertical device integration," *IEEE Transactions on Electron Devices*, vol. 45, no. 9, pp. 1934–1939, 1998.

[30] K. Banerjee, S. J. Souri, P. Kapur, and K. C. Saraswat, "3-d ics: A novel chip design for improving deep-submicrometer interconnect performance and systems-on-chip integration," *Proceedings of the IEEE*, vol. 89, no. 5, pp. 602–633, 2001.

[31] M. Crowley, A. Al-Shamma, D. Bosch, M. Farmwald, L. Fasoli, A. Ilkbahar, M. Johnson, B. Kleveland, T. Lee, T.-y. Liu *et al.*, "512 mb prom with 8 layers of antifuse/diode cells," in *2003 IEEE International Solid-State Circuits Conference, 2003. Digest of Technical Papers. ISSCC.* IEEE, 2003, pp. 284–493.

[32] C.-G. Hwang, "New paradigms in the silicon industry," in *2006 International Electron Devices Meeting.* IEEE, 2006, pp. 1–8.

[33] M. LAPEDUS, "Advanced packaging's next wave," *Semiconductor Engineering*, 2021.

[34] Q. Monnet, "It's time for disaggregated silicon!" *Netronome*, 2018.

[35] B. BAILEY, "Speeding up 3d design," *Semiconductor Engineering*, 2019.

[36] J. Burns, *Three dimensional system integration: IC stacking process and design / Chapter 2 : TSV-based 3D integration.* Springer Science & Business Media, 2010.

[37] K. Warner, J. Burns, C. Keast, R. Kunz, D. Lennon, A. Loomis, W. Mowers, and D. Yost, "Low-temperature oxide-bonded three-dimensional integrated circuits," in *Proceedings of the IEEE International SOI Conference*, 2002, pp. 123–125.

[38] R. Reif, C. S. Tan, A. Fan, K.-N. Chen, S. Das, and N. Checka, "3-d interconnects using cu wafer bonding: Technology and applications," in *Advanced Metallization Conference, San Diego.* Citeseer, 2002.

[39] J. Lasky, S. Stiffler, F. White, and J. Abernathey, "Silicon-on-insulator (soi) by bonding and etch-back," in *1985 International Electron Devices Meeting.* IEEE, 1985, pp. 684–687.

[40] O. Rayssac, "Etude du collage par adhésion moléculaire hydrophile: application au contrôle de l'énergie de collage," Ph.D. dissertation, Grenoble INPG, 1999.

[41] T. Abe, K. Ohki, A. Uchiyama, K. Nakazawa, and Y. Nakazato, "Dislocation-free silicon on sapphire by wafer bonding," *Japanese journal of applied physics*, vol. 33, no. 1S, p. 514, 1994.

[42] H. Moriceau, F. Rieutord, F. Fournel, L. Di Cioccio, C. Moulet, L. Libralesso, P. Gueguen, R. Taibi, and C. Deguet, "Low temperature direct bonding: An attractive technique for heterostructures build-up," *Microelectronics Reliability*, vol. 52, no. 2, pp. 331–341, 2012.

[43] G. Kissinger and W. Kissinger, "Hydrophilicity of silicon wafers for direct bonding," *physica status solidi (a)*, vol. 123, no. 1, pp. 185–192, 1991.

[44] K. Mitani and U. Gösele, "Formation of interface bubbles in bonded silicon wafers: A thermodynamic model," *Applied Physics A*, vol. 54, no. 6, pp. 543–552, 1992.

[45] K. Reinhardt and W. Kern, *Handbook of silicon wafer cleaning technology*. William Andrew, 2018.

[46] U. Gösele and Q.-Y. Tong, "Semiconductor wafer bonding," *Annual review of materials science*, vol. 28, no. 1, pp. 215–241, 1998.

[47] F. Rieutord, B. Bataillou, and H. Moriceau, "Dynamics of a bonding front," *Physical review letters*, vol. 94, no. 23, p. 236101, 2005.

[48] H. Moriceau, F. Rieutord, C. Morales, A. Charvet, O. Rayssac, B. Bataillou, F. Fournel, J. Eymery, A. Pascale, P. Gentile *et al.*, "Direct wafer bonding for nanostructure preparations," in *Solid State Phenomena*, vol. 121. Trans Tech Publ, 2007, pp. 29–32.

[49] F. Rieutord, L. Capello, R. Beneyton, C. Morales, and H. Moriceau, "Ecs-ix wafer bonding conf. p.205," 2006.

[50] C. Ventosa, C. Morales, L. Libralesso, F. Fournel, A. Papon, D. Lafond, H. Moriceau, J. Penot, and F. Rieutord, "Mechanism of thermal silicon oxide direct wafer bonding," *Electrochemical and Solid-State Letters*, vol. 12, no. 10, p. H373, 2009.

[51] C. Rauer, "Collage de silicium et d'oxyde de silicium : mécanismes mis en jeu," Theses, Université de Grenoble, Jul. 2014. [Online]. Available: https://tel.archives-ouvertes.fr/tel-01304195

[52] Ö. Vallin, K. Jonsson, and U. Lindberg, "Adhesion quantification methods for wafer bonding," *Materials Science and Engineering: R: Reports*, vol. 50, no. 4-5, pp. 109–165, 2005.

[53] P. P. Gillis and J. J. Gilman, "Double-cantilever cleavage mode of crack propagation," *Journal of Applied Physics*, vol. 35, no. 3, pp. 647–658, 1964.

[54] J. J. Gilman, "Direct measurements of the surface energies of crystals," *Journal of applied physics*, vol. 31, no. 12, pp. 2208–2218, 1960.

[55] P. P. Gillis, "Surface-energy determinations by cleavage," *Journal of Applied Physics*, vol. 36, no. 4, pp. 1374–1376, 1965.

[56] M. Petzold, H. Knoll, and J. Bagdahn, "Strength assessment of wafer-bonded micromechanical components using the micro-chevron test," in *Reliability, Testing, and Characterization of MEMS/MOEMS*, vol. 4558. SPIE, 2001, pp. 133–142.

[57] K. T. Turner and S. M. Spearing, "Accurate characterization of wafer bond toughness with the double cantilever specimen," *Journal of applied physics*, vol. 103, no. 1, p. 013514, 2008.

[58] S. Sokolov, "On the problem of the propagation of ultrasonic oscillations in various bodies," *Elek Nachr Teck*, vol. 6, pp. 454–460, 1929.

[59] ——, "Means for indicating flaws in materials," *US Patent 2,164,125*, 1939.

[60] F. Dunn and W. J. Fry, "Ultrasonic absorption microscope," *The Journal of the Acoustical Society of America*, vol. 31, no. 5, pp. 632–633, 1959.

[61] J. C. P. McKeon, "Frequency domain filtering for enhanced sam inspection of microelectronic components," in *Acoustical Imaging*, ser. Acoustical Imaging. Boston, MA: Springer US, pp. 353–361.

[62] A. Korpel, L. Kessler, and P. Palermo, "Acoustic microscope operating at 100 mhz," *Nature*, vol. 232, no. 5306, pp. 110–111, 1971.

[63] R. Lemons and C. F. Quate, "Acoustic microscope—scanning version," *Applied Physics Letters*, vol. 24, no. 4, pp. 163–165, 1974.

[64] R. Johnston, A. Atalar, J. Heiserman, V. Jipson, and C. Quate, "Acoustic microscopy: resolution of subcellular detail." *Proceedings of the National Academy of Sciences*, vol. 76, no. 7, pp. 3325–3329, 1979.

[65] M. B. Catherine POTEL, *Acoustique générale : Equations différentielles et intégrales, solutions en milieux fluides et solides, applications.* Ellipses, 2016.

[66] A. Ng and J. Swanevelder, "Resolution in ultrasound imaging," *Continuing Education in Anaesthesia Critical Care & Pain*, vol. 11, no. 5, pp. 186–192, 2011.

[67] B. Moudjed, "Caractérisation expérimentale et théorique des écoulements entrainés par ultrasons. perspectives d'utilisation dans les procédés de solidification du silicium photovoltaïque," Ph.D. dissertation, Lyon, INSA, 2013.

[68] L. E. Kinsler, A. R. Frey, A. B. Coppens, and J. V. Sanders, *Fundamentals of acoustics.* John wiley & sons, 2000.

[69] E. D. Daniel Royer, *Ondes élastiques dans les solides.* MASSON, 1996.

[70] F. Mouhat and F.-X. Coudert, "Necessary and sufficient elastic stability conditions in various crystal systems," *Physical review B*, vol. 90, no. 22, p. 224104, 2014.

[71] D. ROYER and E. DIEULESAINT, "Acoustique-propagation dans un solide," 2001.

[72] E. Le Clézio, "Diffraction des ondes de lamb par des fissures verticales," Ph.D. dissertation, Bordeaux 1, 2001.

[73] J. L. Rose, "Ultrasonic waves in solid media," 2000.

[74] H. Lamb, "On waves in an elastic plate," *Proceedings of the Royal Society of London. Series A, Containing papers of a mathematical and physical character*, vol. 93, no. 648, pp. 114–128, 1917.

[75] A. Pilarski and J. L. Rose, "A transverse-wave ultrasonic oblique-incidence technique for interfacial weakness detection in adhesive bonds," *Journal of Applied Physics*, vol. 63, no. 2, pp. 300–307, 1988.

[76] E. Lloyd, "Non-destructive testing of bonded joints: a case for testing laminated structures by wide-band ultrasound," *Non-Destructive Testing*, vol. 7, no. 6, pp. 331–334, 1974.

[77] F. H. Chang, P. Flynn, D. Gordon, and J. Bell, "Principles and application of ultrasonic spectroscopy in nde of adhesive bonds," *IEEE Transactions on Sonics and Ultrasonics*, vol. 23, no. 5, pp. 334–338, 1976.

[78] G. Biggiero, G. Canella, and A. Mossini, "Ultrasonic scanning and spectrum analysis for inspection of bond efficiency of metal-to-metal structural adhesive joints," *NDT international*, vol. 16, no. 2, pp. 67–73, 1983.

[79] C. Guyott, P. Cawley, and R. Adams, "Use of the fokker bond tester on joints with varying adhesive thickness," *Proceedings of the Institution of Mechanical Engineers, Part B: Management and engineering manufacture*, vol. 201, no. 1, pp. 41–49, 1987.

[80] C. Guyott and P. Cawley, "The ultrasonic vibration characteristics of adhesive joints," *The Journal of the Acoustical Society of America*, vol. 83, no. 2, pp. 632–640, 1988.

[81] S. Rokhlin and D. Marom, "Study of adhesive bonds using low-frequency obliquely incident ultrasonic waves," *The Journal of the Acoustical Society of America*, vol. 80, no. 2, pp. 585–590, 1986.

[82] Y. Tsukahara and K. Ohira, "Detection of smooth bondings of polymer coatings by ultrasonic spectroscopy," *Ultrasonics*, vol. 27, no. 1, pp. 3–7, 1989.

[83] S. Rokhlin, M. Hefets, and M. Rosen, "An ultrasonic interface-wave method for predicting the strength of adhesive bonds," *Journal of applied physics*, vol. 52, no. 4, pp. 2847–2851, 1981.

[84] A. Pilarski, "Ultrasonic evaluation of the adhesion degree in layered joints," *Materials Evaluation*, vol. 43, no. 6, pp. 765–770, 1985.

[85] I. Molinero, "Contribution a l'etude de la diffusion acoustique par des plaques et des fils en incidence oblique: generation d'ondes de surface et d'ondes guidees," Ph.D. dissertation, Paris 7, 1987.

[86] Y. Benel Mostafa, "Étude de la propagation des ondes ultrasonores dans un milieu multicouche: application à l'évaluation non destructive de collages," Ph.D. dissertation, Compiègne, 1990.

[87] M. Lowe and P. Cawley, "The applicability of plate wave techniques for the inspection of adhesive and diffusion bonded joints," *Journal of Nondestructive Evaluation*, vol. 13, no. 4, pp. 185–200, 1994.

[88] C. Gauthier, M. E.-C. El-Kettani, J. Galy, M. Predoi, D. Leduc, and J.-L. Izbicki, "Lamb waves characterization of adhesion levels in aluminum/epoxy bi-layers with different cohesive and adhesive properties," *International Journal of Adhesion and Adhesives*, vol. 74, pp. 15–20, 2017.

[89] A. Shuvalov, E. Le Clezio, and G. Feuillard, "The state-vector formalism and the peano-series solution for modelling guided waves in functionally graded anisotropic piezoelectric plates," *International Journal of Engineering Science*, vol. 46, no. 9, pp. 929–947, 2008.

[90] M. Lam, E. Le Clézio, H. Amorin, M. Alguero, J. Holc, M. Kosec, A. Hladky-Hennion, and G. Feuillard, "Acoustic wave transmission through piezoelectric structured materials," *Ultrasonics*, vol. 49, no. 4-5, pp. 424–431, 2009.

[91] P. B. Nagy and L. Adler, "Nondestructive evaluation of adhesive joints by guided waves," *Journal of Applied Physics*, vol. 66, no. 10, pp. 4658–4663, 1989.

[92] P.-C. Xu and S. Datta, "Guided waves in a bonded plate: A parametric study," *Journal of Applied Physics*, vol. 67, no. 11, pp. 6779–6786, 1990.

[93] M. Karim, A. Mal, and Y. Bar-Cohen, "Inversion of leaky lamb wave data by simplex algorithm," *The Journal of the Acoustical Society of America*, vol. 88, no. 1, pp. 482–491, 1990.

[94] P.-C. Xu, A. Mal, and Y. Bar-Cohen, "Inversion of leaky lamb wave data to determine cohesive properties of bonds," *International journal of engineering science*, vol. 28, no. 4, pp. 331–346, 1990.

[95] O. Behrend, A. Kulik, and G. Gremaud, "Characterization of thin films using numerical inversion of the generalized lamb wave dispersion relation," *Applied physics letters*, vol. 62, no. 22, pp. 2787–2789, 1993.

[96] W. Parmon and H. L. Bertoni, "Ray interpretation of the material signature in the acoustic microscope," *Electronics Letters*, vol. 21, no. 15, pp. 684–686, 1979.

[97] H.-S. Ju and B. R. Tittmann, "Recent advances in scanning acoustic microscopy for adhesion evaluation of thin films," *Journal of the Korean Society for Nondestructive Testing*, vol. 29, no. 6, pp. 534–549, 2009.

[98] K. Kosbi, T. Blum, U. Scheer, and S. Boseck, "Evaluation of imperfect gold/glass interfaces using scanning acoustic microscopy," in *Acousto-Optics and Applications III*, vol. 3581. SPIE, 1998, pp. 314–319.

[99] W. T. Thomson, "Transmission of elastic waves through a stratified solid medium," *Journal of applied Physics*, vol. 21, no. 2, pp. 89–93, 1950.

[100] L. Brekhovskikh, "Waves in layered media, newyork, ny, usa: Academic," 1960.

[101] N. Haskell, "The dispersion of surface waves in multi layered media," 1953.

[102] D. Folds and C. Loggins, "Transmission and reflection of ultrasonic waves in layered media," *The Journal of the Acoustical Society of America*, vol. 62, no. 5, pp. 1102–1109, 1977.

[103] P. Cervenka and P. Challande, "A new efficient algorithm to compute the exact reflection and transmission factors for plane waves in layered absorbing media (liquids and solids)," *The Journal of the Acoustical Society of America*, vol. 89, no. 4, pp. 1579–1589, 1991.

[104] M. Munjal, "Response of a multi-layered infinite plate to an oblique plane wave by means of transfer matrices," *Journal of Sound and Vibration*, vol. 162, no. 2, pp. 333–343, 1993.

[105] B. Hosten, "Bulk heterogeneous plane waves propagation through viscoelastic plates and stratified media with large values of frequency domain," *Ultrasonics*, vol. 29, no. 6, pp. 445–450, 1991.

[106] J. Sastry and M. Munjal, "A transfer matrix approach for evaluation of the response of a multi-layer infinite plate to a two-dimensional pressure excitation," *Journal of sound and vibration*, vol. 182, no. 1, pp. 109–128, 1995.

[107] F. Fournel, A. Dekious, E. Deloffre, G. Despaux, V. Larrey, and E. Le Clezio, "Method and device for checking a bond between two substrates," Jul. 6 2021, uS Patent 11,054,402.

Acronyms

AFM : Atomic force microscopy

CMP : Chemical-mechanical polishing

DCB : Double Cantilever Beam

IC : Integrated circuit

KGD : Known good die

MCM : Multi-chip module

NDT : Nondestructive testing

RMS : Root Mean Square

RT : Room temperature

SiP : System in Packages

TSV : Trough Silicon Vias

WLP : Wafer Level Packaging

XRR : X-Ray Reflectometry

TITRE : Caractérisation acoustique de l'énergie de collage direct

RESUME :

Le collage direct est une technique d'assemblage de semi-conducteur prisée par l'industrie de la microélectronique. Cette méthode ne nécessite pas de matière adhésive pour atteindre des niveaux d'adhésion de qualité. La qualité du collage est définie par deux paramètres : la présence de défauts à l'interface et l'énergie de collage. Le contrôle de l'énergie de collage est effectué actuellement avec la technique de clivage de coin. Cette technique permet de mesurer l'énergie de collage grâce à l'ouverture de l'échantillon, ce qui détériore les wafers. C'est dans ce contexte que la microscopie acoustique peut interagir pour apporter une approche différente comme étant une méthode non destructive. Le premier défi devant la caractérisation de l'énergie de collage est l'épaisseur de la couche de collage qui est de l'ordre de quelques nanomètres. Ces dimensions ne permettent pas de récupérer un signal temporel de l'interface du collage. Pour s'affranchir de cette contrainte, l'analyse dans le domaine des fréquences en s'appuyant sur le concept de résonance d'une plaque multicouche est la méthode proposée. Les résultats présentés ont été obtenus grâce à la modélisation de la propagation d'onde ultrasonore hautes fréquences (de l'ordre de 200 MHz) au sein de structures multicouches. Une étude de sensibilité sera présentée, permettant d'identifier le potentiel de la méthode de caractérisation. D'un point de vue expérimental, les résultats obtenus sur les microscopes acoustiques de laboratoire et industriels permettent de comparer les mesures acoustiques avec celles obtenues par des méthodes usuelles destructives. Les expériences qui ont été menées à ce jour permettent d'identifier les limites actuelles du banc de test et de proposer des changements permettant d'approcher les résultats théoriques.

Mots clés : Acoustique, CND, Ultrasons, Collage direct.

UNIVERSITE DE MONTPELLIER
Institut d'Electronique et des Systèmes - UMR CNRS 5214
860 Rue Saint Priest, 34095 Montpellier

TITLE : Acoustic characterisation of bonding energy

ABSTRACT :

Direct bonding is an essential wafer assembly technique for 3D ICs applications. This process doesn't require any adhesive material. Its quality is mainly defined by two parameters: the presence of imperfections at the interface and the bonding energy. In other to quantify the bonding energy, DCB (Double Cleavage Beam technique) is mainly the current performed technique. But it is not a NDT (None Destructive Technique). Scanning acoustic microscopy (SAM) could relax this issue. The first challenge facing the bonding energy characterization by SAM is the thickness of the bonding layer which is less than one nanometers. In these conditions, the time signal related to the bonding interface isn't recovered. To counterbalance this constraint, frequency domain analysis based on the concept of multilayer resonance is proposed. The results obtained within the propagation modelization of high-frequency ultrasound waves (of the range of 200 MHz) in a multilayer structure shows the feasibility of the detection of bonding quality. Sensibility studies have shown the potential of the technique presented. Experimentally, the results obtained on the bench test allows comparing acoustic measurements with those obtained by destructive methods. The studies carried out so far allow identifying the current limitations of the test bench and to propose changes allowing reaching the theoretical results linking the bonding energy to the frequency of the ultrasonic resonance of the structure.

Keywords : Acoustic, NDT, Direct Bonding Technology.

UNIVERSITE DE MONTPELLIER
Institut d'Electronique et des Systèmes - UMR CNRS 5214
860 Rue Saint Priest, 34095 Montpellier